A thermo-mechanical finite deformation theory of plasticity for amorphous polymers: application to micro-hot-embossing of poly(methyl methacrylate)

by

Nicoli Margret Ames

S.B., Massachusetts Institute of Technology (2000)
S.M., Massachusetts Institute of Technology (2003)

Submitted to the Department of Mechanical Engineering
in partial fulfillment of the requirements for the degree of

Doctor of Philosophy

at the

Massachusetts Institute of Technology

June 2007

Author .....
Department of Mechanical Engineering
May 24, 2007

Certified by .....
Lallit Anand
Professor of Mechanical Engineering
Thesis Supervisor

Accepted by .....
Lallit Anand
Chairman, Department Committee on Graduate Students

A thermo-mechanical finite deformation theory of plasticity for amorphous polymers: application to micro-hot-embossing of poly(methyl methacrylate)

by
Nicoli Margret Ames

Submitted to the Department of Mechanical Engineering
on May 24, 2007, in partial fulfillment of the
requirements for the degree of
Doctor of Philosophy

Abstract

Amorphous thermoplastic polymers are important engineering materials; however, their nonlinear, strongly temperature- and rate-dependent elastic-visco-plastic behavior has, until now, not been very well understood. The behavior has previously been modeled with mixed success by existing constitutive theories. As a result, there is currently no generally agreed upon theory to model the large-deformation, thermo-mechanically coupled, elasto-visco-plastic response of amorphous polymeric materials spanning their glass transition temperatures. What is needed is a unified constitutive framework that is capable of capturing the transition from a visco-elastic-plastic solid-like response below the glass transition temperature, to a rubbery-viscoelastic response above the glass transition temperature, to a fluid-like response at yet higher temperatures.

We have developed a continuum-mechanical constitutive theory aimed to fill this need. The theory has been specialized to represent the salient features of the mechanical response of poly(methyl methacrylate) in a temperature range spanning room temperature to $\approx 60°$C above the glass transition temperature $\vartheta_g \approx 110°$C of the material, in a strain-rate range of $\approx 10^{-4}$/s to 10^{-1}/s, and under compressive stress states in which this material does not exhibit crazing. We have implemented our theory in the finite element program ABAQUS/Explicit. The numerical simulation capability of the theory is demonstrated with simulations of the micron-scale hot-embossing process for manufacture of microfluidic devices.

Thesis Supervisor: Lallit Anand
Title: Professor of Mechanical Engineering

Acknowledgments

I would like to thank Prof Lallit Anand (chair), Prof Mary Boyce, Prof David Hardt, and Prof Catherine Klapperich for serving on my committee. Their advice was incredibly helpful during the course of my PhD program. I would like to extend a special thanks to Prof Anand for being a fantastic advisor during my stay at MIT. He has guided me through 10 of my 11 years as an MIT student. Starting in my sophomore year here, he served as my academic advisor, then later as my UROP supervisor before becoming my thesis advisor throughout my graduate studies. His constant encouragement and guidance, as well as eagerness to participate in my research, even when I was not so optimistic about it, was very motivating.

To all current and past student, faculty, and staff of the Mechanics and Materials group, I'd like to extend my thanks to all that have helped me over the years, including: Ray Hardin, Pierce Hayward, Prof David Parks, Dr Brian Gearing, Dr Prakash Thamburaja, Sauri Gudlavalleti, Dr Rajdeep Sharma, Dr Theodora Tzianetopoulou, Dr Mats Danielsson, Dr Jin Yi, Dr Ethan Parsons, Dr Yujie Wei, Anastassia Paskaleva, Dr Cheng Su, Regina Huang, Vikas Srivastava, Shawn Chester, and David Hennan.

For helping out with my experimental results in the days before my defense, I'd like to thank Hayden Taylor, Matt Dirckx, Emre Ozkumur. If it weren't for them, I would not have finished on time. An extra special thanks is extended to Hayden Taylor who went spent hours helping me complete the microembossing experiments and also gather the SEM and birefringence images.

And finally, I would like to thank my entire family in the great Pacific Northwest, but especially my parents William Ames & Vera Lillig and Pamela & Robert Crowell, my big sister Erin Ames-Miller, and my grandparents Madge & George Ames.

Contents

List of Figures **11**

List of Tables **15**

1 Introduction **17**
Bibliography . . . 19

2 Simple Compression Experiments on PMMA **21**
2.1 Introduction . . . 21
2.2 Procedure . . . 22
2.3 Results . . . 24
Bibliography . . . 33

3 Thermo-mechanically-coupled Finite-deformation Theory **35**
3.1 Introduction . . . 35
3.2 Theory . . . 36
3.2.1 Notation . . . 36
3.2.2 Kinematics . . . 36
3.2.3 Frame-indifference . . . 38
3.2.4 Development of the theory based on the principle of virtual power . . . 39
3.2.5 Balance of energy. Entropy imbalance. Local dissipation inequality . . . 43
3.3 Constitutive theory . . . 46
3.3.1 Thermodynamic restrictions . . . 47
3.3.2 Isotropy . . . 51
3.3.3 Separability hypothesis for the free energy . . . 53
3.3.4 Codirectionality and strong isotropy hypotheses . . . 55
3.4 Summary of the constitutive theory for isotropic materials . . . 56
3.4.1 Partial differential equations for the deformation and temperature fields . . . 58
3.5 Specialization of the constitutive equations . . . 58
3.5.1 Case alpha = 1 . . . 59
3.5.2 Case alpha = 2 — Molecular network resistance . . . 66

3.6 Summary of the specialized constitutive model using two micromechanisms alpha = 1, 2 . . . 69
3.6.1 Constitutive equations for alpha=1, intermolecular resistance . . . 70
3.6.2 Constitutive equations for alpha=2, molecular network resistance . . . 72
3.7 Partial differential equations for the deformation and temperature fields . . . 74
Bibliography . . . 75

4 Application of the theory to PMMA below its glass transition temperature 79
4.1 Introduction . . . 79
4.2 Summary of the Specialized Material Model . . . 79
4.2.1 Summary of Three-Dimensional Constitutive Equations . . . 80
4.2.2 Summary of One-Dimensional Constitutive Equations . . . 88
4.3 Material Parameter Calibration Below the Glass Transition . . . 93
4.3.1 One-Dimensional Model Calibration Procedure . . . 93
4.3.2 Three-Dimensional Model Calibration Procedure . . . 106
4.3.3 Internal Heating . . . 110
4.4 Summary of Equations and Parameters . . . 116
Bibliography . . . 119

5 Application of the theory to PMMA through its glass transition temperature 121
5.1 Introduction . . . 121
5.2 Summary of the Specialized Material Model . . . 121
5.2.1 Summary of Three-Dimensional Constitutive Equations . . . 122
5.2.2 Summary of One-Dimensional Constitutive Equations . . . 130
5.3 Material Parameter Calibration Through the Glass Transition . . . 137
5.3.1 One-Dimensional Material Parameter Calibration Procedure . . . 137
5.3.2 Three-Dimensional Model Calibration Procedure . . . 157
5.3.3 Internal Heating . . . 163
5.4 Summary of Equations and Parameters . . . 171
Bibliography . . . 174

6 Hot Embossing of PMMA 177
6.1 Introduction . . . 177
6.2 Macro-embossing . . . 178
6.2.1 Experiments . . . 178
6.2.2 Axisymmetric Simulations . . . 186
6.3 Micro-embossing . . . 189
6.3.1 Experiments . . . 189
6.3.2 Isothermal Plane-Strain Simulations . . . 196
Bibliography . . . 199

7 Conclusions 201
Bibliography . . . 202

A Experimental Procedure Details **203**
A.1 Introduction 203
A.2 Procedures 203
A.2.1 Strain Control 204
A.2.2 Load Cells 206
A.2.3 Specimen Heating 206
A.2.4 Temperature Measurement and Compensation 217

List of Figures

2-1 Heated compression experiments load train . . . 23
2-2 Compression experiments at 3×10^{-4}/s . . . 25
2-3 Compression experiments at 10^{-3}/s . . . 26
2-4 Compression experiments at 10^{-2}/s . . . 27
2-5 Compression experiments at 10^{-1}/s . . . 28
2-6 Compression experiments at 25 C, 50 C, and 70 C . . . 29
2-7 Compression experiments at 90 C, 100 C, and 110 C . . . 30
2-8 Compression experiments at 120 C and 130 C . . . 31
2-9 Compression experiments at 150 C and 170 C . . . 32

4-1 One-dimensional rheological representation of the proposed model . . . 80
4-2 One-element adiabatic power density contributions of original heat equation . . . 87
4-3 Yield stress selection . . . 94
4-4 Experimental yield stress versus strain rate isotherms . . . 95
4-5 Model fit of yield stress versus strain rate isotherms . . . 97
4-6 Back stress dependence on material parameter γ . . . 98
4-7 MATLAB room-temperature creep results . . . 98
4-8 MATLAB below-Tg results at 3×10^{-4}/s and 10^{-3}/s, no yield peak . . . 100
4-9 MATLAB below-Tg results at 10^{-2}/s and 10^{-1}/s, no yield peak . . . 101
4-10 Effect of varying material parameters $\{b, g, h\}$ . . . 103
4-11 MATLAB below-Tg results at 3×10^{-4}/s and 10^{-3}/s . . . 104
4-12 MATLAB below-Tg results at 10^{-2}/s and 10^{-1}/s . . . 105
4-13 ABAQUS and MATLAB results comparison . . . 107
4-14 ABAQUS one-element isothermal below-Tg results at 3×10^{-4}/s and 10^{-3}/s . . . 108
4-15 ABAQUS one-element isothermal below-Tg results at 10^{-2}/s and 10^{-1}/s . . . 109
4-16 Specific heat of PMMA versus temperature . . . 110
4-17 Thermal conductivity of PMMA versus temperature . . . 111
4-18 Finite element geometry for thermo-mechanically coupled compression . . . 112
4-19 ABAQUS multi-element fully-coupled below-Tg results at 3×10^{-4}/s and 10^{-3}/s . . . 113
4-20 ABAQUS multi-element fully-coupled below-Tg results at 10^{-2}/s and 10^{-1}/s . . . 114
4-21 ABAQUS multi-element fully-coupled below-Tg nodal temperature rise contour at 10^{-1}/s . . . 115

4-22 ABAQUS multi-element fully-coupled below-Tg temperature rise results at 298 K . . 115

5-1 One-dimensional rheological representation of the proposed model 122
5-2 Schematic of phenomenological temperature dependence of the shear modulus G . . 124
5-3 Schematic of phenomenological temperature dependence of the elastic modulus E . . 131
5-4 Yield stress selection 138
5-5 Experimental yield stress versus strain-rate isotherms 139
5-6 Model fit of yield stress versus strain-rate isotherms 140
5-7 WLF fit of $\dot{\epsilon}^*(\vartheta > \vartheta_g)$ 141
5-8 Back stress dependence on material parameter γ 143
5-9 MATLAB room-temperature creep results 143
5-10 Elastic modulus fit 144
5-11 Fit of Gent modulus versus temperature 145
5-12 Fit of Gent locking parameter versus temperature 145
5-13 MATLAB simulation and experiments at 3×10^{-4}/s, no yield peak 147
5-14 MATLAB simulation and experiments at 10^{-3}/s, no yield peak 148
5-15 MATLAB simulation and experiments at 10^{-2}/s, no yield peak 149
5-16 MATLAB simulation and experiments at 10^{-1}/s, no yield peak 150
5-17 Effect of varying material parameters $\{b, g, h\}$ 152
5-18 MATLAB simulation and experiments at 3×10^{-4}/s 153
5-19 MATLAB simulation and experiments at 10^{-3}/s 154
5-20 MATLAB simulation and experiments at 10^{-2}/s 155
5-21 MATLAB simulation and experiments at 10^{-1}/s 156
5-22 ABAQUS and MATLAB results comparison 158
5-23 ABAQUS one-element isothermal results at 3×10^{-4}/s 159
5-24 ABAQUS one-element isothermal results at 10^{-3}/s 160
5-25 ABAQUS one-element isothermal results at 10^{-2}/s 161
5-26 ABAQUS one-element isothermal results at 10^{-1}/s 162
5-27 Specific heat of PMMA versus temperature 163
5-28 Thermal conductivity of PMMA versus temperature 164
5-29 Finite element geometry for thermo-mechanically coupled compression 165
5-30 ABAQUS multi-element fully-coupled below-Tg results at 3×10^{-4}/s 166
5-31 ABAQUS multi-element fully-coupled below-Tg results at 10^{-3}/s 167
5-32 ABAQUS multi-element fully-coupled below-Tg results at 10^{-2}/s 168
5-33 ABAQUS multi-element fully-coupled below-Tg results at 10^{-1}/s 169
5-34 ABAQUS multi-element fully-coupled below-Tg nodal temperature contour at 10^{-1}/s 170
5-35 ABAQUS multi-element fully-coupled below-Tg temperature rise results at 298 K . . 170

6-1 Hot embossing process cycle schematic 177
6-2 Drawing of embossing tool 179
6-3 Drawing of embossing assembly 180
6-4 Load train thermal contraction 181
6-5 Zygo interferometer height contours of macro-embossed PMMA parts and tool . . . 183
6-6 Zygo interferometer height profiles of macro-embossed PMMA parts and tool 183
6-7 SEM image of macro-embossed PMMA part 184

6-8 Birefringence pattern in PMMA disks embossed at 170 C and 100 C 185
6-9 Finite element geometry for embossing simulation 186
6-10 Embossing simulation and experiment profile for 100 C test 187
6-11 Embossing simulation and experiment profile for 170 C test 187
6-12 Simulation residual stresses in PMMA disk embossed at 100 C 188
6-13 Simulation residual stresses in PMMA disk embossed at 170 C 188
6-14 SEM and Zygo images of silicon tool used for micro-embossing experiments 190
6-15 Zygo interferometer height contours of micro-embossed PMMA parts 192
6-16 Zygo interferometer height profiles of micro-embossed PMMA parts 193
6-17 SEM images of micro-embossed PMMA parts 194
6-18 SEM images of failed silicon tool 195
6-19 Finite element geometry for isothermal plane-strain micro-embossing simulation . . . 197
6-20 Micro-embossing simulations and experiments 198

A-1 Heated compression experiments load train 207
A-2 Heated platens load train, second generation 208
A-3 Heated platen top engineering drawing, second generation 209
A-4 Top connector 1 engineering drawing, second generation 210
A-5 Top connector 2 engineering drawing, second generation 211
A-6 Heated platen bottom engineering drawing, second generation 212
A-7 Bottom connector engineering drawing, second generation 213
A-8 Extensometer mount engineering drawing, second generation 214
A-9 Extensometer standoff engineering drawing, second generation 214
A-10 Load cell adapter engineering drawing 215
A-11 Threaded rod engineering drawing 216
A-12 Schematic of dummy specimen for temperature calibration 217

List of Tables

4.1 Summary of the five terms in the heat equation of (4.35) 86
4.2 PMMA material parameters for yield point calibration below ϑ_g 96
4.3 Steel material parameters for thermo-mechanically coupled three-dimensional model 111
4.4 Summary of the the one-dimensional equations 116
4.5 Summary of the the three-dimensional equations 117
4.6 PMMA material parameters for one-dimensional model 118
4.7 PMMA material parameters for three-dimensional model 118

5.1 PMMA material parameters for yield point calibration 141
5.2 Steel material parameters for thermo-mechanically coupled three-dimensional model 164
5.3 Summary of the the one-dimensional equations 171
5.4 Summary of the the three-dimensional equations 172
5.5 PMMA material parameters for one-dimensional model 173
5.6 PMMA material parameters for three-dimensional model 173

Chapter 1

Introduction

Transparent, amorphous thermoplastic polymers such as poly(methyl methacrylate) (PMMA), polycarbonate (PC), cyclic olefin copolymers (COC), and cyclic olefin polymers (COP) are emerging as materials of choice for the manufacture of microfluidic devices for numerous applications [e.g., 1, 2]. Of major importance for making the capillary channels in these types of polymeric substrates is the replication method of hot-embossing [e.g., 3, 4]. The basic process of hot-embossing is as follows: a polymer sheet is placed between a flat rigid platen and a patterned tool. The system is then heated up to the embossing temperature at a nominally low pressure. Once at temperature, higher pressure is applied in order to transfer the tool features to the polymer substrate. While still under pressure, the system is cooled to the demolding temperature and the tool is removed from the plastic part.

To optimize the hot-embossing process for a given polymer and to be able to predict the properties of a polymeric part at the end of the process cycle, it is essential to have (a) a thorough understanding of the polymer's thermo-mechanical behavior over the range of strains, strain-rates, and temperatures of interest; (b) an accurate constitutive model which is able to reproduce that behavior; and (c) a suitable numerical tool, such as a finite element package, which employs the constitutive model for carrying out numerical simulations of the hot-embossing process. While there are numerous successful reports of simulating solid-phase forming processes for metals, until recently there have been few analogous studies for polymeric materials. The reason for this is that almost all thermoplastic polymers are processed in their molten state where they have a low viscosity and are easy to form using well-developed methods such as injection molding and extrusion; accordingly, polymer processing models and simulations have predominantly focused on the these operations. However, recently, it has become clear that when micrometer or sub-micrometer accuracies are desired, other polymer processing methods such as hot-embossing may also be suitable. In contrast to injection molding, during the hot-embossing process the polymer experiences a smaller thermal cycle and undergoes smaller bulk material flow, thus allowing for a more accurate and dimensionally stable final part. Unfortunately, embossing typically takes place below a polymer's melt temperature where its mechanical behavior is far more complex. In a molten state, a polymer is customarily modeled as a viscoelastic non-Newtonian fluid. Upon cooling, however, the polymer transitions into a visco-elastic rubbery state, and with further cooling below its glass transition

temperature, the polymer transforms into a compressible visco-elastic-plastic glassy solid with a drastically higher stiffness and viscosity. It is within these rubbery and glassy regions that typical embossing operations take place, yet there is still not a generally agreed upon constitutive theory that is capable of capturing the large-deformation, thermo-mechanically coupled response of these materials for temperatures spanning these regions. Because of this material modeling challenge, the field of hot-embossing process modeling is still not well developed and there are many contributions to the modeling of the hot-embossing process to be made.

In this thesis, it is our goal to model the complete embossing process cycle for PMMA. Because there is currently no comprehensive set of experimental data covering the entire strain rate and temperature process window necessary for hot embossing, it is first necessary to completely characterize the large strain thermo-mechanical behavior of PMMA from room temperature to well above its glass transition. Once the experimental data has been gathered, a constitutive theory can be developed. There are existing theories in the literature, but as with the experimental data, they are limited in their scope. What we need is a single unified framework that can capture the entire large deformation response of the polymer from a visco-elastic-plastic solid below the glass transition to a viscoelastic rubbery fluid above it. With the theory in place and suitably calibrated for our polymer, we can implement it in a finite element package so that we can then simulate hot-embossing process.

The structure of this thesis is as follows. In Chapter 2 we first present the simple compression experiments which were conducted on poly(methyl methacrylate) (PMMA), the material that is the focus of our study. Next we present our recently developed visco-elastic-plastic, themo-mechanically-coupled, large-deformation theory for amorphous polymers in Chapter 3. A specialization of the theory which is useful for polymer processing below the glass transition is presented in Chapter 4 along with a detailed calibration procedure. We further specialize the constitutive theory in Chapter 5 to capture the polymer behavior continuously through the glass transition; calibration of this specialized model is also presented in the chapter. Finally in Chapter 6 we show the utility of our constitutive model and computational procedures in predicting the hot embossing of PMMA with features at the millimeter, and also the micron-scales.

Bibliography

[1] C. H. Ahn, J. W. Choi, G. Beaucage, J. H. Nevin, J.-B. Lee, A. Puntaambekar, and J. Y. Lee. Disposable smart lab on chip for point-of-care clinical diagnostics. *Proceedings of the IEEE*, 92: 154–173, 2004. doi: 10.1109/JPROC.2003.820548.

[2] D.-S. Lee, H. Yang, K.-H. Chung, and H.-B. Pyo. Wafer-scale fabrication of polymer-based microdevices via injection molding and photolithographic micropatterning protocols. *Analytical Chemistry*, 77:5414–5420, 2005. doi: 10.1021/ac050286w.

[3] S. Y. Chou. Nanoimprint lithography and lithographically induced self-assembly. *MRS Bulletin*, pages 512–517, 2001.

[4] B. Billenberg, M. Hansen, D. Johansen, V. Özkapici, C. Jeppesen, P. Szabo, I. M. Obieta, O. Arroyo, J. O. Tegenfeldt, and A. Kristensen. Topas-based lab-on-a-chip microsystems fabricated by thermal nanoimprint lithography. *Journal of Vacuum Science and Technology B: Microelectronics and Nanometer Structures*, 23:2944–2949, 2005. doi: 10.1116/1.2091089.

Chapter 2

Simple Compression Experiments on PMMA

2.1 Introduction

This chapter presents the results of the simple compression experiments which were conducted on poly(methyl methacrylate) (PMMA), the material that is the focus of our study and that which we will use in later chapters to calibrate and verify our model. To accomplish the calibration, we need a set of experimental data that satisfies the following requirements: (i) continuous stress/strain data to at least 100% strain; (ii) a variety of quasi-static strain rates; (iii) temperatures ranging from room temperature through the PMMA glass transition ($\approx$ 110 C) and into its rubbery regime ($>$ 150 C). While there is quite a bit of data on PMMA in the literature, there is no single data-set that satisfies all of these requirements.

Some of the earliest experiments at elevated temperatures on PMMA [1–4] covered a wide range of strain rates at several temperatures up to the glass transition, however these papers report only the yield point data and not complete stress/strain curves. More recent data sets have been published [5–11] which display the complete stress/strain curves for PMMA at various elevated temperatures, however, they are all limited to narrow temperature or strain-rate ranges, or small maximum strain ranges, or they are lacking unloading results. Only the data from Dooling et al. and Palm et al. have results above the glass transition, and those are very limited. Because none of these existing data sets completely satisfy our requirements, we have conducted our own set of compression experiments on PMMA to calibrate and verify the model. These experiments span the temperature range 25 C to 170 C at four strain-rates (3×10^{-4}, 10^{-3}, 10^{-2}, and 10^{-1} /s) and to maximum compressive strains of 100%. The experimental procedure and setup are discussed briefly in the next section, followed by the stress/strain results.

2.2 Procedure

Because PMMA crazes in tension and is known to undergo deformation by shear-yielding in compression, compression is the optimum mode of deformation for hot-embossing in which the stress-states are primarily compressive in nature.

The material used in these experiments was purchased from McMaster-Carr (a commercial vendor) in the form of 0.5" diameter cast rods which were cut into 0.5" tall specimens. Specimens were annealed before and after machining by heating in a furnace to slightly above the glass transition temperature of 110 C and holding at that temperature for two hours. The specimens were then allowed to slowly cool in the furnace to room temperature over a period of several hours. Before a given experiment, the specimen was allowed to anneal at the testing temperature for one hour prior to testing.

To reduce friction at the platen/specimen interface, the platens were polished and thin Teflon (PTFE) films were placed between the specimen and the platens. Oils and greases were not used as lubricants because they may attack or dissolve the PMMA specimens, or cause them to craze.

All experiments were conducted using a biaxial servo-hydraulic Instron testing machine having a normal load capacity of 220 kN over an axial travel of 100 mm and a torque capacity of 2.2 kN-m over a rotational travel of 95°. All strains were measured using an extensometer with a 12.7 mm gauge section and ± 5.08 mm travel. All compression tests were carried out using constant true strain-rate; the details of how this was achieved are given in Appendix A.

Data acquisition was performed on a desktop PC. LabVIEW 6, a customizable data acquisition software package, interfaces with the Instron through a National Instruments PCI card[1] installed in the PC. Raw data was sampled at 1 kHz, however, LabVIEW performed real time averaging before recording data, resulting in a smoothed output with an artificial sampling rate ranging from 5 Hz to 100 Hz depending on the speed of the test.

Because PMMA is a poor thermal conductor, in order to heat the compression specimens thoroughly and efficiently, we were required to use both heated compression platens and an oven. A custom-sized oven was manufactured by ATS.[2] Images of the heated compression platen load train are shown in Figure 2-1. The platens are manufactured from H13 hot-working tool steel.[3] The top platen has a spherical seat integrated into it to help minimize misalignment. The spherical seat is suspended from the steel connecting rod with metal springs. Mounting points for the extensometer are integrated into the load train. The platen temperature is controlled with cartridge heaters and thermocouples inserted into each platen. More details of the setup, including engineering drawings, are given given in Appendix A.

[1] National Instruments PCI Multifunction Data Acquisition Card, Model AT-MIO-16E-10. Analog In: 12bit, 100 kS/s, ranges: ±10V, ±5V, ±2.5V, ±1V, ±500mV, ±250mV, ±100mV, ±50mV; Analog Out: 12bit, 100kS/s, ±10V

[2] ATS Box Oven, Model 3710 Custom. Max 425C; K-type Thermocouple; Internal: 18.5"W x 18.5"D x 10.5"H; External: 23.75"W x 30.5"D x 15"H; 4" x 6" viewport; 2208W; 10.6A; 208VAC, single-phase, 60Hz; Cooling option installed

[3] Carpenter Powder Products H13 Tool Steel (Designation 2101308-0000). 2" dia x 24" long stock

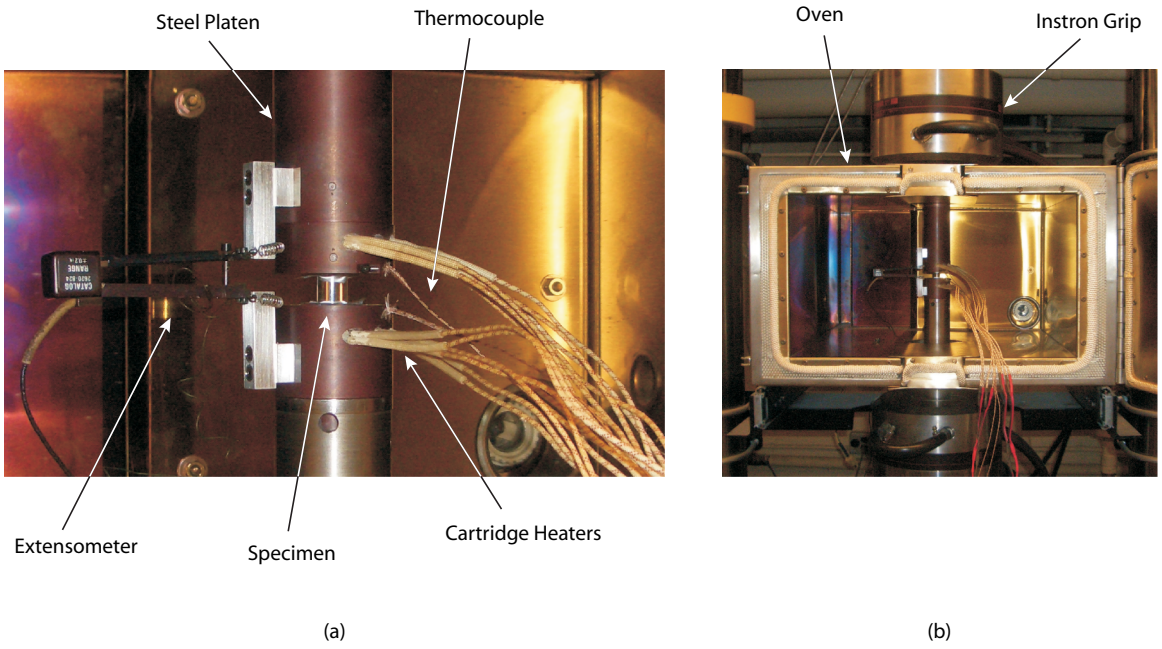

Figure 2-1: Images of the experimental setup used for the heated compression experiments on PMMA. (a) Close up of setup showing the cylindrical PMMA specimen between the two heated platens. The extensometer is mounted on the left side. Cartridge heaters and thermocouples for temperature control are shown on the right. (b) Larger view of setup showing enclosing temperature-controlled oven and Instron grips.

2.3 Results

The results of simple compression experiments on PMMA at 10 temperatures ranging from room temperature through 170 C and at a strain rate of 3×10^{-4} /s is shown in Figure 2-2. As the temperature increases into the glassy region, from 25C to 110 C, the yield strength decreases by an order of magnitude from $\approx$ 100 MPa to $\approx$ 10 MPa, and the strain-hardening observed at large strains due to limited extensibility of the polymer chains diminishes. Approximately 10% strain is recovered upon unloading in this region. Close to the glassy region, at about 100 C, the initial modulus of the material begins to drop and rapidly falls off by three orders of magnitude as the temperature is increased to 130 C. At about 120 C, the yield peak disappears and the material has clearly transitioned into a classical rubber-like response with almost 100% strain-recovery upon unloading. With a further temperature increase to about 150 C, the molecular network begins to slip, and the amount of strain recovered upon unloading reduces to 90%; this is reduced even further to 75% at 170 C.

Experimental results over the same temperature range are shown for strain rates of 10^{-3}, 10^{-2}, and 10^{-1}/s in Figures 2-3, 2-4, and 2-5, respectively. The results are also presented for a fixed temperature and varying strain rates in Figures 2-6, 2-7, 2-8, and 2-9. There are obvious strain-rate dependent features of the material response. In the low-temperature glassy region, the yield strength of the material increases by about 10% for a one-decade increase in strain-rate at any given temperature. Additionally, the glass transition region appears to shift to a higher temperature range with an increase in strain rate. This is most obvious in the results at 120 C (Figure 2-8 top). At the lowest strain rate of 3×10^{-4}/s, the material response is rubber-like, however, at the highest strain rate of 10^{-1}/s, the material behavior looks more similar to a glassy-type response.

Another strain-rate dependent feature is the softening observed at the higher strain rates of 10^{-2} and 10^{-1}/s at the lower temperatures of 25 C, 50 C and 70 C, at large strains (Figure 2-6). In these tests, inelastic dissipation causes internal heating in the compression specimen. No measurements of the actual internal heating were taken during these experiments, however, Arruda et al. [5] showed that the temperature of a compression specimen could increase by as much about 20 C at a strain rate of 10^{-1}/s at an initial temperature of 20 C.

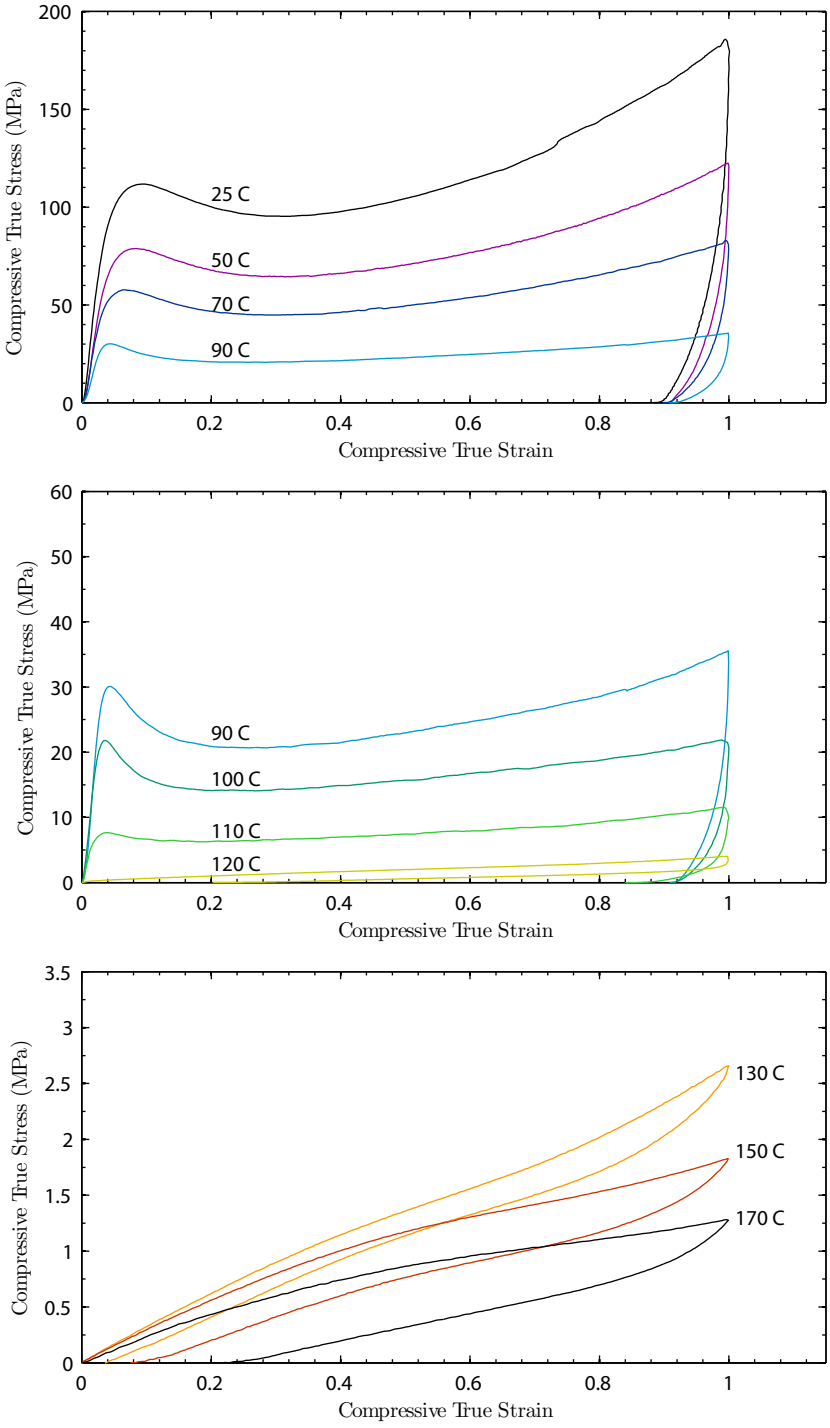

Figure 2-2: Simple compression tests at a strain rate of 3×10^{-4}/s and various temperatures ranging from room temperature through 170 C.

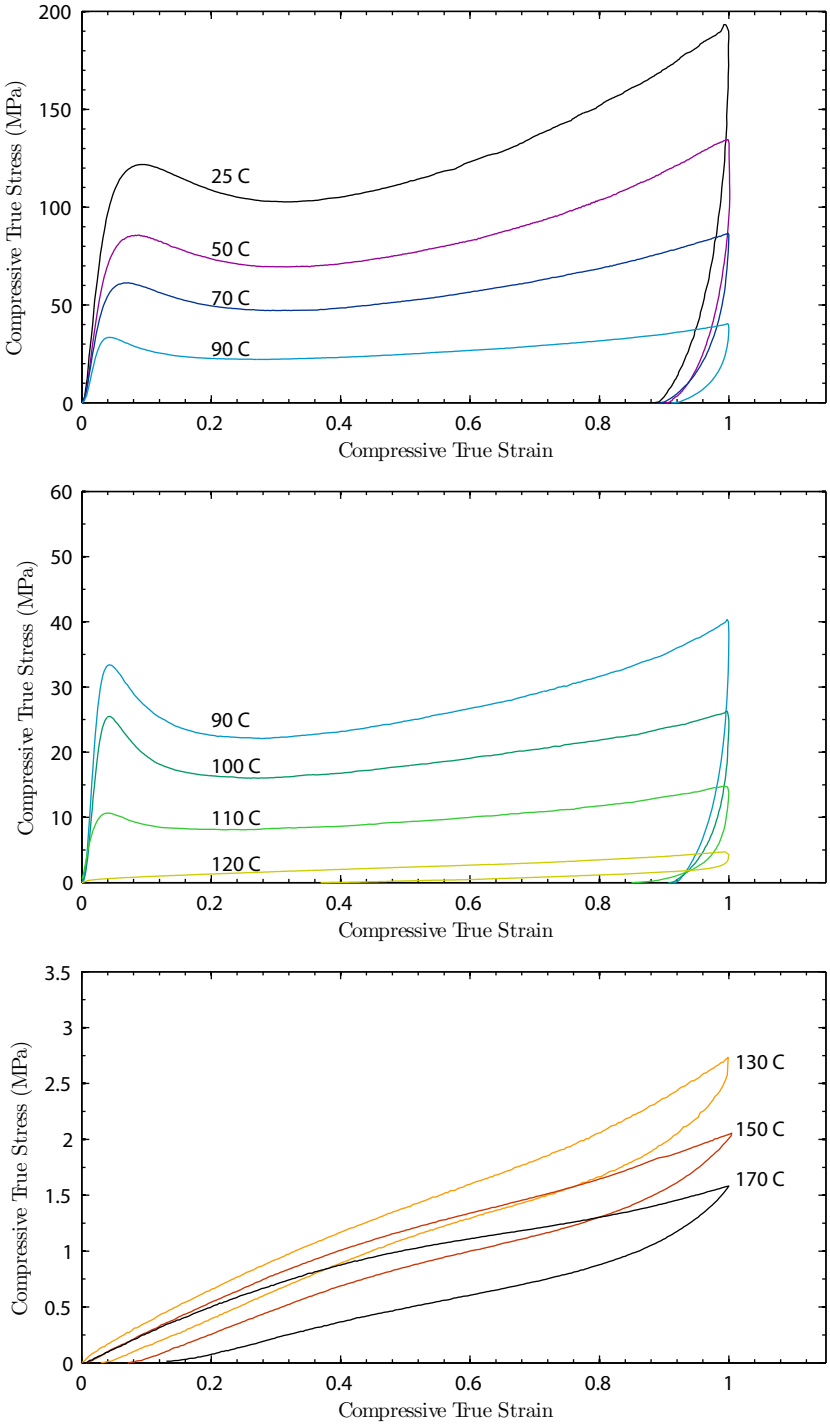

Figure 2-3: Simple compression tests at a strain rate of 10^{-3}/s and various temperatures ranging from room temperature through 170 C.

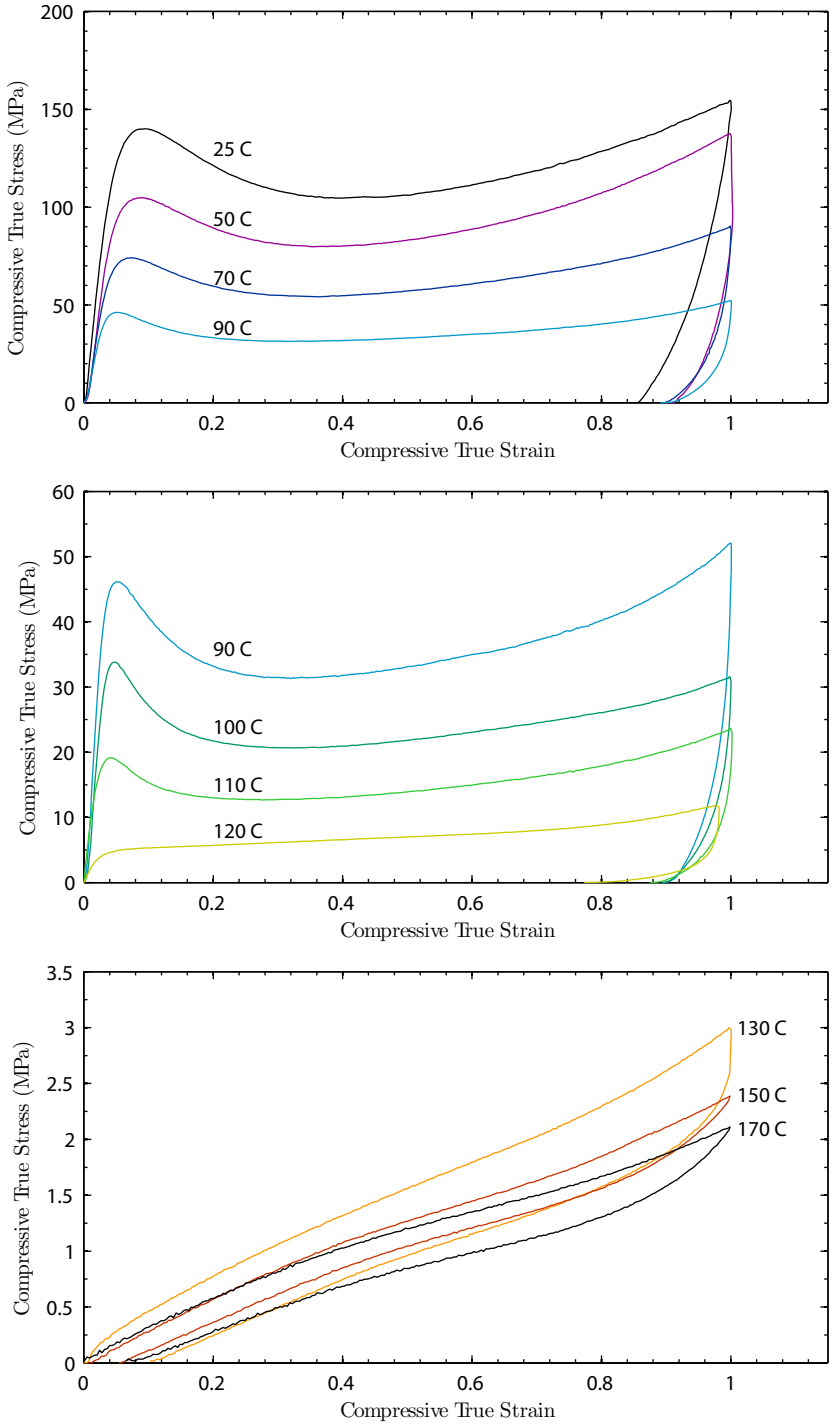

Figure 2-4: Simple compression tests at a strain rate of $10^{-2}/\text{s}$ and various temperatures ranging from room temperature through 170 C.

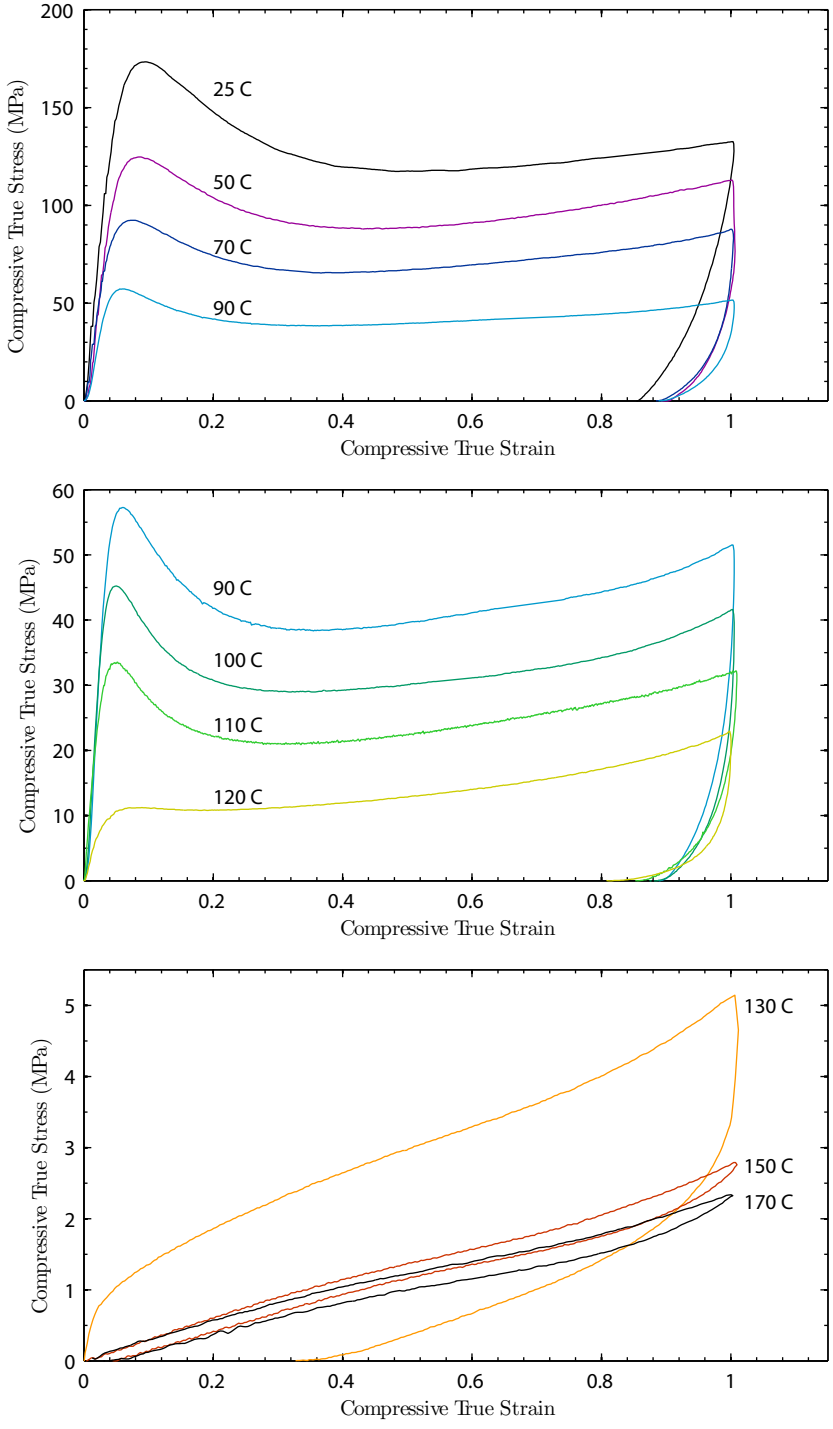

Figure 2-5: Simple compression tests at a strain rate of $10^{-1}/\text{s}$ and various temperatures ranging from room temperature through 170 C.

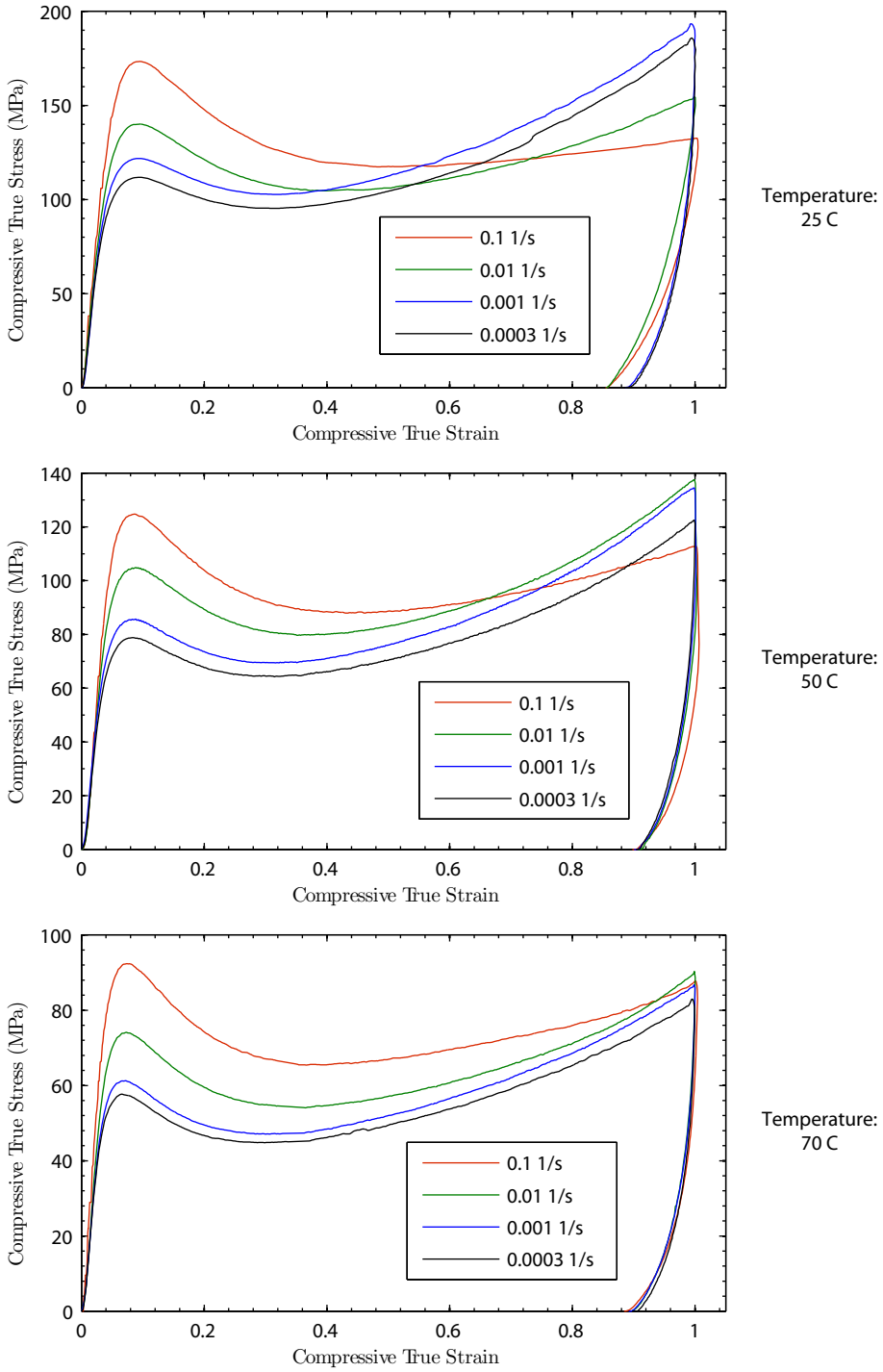

Figure 2-6: Simple compression tests at strain rates of 3×10^{-4}, 10^{-3}, 10^{-2}, and 10^{-1}/s and temperatures of 25 C, 50 C, and 70 C.

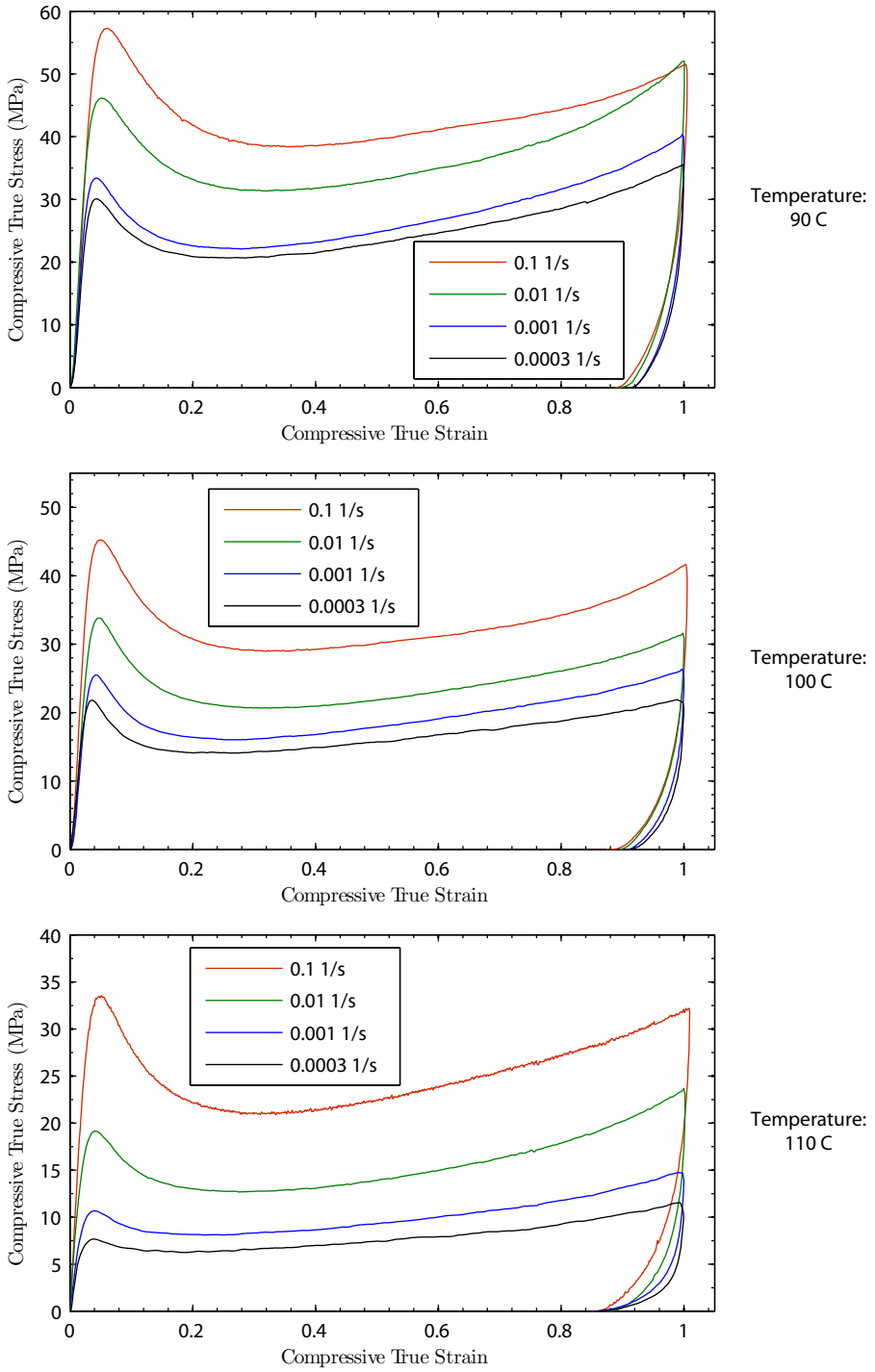

Figure 2-7: Simple compression tests at strain rates of 3×10^{-4}, 10^{-3}, 10^{-2}, and 10^{-1}/s and temperatures of 90 C, 100 C, and 110 C.

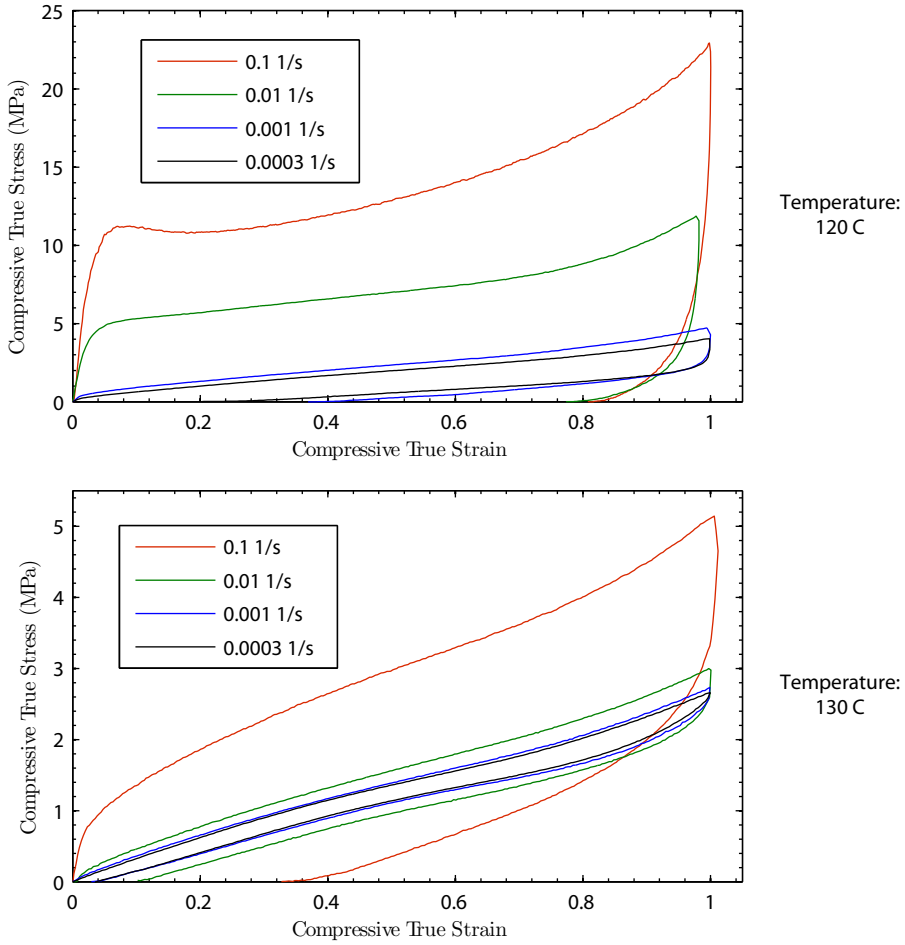

Figure 2-8: Simple compression tests at strain rates of 3×10^{-4}, 10^{-3}, 10^{-2}, and 10^{-1}/s and temperatures of 120 C and 130 C.

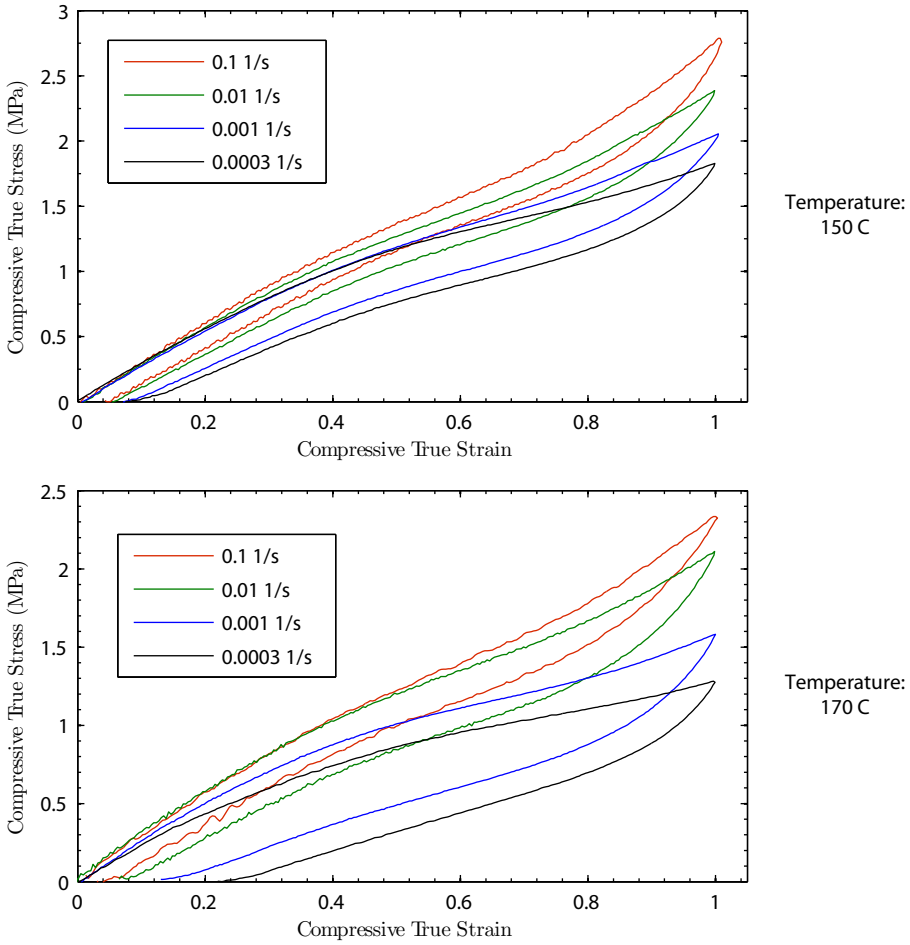

Figure 2-9: Simple compression tests at strain rates of 3×10^{-4}, 10^{-3}, 10^{-2}, and 10^{-1}/s and temperatures of 150 C and 170 C.

Bibliography

[1] C. Bauwens-Crowet and G. A. Homés. Plastic deformation of polymethyl methacrylate in the vitreous domain. *Comptes Rendus Hebdomadaires des Seances de l'Academie des Sciences*, 259:3434–3436, 1964.

[2] J. A. Roetling. Yield stress behaviour of polymethylmethacrylate. *Polymer*, 6:311–317, 1965. doi: 10.1016/0032-3861(65)90081-9.

[3] R. E. Robertson. Theory for the plasticity of glassy polymers. *Journal of Chemical Physics*, 44:3950–3956, 1966. doi: 10.1063/1.1726558.

[4] C. Bauwens-Crowet. The compression yield behaviour of polymethyl methacrylate over a wide range of temperatures and strain-rates. *Journal of Materials Science*, 8:968–979, 1973. doi: 10.1007/BF00756628.

[5] E. M. Arruda, M. C. Boyce, and R. Jayachandran. Effects of strain rate, temperature and thermomechanical coupling on the finite strain deformation of glassy polymers. *Mechanics of Materials*, 19:193–212, 1995. doi: 10.1016/0167-6636(94)00034-E.

[6] O. A. Hasan and M. C. Boyce. A constitutive model for the nonlinear viscoelastic viscoplastic behavior of glassy polymers. *Polymer Engineering and Science*, 35:331–344, 1995. doi: 10.1002/pen.760350407.

[7] P. Tordjeman, L. Teze, J. L. Halary, and L. Monnerie. On the plastic and viscoelastic behavior of methylmethacrylate-based random copolymers. *Polymer Engineering and Science*, 37:1621–1632, 1997. doi: 10.1002/pen.11810.

[8] P. J. Dooling, C. P. Buckley, S. Rostami, and N. Zahlan. Hot-drawing of poly(methylmethacrylate) and simulation using a glass-rubber constitutive model. *Polymer*, 43:2451–2465, 2002. doi: 10.1016/S0032-3861(01)00799-6.

[9] J. Richeton, S. Ahzi, K. S. Vecchio, F. C. Jiang, and R. R. Adharapurapu. Influence of temperature and strain rate on the mechanical behavior of three amorphous polymers: Characterization and modeling of the compressive yield stress. *InternationalJournal of Solids and Structures*, 43:2318–2335, 2006. doi: 10.1016/j.ijsolstr.2005.06.040.

[10] S. F. Lee and G. M. Swallowe. Quasi-static and dynamic compressive behaviour of poly(methyl methacrylate) and polystyrene at temperatures from 293 k to 363 k. *Journal of Materials Science*, 41:6280–6289, 2006. doi: 10.1007/s10853-006-0506-9.

[11] G. Palm, R. B. Dupaix, and J. Castro. Large strain mechanical behavior of poly(methyl methacrylate) (pmma) near the glass transition temperature. *Journal of Engineering Materials and Technology*, 128:559–563, 2006. doi: doi:10.1115/1.2345447.

Chapter 3

Thermo-mechanically-coupled Finite-deformation Theory for Isotropic Elastic-Viscoplastic Materials

3.1 Introduction

An accurate quantitative description of the visco-elastic-plastic constitutive response of amorphous polymeric material *spanning their glass transition temperatures* is crucial for the development of a numerical capability for simulation of polymer processing, and for predicting the relationship between processing methods and the subsequent mechanical properties of polymeric products. In addition to the relatively recent *microscale* hot-embossing process for manufacture of microfluidic devices, there are numerous other important *macroscale* polymer manufacturing processes such as thermoforming and bottle-blowing, where amorphous thermoplastic polymers are subjected to large stretching deformations above their glass transition temperatures. Constitutive theories aimed at this class of applications have been recently proposed by Buckley and co-workers [e.g., 1, 2], as well as Boyce and co-workers [e.g., 3, 4]. Guided by the work of Buckley, Boyce, and their co-workers, it is the purpose of this chapter to develop a large-deformation, thermo-mechanically coupled, visco-elastic-plastic theory, aimed at providing a numerically-based capability for the design and analysis of the micro-hot-embossing processes for the manufacture of microfluidic devices. The constitutive theory developed here is based on the unpublished work of Prof. L. Anand of MIT

An essential kinematical ingredient of visco-elastic-plastic constitutive theories for amorphous polymers *below* their glass transition temperatures, is the classical Kroner [5]- Lee [6] multiplicative decomposition

$$\mathbf{F} = \mathbf{F}^e\mathbf{F}^p \tag{3.1}$$

of the deformation gradient $\mathbf{F}$ into elastic and plastic parts $\mathbf{F}^e$ and $\mathbf{F}^p$ [e.g., 7–11]. For modeling the behavior of glassy polymers in the technologically important temperature range which *spans their glass transition temperatures* we base our theory on a "multi-mechanism" generalization of

the decomposition (3.1),

$$\mathbf{F} = \mathbf{F}^{e\,(\alpha)}\mathbf{F}^{p\,(\alpha)}, \qquad \alpha = 1, \ldots, M, \tag{3.2}$$

where each α denotes a local micromechanism of deformation. Such a multimechanism generalization forms the basis of the recent work of Buckley, Boyce, and their co-workers [e.g., 1–4]. It has also been used to model the visco-hyperelastic behavior of rubber-like materials [e.g., 12–16].

It is important to note from the outset that each $\mathbf{F}^{p\,(\alpha)}$ is to be regarded as an internal variable of the theory whose evolution is determined by an equation of the form $\dot{\mathbf{F}}^{p\,(\alpha)} = \mathbf{L}^{p\,(\alpha)}\mathbf{F}^{p\,(\alpha)}$ (to be discussed shortly), with $\mathbf{F}^{e\,(\alpha)}$ then defined by $\mathbf{F}^{e\,(\alpha)} \stackrel{\text{def}}{=} \mathbf{F}\mathbf{F}^{p\,(\alpha)-1}$. Hence $\mathbf{F}^{p\,(\alpha)}$ and $\mathbf{F}^{e\,(\alpha)}$ in the decomposition (3.2) are not purely kinematical in nature, as they are not defined independently of constitutive equations.

3.2 Theory

The purpose of this section is to present a detailed continuum-mechanical development of the theory.

3.2.1 Notation

We use standard notation of modern continuum mechanics. Specifically: ∇ and Div denote the gradient and divergence with respect to the material point $\mathbf{X}$ in the *reference configuration*; grad and div denote these operators with respect to the point $\mathbf{x} = \boldsymbol{\chi}(\mathbf{X}, t)$ in the *deformed body*; a superposed dot denotes the material time-derivative. Throughout, we write $\mathbf{F}^{e-1} = (\mathbf{F}^e)^{-1}$, $\mathbf{F}^{p-\top} = (\mathbf{F}^p)^{-\top}$, etc. We write $\operatorname{tr}\mathbf{A}$, $\operatorname{sym}\mathbf{A}$, $\operatorname{skw}\mathbf{A}$, $\mathbf{A}_0$, and $\operatorname{sym}_0\mathbf{A}$ respectively, for the trace, symmetric, skew, deviatoric, and symmetric-deviatoric parts of a tensor $\mathbf{A}$. Also, the inner product of tensors $\mathbf{A}$ and $\mathbf{B}$ is denoted by $\mathbf{A}:\mathbf{B}$, and the magnitude of $\mathbf{A}$ by $|\mathbf{A}| = \sqrt{\mathbf{A}:\mathbf{A}}$.

3.2.2 Kinematics

We consider a homogeneous body B identified with the region of space it occupies in a fixed *reference configuration*, and denote by $\mathbf{X}$ an arbitrary material point of B. A *motion* of B is then a smooth one-to-one mapping $\mathbf{x} = \boldsymbol{\chi}(\mathbf{X}, t)$ with *deformation gradient*, *velocity*, and *velocity gradient* given by

$$\mathbf{F} = \nabla\boldsymbol{\chi}, \qquad \mathbf{v} = \dot{\boldsymbol{\chi}}, \qquad \mathbf{L} = \operatorname{grad}\mathbf{v} = \dot{\mathbf{F}}\mathbf{F}^{-1}. \tag{3.3}$$

To model the inelastic response of the material we assume that the deformation gradient $\mathbf{F}$ may be decomposed as

$$\mathbf{F} = \mathbf{F}^{e\,(\alpha)}\mathbf{F}^{p\,(\alpha)}, \qquad \alpha = 1, \ldots, M, \tag{3.4}$$

where each α denotes a local micromechanism of deformation. As is standard, we assume that

$$J = \det\mathbf{F} > 0,$$

and consistent with this we assume that

$$J^{e\,(\alpha)} \stackrel{\text{def}}{=} \det\mathbf{F}^{e\,(\alpha)} > 0, \qquad J^{p\,(\alpha)} \stackrel{\text{def}}{=} \det\mathbf{F}^{p\,(\alpha)} > 0, \tag{3.5}$$

so that $\mathbf{F}^{e\,(\alpha)}$ and $\mathbf{F}^{p\,(\alpha)}$ are invertible.

Restrict attention to a prescribed *material point* $\mathbf{X}$, and let $\mathbf{x}$ denote its place in the deformed configuration at a fixed time t. Then, bearing in mind that (for $\mathbf{X}$ fixed) the linear transformations $\mathbf{F}^{e\,(\alpha)}(\mathbf{X})$ and $\mathbf{F}^{p\,(\alpha)}(\mathbf{X})$ at $\mathbf{X}$ are invertible, we let

$$\mathcal{M}_{\mathbf{X}}{}^{(\alpha)} \stackrel{\text{def}}{=} \text{range of } \mathbf{F}^{p\,(\alpha)}(\mathbf{X}) = \text{domain of } \mathbf{F}^{e\,(\alpha)}(\mathbf{X}), \tag{3.6}$$

and refer to $\mathcal{M}_{\mathbf{X}}{}^{(\alpha)}$ as the *intermediate space* at $\mathbf{X}$ for the α-th micromechanism. $\mathcal{M}_{\mathbf{X}}{}^{(\alpha)}$ plays roles for $\mathbf{F}^{p\,(\alpha)}(\mathbf{X})$ and $\mathbf{F}^{e\,(\alpha)}(\mathbf{X})$ analogous to those played by the infinitesimal neighborhoods of $\mathbf{X}$ and $\mathbf{x}$ for $\mathbf{F}$: $\mathbf{F}^{p\,(\alpha)}(\mathbf{X})$ is a linear transformation of an infinitesimal neighborhood of $\mathbf{X}$ to $\mathcal{M}_{\mathbf{X}}{}^{(\alpha)}$; $\mathbf{F}^{e\,(\alpha)}(\mathbf{X})$ is a linear transformation from $\mathcal{M}_{\mathbf{X}}{}^{(\alpha)}$ to an infinitesimal neighborhood of $\mathbf{x}$. Unlike the reference and deformed configurations, which are *global*, each intermediate space $\mathcal{M}_{\mathbf{X}}{}^{(\alpha)}$ is *local*. *Note that the local intermediate spaces $\mathcal{M}_{\mathbf{X}}{}^{(\alpha)}$ are only mathematical constructs, they are not local "configurations" actually occupied by the body.*

For each micromechanism indexed by α, we refer to $\mathbf{F}^{p\,(\alpha)}$ and $\mathbf{F}^{e\,(\alpha)}$ as the *plastic and elastic parts* of $\mathbf{F}$. Physically, for each α,

- $\mathbf{F}^{p\,(\alpha)}(\mathbf{X})$ represents the local inelastic distortion of the material at $\mathbf{X}$ due to a "plastic mechanism" such as the relative chain slippage of the long-chain polymer molecules, or the cumulative effects of destruction of temporary mechanical cross-links. This local deformation carries the material into — and ultimately "pins" the material to — a *coherent structure* that resides in the *intermediate space* at $\mathbf{X}$ for each α (as represented by the range of $\mathbf{F}^{p\,(\alpha)}(\mathbf{X})$);

- $\mathbf{F}^{e\,(\alpha)}(\mathbf{X})$ represents the subsequent stretching and rotation of this coherent structure, and thereby represents the corresponding "elastic distortion," such as stretching and rotation of the intermolecular bonds and the long-chain polymer molecules.

By $(3.3)_3$ and (3.4),

$$\mathbf{L} = \operatorname{grad} \mathbf{v} = \mathbf{L}^{e\,(\alpha)} + \mathbf{F}^{e\,(\alpha)}\mathbf{L}^{p\,(\alpha)}\mathbf{F}^{e\,(\alpha)-1}, \tag{3.7}$$

with

$$\mathbf{L}^{e} = \dot{\mathbf{F}}^{e(\alpha)}\mathbf{F}^{e\,(\alpha)-1}, \qquad \mathbf{L}^{p\,(\alpha)} = \dot{\mathbf{F}}^{p(\alpha)}\mathbf{F}^{p\,(\alpha)-1}. \tag{3.8}$$

As is standard, we define the total, elastic, and plastic stretching and spin tensors through

$$\left.\begin{aligned} &\mathbf{D} = \operatorname{sym}\mathbf{L}, && \mathbf{W} = \operatorname{skw}\mathbf{L}, \\ &\mathbf{D}^{e\,(\alpha)} = \operatorname{sym}\mathbf{L}^{e\,(\alpha)}, && \mathbf{W}^{e\,(\alpha)} = \operatorname{skw}\mathbf{L}^{e\,(\alpha)}, \\ &\mathbf{D}^{p\,(\alpha)} = \operatorname{sym}\mathbf{L}^{p\,(\alpha)}, && \mathbf{W}^{p\,(\alpha)} = \operatorname{skw}\mathbf{L}^{p\,(\alpha)}, \end{aligned}\right\} \tag{3.9}$$

so that $\mathbf{L} = \mathbf{D} + \mathbf{W}$, $\mathbf{L}^{e\,(\alpha)} = \mathbf{D}^{e\,(\alpha)} + \mathbf{W}^{e\,(\alpha)}$, and $\mathbf{L}^{p\,(\alpha)} = \mathbf{D}^{p\,(\alpha)} + \mathbf{W}^{p\,(\alpha)}$.

We assume that the *plastic flow is incompressible* so that

$$J^{p\,(\alpha)} = 1, \tag{3.10}$$

and

$$\operatorname{tr}\mathbf{L}^{p\,(\alpha)} = \operatorname{tr}\mathbf{D}^{p\,(\alpha)} = 0\,. \tag{3.11}$$

Hence

$$J^{e\,(\alpha)} = J \quad \text{for all } \alpha\,. \tag{3.12}$$

The right and left and polar decompositions of $\mathbf{F}^{e\,(\alpha)}$ are given by

$$\mathbf{F}^{e\,(\alpha)} = \mathbf{R}^{e\,(\alpha)}\mathbf{U}^{e\,(\alpha)} = \mathbf{V}^{e\,(\alpha)}\mathbf{R}^{e\,(\alpha)}, \tag{3.13}$$

where $\mathbf{R}^{e\,(\alpha)}$ is a rotation (proper orthogonal tensor), while $\mathbf{U}^{e\,(\alpha)}$ and $\mathbf{V}^{e\,(\alpha)}$ are symmetric, positive-definite tensors with

$$\mathbf{U}^{e\,(\alpha)} = \sqrt{\mathbf{F}^{e\,(\alpha)\top}\,\mathbf{F}^{e\,(\alpha)}}, \qquad \mathbf{V}^{e\,(\alpha)} = \sqrt{\mathbf{F}^{e\,(\alpha)}\mathbf{F}^{e\,(\alpha)\top}}\,. \tag{3.14}$$

Also, the right and left elastic Cauchy-Green tensors are given by

$$\mathbf{C}^{e\,(\alpha)} = \mathbf{U}^{e\,(\alpha)2} = \mathbf{F}^{e\,(\alpha)\top}\,\mathbf{F}^{e\,(\alpha)}, \qquad \mathbf{B}^{e\,(\alpha)} = \mathbf{V}^{e\,(\alpha)2} = \mathbf{F}^{e\,(\alpha)}\mathbf{F}^{e\,(\alpha)\top}\,, \tag{3.15}$$

and the right and left inelastic Cauchy-Green tensors by

$$\mathbf{C}^{p\,(\alpha)} = \mathbf{U}^{p\,(\alpha)2} = \mathbf{F}^{p\,(\alpha)\top}\,\mathbf{F}^{p\,(\alpha)}, \qquad \mathbf{B}^{p\,(\alpha)} = \mathbf{V}^{p\,(\alpha)2} = \mathbf{F}^{p\,(\alpha)}\mathbf{F}^{p\,(\alpha)\top}. \tag{3.16}$$

3.2.3 Frame-indifference

Changes in frame (observer) are smooth time-dependent rigid transformations of the Euclidean space through which the body moves. We require that the theory be invariant under such transformations, and hence under transformations of the form

$$\boldsymbol{\chi}(\mathbf{X}, t) \to \mathbf{Q}(t)(\boldsymbol{\chi}(\mathbf{X}, t) - \mathbf{o}) + \mathbf{y}(t) \tag{3.17}$$

with $\mathbf{Q}(t)$ a rotation (proper-orthogonal tensor), $\mathbf{y}(t)$ a point at each t, and $\mathbf{o}$ a fixed origin. Then, under a change in observer, the deformation gradient transforms according to

$$\mathbf{F} \to \mathbf{Q}\mathbf{F}. \tag{3.18}$$

Thus, $\dot{\mathbf{F}} \to \mathbf{Q}\dot{\mathbf{F}} + \dot{\mathbf{Q}}\mathbf{F}$, and by $(3.3)_3$,

$$\mathbf{L} \to \mathbf{Q}\mathbf{L}\mathbf{Q}^{\top} + \dot{\mathbf{Q}}\mathbf{Q}^{\top}. \tag{3.19}$$

Hence,

$$\mathbf{D} \to \mathbf{Q}\mathbf{D}\mathbf{Q}^{\top}, \qquad \mathbf{W} \to \mathbf{Q}\mathbf{W}\mathbf{Q}^{\top} + \dot{\mathbf{Q}}\mathbf{Q}^{\top}\,. \tag{3.20}$$

Moreover, $\mathbf{F}^{e\,(\alpha)}\mathbf{F}^{p\,(\alpha)} \to \mathbf{Q}\mathbf{F}^{e\,(\alpha)}\mathbf{F}^{p\,(\alpha)}$, and therefore, since *observers view only the deformed configuration*,

$$\mathbf{F}^{e\,(\alpha)} \to \mathbf{Q}\mathbf{F}^{e\,(\alpha)}, \qquad \mathbf{F}^{p\,(\alpha)} \text{ are invariant,} \tag{3.21}$$

and, by (3.8),

$$\mathbf{L}^{e\,(\alpha)} \to \mathbf{Q}\mathbf{L}^{e\,(\alpha)}\mathbf{Q}^{\top} + \dot{\mathbf{Q}}\mathbf{Q}^{\top}, \tag{3.22}$$

and

$$\mathbf{L}^{p\,(\alpha)},\ \mathbf{D}^{p\,(\alpha)},\ \text{and } \mathbf{W}^{p\,(\alpha)} \text{ are invariant.} \tag{3.23}$$

Further, by (3.13),

$$\mathbf{F}^{e\,(\alpha)} = \mathbf{R}^{e\,(\alpha)}\mathbf{U}^{e\,(\alpha)} \to \mathbf{Q}\mathbf{F}^{e\,(\alpha)} = \underline{\mathbf{Q}\mathbf{R}^{e\,(\alpha)}}\mathbf{U}^{e\,(\alpha)},$$
$$\mathbf{F}^{e\,(\alpha)} = \mathbf{V}^{e\,(\alpha)}\mathbf{R}^{e\,(\alpha)} \to \mathbf{Q}\mathbf{F}^{e\,(\alpha)} = \underline{\mathbf{Q}\mathbf{V}^{e\,(\alpha)}\mathbf{Q}^{\top}}\ \mathbf{Q}\mathbf{R}^{e\,(\alpha)},$$

and we may conclude from the uniqueness of the polar decomposition that

$$\mathbf{R}^{e\,(\alpha)} \to \mathbf{Q}\mathbf{R}^{e\,(\alpha)}, \qquad \mathbf{V}^{e\,(\alpha)} \to \mathbf{Q}\mathbf{V}^{e\,(\alpha)}\mathbf{Q}^{\top}, \qquad \mathbf{U}^{e\,(\alpha)} \text{ are invariant.} \tag{3.24}$$

Hence, from (3.15), $\mathbf{B}^{e\,(\alpha)}$ and $\mathbf{C}^{e\,(\alpha)}$ transform as

$$\mathbf{B}^{e\,(\alpha)} \to \mathbf{Q}\mathbf{B}^{e\,(\alpha)}\mathbf{Q}^{\top}, \qquad \text{and} \qquad \mathbf{C}^{e\,(\alpha)} \text{ are invariant.} \tag{3.25}$$

3.2.4 Development of the theory based on the principle of virtual power

Following Anand and Gurtin [11], Gurtin [17] and Gurtin and Anand [18], the theory presented here is based on the belief that

- *the power expended by each independent "rate-like" kinematical descriptor be expressible in terms of an associated force system consistent with its own balance.*

However, the basic "rate-like" descriptors, namely, $\mathbf{v}$, $\mathbf{L}^{e\,(\alpha)}$, and $\mathbf{L}^{p\,(\alpha)}$ *are not independent*, since by (3.7) they are constrained by

$$\operatorname{grad}\mathbf{v} = \mathbf{L}^{e\,(\alpha)} + \mathbf{F}^{e\,(\alpha)}\,\mathbf{L}^{p\,(\alpha)}\,\mathbf{F}^{e\,(\alpha)-1}, \qquad \operatorname{tr}\mathbf{L}^{p\,(\alpha)} = 0, \tag{3.26}$$

and it is not apparent what forms the associated force balances should take. It is in such situations that the strength of the principle of virtual power becomes apparent, since *the principle of virtual power automatically determines the underlying force balances.*

External and internal expenditures of power

We write $\mathcal{B}_t = \boldsymbol{\chi}(\mathrm{B}, t)$ for the *deformed body*. We use the term *part* to denote an arbitrary time-dependent subregion $\mathcal{P}_t$ of $\mathcal{B}_t$ that *deforms* with the body, so that

$$\mathcal{P}_t = \boldsymbol{\chi}(\mathrm{P}, t) \tag{3.27}$$

for some *fixed* subregion P of B. The outward unit normal on the boundary $\partial\mathcal{P}_t$ of $\mathcal{P}_t$ is denoted by $\mathbf{n}$.

The power expended on $\mathcal{P}_t$ by material or bodies exterior to $\mathcal{P}_t$ results from a *macroscopic surface traction* $\mathbf{t}(\mathbf{n})$, measured per unit area in the deformed body, and a *macroscopic body force* $\mathbf{b}$, measured per unit volume in the deformed body, each of whose working accompanies the macroscopic motion of the body. The body force $\mathbf{b}$ is assumed to include inertial forces; that is, granted that the underlying frame is inertial,

$$\mathbf{b} = \mathbf{b}_0 - \rho\dot{\mathbf{v}}, \tag{3.28}$$

with $\mathbf{b}_0$ the noninertial body force, and $\rho(\mathbf{x},t) > 0$ is the mass density in the deformed body. We therefore write the *external power* as

$$\mathcal{W}_{\text{ext}}(\mathcal{P}_t) = \int_{\partial\mathcal{P}_t} \mathbf{t}(\mathbf{n}) \cdot \mathbf{v}\, da + \int_P \mathbf{b} \cdot \mathbf{v}\, dv, \tag{3.29}$$

with $\mathbf{t}(\mathbf{n})$ (for each unit vector $\mathbf{n}$) and $\mathbf{b}$ defined over the body for all time.

We assume that power is expended internally by

- *elastic stresses* $\mathbf{T}^{e\,(\alpha)}$ power-conjugate to $\mathbf{L}^{e\,(\alpha)}$, and
- *microstresses* $\mathbf{T}^{p\,(\alpha)}$ power-conjugate to $\mathbf{L}^{p\,(\alpha)}$,

and we write the *internal power* as

$$\mathcal{W}_{\text{int}}(\mathcal{P}_t) = \int_{\mathcal{P}_t} \sum_{\alpha=1}^{M} \left(\mathbf{T}^{e\,(\alpha)} : \mathbf{L}^{e\,(\alpha)} + J^{e\,(\alpha)-1}\, \mathbf{T}^{p\,(\alpha)} : \mathbf{L}^{p\,(\alpha)} \right) dv\,. \tag{3.30}$$

Here $\mathbf{T}^{e\,(\alpha)}$ and $\mathbf{T}^{p\,(\alpha)}$ are defined over the body for all time. We assume that $\mathbf{T}^{p\,(\alpha)}$ are *deviatoric*, since $\mathbf{L}^{p\,(\alpha)}$ are deviatoric. The term $J^{e\,(\alpha)-1}$ arises because the microstress-power $\mathbf{T}^{p\,(\alpha)} : \mathbf{L}^{p\,(\alpha)}$ is measured per unit volume in the corresponding intermediate space, but the integration is carried out within the deformed body.

We require that the internal power be invariant under a change in frame. Thus, consider the internal power $\mathcal{W}_{\text{int}}(\mathcal{P}_t)$ under an arbitrary change in frame. In the new frame $\mathcal{P}_t$ transforms rigidly to a region $\mathcal{P}_t^*$, $\mathbf{L}^{e\,(\alpha)}$ transforms to

$$\mathbf{L}^{e\,(\alpha)*} = \mathbf{Q}\mathbf{L}^{e\,(\alpha)}\mathbf{Q}^\top + \dot{\mathbf{Q}}\mathbf{Q}^\top\,,$$

$\mathbf{T}^{e\,(\alpha)}$ to $\mathbf{T}^{e\,(\alpha)*}$, while

$$\mathbf{T}^{p\,(\alpha)*} = \mathbf{T}^{p\,(\alpha)},$$

since it is conjugate to $\mathbf{L}^{p\,(\alpha)}$ which is invariant under a change in frame. Hence

$$\begin{aligned}
\mathcal{W}^*_{\text{int}}(\mathcal{P}_t^*) &= \int_{\mathcal{P}_t^*} \sum_{\alpha=1}^{M} \left\{ \mathbf{T}^{e\,(\alpha)*} : \left(\mathbf{Q}\mathbf{L}^{e\,(\alpha)}\mathbf{Q}^\top + \dot{\mathbf{Q}}\mathbf{Q}^\top \right) + J^{e\,(\alpha)-1}\, \mathbf{T}^{p\,(\alpha)} : \mathbf{L}^{p\,(\alpha)} \right\} dv, \\
&= \int_{\mathcal{P}_t} \sum_{\alpha=1}^{M} \left\{ \mathbf{T}^{e\,(\alpha)*} : \left(\mathbf{Q}\mathbf{L}^{e\,(\alpha)}\mathbf{Q}^\top + \dot{\mathbf{Q}}\mathbf{Q}^\top \right) + J^{e\,(\alpha)-1}\, \mathbf{T}^{p\,(\alpha)} : \mathbf{L}^{p\,(\alpha)} \right\} dv,
\end{aligned}$$

where in the second of the equations above, since $\mathcal{P}_t^*$ is simply $\mathcal{P}_t$ transformed *rigidly*, we have replaced the region of integration $\mathcal{P}_t^*$ by $\mathcal{P}_t$. Thus, we require that

$$\mathcal{W}^*_{\text{int}}(\mathcal{P}_t^*) = \mathcal{W}_{\text{int}}(\mathcal{P}_t).$$

Since the region $\mathcal{P}_t$ is arbitrary, this requirement yields the relation

$$\mathbf{T}^{e\,(\alpha)*} : \left(\mathbf{Q}\mathbf{L}^{e\,(\alpha)}\mathbf{Q}^\top + \dot{\mathbf{Q}}\mathbf{Q}^\top \right) = \mathbf{T}^{e\,(\alpha)} : \mathbf{L}^{e\,(\alpha)},$$

for each α. Also, since the change in frame is arbitrary, if we choose it such that $\mathbf{Q}$ is an arbitrary *time-independent* rotation, so that $\dot{\mathbf{Q}} = \mathbf{0}$, we find that

$$\mathbf{T}^{e\,(\alpha)} : \mathbf{L}^{e\,(\alpha)} = \mathbf{T}^{e\,(\alpha)*} : (\mathbf{Q}\mathbf{L}^{e\,(\alpha)}\mathbf{Q}^{\top}) = (\mathbf{Q}^{\top}\mathbf{T}^{e\,(\alpha)*}\mathbf{Q}) : \mathbf{L}^{e\,(\alpha)},$$

or

$$\Big(\mathbf{T}^{e\,(\alpha)} - (\mathbf{Q}^{\top}\mathbf{T}^{e\,(\alpha)*}\mathbf{Q})\Big) : \mathbf{L}^{e\,(\alpha)} = 0\,.$$

Since this must hold for all $\mathbf{L}^{e\,(\alpha)}$, we find that the stresses $\mathbf{T}^{e\,(\alpha)}$ transform according to

$$\mathbf{T}^{e\,(\alpha)*} = \mathbf{Q}\mathbf{T}^{e\,(\alpha)}\mathbf{Q}^{\top}. \tag{3.31}$$

Next, if we assume that $\mathbf{Q} = \mathbf{1}$ at the time in question, so that $\dot{\mathbf{Q}}$ is an arbitrary skew tensor, we find that

$$\mathbf{T}^{e\,(\alpha)} : \dot{\mathbf{Q}} = 0,$$

or that the elastic stresses $\mathbf{T}^{e\,(\alpha)}$ are symmetric,

$$\mathbf{T}^{e\,(\alpha)} = \mathbf{T}^{e\,(\alpha)\top}\,. \tag{3.32}$$

Finally, using (3.32) we may write the internal power (3.30) as

$$\mathcal{W}_{\text{int}}(\mathcal{P}_t) = \int_{\mathcal{P}_t} \sum_{\alpha=1}^{M} (\mathbf{T}^{e\,(\alpha)} : \mathbf{D}^{e\,(\alpha)} + J^{e\,(\alpha)-1}\,\mathbf{T}^{p\,(\alpha)} : \mathbf{L}^{p\,(\alpha)})\,dv. \tag{3.33}$$

Principle of virtual power. Macroscopic force balance. Microscopic force balance

Assume that, at some arbitrarily chosen but *fixed time*, the fields $\boldsymbol{\chi}$, $\mathbf{F}^{e\,(\alpha)}$ (and hence $\mathbf{F}$ and $\mathbf{F}^{p\,(\alpha)}$) are known, and consider the fields $\mathbf{v}$, $\mathbf{L}^{e\,(\alpha)}$, and $\mathbf{L}^{p\,(\alpha)}$ as virtual velocities to be specified independently in a manner consistent with (3.26); that is, denoting the virtual fields by $\tilde{\mathbf{v}}$, , $\tilde{\mathbf{L}}^{e\,(\alpha)}$, and $\tilde{\mathbf{L}}^{p\,(\alpha)}$ to differentiate them from fields associated with the actual evolution of the body. We require that

$$\operatorname{grad}\tilde{\mathbf{v}} = \tilde{\mathbf{L}}^{e\,(\alpha)} + \mathbf{F}^{e\,(\alpha)}\tilde{\mathbf{L}}^{p\,(\alpha)}\mathbf{F}^{e\,(\alpha)-1}\,, \quad \text{and} \quad \operatorname{tr}\tilde{\mathbf{L}}^{p\,(\alpha)} = 0 \quad \text{for each } \alpha\,. \tag{3.34}$$

More specifically, we define a *generalized virtual velocity* to be a list

$$\mathcal{V} = (\tilde{\mathbf{v}}, \tilde{\mathbf{L}}^{e\,(\alpha)}, \tilde{\mathbf{L}}^{p\,(\alpha)})$$

consistent with (3.34).

We write

$$\left.\begin{aligned} \mathcal{W}_{\text{ext}}(\mathcal{P}_t, \mathcal{V}) &= \int_{\partial\mathcal{P}_t} \mathbf{t}(\mathbf{n}) \cdot \tilde{\mathbf{v}}\,da + \int_{\mathcal{P}_t} \mathbf{b} \cdot \tilde{\mathbf{v}}\,dv, \\ \mathcal{W}_{\text{int}}(\mathcal{P}_t, \mathcal{V}) &= \int_{\mathcal{P}_t} \sum_{\alpha=1}^{M} (\mathbf{T}^{e\,(\alpha)} : \tilde{\mathbf{L}}^{e\,(\alpha)} + J^{e\,(\alpha)-1}\,\mathbf{T}^{p\,(\alpha)} : \tilde{\mathbf{L}}^{p\,(\alpha)})\,dv, \end{aligned}\right\} \tag{3.35}$$

respectively, for the external and internal expenditures of *virtual power*. Then, the *principle of virtual power* is the requirement that the external and internal powers be balanced. That is

- *given any part* $\mathcal{P}_t$,

$$\mathcal{W}_{\text{ext}}(\mathcal{P}_t, \mathcal{V}) = \mathcal{W}_{\text{int}}(\mathcal{P}_t, \mathcal{V}) \quad \textit{for all generalized virtual velocities } \mathcal{V}. \tag{3.36}$$

To deduce the consequences of the principle of virtual power, assume that (3.36) is satisfied. In applying the virtual balance (3.36) we are at liberty to choose any $\mathcal{V}$ consistent with the constraint (3.34).

First consider a generalized virtual velocity which is strictly elastic in the sense that

$$\tilde{\mathbf{L}}^{p\,(\alpha)} \equiv \mathbf{0}, \quad \text{so that by (3.34)} \quad \operatorname{grad} \tilde{\mathbf{v}} = \tilde{\mathbf{L}}^{e\,(\alpha)}. \tag{3.37}$$

For this choice of $\mathcal{V}$, (3.36) yields

$$\int_{\partial\mathcal{P}_t} \mathbf{t}(\mathbf{n}) \cdot \tilde{\mathbf{v}}\, da + \int_{\mathcal{P}_t} \mathbf{b} \cdot \tilde{\mathbf{v}}\, dv = \int_{\mathcal{P}_t} \Big(\sum_{\alpha=1}^{M} \mathbf{T}^{e\,(\alpha)} \Big) : \operatorname{grad} \tilde{\mathbf{v}}\, dv = \int_{\mathcal{P}_t} \mathbf{T} : \operatorname{grad} \tilde{\mathbf{v}}\, dv\,,$$

where we have written

$$\mathbf{T} \stackrel{\text{def}}{=} \sum_{\alpha=1}^{M} \mathbf{T}^{e\,(\alpha)}\,, \tag{3.38}$$

and note that on account of (3.32),

$$\mathbf{T} = \mathbf{T}^{\top}. \tag{3.39}$$

Then, using the divergence theorem,

$$\int_{\partial\mathcal{P}_t} \big(\mathbf{t}(\mathbf{n}) - \mathbf{T}\mathbf{n}\big) \cdot \tilde{\mathbf{v}}\, da + \int_{\mathcal{P}_t} (\operatorname{div} \mathbf{T} + \mathbf{b}) \cdot \tilde{\mathbf{v}}\, dv = 0.$$

Since this relation must hold for all $\mathcal{P}_t$ and all $\tilde{\mathbf{v}}$, standard variational arguments yield the traction condition

$$\mathbf{t}(\mathbf{n}) = \mathbf{T}\mathbf{n}\,, \tag{3.40}$$

and the local force balance

$$\operatorname{div} \mathbf{T} + \mathbf{b} = \mathbf{0}. \tag{3.41}$$

Recall that we have assumed that $\mathbf{b}$ includes inertial body forces. Thus, recalling (3.28), the local force balance (3.41) becomes

$$\operatorname{div} \mathbf{T} + \mathbf{b}_0 = \rho \dot{\mathbf{v}}, \tag{3.42}$$

with $\mathbf{b}_0$ the noninertial body force. Therefore, the symmetric stress $\mathbf{T}$ plays the role of the macroscopic *Cauchy stress*, and (3.42) and (3.39) represent the classical *macroscopic force and moment balances.*

Further, as is standard, with

$$\mathbf{T}_{\text{R}} = J\mathbf{T}\mathbf{F}^{-\top} \tag{3.43}$$

denoting the first Piola stress,

$$\mathbf{b}_{0\mathrm{R}} = J\mathbf{b}_0, \tag{3.44}$$

the conventional body force measured per unit volume of the reference configuration, and

$$\rho_{\mathrm{R}} = J\rho \tag{3.45}$$

denoting the mass density in the reference configuration, referential forms of (3.42) and (3.39) are

$$\mathrm{Div}\,\mathbf{T}_{\mathrm{R}} + \mathbf{b}_{0\mathrm{R}} = \rho_{\mathrm{R}}\,\ddot{\boldsymbol{\chi}} \tag{3.46}$$

and

$$\mathbf{T}_{\mathrm{R}}\mathbf{F}^{\top} = \mathbf{F}\mathbf{T}_{\mathrm{R}}^{\top}, \tag{3.47}$$

respectively.

Next, to discuss the microscopic counterparts of these results, we choose a generalized virtual velocity field $\mathcal{V}$ for which

$$\tilde{\mathbf{v}} \equiv \mathbf{0}, \quad \text{so that by (3.34)} \quad \tilde{\mathbf{L}}^{e\,(\alpha)} = -\mathbf{F}^{e\,(\alpha)}\tilde{\mathbf{L}}^{p\,(\alpha)}\mathbf{F}^{e\,(\alpha)-1}. \tag{3.48}$$

Then, the external power vanishes identically, so that, by (3.36), the internal power must also vanish, and satisfy

$$\mathcal{W}_{\mathrm{int}}(\mathcal{P}_t, \mathcal{V}) = \int_{\mathcal{P}_t} \sum_{\alpha=1}^{M} J^{e\,(\alpha)-1}\Big(\mathbf{T}^{p\,(\alpha)} - J^{e\,(\alpha)}\,\mathbf{F}^{e\,(\alpha)\top}\mathbf{T}^{e\,(\alpha)}\mathbf{F}^{e\,(\alpha)-\top}\Big) : \tilde{\mathbf{L}}^{p\,(\alpha)}\,dv = 0.$$

Since this must be satisfied for all $\mathcal{P}_t$ and all deviatoric tensors $\tilde{\mathbf{L}}^{p\,(\alpha)}$, a standard argument yields the *microforce balance*

$$\mathbf{M}_0^{e\,(\alpha)} = \mathbf{T}^{p\,(\alpha)}, \tag{3.49}$$

where

$$\mathbf{M}^{e\,(\alpha)} \stackrel{\mathrm{def}}{=} J^{e\,(\alpha)}\mathbf{F}^{e\,(\alpha)\top}\mathbf{T}^{e\,(\alpha)}\mathbf{F}^{e\,(\alpha)-\top}, \tag{3.50}$$

is called a Mandel stress. *The balances of* (3.49) *characterize the interaction between internal forces associated with the elastic response of the material and internal forces associated with inelasticity for each micromechanism* α.

For later use we introduce a stress measure

$$\mathbf{P}^{e\,(\alpha)} \stackrel{\mathrm{def}}{=} J^{e\,(\alpha)}\mathbf{F}^{e\,(\alpha)-1}\mathbf{T}^{e\,(\alpha)}\mathbf{F}^{e\,(\alpha)-\top}, \tag{3.51}$$

and the corresponding Mandel stress is given by

$$\mathbf{M}^{e\,(\alpha)} = \mathbf{C}^{e\,(\alpha)}\mathbf{P}^{e\,(\alpha)}. \tag{3.52}$$

3.2.5 Balance of energy. Entropy imbalance. Local dissipation inequality

Let

- $\vartheta > 0$ denote the absolute temperature,

- ε and η represent the *specific internal energy* and *specific entropy* densities, measured per unit mass in the deformed body,
- $\mathbf{q}$ denote the *heat flux*, measured per unit area in the deformed body, and
- q denote the scalar heat supply, measured per unit volume in the deformed body.

Then, *balance of energy* is the requirement that

$$\overset{\cdot}{\overline{\int_{\mathcal{P}_t} \rho\,\varepsilon\,dv}} = -\int_{\partial\mathcal{P}_t} \mathbf{q}\cdot\mathbf{n}\,da + \int_{\mathcal{P}_t} q\,dv + \mathcal{W}_{\text{ext}}(\mathcal{P}_t), \tag{3.53}$$

while the *second law* takes the form of an *entropy imbalance*

$$\overset{\cdot}{\overline{\int_{\mathcal{P}_t} \rho\,\eta\,dv}} \geq -\int_{\partial\mathcal{P}_t} \frac{\mathbf{q}\cdot\mathbf{n}}{\vartheta}\,da + \int_{\mathcal{P}_t} \frac{q}{\vartheta}\,dv. \tag{3.54}$$

Thus, since $\mathcal{W}_{\text{ext}}(\mathcal{P}_t) = \mathcal{W}_{\text{int}}(\mathcal{P}_t)$ and since $\mathcal{P}_t$ is arbitrary, we may use (3.33) to obtain local forms of (3.53) and (3.54):

$$\left.\begin{aligned} \rho\,\dot{\varepsilon} &= -\operatorname{div}\mathbf{q} + q + \sum_{\alpha=1}^{M} \mathbf{T}^{e\,(\alpha)} : \mathbf{D}^{e\,(\alpha)} + \sum_{\alpha=1}^{M} J^{e\,(\alpha)-1}\,\mathbf{T}^{p\,(\alpha)} : \mathbf{L}^{p\,(\alpha)}, \\ \rho\,\dot{\eta} &\geq -\frac{1}{\vartheta}\operatorname{div}\mathbf{q} + \frac{1}{\vartheta^2}\mathbf{q}\cdot\mathbf{g} + \frac{q}{\vartheta}\,, \end{aligned}\right\} \tag{3.55}$$

where we have written

$$\mathbf{g} \overset{\text{def}}{=} \operatorname{grad}\vartheta \tag{3.56}$$

for the temperature gradient.

Let

$$\psi \overset{\text{def}}{=} \varepsilon - \vartheta\eta \tag{3.57}$$

denote the *specific (Helmholtz) free energy*. Then (3.55) yields the *local dissipation inequality*

$$\rho\dot{\psi} + \rho\,\eta\dot{\vartheta} + \frac{1}{\vartheta}\,\mathbf{q}\cdot\mathbf{g} - \sum_{\alpha=1}^{M} \mathbf{T}^{e\,(\alpha)} : \mathbf{D}^{e\,(\alpha)} - \sum_{\alpha=1}^{M} J^{e\,(\alpha)-1}\,\mathbf{T}^{p\,(\alpha)} : \mathbf{L}^{p\,(\alpha)} \leq 0\,. \tag{3.58}$$

The free-energy density and entropy density per unit volume of the reference configuration are given by

$$\psi_{\text{R}} = \rho_{\text{R}}\,\psi, \quad \eta_{\text{R}} = \rho_{\text{R}}\,\eta. \tag{3.59}$$

Note that since $J = J^{e\,(\alpha)}$,

$$\rho_{\text{R}} = \rho\,J = \rho\,J^{e\,(\alpha)} = \rho_{\text{I}}^{(\alpha)}, \tag{3.60}$$

and the free-energy density ψ_{R} and entropy density η_{R} per unit volume of the reference configuration are equal to the free-energy density and entropy density when reckoned per unit volume of the intermediate space for each α. Then multiplying (3.58) through by $J = J^{e\,(\alpha)}$, and using (3.59),

(3.60), and the microforce balance (3.49) we obtain

$$\dot{\psi}_{\mathrm{R}} + \eta_{\mathrm{R}}\dot{\vartheta} + \Big(\frac{J}{\vartheta}\Big)\,\mathbf{q}\cdot\mathbf{g} - \sum_{\alpha=1}^{M} J^{e\,(\alpha)}\,\mathbf{T}^{e\,(\alpha)} : \mathbf{D}^{e\,(\alpha)} - \sum_{\alpha=1}^{M} \mathbf{M}_0^{e\,(\alpha)} : \mathbf{L}^{p\,(\alpha)} \leq 0. \tag{3.61}$$

From a standard result in continuum mechanics, the referential heat flux and temperature gradient $\mathbf{q}_{\mathrm{R}}$ and $\nabla\vartheta$ are related to their spatial counterparts $\mathbf{q}$ and $\mathbf{g} = \operatorname{grad}\vartheta$ by

$$\mathbf{q}_{\mathrm{R}} = J\mathbf{F}^{-1}\mathbf{q} \qquad \text{and} \qquad \nabla\vartheta = \mathbf{F}^{\top}\mathbf{g}, \tag{3.62}$$

and therefore

$$J\mathbf{q}\cdot\mathbf{g} = \mathbf{q}_{\mathrm{R}}\cdot\nabla\vartheta. \tag{3.63}$$

Further, differentiating $(3.15)_1$ results in the following expression for the rate of change of $\mathbf{C}^{e\,(\alpha)}$:

$$\begin{aligned}
\dot{\overline{\mathbf{C}^{e\,(\alpha)}}} &= \big(\mathbf{F}^{e\,(\alpha)\top}\dot{\overline{\mathbf{F}^{e\,(\alpha)}}} + \dot{\overline{\mathbf{F}^{e\,(\alpha)\top}}}\mathbf{F}^{e\,(\alpha)}\big) \\
&= \mathbf{F}^{e\,(\alpha)\top}\big(\dot{\overline{\mathbf{F}^{e\,(\alpha)}}}\mathbf{F}^{e\,(\alpha)-1} + \mathbf{F}^{e\,(\alpha)-\top}\dot{\overline{\mathbf{F}^{e\,(\alpha)\top}}}\big)\mathbf{F}^{e\,(\alpha)} \\
&= 2\,\mathbf{F}^{e\,(\alpha)\top}\mathbf{D}^{e\,(\alpha)}\mathbf{F}^{e\,(\alpha)}.
\end{aligned} \tag{3.64}$$

Hence

$$\mathbf{D}^{e\,(\alpha)} = \tfrac{1}{2}\mathbf{F}^{e\,(\alpha)-\top}\dot{\overline{\mathbf{C}^{e\,(\alpha)}}}\mathbf{F}^{e\,(\alpha)-1}, \tag{3.65}$$

and therefore

$$J^{e\,(\alpha)}\mathbf{T}^{e\,(\alpha)} : \mathbf{D}^{e\,(\alpha)} = J^{e\,(\alpha)}\mathbf{T}^{e\,(\alpha)} : \Big(\tfrac{1}{2}\mathbf{F}^{e\,(\alpha)-\top}\dot{\overline{\mathbf{C}^{e\,(\alpha)}}}\mathbf{F}^{e\,(\alpha)-1}\Big) \tag{3.66}$$

$$= \tfrac{1}{2}\Big(J^{e\,(\alpha)}\mathbf{F}^{e\,(\alpha)-1}\mathbf{T}^{e\,(\alpha)}\mathbf{F}^{e\,(\alpha)-\top}\Big) : \dot{\overline{\mathbf{C}^{e\,(\alpha)}}}. \tag{3.67}$$

Thus using (3.51), we obtain

$$J^{e\,(\alpha)}\mathbf{T}^{e\,(\alpha)} : \mathbf{D}^{e\,(\alpha)} = \tfrac{1}{2}\,\mathbf{P}^{e\,(\alpha)} : \dot{\overline{\mathbf{C}^{e\,(\alpha)}}} \tag{3.68}$$

For later use, from (3.33), (3.49) and (3.68), we note that the internal power per unit volume of the reference space is

$$\tfrac{1}{2}\textstyle\sum_{\alpha=1}^{M}\,\mathbf{P}^{e\,(\alpha)} : \dot{\overline{\mathbf{C}^{e\,(\alpha)}}} + \sum_{\alpha=1}^{M}\,\mathbf{M}_0^{e\,(\alpha)} : \mathbf{L}^{p\,(\alpha)}\,. \tag{3.69}$$

Also, the referential form of the energy balance $(3.55)_1$ is

$$\dot{\varepsilon}_{\mathrm{R}} = -\operatorname{Div}\mathbf{q}_{\mathrm{R}} + q_{\mathrm{R}} + \tfrac{1}{2}\textstyle\sum_{\alpha=1}^{M}\,\mathbf{P}^{e\,(\alpha)} : \dot{\overline{\mathbf{C}^{e\,(\alpha)}}} + \sum_{\alpha=1}^{M}\,\mathbf{M}_0^{e\,(\alpha)} : \mathbf{L}^{p\,(\alpha)}, \tag{3.70}$$

where $q_{\mathrm{R}} = Jq$ is the heat supply per unit volume of the reference body, and Div is the referential divergence.

Finally, using (3.63) and (3.68) we may rewrite the free-energy imbalance as

$$\dot{\psi}_{\mathrm{R}} + \eta_{\mathrm{R}}\dot{\vartheta} + \frac{1}{\vartheta}\,\mathbf{q}_{\mathrm{R}} \cdot \nabla\vartheta - \tfrac{1}{2}\sum_{\alpha=1}^{M} \mathbf{P}^{e\,(\alpha)} : \overset{\cdot}{\overline{\mathbf{C}^{e\,(\alpha)}}} - \sum_{\alpha=1}^{M} \mathbf{M}_0^{e\,(\alpha)} : \mathbf{L}^{p\,(\alpha)} \leq 0, \tag{3.71}$$

Finally, we note that ψ_{R}, η_{R} and ϑ are invariant under a change in frame since they are scalar fields, and on account of the transformation rules (3.23), (3.25), (3.31) and the definitions (3.50) and (3.51), the fields

$$\mathbf{C}^{e\,(\alpha)}, \quad \mathbf{L}^{p\,(\alpha)}, \quad \mathbf{P}^{e\,(\alpha)}, \quad \text{and} \quad \mathbf{M}^{e\,(\alpha)}, \tag{3.72}$$

are also invariant, as are the fields

$$\mathbf{q}_{\mathrm{R}}, \quad \nabla\vartheta, \tag{3.73}$$

since they are referential vector fields.

3.3 Constitutive theory

To account for the major strain-hardening characteristics of materials observed during plastic deformation, we introduce **internal state variables** which represent important aspects of the microstructural resistance to plastic flow. Specifically we introduce

- A list of m scalar *internal state-variables*

  $$\boldsymbol{\xi}^{(\alpha)} = (\xi_1^{(\alpha)}, \xi_2^{(\alpha)}, \ldots, \xi_m^{(\alpha)})$$

  for each α. Since $\boldsymbol{\xi}^{(\alpha)}$ are scalar fields they are invariant under a change in frame.

- A *symmetric and unimodular* tensor field

  $$\mathbf{A}^{(\alpha)}(\mathbf{X}, t), \quad \mathbf{A}^{(\alpha)} = \mathbf{A}^{(\alpha)\top}, \quad \det \mathbf{A}^{(\alpha)} = 1$$

  for each α. Each such tensor field represents a dimensionless *squared stretch-like* quantity, which as a linear transformation, maps vectors in the intermediate space for each α, into vectors in the same space. Thus, $\mathbf{A}^{(\alpha)}$ is a *structural tensor field*, and therefore invariant under a change in frame.

Guided by the dissipation inequality (3.71), we assume the following special set of constitutive equations:

$$\left.\begin{aligned}
\psi_{\mathrm{R}} &= \sum_{\alpha=1}^{M} \bar{\psi}^{(\alpha)}(\mathbf{C}^{e\,(\alpha)}, \mathbf{A}^{(\alpha)}, \vartheta), \\
\eta_{\mathrm{R}} &= \sum_{\alpha=1}^{M} \bar{\eta}^{(\alpha)}(\mathbf{C}^{e\,(\alpha)}, \mathbf{A}^{(\alpha)}, \vartheta), \\
\mathbf{P}^{e\,(\alpha)} &= \bar{\mathbf{P}}^{e\,(\alpha)}(\mathbf{C}^{e\,(\alpha)}, \mathbf{A}^{(\alpha)}, \vartheta), \\
\mathbf{L}^{p\,(\alpha)} &= \bar{\mathbf{L}}^{p(\alpha)}(\mathbf{M}^{e\,(\alpha)}, \boldsymbol{\xi}^{(\alpha)}, \mathbf{A}^{(\alpha)}, \vartheta), \\
\dot{\xi}_i^{(\alpha)} &= h_i^{(\alpha)}(\mathbf{L}^{p\,(\alpha)}, \boldsymbol{\xi}^{(\alpha)}, \mathbf{A}^{(\alpha)}, \vartheta), \\
\overset{\cdot}{\overline{\mathbf{A}^{(\alpha)}}} &= \mathbf{L}^{p\,(\alpha)}\mathbf{A}^{(\alpha)} + \mathbf{A}^{(\alpha)}\mathbf{L}^{p\,(\alpha)\top} - \mathbf{G}^{(\alpha)}(\boldsymbol{\xi}^{(\alpha)}, \mathbf{A}^{(\alpha)}, \vartheta)\, l^{p\,(\alpha)},
\end{aligned}\right\} \tag{3.74}$$

where

$$l^{p\,(\alpha)} \overset{\mathrm{def}}{=} |\mathbf{L}^{p\,(\alpha)}| = \bar{l}^{p\,(\alpha)}(\mathbf{M}^{e\,(\alpha)}, \boldsymbol{\xi}^{(\alpha)}, \mathbf{A}^{(\alpha)}, \vartheta), \tag{3.75}$$

denotes a **scalar flow rate**; correspondingly, the **plastic flow direction** for each α is given by

$$\mathbf{N}^{p\,(\alpha)} = \frac{\mathbf{L}^{p\,(\alpha)}}{l^{p\,(\alpha)}} = \bar{\mathbf{N}}^{p\,(\alpha)}(\mathbf{M}^{e\,(\alpha)}, \boldsymbol{\xi}^{(\alpha)}, \mathbf{A}^{(\alpha)}, \vartheta). \tag{3.76}$$

To these equations we append a simple Fourier's relation for the heat flux,

$$\mathbf{q}_{\mathrm{R}} = -\mathbf{K}(\vartheta)\, \nabla\vartheta\,, \tag{3.77}$$

where $\mathbf{K}$ is a positive definite thermal conductivity.

Note that on account of the transformation rules listed in the paragraph containing (3.72) and (3.73), and since $(\boldsymbol{\xi}^{(\alpha)}, \mathbf{A}^{(\alpha)})$ are also invariant,

- *the constitutive equations* (3.74) *and* (3.77) *are frame-indifferent.*

3.3.1 Thermodynamic restrictions

Since

$$\begin{aligned}
\overset{\cdot}{\overline{\bar{\psi}^{(\alpha)}(\mathbf{C}^{e\,(\alpha)}, \mathbf{A}^{(\alpha)}, \vartheta)}} = {} & \frac{\partial \bar{\psi}^{(\alpha)}(\mathbf{C}^{e\,(\alpha)}, \mathbf{A}^{(\alpha)}, \vartheta)}{\partial \mathbf{C}^{e\,(\alpha)}} : \overset{\cdot}{\overline{\mathbf{C}^{e\,(\alpha)}}} \\
& + \frac{\partial \bar{\psi}^{(\alpha)}(\mathbf{C}^{e\,(\alpha)}, \mathbf{A}^{(\alpha)}, \vartheta)}{\partial \mathbf{A}^{(\alpha)}} : \overset{\cdot}{\overline{\mathbf{A}^{(\alpha)}}} + \frac{\partial \bar{\psi}^{(\alpha)}(\mathbf{C}^{e\,(\alpha)}, \mathbf{A}^{(\alpha)}, \vartheta)}{\partial \vartheta}\, \dot{\vartheta},
\end{aligned}$$

and, using $(3.74)_6$,

$$\begin{aligned}
&\frac{\partial\bar{\psi}^{(\alpha)}(\mathbf{C}^{e\,(\alpha)},\mathbf{A}^{(\alpha)},\vartheta)}{\partial\mathbf{A}^{(\alpha)}}:\overset{\cdot}{\mathbf{A}^{(\alpha)}}\\
&\quad=\frac{\partial\bar{\psi}^{(\alpha)}(\mathbf{C}^{e\,(\alpha)},\mathbf{A}^{(\alpha)},\vartheta)}{\partial\mathbf{A}^{(\alpha)}}:\Big(\mathbf{L}^{p\,(\alpha)}\mathbf{A}^{(\alpha)}+\mathbf{A}^{(\alpha)}\mathbf{L}^{p\,(\alpha)\top}-\mathbf{G}^{(\alpha)}(\boldsymbol{\xi}^{(\alpha)},\mathbf{A}^{(\alpha)},\vartheta)\,l^{p\,(\alpha)}\Big)\\
&=\Big(2\frac{\partial\bar{\psi}^{(\alpha)}(\mathbf{C}^{e\,(\alpha)},\mathbf{A}^{(\alpha)},\vartheta)}{\partial\mathbf{A}^{(\alpha)}}\mathbf{A}^{(\alpha)}\Big):\mathbf{L}^{p\,(\alpha)}-\Big(\frac{\partial\bar{\psi}^{(\alpha)}(\mathbf{C}^{e\,(\alpha)},\mathbf{A}^{(\alpha)},\vartheta)}{\partial\mathbf{A}^{(\alpha)}}:\mathbf{G}^{(\alpha)}(\boldsymbol{\xi}^{(\alpha)},\mathbf{A}^{(\alpha)},\vartheta)\Big)\,l^{p\,(\alpha)},
\end{aligned}$$

the free-energy imbalance (3.71) requires that the constitutive equations (3.74) and (3.77) satisfy

$$\begin{aligned}
&\sum_{\alpha=1}^{M}\left[\tfrac{1}{2}\bar{\mathbf{P}}^{e\,(\alpha)}(\mathbf{C}^{e\,(\alpha)},\mathbf{A}^{(\alpha)},\vartheta)-\frac{\partial\bar{\psi}^{(\alpha)}(\mathbf{C}^{e\,(\alpha)},\mathbf{A}^{(\alpha)},\vartheta)}{\partial\mathbf{C}^{e\,(\alpha)}}\right]:\overset{\cdot}{\mathbf{C}^{e\,(\alpha)}}\\
&-\sum_{\alpha=1}^{M}\left[\bar{\eta}^{(\alpha)}(\mathbf{C}^{e\,(\alpha)},\mathbf{A}^{(\alpha)},\vartheta)+\frac{\partial\bar{\psi}^{(\alpha)}(\mathbf{C}^{e\,(\alpha)},\mathbf{A}^{(\alpha)},\vartheta)}{\partial\vartheta}\right]\dot{\vartheta}\\
&+\sum_{\alpha=1}^{M}\left[\left\{\mathbf{M}^{e\,(\alpha)}-2\,\frac{\partial\bar{\psi}^{(\alpha)}(\mathbf{C}^{e\,(\alpha)},\mathbf{A}^{(\alpha)},\vartheta)}{\partial\mathbf{A}^{(\alpha)}}\mathbf{A}^{(\alpha)}\right\}_{0}:\bar{\mathbf{N}}^{p\,(\alpha)}(\mathbf{M}^{e\,(\alpha)},\boldsymbol{\xi}^{(\alpha)},\mathbf{A}^{(\alpha)},\vartheta)\right.\\
&\left.+\Big(\frac{\partial\bar{\psi}^{(\alpha)}(\mathbf{C}^{e\,(\alpha)},\mathbf{A}^{(\alpha)},\vartheta)}{\partial\mathbf{A}^{(\alpha)}}:\mathbf{G}^{(\alpha)}(\boldsymbol{\xi}^{(\alpha)},\mathbf{A}^{(\alpha)},\vartheta)\Big)\right]\bar{l}^{p\,(\alpha)}(\mathbf{M}^{e\,(\alpha)},\boldsymbol{\xi}^{(\alpha)},\mathbf{A}^{(\alpha)},\vartheta)\\
&+\frac{1}{\vartheta}\,\nabla\vartheta\cdot\mathbf{K}(\vartheta)\nabla\vartheta\geq 0,
\end{aligned}\tag{3.78}$$

and hold for all arguments in the domains of the constitutive functions, and in all motions of the body.

Thus, *sufficient* conditions that the constitutive equations satisfy the free-energy imbalance are

(i) *the free energy determines the stress and the entropy via the* **stress relations** and **entropy relations:**

$$\bar{\mathbf{P}}^{e\,(\alpha)}(\mathbf{C}^{e\,(\alpha)},\mathbf{A}^{(\alpha)},\vartheta)=2\,\frac{\partial\bar{\psi}^{(\alpha)}(\mathbf{C}^{e\,(\alpha)},\mathbf{A}^{(\alpha)},\vartheta)}{\partial\mathbf{C}^{e\,(\alpha)}},\tag{3.79}$$

$$\bar{\eta}^{(\alpha)}(\mathbf{C}^{e\,(\alpha)},\mathbf{A}^{(\alpha)},\vartheta)=-\frac{\partial\bar{\psi}^{(\alpha)}(\mathbf{C}^{e\,(\alpha)},\mathbf{A}^{(\alpha)},\vartheta)}{\partial\vartheta}.\tag{3.80}$$

(ii) *the plastic distortion-rates* $\mathbf{L}^{p\,(\alpha)}$ *and the temperature gradient* $\nabla\vartheta$ *satisfy the* **reduced dissipation inequality**

$$\begin{aligned}
&\sum_{\alpha=1}^{M}\left[\left\{\mathbf{M}^{e\,(\alpha)}-2\,\frac{\partial\bar{\psi}^{(\alpha)}(\mathbf{C}^{e\,(\alpha)},\mathbf{A}^{(\alpha)},\vartheta)}{\partial\mathbf{A}^{(\alpha)}}\mathbf{A}^{(\alpha)}\right\}_{0}:\bar{\mathbf{N}}^{p\,(\alpha)}(\mathbf{M}^{e\,(\alpha)},\boldsymbol{\xi}^{(\alpha)},\mathbf{A}^{(\alpha)},\vartheta)\right.\\
&\left.+\Big(\frac{\partial\bar{\psi}^{(\alpha)}(\mathbf{C}^{e\,(\alpha)},\mathbf{A}^{(\alpha)},\vartheta)}{\partial\mathbf{A}^{(\alpha)}}:\mathbf{G}^{(\alpha)}(\boldsymbol{\xi}^{(\alpha)},\mathbf{A}^{(\alpha)},\vartheta)\Big)\right]\bar{l}^{p\,(\alpha)}(\mathbf{M}^{e\,(\alpha)},\boldsymbol{\xi}^{(\alpha)},\mathbf{A}^{(\alpha)},\vartheta)\\
&+\frac{1}{\vartheta}\,\nabla\vartheta\cdot\mathbf{K}(\vartheta)\nabla\vartheta\geq 0,
\end{aligned}\tag{3.81}$$

We assume henceforth that (3.79) and (3.80) hold in all motions of the body, and that the material is **strictly dissipative** in the sense that it satisfies the **mechanical dissipation inequality**

$$\Bigg[\Bigg\{\mathbf{M}^{e\,(\alpha)} - 2\,\frac{\partial\bar{\psi}^{(\alpha)}(\mathbf{C}^{e\,(\alpha)},\mathbf{A}^{(\alpha)},\vartheta)}{\partial\mathbf{A}^{(\alpha)}}\mathbf{A}^{(\alpha)}\Bigg\}_0 : \bar{\mathbf{N}}^{p\,(\alpha)}(\mathbf{M}^{e\,(\alpha)},\boldsymbol{\xi}^{(\alpha)},\mathbf{A}^{(\alpha)},\vartheta) + \Big(\frac{\partial\bar{\psi}^{(\alpha)}(\mathbf{C}^{e\,(\alpha)},\mathbf{A}^{(\alpha)},\vartheta)}{\partial\mathbf{A}^{(\alpha)}} : \mathbf{G}^{(\alpha)}(\boldsymbol{\xi}^{(\alpha)},\mathbf{A}^{(\alpha)},\vartheta)\Big)\Bigg]\,\bar{l}^{p\,(\alpha)}(\mathbf{M}^{e\,(\alpha)},\boldsymbol{\xi}^{(\alpha)},\mathbf{A}^{(\alpha)},\vartheta) > 0 \quad (3.82)$$

whenever $\mathbf{L}^{p\,(\alpha)} \neq \mathbf{0}$ for each α, and that it separately satisfies the **heat conduction inequality**

$$\frac{1}{\vartheta}\,\nabla\vartheta\cdot\mathbf{K}(\vartheta)\nabla\vartheta > 0 \quad \text{whenever} \quad \nabla\vartheta \neq \mathbf{0}. \quad (3.83)$$

The last inequality implies that the thermal conductivity tensor is positive definite.

Further consequences of thermodynamics: Gibbs relations. Entropy relation. Partial differential equation for temperature

In view of (3.74), (3.79) and (3.80), we have the *first Gibbs relation*,

$$\begin{aligned}\dot{\psi}_{\mathrm{R}} = {}& \tfrac{1}{2}\textstyle\sum_{\alpha=1}^{M}\,\mathbf{P}^{e\,(\alpha)} : \overset{\cdot}{\overline{\mathbf{C}^{e\,(\alpha)}}} - \eta_{\mathrm{R}}\dot{\vartheta} \\ & + \Big(2\frac{\partial\bar{\psi}^{(\alpha)}(\mathbf{C}^{e\,(\alpha)},\mathbf{A}^{(\alpha)},\vartheta)}{\partial\mathbf{A}^{(\alpha)}}\mathbf{A}^{(\alpha)}\Big)_0 : \mathbf{L}^{p\,(\alpha)} \\ & - \Big(\frac{\partial\bar{\psi}^{(\alpha)}(\mathbf{C}^{e\,(\alpha)},\mathbf{A}^{(\alpha)},\vartheta)}{\partial\mathbf{A}^{(\alpha)}} : \mathbf{G}^{(\alpha)}(\boldsymbol{\xi}^{(\alpha)},\mathbf{A}^{(\alpha)},\vartheta)\Big)\,l^{p\,(\alpha)},\end{aligned} \quad (3.84)$$

which, with (3.57), yields the *second Gibbs relation*

$$\begin{aligned}\dot{\varepsilon}_{\mathrm{R}} = {}& \vartheta\dot{\eta}_{\mathrm{R}} + \tfrac{1}{2}\textstyle\sum_{\alpha=1}^{M}\,\mathbf{P}^{e\,(\alpha)} : \overset{\cdot}{\overline{\mathbf{C}^{e\,(\alpha)}}} \\ & - \Big(2\frac{\partial\bar{\psi}^{(\alpha)}(\mathbf{C}^{e\,(\alpha)},\mathbf{A}^{(\alpha)},\vartheta)}{\partial\mathbf{A}^{(\alpha)}}\mathbf{A}^{(\alpha)}\Big)_0 : \mathbf{L}^{p\,(\alpha)} \\ & + \Big(\frac{\partial\bar{\psi}^{(\alpha)}(\mathbf{C}^{e\,(\alpha)},\mathbf{A}^{(\alpha)},\vartheta)}{\partial\mathbf{A}^{(\alpha)}} : \mathbf{G}^{(\alpha)}(\boldsymbol{\xi}^{(\alpha)},\mathbf{A}^{(\alpha)},\vartheta)\Big)\,l^{p\,(\alpha)},\end{aligned} \quad (3.85)$$

where $\varepsilon_{\mathrm{R}} \overset{\mathrm{def}}{=} \rho\,J\,\varepsilon$ is the internal energy density per unit reference volume.

Using the second Gibbs relation, the balance of energy (3.70) may be written as an *entropy balance*

$$\begin{aligned}\vartheta\dot{\eta}_{\mathrm{R}} = &-\mathrm{Div}\,\mathbf{q}_{\mathrm{R}} + q_{\mathrm{R}} \\ &+ \sum_{\alpha=1}^{M} \left\{ \mathbf{M}^{e\,(\alpha)} - 2\,\frac{\partial \bar{\psi}^{(\alpha)}(\mathbf{C}^{e\,(\alpha)}, \mathbf{A}^{(\alpha)}, \vartheta)}{\partial \mathbf{A}^{(\alpha)}} \mathbf{A}^{(\alpha)} \right\}_0 : \mathbf{L}^{p\,(\alpha)} \\ &+ \sum_{\alpha=1}^{M} \Big(\frac{\partial \bar{\psi}^{(\alpha)}(\mathbf{C}^{e\,(\alpha)}, \mathbf{A}^{(\alpha)}, \vartheta)}{\partial \mathbf{A}^{(\alpha)}} : \mathbf{G}^{(\alpha)}(\boldsymbol{\xi}^{(\alpha)}, \mathbf{A}^{(\alpha)}, \vartheta) \Big) l^{p\,(\alpha)} \,. \end{aligned} \tag{3.86}$$

Granted the thermodynamically restricted constitutive relations (3.79) and (3.80), this entropy relation is equivalent to balance of energy.

Next, the internal energy density for each α is given by

$$\bar{\varepsilon}^{(\alpha)}(\mathbf{C}^{e\,(\alpha)}, \mathbf{A}^{(\alpha)}, \vartheta) \stackrel{\mathrm{def}}{=} \bar{\psi}^{(\alpha)}(\mathbf{C}^{e\,(\alpha)}, \mathbf{A}^{(\alpha)}, \vartheta) + \vartheta\, \bar{\eta}^{(\alpha)}(\mathbf{C}^{e\,(\alpha)}, \mathbf{A}^{(\alpha)}, \vartheta), \tag{3.87}$$

so that the total internal energy is

$$\varepsilon_{\mathrm{R}} = \sum_{\alpha=1}^{M} \bar{\varepsilon}^{(\alpha)}(\mathbf{C}^{e\,(\alpha)}, \mathbf{A}^{(\alpha)}, \vartheta) \,. \tag{3.88}$$

Then, the *specific heat* is defined by

$$c \stackrel{\mathrm{def}}{=} \sum_{\alpha=1}^{M} \frac{\partial \bar{\varepsilon}^{(\alpha)}(\mathbf{C}^{e\,(\alpha)}, \mathbf{A}^{(\alpha)}, \vartheta)}{\partial \vartheta} \,. \tag{3.89}$$

Hence, from (3.87)

$$c \stackrel{\mathrm{def}}{=} \sum_{\alpha=1}^{M} \Big[\frac{\partial \bar{\psi}^{(\alpha)}(\mathbf{C}^{e\,(\alpha)}, \mathbf{A}^{(\alpha)}, \vartheta)}{\partial \vartheta} + \bar{\eta}^{(\alpha)}(\mathbf{C}^{e\,(\alpha)}, \mathbf{A}^{(\alpha)}, \vartheta) + \vartheta\, \frac{\partial \bar{\eta}^{(\alpha)}(\mathbf{C}^{e\,(\alpha)}, \mathbf{A}^{(\alpha)}, \vartheta)}{\partial \vartheta} \Big] \,, \tag{3.90}$$

and use of (3.80) gives

$$c \stackrel{\mathrm{def}}{=} -\vartheta \sum_{\alpha=1}^{M} \frac{\partial^2 \bar{\psi}^{(\alpha)}(\mathbf{C}^{e\,(\alpha)}, \mathbf{A}^{(\alpha)}, \vartheta)}{\partial \vartheta^2} \,. \tag{3.91}$$

Next, from (3.80),

$$\begin{aligned}\dot{\eta}_r = &-\sum_{\alpha=1}^{M} \frac{\partial^2 \bar{\psi}^{(\alpha)}(\mathbf{C}^{e\,(\alpha)}, \mathbf{A}^{(\alpha)}, \vartheta)}{\partial \vartheta\, \partial \mathbf{C}^{e\,(\alpha)}} : \dot{\mathbf{C}}^{e\,(\alpha)} \\ &-\sum_{\alpha=1}^{M} \frac{\partial^2 \bar{\psi}^{(\alpha)}(\mathbf{C}^{e\,(\alpha)}, \mathbf{A}^{(\alpha)}, \vartheta)}{\partial \vartheta\, \partial \mathbf{A}^{(\alpha)}} : \dot{\mathbf{A}}^{(\alpha)} \\ &-\sum_{\alpha=1}^{M} \frac{\partial^2 \bar{\psi}^{(\alpha)}(\mathbf{C}^{e\,(\alpha)}, \mathbf{A}^{(\alpha)}, \vartheta)}{\partial \vartheta^2}\, \dot{\vartheta}\,. \end{aligned} \tag{3.92}$$

Then, using (3.91) and (3.92) in (3.86) gives the following partial differential equation for the temperature

$$\begin{aligned} c\dot{\vartheta} = &-\mathrm{Div}\, \mathbf{q}_{\mathrm{R}} + q_{\mathrm{R}} \\ &+ \sum_{\alpha=1}^{M} \left\{ \mathbf{M}^{e\,(\alpha)} - 2\, \frac{\partial \bar{\psi}^{(\alpha)}(\mathbf{C}^{e\,(\alpha)}, \mathbf{A}^{(\alpha)}, \vartheta)}{\partial \mathbf{A}^{(\alpha)}} \mathbf{A}^{(\alpha)} \right\}_0 : \mathbf{L}^{p\,(\alpha)} \\ &+ \sum_{\alpha=1}^{M} \Big(\frac{\partial \bar{\psi}^{(\alpha)}(\mathbf{C}^{e\,(\alpha)}, \mathbf{A}^{(\alpha)}, \vartheta)}{\partial \mathbf{A}^{(\alpha)}} : \mathbf{G}^{(\alpha)}(\boldsymbol{\xi}^{(\alpha)}, \mathbf{A}^{(\alpha)}, \vartheta) \Big) l^{p\,(\alpha)} \\ &+ \vartheta \sum_{\alpha=1}^{M} \frac{\partial^2 \bar{\psi}^{(\alpha)}(\mathbf{C}^{e\,(\alpha)}, \mathbf{A}^{(\alpha)}, \vartheta)}{\partial \vartheta\, \partial \mathbf{C}^{e\,(\alpha)}} : \dot{\mathbf{C}}^{e\,(\alpha)} \\ &+ \vartheta \sum_{\alpha=1}^{M} \frac{\partial^2 \bar{\psi}^{(\alpha)}(\mathbf{C}^{e\,(\alpha)}, \mathbf{A}^{(\alpha)}, \vartheta)}{\partial \vartheta\, \partial \mathbf{A}^{(\alpha)}} : \dot{\mathbf{A}}^{(\alpha)}. \end{aligned} \tag{3.93}$$

3.3.2 Isotropy

The following definitions help to make precise our notion of an isotropic material:

(i) Orth^+ = the group of all rotations (the proper orthogonal group);

(ii) the *symmetry group* $\mathcal{G}_{\mathrm{R}}$, is the group of all rotations of the *reference* configuration that leaves the response of the material unaltered;

(ii) the *symmetry group* $\mathcal{G}_{\mathrm{I}}^{(\alpha)}$ at each time t, is the group of all rotations of the *intermediate* structural space for each α that leaves the response of the material unaltered.

We now discuss the manner in which the basic fields transform under such transformations, granted the physically natural requirement of invariance of the internal power (3.69), or equivalently, the requirement that

$$\mathbf{P}^{e\,(\alpha)} : \dot{\mathbf{C}}^{e\,(\alpha)} \quad \text{and} \quad \mathbf{M}^{e\,(\alpha)} : \mathbf{L}^{p\,(\alpha)} \quad \text{be invariant.} \tag{3.94}$$

Fix attention on a given micromechanism α, and let $\mathbf{Q}$ be a *time-independent rotation of the reference configuration*. Then $\mathbf{F} \to \mathbf{FQ}$, and hence

$$\mathbf{F}^{p\,(\alpha)} \to \mathbf{F}^{p\,(\alpha)}\mathbf{Q} \quad \text{and} \quad \mathbf{F}^{e\,(\alpha)} \text{ are invariant,} \tag{3.95}$$

so that, by (3.8) and (3.15), $\dot{\mathbf{C}}^{e\,(\alpha)}$ and $\mathbf{L}^{p\,(\alpha)}$ are invariant. We may therefore use (3.94) to conclude that $\mathbf{P}^{e\,(\alpha)}$ and $\mathbf{M}^{e\,(\alpha)}$ are invariant. Further, since the tensor $\mathbf{A}^{(\alpha)}$ maps vectors in the intermediate space into vectors in the same space, $\mathbf{A}^{(\alpha)}$ is invariant, and since $\boldsymbol{\xi}^{(\alpha)}$ are scalars, they too are invariant. Thus

- the constitutive equations (3.74) are unaffected by such rotations of the reference configuration.

Turning our attention next to the constitutive equation (3.77) for the heat flux, a standard result from the theory of finite thermoelasticity is that under a symmetry transformation $\mathbf{Q}$ for the reference configuration, the temperature gradient $\nabla\vartheta$ and the heat flux $\mathbf{q}_{\mathrm{R}}$ transform as

$$\nabla\vartheta \to \mathbf{Q}^{\top}\nabla\vartheta, \qquad \mathbf{q}_{\mathrm{R}} \to \mathbf{Q}^{\top}\mathbf{q}_{\mathrm{R}}.$$

Hence, from (3.77) the thermal conductivity tensor must obey

$$\mathbf{K}(\vartheta) = \mathbf{Q}^{\top}\mathbf{K}(\vartheta)\mathbf{Q} \tag{3.96}$$

for all rotations $\mathbf{Q}$ in the symmetry group $\mathcal{G}_{\mathrm{R}}$.

Next, fix attention on a given micromechanism α, and let $\mathbf{Q}$, a *time-independent rotation of the corresponding intermediate space*, be a symmetry transformation. Then $\mathbf{F}$ is unaltered by such a rotation, and hence

$$\mathbf{F}^{e\,(\alpha)} \to \mathbf{F}^{e\,(\alpha)}\mathbf{Q} \quad \text{and} \quad \mathbf{F}^{p\,(\alpha)} \to \mathbf{Q}^{\top}\mathbf{F}^{p\,(\alpha)}, \tag{3.97}$$

and also

$$\mathbf{C}^{e\,(\alpha)} \to \mathbf{Q}^{\top}\mathbf{C}^{e\,(\alpha)}\mathbf{Q}, \qquad \dot{\mathbf{C}}^{e\,(\alpha)} \to \mathbf{Q}^{\top}\dot{\mathbf{C}}^{e\,(\alpha)}\mathbf{Q}, \qquad \mathbf{L}^{p\,(\alpha)} \to \mathbf{Q}^{\top}\mathbf{L}^{p\,(\alpha)}\mathbf{Q}. \tag{3.98}$$

Further, since the tensor $\mathbf{A}^{(\alpha)}$ maps vectors in the intermediate space into vectors in the same space, we assume that $\mathbf{A}^{(\alpha)}$ transforms as

$$\mathbf{A}^{(\alpha)} \to \mathbf{Q}^{\top}\mathbf{A}^{(\alpha)}\mathbf{Q},$$

and hence

$$\dot{\mathbf{A}}^{(\alpha)} \to \mathbf{Q}^{\top}\dot{\mathbf{A}}^{(\alpha)}\mathbf{Q}.$$

Then (3.98) and (3.94) yield the transformation laws

$$\mathbf{P}^{e\,(\alpha)} \to \mathbf{Q}^{\top}\mathbf{P}^{e\,(\alpha)}\mathbf{Q}, \qquad \mathbf{M}^{e\,(\alpha)} \to \mathbf{Q}^{\top}\mathbf{M}^{e\,(\alpha)}\mathbf{Q}. \tag{3.99}$$

Thus, with reference to the constitutive equations (3.74) we conclude that

$$\left.\begin{aligned}
\bar{\psi}^{(\alpha)}(\mathbf{C}^{e\,(\alpha)}, \mathbf{A}^{(\alpha)}, \vartheta) &= \bar{\psi}^{(\alpha)}(\mathbf{Q}^{\top}\mathbf{C}^{e\,(\alpha)}\mathbf{Q}, \mathbf{Q}^{\top}\mathbf{A}^{(\alpha)}\mathbf{Q}, \vartheta),\\
\bar{\eta}^{(\alpha)}(\mathbf{C}^{e\,(\alpha)}, \mathbf{A}^{(\alpha)}, \vartheta) &= \bar{\eta}^{(\alpha)}(\mathbf{Q}^{\top}\mathbf{C}^{e\,(\alpha)}\mathbf{Q}, \mathbf{Q}^{\top}\mathbf{A}^{(\alpha)}\mathbf{Q}, \vartheta),\\
\mathbf{Q}^{\top}\bar{\mathbf{P}}^{e\,(\alpha)}(\mathbf{C}^{e\,(\alpha)}, \mathbf{A}^{(\alpha)}, \vartheta)\mathbf{Q} &= \bar{\mathbf{P}}^{e\,(\alpha)}(\mathbf{Q}^{\top}\mathbf{C}^{e\,(\alpha)}\mathbf{Q}, \mathbf{Q}^{\top}\mathbf{A}^{(\alpha)}\mathbf{Q}, \vartheta),\\
\mathbf{Q}^{\top}\bar{\mathbf{N}}^{p\,(\alpha)}(\mathbf{M}^{e\,(\alpha)}, \mathbf{A}^{(\alpha)}, \boldsymbol{\xi}^{(\alpha)}, \vartheta)\mathbf{Q} &= \bar{\mathbf{N}}^{p\,(\alpha)}(\mathbf{Q}^{\top}\mathbf{M}^{e\,(\alpha)}\mathbf{Q}, \mathbf{Q}^{\top}\mathbf{A}^{(\alpha)}\mathbf{Q}, \boldsymbol{\xi}^{(\alpha)}, \vartheta),\\
\bar{l}^{p\,(\alpha)}(\mathbf{M}^{e\,(\alpha)}, \mathbf{A}^{(\alpha)}, \boldsymbol{\xi}^{(\alpha)}, \vartheta) &= \bar{l}^{p\,(\alpha)}(\mathbf{Q}^{\top}\mathbf{M}^{e\,(\alpha)}\mathbf{Q}, \mathbf{Q}^{\top}\mathbf{A}^{(\alpha)}\mathbf{Q}, \boldsymbol{\xi}^{(\alpha)}, \vartheta),\\
h_i^{(\alpha)}(l^{p\,(\alpha)}, \mathbf{N}^{p\,(\alpha)}, \boldsymbol{\xi}^{(\alpha)}\mathbf{A}^{(\alpha)}, \vartheta) &= h_i^{(\alpha)}(l^{p\,(\alpha)}, \mathbf{Q}^{\top}\mathbf{N}^{p\,(\alpha)}\mathbf{Q}, \boldsymbol{\xi}^{(\alpha)}, \mathbf{Q}^{\top}\mathbf{A}^{(\alpha)}\mathbf{Q}, \vartheta),\\
\mathbf{Q}^{\top}\mathbf{G}^{(\alpha)}(\boldsymbol{\xi}^{(\alpha)}, \mathbf{A}^{(\alpha)}, \vartheta)\mathbf{Q} &= \mathbf{G}^{(\alpha)}(\boldsymbol{\xi}^{(\alpha)}, \mathbf{Q}^{\top}\mathbf{A}^{(\alpha)}\mathbf{Q}), \vartheta,
\end{aligned}\right\} \tag{3.100}$$

must hold for all rotations $\mathbf{Q}$ in the *symmetry group* $\mathcal{G}_{\mathrm{I}}^{(\alpha)}$ at each time t.

We refer to the material as *isotropic* (and to the reference configuration and intermediate spaces as undistorted) if

$$\mathcal{G}_{\mathrm{R}} = \mathrm{Orth}^{+}, \qquad \mathcal{G}_{\mathrm{I}}^{(\alpha)} = \mathrm{Orth}^{+}, \tag{3.101}$$

so that the response of the material is invariant under arbitrary rotations of the reference and intermediate space for each α at each time t.[1] Henceforth

- *we restrict attention to materials that are* **isotropic**.

In this case,

- the response functions $\bar{\psi}^{(\alpha)}$, $\bar{\eta}^{(\alpha)}$, $\bar{\mathbf{P}}^{e\,(\alpha)}$, $\bar{\mathbf{N}}^{p\,(\alpha)}$, $\bar{l}^{p\,(\alpha)}$, $h_i^{(\alpha)}$, and $\mathbf{G}^{(\alpha)}$ must each be *isotropic*,

and that the thermal conductivity has the representation

$$\mathbf{K}(\vartheta) = \kappa(\vartheta)\mathbf{1}, \qquad \text{with} \qquad \kappa(\vartheta) > 0, \tag{3.102}$$

a scalar thermal conductivity.

3.3.3 Separability hypothesis for the free energy

We assume that the free energy has the separable form

$$\psi_{\mathrm{R}} = \sum_{\alpha=1}^{M} \bar{\psi}^{e\,(\alpha)}(\mathbf{C}^{e\,(\alpha)}, \vartheta) + \sum_{\alpha=1}^{M} \bar{\psi}^{d\,(\alpha)}(\mathbf{A}^{(\alpha)}, \vartheta) \tag{3.103}$$

with $\bar{\psi}^{e\,(\alpha)}$ an elastic energy, and $\bar{\psi}^{d\,(\alpha)}$ a defect energy associated with plastic flow, for each α.

[1] For polymer glasses this notion attempts to characterize situations in which the material has a completely disordered molecular structure.

Consequences of isotropy of the elastic energy

Since $\bar{\psi}^{e\,(\alpha)}(\mathbf{C}^{e\,(\alpha)}, \vartheta)$ is an isotropic function of $\mathbf{C}^{e\,(\alpha)}$, it has the representation

$$\bar{\psi}^{e\,(\alpha)}(\mathbf{C}^{e\,(\alpha)}, \vartheta) = \tilde{\psi}^{e\,(\alpha)}(\mathcal{I}_{\mathbf{C}^{e\,(\alpha)}}, \vartheta), \tag{3.104}$$

where

$$\mathcal{I}_{\mathbf{C}^{e\,(\alpha)}} = \Big(I_1(\mathbf{C}^{e\,(\alpha)}), I_2(\mathbf{C}^{e\,(\alpha)}), I_3(\mathbf{C}^{e\,(\alpha)})\Big)$$

is the list of principal invariants of $\mathbf{C}^{e\,(\alpha)}$. Thus, from (3.79)

$$\mathbf{P}^{e\,(\alpha)} = 2\frac{\partial\tilde{\psi}^{e\,(\alpha)}(\mathcal{I}_{\mathbf{C}^{e\,(\alpha)}})}{\partial\mathbf{C}^{e\,(\alpha)}}, \tag{3.105}$$

and we note that $\mathbf{P}^{e\,(\alpha)}$ is an *isotropic function of* $\mathbf{C}^{e\,(\alpha)}$. Then since (cf. (3.52))

$$\mathbf{M}^{e\,(\alpha)} = \mathbf{C}^{e\,(\alpha)}\mathbf{P}^{e\,(\alpha)},$$

and $\mathbf{P}^{e\,(\alpha)}$ is isotropic, we find that $\mathbf{P}^{e\,(\alpha)}$ and $\mathbf{C}^{e\,(\alpha)}$ commute,

$$\mathbf{C}^{e\,(\alpha)}\mathbf{P}^{e\,(\alpha)} = \mathbf{P}^{e\,(\alpha)}\mathbf{C}^{e\,(\alpha)}, \tag{3.106}$$

and hence that

- *the Mandel stress* $\mathbf{M}^{e\,(\alpha)}$ *for each* α *is* **symmetric**.

Consequences of isotropy of the defect energy

Let

$$\mathcal{I}_{\mathbf{A}^{(\alpha)}} = \Big(I_1(\mathbf{A}^{(\alpha)}), I_2(\mathbf{A}^{(\alpha)}), I_3(\mathbf{A}^{(\alpha)}), \vartheta\Big)$$

denote the list of principal invariants of $\mathbf{A}^{(\alpha)}$, then the defect free energy has a representation

$$\bar{\psi}^{d\,(\alpha)} = \tilde{\psi}^{d\,(\alpha)}(\mathcal{I}_{\mathbf{A}^{(\alpha)}}, \vartheta), \tag{3.107}$$

and this yields a *symmetric* tensor

$$\mathbf{M}^{(\alpha)}_{\text{back}} = 2\,\frac{\partial\bar{\psi}^{d}_{\text{I}}(\mathcal{I}_{\mathbf{A}^{(\alpha)}}), \vartheta}{\partial\mathbf{A}^{(\alpha)}}\,\mathbf{A}^{(\alpha)}, \tag{3.108}$$

which we call a **back-stress**. Then, defining *effective stress* by

$$\mathbf{M}^{e\,(\alpha)}_{\text{eff}} \overset{\text{def}}{=} \mathbf{M}^{e\,(\alpha)} - \mathbf{M}^{(\alpha)}_{\text{back}}, \tag{3.109}$$

we may write the mechanical dissipation inequality (3.82) for each α as:

$$\Big[\Big\{\mathbf{M}^{e\,(\alpha)}_{\text{eff}}\Big\}_0 : \bar{\mathbf{N}}^{p\,(\alpha)}(\mathbf{M}^{e\,(\alpha)}, \boldsymbol{\xi}^{(\alpha)}, \mathbf{A}^{(\alpha)}, \vartheta) + \Big(\frac{\partial \bar{\psi}^{d\,(\alpha)}(\mathbf{A}^{(\alpha)}, \vartheta)}{\partial \mathbf{A}^{(\alpha)}} : \mathbf{G}^{(\alpha)}(\boldsymbol{\xi}^{(\alpha)}, \mathbf{A}^{(\alpha)}, \vartheta)\Big)\Big] \bar{l}^{p\,(\alpha)}(\mathbf{M}^{e\,(\alpha)}, \boldsymbol{\xi}^{(\alpha)}, \mathbf{A}^{(\alpha)}, \vartheta) > 0 \quad (3.110)$$

whenever $l^{p\,(\alpha)} > 0$.

3.3.4 Codirectionality and strong isotropy hypotheses

We now make two major assumptions concerning the plastic flow for isotropic materials:

(1) **Codirectionality hypotheses:** Guided by the dissipation inequality (3.110), we assume henceforth that $\mathbf{N}^{p\,(\alpha)}$ is codirectional with $(\mathbf{M}^{e\,(\alpha)}_{\text{eff}})_0$,

$$\mathbf{N}^{p\,(\alpha)} = \frac{(\mathbf{M}^{e\,(\alpha)}_{\text{eff}})_0}{|(\mathbf{M}^{e\,(\alpha)}_{\text{eff}})_0|}; \quad (3.111)$$

an assumption we refer to as the **codirectionality hypothesis**.

Since both $\mathbf{M}^{e\,(\alpha)}$ and $\mathbf{M}^{(\alpha)}_{\text{back}}$ are symmetric, so also is $\mathbf{M}^{e\,(\alpha)}_{\text{eff}}$, and a consequence of this assumption is that the skew part of $\mathbf{L}^{p\,(\alpha)}$, that is the plastic spin, is assumed to vanish,

$$\mathbf{W}^{p\,(\alpha)} = \mathbf{0}. \quad (3.112)$$

Consistent with this we replace $l^{p\,(\alpha)}$ by the norm of the plastic stretching,

$$d^{p\,(\alpha)} = |\mathbf{D}^{p\,(\alpha)}|, \quad (3.113)$$

and assume that it is given by

$$d^p = \hat{d}^p(\mathbf{M}^{e\,(\alpha)}_{\text{eff}}, \boldsymbol{\xi}^{(\alpha)}, \vartheta). \quad (3.114)$$

On account of the isotropy of the scalar flow rate function (3.114), we have that

$$d^p = \tilde{d}^p(\mathcal{I}_{\mathbf{M}^{e\,(\alpha)}_{\text{eff}}}, \boldsymbol{\xi}^{(\alpha)}, \vartheta) \geq 0, \quad (3.115)$$

where $\mathcal{I}_{\mathbf{M}^{e\,(\alpha)}_{\text{eff}}}$ is a list of invariants of $\mathbf{M}^{e\,(\alpha)}_{\text{eff}}$.

Under the codirectionality assumption, the dissipation inequality (3.110) reduces to

$$\Big[|\mathbf{M}^{e\,(\alpha)}_{\text{eff}}{}_0| + \Big(\frac{\partial \tilde{\psi}^{d\,(\alpha)}(\mathcal{I}_{\mathbf{A}^{(\alpha)}}, \vartheta)}{\partial \mathbf{A}} : \mathbf{G}^{(\alpha)}(\boldsymbol{\xi}^{(\alpha)}, \mathbf{A}^{(\alpha)}, \vartheta)\Big)\Big] \tilde{d}^p(\mathcal{I}_{\mathbf{M}^{e\,(\alpha)}_{\text{eff}}}, \boldsymbol{\xi}^{(\alpha)}, \vartheta) > 0, \quad (3.116)$$

whenever $d^{p\,(\alpha)} \neq 0$. In this case, the recovery function $\mathbf{G}(\boldsymbol{\xi}^{(\alpha)}, \mathbf{A}^{(\alpha)}, \vartheta)$ *must satisfy the constraint*

$$\left[|\mathbf{M}^{e\,(\alpha)}_{\text{eff}}{}_0| + \Big(\frac{\partial \tilde{\psi}^{d\,(\alpha)}(\mathcal{I}_{\mathbf{A}^{(\alpha)}}, \vartheta)}{\partial \mathbf{A}} : \mathbf{G}^{(\alpha)}(\boldsymbol{\xi}^{(\alpha)}, \mathbf{A}^{(\alpha)}, \vartheta) \Big) \right] > 0 \quad \text{whenever} \quad d^{p\,(\alpha)} \neq 0. \tag{3.117}$$

The codirectionality hypothesis above, while central to our definition of an isotropic plastic material, is not sufficient. We additionally require the:

(2) **Strong isotropy hypothesis:**

The function $h_i^{(\alpha)}(d^{p\,(\alpha)}, \mathbf{N}^{p\,(\alpha)}, \boldsymbol{\xi}^{(\alpha)}, \mathbf{A}^{(\alpha)}, \vartheta)$ characterizing the evolution of the scalar internal variable $\xi_i^{(\alpha)}$ is independent of the flow direction $\mathbf{N}^{p\,(\alpha)}$, an assumption we refer to as the **strong isotropy hypothesis**.

3.4 Summary of the constitutive theory for isotropic materials

The underlying constitutive equations relate the following basic fields:

$\mathbf{x} = \boldsymbol{\chi}(\mathbf{X}, t)$,	motion;
$\mathbf{F} = \nabla \boldsymbol{\chi}, \quad J = \det \mathbf{F} > 0$,	deformation gradient;
$\mathbf{F} = \mathbf{F}^{e\,(\alpha)} \mathbf{F}^{p\,(\alpha)}, \quad \alpha = 1, \ldots, M$,	elastic-plastic decomposition of $\mathbf{F}$;
$\mathbf{F}^{p\,(\alpha)}, \quad J^{p\,(\alpha)} = \det \mathbf{F}^{p\,(\alpha)} = 1$,	inelastic distortion;
$\mathbf{F}^{e\,(\alpha)}, \quad J^{e\,(\alpha)} = \det \mathbf{F}^{e\,(\alpha)} = J > 0$,	elastic distortion;
$\mathbf{F}^{e\,(\alpha)} = \mathbf{R}^{e\,(\alpha)} \mathbf{U}^{e\,(\alpha)} = \mathbf{V}^{e\,(\alpha)} \mathbf{R}^{e\,(\alpha)}$,	polar decompositions of $\mathbf{F}^{e\,(\alpha)}$;
$\mathbf{C}^{e\,(\alpha)} = \mathbf{F}^{e\,(\alpha)\top} \mathbf{F}^{e\,(\alpha)}$,	elastic right Cauchy-Green tensors;
$\vartheta > 0$,	absolute temperature;
$\nabla \vartheta$,	referential temperature gradient;
$\psi_{\text{R}} = \sum_{\alpha=1}^{M} \bar{\psi}^{(\alpha)}$,	free energy density per unit reference volume;
$\eta_{\text{R}} = \sum_{\alpha=1}^{M} \bar{\eta}^{(\alpha)}$,	entropy density per unit reference volume;
$\boldsymbol{\xi}^{(\alpha)} = (\xi_1^{(\alpha)}, \xi_2^{(\alpha)}, \ldots, \xi_m^{(\alpha)})$	m scalar internal variables for each α;
$\mathbf{A}^{(\alpha)}, \quad \mathbf{A}^{(\alpha)} = \mathbf{A}^{(\alpha)\top}, \quad \det \mathbf{A}^{(\alpha)} = 1$	tensorial internal variables for each α;
$\mathbf{q}_{\text{R}}$,	referential heat flux vector.

The constitutive equations are:

1. **Free energy:**

$$\psi_{\text{R}} = \sum_{\alpha=1}^{M} \bar{\psi}^{e\,(\alpha)}(\mathcal{I}_{\mathbf{C}^{e\,(\alpha)}}, \vartheta) + \sum_{\alpha=1}^{M} \bar{\psi}^{d\,(\alpha)}(\mathcal{I}_{\mathbf{A}^{(\alpha)}}, \vartheta), \tag{3.118}$$

where $\mathcal{I}_{\mathbf{C}^{e\,(\alpha)}}$ and $\mathcal{I}_{\mathbf{A}^{(\alpha)}}$ are the lists of the principal invariants of $\mathbf{C}^{e\,(\alpha)}$ and $\mathbf{A}^{(\alpha)}$, respectively.

2. **Cauchy stress:**

$$\mathbf{T} = \sum_{\alpha=1}^{M} \mathbf{T}^{e\,(\alpha)}, \tag{3.119}$$

with

$$\mathbf{T}^{e\,(\alpha)} \stackrel{\text{def}}{=} J^{-1}\left(\mathbf{F}^{e\,(\alpha)}\mathbf{P}^{e\,(\alpha)}\mathbf{F}^{e\,(\alpha)\top}\right), \tag{3.120}$$

where

$$\mathbf{P}^{e\,(\alpha)} = 2\,\frac{\partial\bar{\psi}^{e\,(\alpha)}(\mathcal{I}_{\mathbf{C}^{e\,(\alpha)}},\vartheta)}{\partial\mathbf{C}^{e\,(\alpha)}}\,. \tag{3.121}$$

3. Driving stresses for plastic flow:

The *symmetric* Mandel stress for each α is given by

$$\mathbf{M}^{e\,(\alpha)} = \mathbf{C}^{e\,(\alpha)}\mathbf{P}^{e\,(\alpha)}\,, \tag{3.122}$$

and the *symmetric* back stress is given by

$$\mathbf{M}^{(\alpha)}_{\text{back}} = 2\,\frac{\partial\bar{\psi}^{d\,(\alpha)}(\mathcal{I}_{\mathbf{A}^{(\alpha)}},\vartheta)}{\partial\mathbf{A}^{(\alpha)}}\,\mathbf{A}^{(\alpha)}. \tag{3.123}$$

Then, the stress difference

$$\mathbf{M}^{e\,(\alpha)}_{\text{eff}} \stackrel{\text{def}}{=} \mathbf{M}^{e\,(\alpha)} - \mathbf{M}^{(\alpha)}_{\text{back}}, \tag{3.124}$$

called the *effective stress*, is taken to be the driving stress for plastic flow.

4. Flow rules:

The evolution equation for each $\mathbf{F}^{p\,(\alpha)}$ is

$$\dot{\mathbf{F}}^{p\,(\alpha)} = \mathbf{L}^{p\,(\alpha)}\,\mathbf{F}^{p\,(\alpha)}, \qquad \mathbf{F}^{p\,(\alpha)}(\mathbf{X},0) = \mathbf{1}, \tag{3.125}$$

with

$$\mathbf{W}^{p\,(\alpha)} \equiv \operatorname{skw}\mathbf{L}^{p\,(\alpha)} = \mathbf{0}, \tag{3.126}$$

and $\mathbf{D}^{p\,(\alpha)} = \operatorname{sym}\mathbf{L}^{p\,(\alpha)}$ given by

$$\mathbf{D}^{p\,(\alpha)} = d^{p\,(\alpha)}\,\mathbf{N}^{p\,(\alpha)}, \tag{3.127}$$

$$\mathbf{N}^{p\,(\alpha)} = \frac{(\mathbf{M}^{e\,(\alpha)}_{\text{eff}})_0}{|(\mathbf{M}^{e\,(\alpha)}_{\text{eff}})_0|}, \tag{3.128}$$

$$d^{p\,(\alpha)} = \tilde{d}^{p}(\mathcal{I}_{\mathbf{M}^{e\,(\alpha)}_{\text{eff}}},\boldsymbol{\xi}^{(\alpha)},\vartheta) \geq 0. \tag{3.129}$$

5. Evolution equations for internal variables:

$$\left.\begin{aligned}\dot{\xi}^{(\alpha)}_i &= h^{(\alpha)}_i(d^{p\,(\alpha)},\boldsymbol{\xi}^{(\alpha)},\mathbf{A}^{(\alpha)},\vartheta),\\ \dot{\mathbf{A}}^{(\alpha)} &= \mathbf{D}^{p\,(\alpha)}\mathbf{A}^{(\alpha)} + \mathbf{A}^{(\alpha)}\mathbf{D}^{p\,(\alpha)} - \mathbf{G}^{(\alpha)}(\boldsymbol{\xi}^{(\alpha)},\mathbf{A}^{(\alpha)},\vartheta)d^{p\,(\alpha)},\end{aligned}\right\} \tag{3.130}$$

with the functions $h^{(\alpha)}_i$ and $\mathbf{G}^{(\alpha)}$ isotropic functions of their arguments.

The evolution equations for $\mathbf{F}^{p\,(\alpha)}$, $\boldsymbol{\xi}^{(\alpha)}$ and $\mathbf{A}^{(\alpha)}$ need to be accompanied by initial conditions. Typical initial conditions presume that the body is initially (at time $t = 0$, say) in a **virgin**

state in the sense that

$$\mathbf{F}(\mathbf{X},0)=\mathbf{F}^{p\,(\alpha)}(\mathbf{X},0)=\mathbf{A}^{(\alpha)}(\mathbf{X},0)=\mathbf{1},\qquad \xi_i^{(\alpha)}(\mathbf{X},0)=\xi_{i,0}^{(\alpha)}\ (=\text{constant}), \tag{3.131}$$

so that by $\mathbf{F}=\mathbf{F}^{e\,(\alpha)}\mathbf{F}^{p\,(\alpha)}$ we also have $\mathbf{F}^{e\,(\alpha)}(\mathbf{X},0)=\mathbf{1}$.

6. Entropy relation. Fourier's Law:

Finally, we have the entropy relation

$$\eta_{\mathrm{R}}=\sum_{\alpha=1}^{M}\eta^{(\alpha)},\qquad \eta^{(\alpha)}=-\left[\frac{\partial\bar{\psi}^{e\,(\alpha)}(\mathcal{I}_{\mathbf{C}^{e\,(\alpha)}},\vartheta)}{\partial\vartheta}+\frac{\partial\bar{\psi}^{d\,(\alpha)}(\mathcal{I}_{\mathbf{A}^{(\alpha)}},\vartheta)}{\partial\vartheta}\right], \tag{3.132}$$

together with Fourier's law

$$\mathbf{q}_{\mathrm{R}}=-\kappa\,\nabla\vartheta, \tag{3.133}$$

with $\kappa(\vartheta)>0$ the thermal conductivity.

3.4.1 Partial differential equations for the deformation and temperature fields

The partial differential equation for the deformation is obtained from the local force balance (cf. (3.46)):

$$\mathrm{Div}\,\mathbf{T}_{\mathrm{R}}+\mathbf{b}_{0\mathrm{R}}=\rho_{\mathrm{R}}\,\ddot{\boldsymbol{\chi}}. \tag{3.134}$$

The specific heat in the theory is given by

$$c\overset{\text{def}}{=}-\vartheta\left[\sum_{\alpha=1}^{M}\frac{\partial^2\bar{\psi}^{e\,(\alpha)}(\mathcal{I}_{\mathbf{C}^{e\,(\alpha)}},\vartheta)}{\partial\vartheta^2}+\sum_{\alpha=1}^{M}\frac{\partial^2\bar{\psi}^{d\,(\alpha)}(\mathcal{I}_{\mathbf{A}^{(\alpha)}},\vartheta)}{\partial\vartheta^2}\right]. \tag{3.135}$$

Then, balance of energy gives the following partial differential equation for the temperature (cf. (3.93))

$$\begin{aligned}c\dot{\vartheta}=&-\mathrm{Div}\,\mathbf{q}_{\mathrm{R}}+q_{\mathrm{R}}\\&+\left[|\mathbf{M}^{e\,(\alpha)}_{\text{eff}}{}_0|+\Big(\frac{\partial\tilde{\psi}^{d\,(\alpha)}(\mathcal{I}_{\mathbf{A}^{(\alpha)}},\vartheta)}{\partial\mathbf{A}}:\mathbf{G}^{(\alpha)}(\boldsymbol{\xi}^{(\alpha)},\mathbf{A}^{(\alpha)},\vartheta)\Big)\right]d^{p\,(\alpha)}\\&+\vartheta\sum_{\alpha=1}^{M}\frac{\partial^2\bar{\psi}^{e\,(\alpha)}(\mathcal{I}_{\mathbf{C}^{e\,(\alpha)}},\vartheta)}{\partial\vartheta\,\partial\mathbf{C}^{e\,(\alpha)}}:\dot{\mathbf{C}}^{e\,(\alpha)}\\&+\vartheta\sum_{\alpha=1}^{M}\frac{\partial^2\bar{\psi}^{d\,(\alpha)}(\mathcal{I}_{\mathbf{A}^{(\alpha)}},\vartheta)}{\partial\vartheta\,\partial\mathbf{A}^{(\alpha)}}:\dot{\mathbf{A}}^{(\alpha)}.\end{aligned} \tag{3.136}$$

3.5 Specialization of the constitutive equations

The constitutive equations listed above are fairly general. With a view towards applications, we specialize the the theory by imposing additional constitutive assumptions based on experience with existing recent theories of isotropic viscoplasticity of polymeric materials [e.g., 1–4, 19–21].

To begin, we follow Buckley and Jones [1], Dooling et al. [2] and Boyce et al. [3] and assume that that the change in the stress of an amorphous polymer arises due to two basic reasons: (i) changes due to the stretching of intermolecular (and perhaps intramolecular) bonds, and (ii) changes in the configurational entropy due to changes in the molecular conformations. Accordingly, we take a micromechanism, indexed by $\alpha = 1$, to represent the contribution to the stress due to intermolecular bond-stretching, and we take an additional micromechanism, indexed by $\alpha = 2$, to represent contributions to stress changes due to entropic changes in molecular conformations and molecular relaxations. We specialize the constitutive equations for $\alpha = 1$ and $\alpha = 2$ in the subsections below.

3.5.1 Case alpha = 1

Here the free-energy is

$$\psi^{(1)} = \underbrace{\bar{\psi}^{e\,(1)}(\mathbf{C}^{e(1)}, \vartheta)}_{\text{energetic, bond-stretching contribution}} + \underbrace{\bar{\psi}^{d\,(1)}(\mathbf{A}^{(1)}, \vartheta)}_{\text{defect energy}}. \tag{3.137}$$

For most of the rest of this section, to ease the notation, we suppress the superscript $\alpha = 1$.

Elastic energy and stress

The spectral representation of $\mathbf{C}^e$ is

$$\mathbf{C}^e = \sum_{i=1}^{3} \omega_i^e \mathbf{r}_i^e \otimes \mathbf{r}_i^e. \tag{3.138}$$

where $(\omega_1^e, \omega_2^e, \omega_3^e)$ are the positive eigenvalues, and $(\mathbf{r}_1^e, \mathbf{r}_2^e, \mathbf{r}_3^e)$ are the orthonormal eigenvectors of $\mathbf{C}^e$. Let

$$\lambda_i^e = \sqrt{\omega_i^e}, \tag{3.139}$$

denote the positive eigenvalues of $\mathbf{U}^e = \sqrt{\mathbf{C}^e}$. Then the principal invariants of $\mathbf{C}^e$ may be expressed as

$$\left.\begin{aligned} I_1(\mathbf{C}^e) &= \lambda_1^{e\,2} + \lambda_2^{e\,2} + \lambda_3^{e\,2}, \\ I_2(\mathbf{C}^e) &= \lambda_1^{e\,2}\lambda_2^{e\,2} + \lambda_2^{e\,2}\lambda_3^{e\,2} + \lambda_3^{e\,2}\lambda_1^{e\,2}, \\ I_3(\mathbf{C}^e) &= \lambda_1^{e\,2}\lambda_2^{e\,2}\lambda_3^{e\,2}; \end{aligned}\right\} \tag{3.140}$$

Using (3.140) in (3.118) to express the free energy in terms of the principal stretches, we obtain:

$$\begin{aligned} \psi^e &= \tilde{\psi}^e(\mathcal{I}_{\mathbf{C}^e}, \vartheta) \\ &= \breve{\psi}^e(\lambda_1^e, \lambda_2^e, \lambda_3^e, \vartheta). \end{aligned} \tag{3.141}$$

Then, by the chain-rule and (3.121), the stress $\mathbf{P}^e$ is given by

$$\begin{aligned}\mathbf{P}^e &= 2\,\frac{\partial \breve{\psi}^e(\lambda_1^e,\lambda_2^e,\lambda_3^e,\vartheta)}{\partial \mathbf{C}^e}\\ &= 2\sum_{i=1}^{3}\frac{\partial \breve{\psi}^e(\lambda_1^e,\lambda_2^e,\lambda_3^e,\vartheta)}{\partial \lambda_i^e}\,\frac{\partial \lambda_i^e}{\partial \mathbf{C}^e}\\ &= \sum_{i=1}^{3}\frac{1}{\lambda_i^e}\,\frac{\partial \breve{\psi}^e(\lambda_1^e,\lambda_2^e,\lambda_3^e,\vartheta)}{\partial \lambda_i^e}\,\frac{\partial \omega_i^e}{\partial \mathbf{C}^e}.\end{aligned} \tag{3.142}$$

Assume that the squared principal stretches ω_i^e are distinct, so that the ω_i^e and the principal directions $\mathbf{r}_i^e$ may be considered as functions of $\mathbf{C}^e$. Then, from (3.138),

$$\frac{\partial \omega_i^e}{\partial \mathbf{C}^e} = \mathbf{r}_i^e \otimes \mathbf{r}_i^e, \tag{3.143}$$

and, granted this, (3.143) and (3.142) imply that

$$\mathbf{P}^e = \sum_{i=1}^{3}\frac{1}{\lambda_i^e}\,\frac{\partial \breve{\psi}^e(\lambda_1^e,\lambda_2^e,\lambda_3^e,\vartheta)}{\partial \lambda_i^e}\,\mathbf{r}_i^e \otimes \mathbf{r}_i^e. \tag{3.144}$$

Also, use of (3.138) and (3.144) in (3.122) gives

$$\mathbf{M}^e = \sum_{i=1}^{3}\lambda_i^e\,\frac{\partial \breve{\psi}^e(\lambda_1^e,\lambda_2^e,\lambda_3^e,\vartheta)}{\partial \lambda_i^e}\,\mathbf{r}_i^e \otimes \mathbf{r}_i^e. \tag{3.145}$$

Next, since

$$\mathbf{F}^e = \sum_{i=1}^{3}\lambda_i^e\,\mathbf{l}_i^e \otimes \mathbf{r}_i^e, \tag{3.146}$$

where

$$\mathbf{l}_i^e = \mathbf{R}^e\,\mathbf{r}_i^e,$$

are the eigenvectors of $\mathbf{V}^e$ (or $\mathbf{B}^e$), use of (3.120) and (3.144) gives

$$\mathbf{T}^e = J^{e-1}\Big(\sum_{i=1}^{3}\lambda_i^e\,\mathbf{l}_i^e \otimes \mathbf{r}_i^e\Big)\Big(\sum_{i=1}^{3}\frac{1}{\lambda_i^e}\,\frac{\partial \breve{\psi}^e(\lambda_1^e,\lambda_2^e,\lambda_3^e,\vartheta)}{\partial \lambda_i^e}\,\mathbf{r}_i^e \otimes \mathbf{r}_i^e\Big)\Big(\sum_{i=1}^{3}\lambda_i^e\,\mathbf{r}_i^e \otimes \mathbf{l}_i^e\Big),$$

or

$$\mathbf{T}^e = J^{e-1}\sum_{i=1}^{3}\lambda_i^e\,\frac{\partial \breve{\psi}^e(\lambda_1^e,\lambda_2^e,\lambda_3^e,\vartheta)}{\partial \lambda_i^e}\,\mathbf{l}_i^e \otimes \mathbf{l}_i^e. \tag{3.147}$$

Further, (3.147) and (3.145) yield the important relation

$$\mathbf{M}^e = J^e\,\mathbf{R}^{e\top}\mathbf{T}^e\mathbf{R}^e. \tag{3.148}$$

Next, let

$$E_i^e \stackrel{\text{def}}{=} \ln \lambda_i^e \tag{3.149}$$

define *principal elastic logarithmic strains*, and consider a free energy function of the form

$$\breve{\psi}^e(\lambda_1^e, \lambda_2^e, \lambda_3^e, \vartheta) = \hat{\psi}^e(E_1^e, E_2^e, E_3^e, \vartheta) \tag{3.150}$$

so that, using (3.147),

$$\mathbf{T}^e = J^{e-1} \sum_{i=1}^{3} \frac{\partial \hat{\psi}^e(E_1^e, E_2^e, E_3^e, \vartheta)}{\partial E_i^e} \, \mathbf{l}_i^e \otimes \mathbf{l}_i^e. \tag{3.151}$$

We consider the following simple generalization of the classical strain energy function of infinitesimal isotropic elasticity which uses a logarithmic measure of finite strain,

$$\begin{aligned} \hat{\psi}^e(E_1^e, E_2^e, E_3^e, \vartheta) = G \, \left[(E_1^e)^2 + (E_2^e)^2 + (E_3^e)^2\right] + \tfrac{1}{2} \, (K - \tfrac{2}{3}G) \, (E_1^e + E_2^e + E_3^e)^2 \, , \\ - (\vartheta - \vartheta_0)(3\,K\,\alpha) \, (E_1^e + E_2^e + E_3^e) + c(\vartheta - \vartheta_0) - c\,\vartheta \ln\Big(\frac{\vartheta}{\vartheta_0}\Big), \end{aligned} \tag{3.152}$$

where the temperature-dependent parameters

$$G(\vartheta) > 0, \quad K(\vartheta) > 0, \quad \alpha(\vartheta) > 0, \quad c(\vartheta) > 0, \tag{3.153}$$

are the shear modulus, bulk modulus, coefficient of thermal expansion, and specific heat; ϑ_0 is a reference temperature. Then, (3.151) gives

$$\mathbf{T}^e = J^{e-1} \left\{ \sum_{i=1}^{3} \Big(2GE_i^e + (K - \frac{2}{3}G) \, (E_1^e + E_2^e + E_3^e) - (\vartheta - \vartheta_0)(3\,K\,\alpha) \Big) \, \mathbf{l}_i^e \otimes \mathbf{l}_i^e \right\}. \tag{3.154}$$

Let

$$\mathbf{H}^e \stackrel{\text{def}}{=} \sum_{i=1}^{3} E_i^e \, \mathbf{l}_i^e \otimes \mathbf{l}_i^e, \tag{3.155}$$

denote the logarithmic elastic strain tensor in the deformed body, and

$$\mathbf{E}^e \stackrel{\text{def}}{=} \sum_{i=1}^{3} E_i^e \, \mathbf{r}_i^e \otimes \mathbf{r}_i^e, \tag{3.156}$$

denote the logarithmic elastic strain tensor in the intermediate space, so that

$$\mathbf{E}^e = \mathbf{R}^{e\top} \mathbf{H}^e \mathbf{R}^e. \tag{3.157}$$

Then, (3.154) gives

$$\mathbf{T}^e = J^{e-1} \left\{ 2G\mathbf{H}_0^e + K\big(\operatorname{tr} \mathbf{H}^e - 3\alpha(\vartheta - \vartheta_0)\big)\mathbf{1} \right\}. \tag{3.158}$$

Further, using (3.148) and (3.158), we find that the Mandel stress is given by the simple relation

$$\mathbf{M}^e = 2G\mathbf{E}_0^e + K\ (\mathrm{tr}\,\mathbf{E}^e - 3\alpha(\vartheta - \vartheta_0))\,\mathbf{1}. \tag{3.159}$$

Thus, reinstating the superscript $\alpha = 1$ and summarizing, with

$$\mathbf{C}^{e\,(1)} = \sum_{i=1}^{3} \omega_i^e\, \mathbf{r}_i^e \otimes \mathbf{r}_i^e, \tag{3.160}$$

the spectral representation of $\mathbf{C}^{e(1)}$, and with

$$\mathbf{E}^{e(1)} \stackrel{\text{def}}{=} \frac{1}{2}\,\ln \mathbf{C}^{e(1)} \tag{3.161}$$

denoting a logarithmic strain measure, we consider an elastic free energy of the form:

$$\tilde{\psi}^{(1)}(\mathbf{E}^{e\,(1)}, \vartheta) = G|\mathbf{E}_0^{e\,(1)}|^2 + \tfrac{1}{2}K(\mathrm{tr}\,\mathbf{E}^{e\,(1)})^2 \\ - (\vartheta - \vartheta_0)(3\,K\,\alpha)(\mathrm{tr}\,\mathbf{E}^{e\,(1)}) + c(\vartheta - \vartheta_0) - c\,\vartheta \ln\Big(\frac{\vartheta}{\vartheta_0}\Big), \tag{3.162}$$

where the temperature-dependent parameters

$$G(\vartheta) > 0, \quad K(\vartheta) > 0, \quad \alpha(\vartheta) > 0, \quad c(\vartheta) > 0, \tag{3.163}$$

are the shear modulus, bulk modulus, coefficient of thermal expansion, and specific heat; ϑ_0 is a reference temperature.

In this case the constitutive equations for the Mandel stress becomes

$$\mathbf{M}^{e\,(1)} = 2G\mathbf{E}_0^{e\,(1)} + K\left\{\mathrm{tr}\,\mathbf{E}^{e\,(1)} - 3\,\alpha\,(\vartheta - \vartheta_0)\right\}\mathbf{1}\,. \tag{3.164}$$

and the corresponding Cauchy stress, using (3.148), is

$$\mathbf{T}^{e\,(1)} = J^{-1}\mathbf{R}^{e\,(1)}\mathbf{M}^{e\,(1)}\mathbf{R}^{e\,(1)\top}. \tag{3.165}$$

Defect energy and back stress

The spectral representation of $\mathbf{A}$ is

$$\mathbf{A} = \sum_{i=1}^{3} a_i \mathbf{l}_i^d \otimes \mathbf{l}_i^d, \tag{3.166}$$

where (a_1, a_2, a_3) are the positive eigenvalues, and $(\mathbf{l}_1^d, \mathbf{l}_2^d, \mathbf{l}_3^d)$ are the orthonormal eigenvectors of $\mathbf{A}$. The principal invariants of $\mathbf{A}$ are:

$$\left.\begin{aligned} I_1(\mathbf{A}) &= a_1 + a_2 + a_3, \\ I_2(\mathbf{A}) &= a_1a_2 + a_2a_3 + a_3a_1, \\ I_3(\mathbf{A}) &= a_1a_2a_3 = 1 \quad (\text{since } \det\mathbf{A} = 1). \end{aligned}\right\} \tag{3.167}$$

Thus, using (3.167) in (3.137), we express the defect energy as:

$$\begin{aligned}\psi^d &= \tilde{\psi}^d(\mathcal{I}_{\mathbf{A}}, \vartheta) \\ &= \breve{\psi}^d(a_1, a_2, a_3, \vartheta).\end{aligned} \tag{3.168}$$

Then, by the chain-rule

$$\frac{\partial \breve{\psi}^d(a_1, a_2, a_3, \vartheta)}{\partial \mathbf{A}} = \sum_{i=1}^{3} \frac{\partial \breve{\psi}^d(a_1, a_2, a_3, \vartheta)}{\partial a_i} \frac{\partial a_i}{\partial \mathbf{A}}. \tag{3.169}$$

Assume that a_i are distinct, so that the a_i and the principal directions $\mathbf{l}_i^d$ may be considered as functions of $\mathbf{A}$. Then,

$$\frac{\partial a_i}{\partial \mathbf{A}} = \mathbf{l}_i^d \otimes \mathbf{l}_i^d, \tag{3.170}$$

and, granted this, (3.169) implies that

$$\frac{\partial \breve{\psi}^d(a_1, a_2, a_3, \vartheta)}{\partial \mathbf{A}} = \sum_{i=1}^{3} \frac{\partial \breve{\psi}^d(a_1, a_2, a_3, \vartheta)}{\partial a_i} \mathbf{l}_i^d \otimes \mathbf{l}_i^d \tag{3.171}$$

Also, use of (3.166) and (3.171) in (3.123) gives

$$\mathbf{M}_{\text{back}} = 2 \sum_{i=1}^{3} a_i \frac{\partial \breve{\psi}^d(a_1, a_2, a_3, \vartheta)}{\partial a_i} \mathbf{l}_i^d \otimes \mathbf{l}_i^d. \tag{3.172}$$

Next, we consider the following simple defect energy:

$$\breve{\psi}^d(a_1, a_2, a_3, \vartheta) = \frac{1}{4} C \left[(\ln a_1)^2 + (\ln a_2)^2 + (\ln a_3)^2 \right], \tag{3.173}$$

with $C(\vartheta) > 0$ a defect energy modulus. Then

$$\frac{\partial \breve{\psi}^d(a_1, a_2, a_3, \vartheta)}{\partial \mathbf{A}} = \tfrac{1}{2} C \sum_{i=1}^{3} \frac{\ln a_i}{a_i} \mathbf{l}_i^d \otimes \mathbf{l}_i^d = \tfrac{1}{2} C (\ln \mathbf{A}) \mathbf{A}^{-1}, \tag{3.174}$$

where

$$\ln \mathbf{A} \stackrel{\text{def}}{=} \sum_{i=1}^{3} \ln a_i \, \mathbf{l}_i^d \otimes \mathbf{l}_i^d, \tag{3.175}$$

denotes the *defect logarithimic strain tensor*, and

$$\mathbf{A}^{-1} = \sum_{i=1}^{3} a_i^{-1} \, \mathbf{l}_i^d \otimes \mathbf{l}_i^d. \tag{3.176}$$

Then, using (3.174) in (3.172) gives

$$\mathbf{M}_{\text{back}} = C \ln \mathbf{A}; \tag{3.177}$$

where we call the positive-valued constitutive parameter $C(\vartheta) \geq 0$ the *back stress modulus*.

Note that since $a_1 a_2 a_3 = 1$ (on account of $(3.167)_3$),

$$\operatorname{tr}(\ln \mathbf{A}) = \ln a_1 + \ln a_2 + \ln a_3 = \ln(a_1 a_2 a_3) = 0.$$

Hence the defect strain tensor $(\ln \mathbf{A})$ is *traceless*, and therefore

- the back stress $\mathbf{M}_{\text{back}}$ is not only *symmetric*, but also *deviatoric*.

Thus, reinstating the superscript $\alpha = 1$ and summarizing, we have that with

$$\mathbf{A}^{(1)} = \sum_{i=1}^{3} a_i \, \mathbf{l}_i^d \otimes \mathbf{l}_i^d, \tag{3.178}$$

the spectral representation of $\mathbf{A}^{(1)}$, and with

$$\ln \mathbf{A}^{(1)} = \sum_{i=1}^{3} \ln a_i \, \mathbf{l}_i^d \otimes \mathbf{l}_i^d, \tag{3.179}$$

denoting a defect logarithmic strain measure, we consider a simple defect free energy of the form

$$\tilde{\psi}^{d\,(1)}(\mathbf{A}^{(1)}, \vartheta) = \frac{1}{4} C(\vartheta) \, \left[(\ln a_1)^2 + (\ln a_2)^2 + (\ln a_3)^2 \right], \tag{3.180}$$

where the positive-valued temperature-dependent parameter

$$C(\vartheta) \geq 0, \tag{3.181}$$

is a back-stress modulus. In this case the constitutive equation for the symmetric and deviatoric back stress becomes

$$\mathbf{M}_{\text{back}}^{(1)} = C \ln \mathbf{A}^{(1)}. \tag{3.182}$$

Thus, with the symmetric Mandel stress and the symmetric and deviatoric back stress for $\alpha = 1$ given by (3.164) and (3.182), respectively, the driving stress for plastic flow is the effective stress given by

$$\mathbf{M}_{\text{eff}}^{e\,(1)} = \mathbf{M}^{e\,(1)} - \mathbf{M}_{\text{back}}^{(1)}. \tag{3.183}$$

Flow function. Internal variables

Here we are concerned with specializing the functions (3.127)–(3.129). First, consider the isotropic function for the scalar flow rate

$$d^{p(1)}(\mathcal{I}_{\mathbf{M}_{\text{eff}}^{e\,(1)}}, \boldsymbol{\xi}^{(1)}, \vartheta).$$

Noting that $\mathbf{M}_{\text{back}}^{(1)}$ is deviatoric, and recalling (3.164) for $\mathbf{M}^{e\,(1)}$, we define the mean normal pressure by

$$\bar{p}^{(1)} \stackrel{\text{def}}{=} -\frac{1}{3} \operatorname{tr} \mathbf{M}_{\text{eff}}^{e\,(1)} = -\frac{1}{3} \operatorname{tr} \mathbf{M}^{e\,(1)} = -K \, \left\{ \operatorname{tr} \mathbf{E}^{e\,(1)} - 3\,\alpha\,(\vartheta - \vartheta_0) \right\}. \tag{3.184}$$

We also define an *equivalent shear stress* by

$$\bar{\tau}^{(1)} \stackrel{\text{def}}{=} \frac{1}{\sqrt{2}} \, |(\mathbf{M}^{e\,(1)}_{\text{eff}})_0|, \tag{3.185}$$

and an *equivalent shear strain rate* by

$$\nu^{p\,(1)} \stackrel{\text{def}}{=} \sqrt{2}\, d^{p\,(1)} = \sqrt{2}\, |\mathbf{D}^{p(1)}| \,, \tag{3.186}$$

respectively. Further, we restrict the list $\boldsymbol{\xi}^{(1)}$ of internal variables to two, positive-valued variables

$$S^{(1)} \geq 0 \qquad \text{and} \qquad \varphi \geq 0,$$

that represent aspects of the *intermolecular shear resistance to plastic flow*. The parameter $S^{(1)}$ has dimensions of stress and represents an *isotropic resistance to plastic flow*, while φ is a dimensionless order-parameter representing the local *free-volume* (a measure of disorder) of the polymeric glass.

With these definitions and specializations, we rewrite the flow equations (3.127)–(3.129) as

$$\mathbf{D}^{p(1)} = \nu^{p\,(1)} \Big(\frac{(\mathbf{M}^{e\,(1)}_{\text{eff}})_0}{2\,\bar{\tau}^{(1)}} \Big), \quad \nu^{p\,(1)} = f^{(1)}(\bar{\tau}^{(1)}, \bar{p}^{(1)}, \vartheta, S^{(1)}, \varphi) \geq 0 \,. \tag{3.187}$$

Let

$$\bar{\tau}^{(1)}_{\text{e}} \stackrel{\text{def}}{=} \bar{\tau}^{(1)} - S^{(1)} - \alpha_p \, \bar{p}^{(1)} \tag{3.188}$$

denote an effective shear stress, where the parameter $\alpha_p \geq 0$ denotes the *pressure sensitivity* of plastic flow. Then, guided by the literature [21–25], for the flow function $f^{(1)}$ we choose a thermally-activated relation in the specific form:

$$\nu^{p\,(1)} = \begin{cases} 0 & \text{if} \quad \bar{\tau}^{(1)}_{\text{e}} \leq 0, \\ \nu^{(1)}_0 \, \exp\left\{ -\dfrac{\Delta F^{(1)}}{k_B \, \vartheta} \right\} \left[\sinh\left(\dfrac{\bar{\tau}^{(1)}_{\text{e}} V}{2 k_B \vartheta} \right) \right]^{1/m^{(1)}} & \text{if} \quad \bar{\tau}^{(1)}_{\text{e}} > 0. \end{cases} \tag{3.189}$$

Here $\nu^{(1)}_0$ is a *pre-exponential factor* with units of 1/time, $\Delta F^{(1)}$ is an *activation energy*, k_B is Boltzmann's constant, V is a *shear activation volume*, and $m^{(1)}$ is a *strain rate sensitivity parameter*.

Evolution equations for the internal variables $S^{(1)}$, φ, and $\mathbf{A}^{(1)}$

The evolution equations for $S^{(1)}$ and φ are taken in the coupled form

$$\left.\begin{aligned} \dot{S}^{(1)} &= h^{(1)}(S^{(1)}, \varphi, \vartheta, \nu^{p\,(1)}), \qquad & S^{(1)}(\mathbf{X}, 0) &= S^{(1)}_0, \\ \dot{\varphi} &= g^{(1)}(S^{(1)}, \varphi, \vartheta, \nu^{p\,(1)}), \qquad & \varphi(\mathbf{X}, 0) &= \varphi_0, \end{aligned}\right\} \tag{3.190}$$

while that for $\mathbf{A}^{(1)}$ is taken as

$$\dot{\mathbf{A}}^{(1)} = \mathbf{D}^{p(1)} \mathbf{A}^{(1)} + \mathbf{A}^{(1)} \mathbf{D}^{p(1)} - \gamma \, \mathbf{A}^{(1)} \ln \mathbf{A}^{(1)} \, \nu^{p\,(1)}, \qquad \mathbf{A}^{(1)}(\mathbf{X}, 0) = \mathbf{1}, \tag{3.191}$$

where $\gamma(\vartheta) \geq 0$ is a constitutive parameter which governs the recovery of $\mathbf{A}^{(1)}$.

3.5.2 Case alpha = 2 — Molecular network resistance

Free energy function

Here, we neglect any defect energy, and take

$$\psi^{(2)} = \underbrace{\bar{\psi}^{e\,(2)}(\mathbf{C}^{e\,(2)}, \vartheta)}_{\text{entropic, molecular conformation-change contribution}} . \tag{3.192}$$

We denote the distortional part of $\mathbf{F}^{e\,(2)}$ by

$$\mathbf{F}^{e\,(2)}_{\text{dis}} \stackrel{\text{def}}{=} J^{-1/3}\,\mathbf{F}^{e(2)}, \quad \det \mathbf{F}^{e\,(2)}_{\text{dis}} = 1. \tag{3.193}$$

Correspondingly, let

$$\mathbf{C}^{e\,(2)}_{\text{dis}} \stackrel{\text{def}}{=} (\mathbf{F}^{e\,(2)}_{\text{dis}})^{\top}\mathbf{F}^{e\,(2)}_{\text{dis}} = J^{-2/3}\mathbf{C}^{e(2)}, \tag{3.194}$$

denote the distortional elastic right Cauchy-Green tensor, and consider a free-energy function in the special form[2]

$$\psi^{(2)} = \bar{\psi}^{e\,(2)}(\mathbf{C}^{e\,(2)}_{\text{dis}}, \vartheta) \tag{3.195}$$

For ease of notation, suppress for the time being the superscript $\alpha = 2$. Then using (3.121) the Piola stress with a free energy of the form above is

$$\begin{aligned}\mathbf{P}^e &= 2\frac{\partial \bar{\psi}^e(\mathbf{C}^e_{\text{dis}}, \vartheta)}{\partial \mathbf{C}^e} \\ &= 2\left\{\frac{\partial \mathbf{C}^e_{\text{dis}}}{\partial \mathbf{C}^e}\right\}^{\top} \frac{\partial \bar{\psi}^e(\mathbf{C}^e_{\text{dis}}, \vartheta)}{\partial \mathbf{C}^e_{\text{dis}}} .\end{aligned} \tag{3.196}$$

Next, since $J = \sqrt{\det \mathbf{C}^e}$, and

$$\frac{\partial \det \mathbf{C}^e}{\partial \mathbf{C}^e} = (\det \mathbf{C}^e)\,\mathbf{C}^{e-1} = J^2\,\mathbf{C}^{e-1},$$

we have

$$\frac{\partial J}{\partial \mathbf{C}^e} = \frac{1}{2}\,J\,\mathbf{C}^{e-1}, \quad \text{and} \quad \frac{\partial J^{-2/3}}{\partial \mathbf{C}^e} = -\frac{1}{3}J^{-2/3}\mathbf{C}^{e-1} . \tag{3.197}$$

Also,

$$\frac{\partial \mathbf{C}^e_{\text{dis}}}{\partial \mathbf{C}^e} = \frac{\partial (J^{-2/3}\mathbf{C}^e)}{\partial \mathbf{C}^e} = J^{-2/3}\Big(\mathbb{I} + J^{2/3}\mathbf{C}^e \otimes \frac{\partial J^{-2/3}}{\partial \mathbf{C}^e}\Big),$$

[2]Since $J^{e\,(\alpha)} = J$ for all α, and we have already accounted for a volumetric elastic energy for $\alpha = 1$, it would appear physically incorrect to also allow for a volumetric elastic energy for $\alpha = 2$.

or using $(3.197)_2$,

$$\begin{aligned}\frac{\partial \mathbf{C}^e_{\rm dis}}{\partial \mathbf{C}^e} &= J^{-2/3}\Big(\mathbb{I} - \frac{1}{3}\mathbf{C}^e \otimes \mathbf{C}^{e\,-1}\Big),\\ &= J^{-2/3}\Big(\mathbb{I} - \frac{1}{3}\mathbf{C}^e_{\rm dis} \otimes \mathbf{C}^{e\,-1}_{\rm dis}\Big),\end{aligned} \tag{3.198}$$

where $\mathbb{I}$ is the fourth-order identity tensor. Thus, using (3.198) in (3.196), the second Piola stress has the form

$$\begin{aligned}\mathbf{P}^e &= 2J^{-2/3}(\mathbb{I} - \tfrac{1}{3}\mathbf{C}^{e\,-1}_{\rm dis} \otimes \mathbf{C}^e_{\rm dis})\frac{\partial \bar{\psi}^e(\mathbf{C}^e_{\rm dis},\vartheta)}{\partial \mathbf{C}^e_{\rm dis}}\\ &= 2J^{-2/3}\left[\frac{\partial \bar{\psi}^e(\mathbf{C}^e_{\rm dis},\vartheta)}{\partial \mathbf{C}^e_{\rm dis}} - \frac{1}{3}\left(\mathbf{C}^e_{\rm dis} : \frac{\partial \bar{\psi}^e(\mathbf{C}^e_{\rm dis},\vartheta)}{\partial \mathbf{C}^e_{\rm dis}}\right)\mathbf{C}^{e\,-1}_{\rm dis}\right].\end{aligned} \tag{3.199}$$

Then, with

$$I_1 \stackrel{\rm def}{=} \operatorname{tr}\mathbf{C}^e_{\rm dis} \tag{3.200}$$

denoting the first principal invariant of $\mathbf{C}^e_{\rm dis}$, we consider a special free energy of the form [26]

$$\psi^e = -\tfrac{1}{2}\mu_{\rm R}\, I_{1,\max}\, \ln\Big(1 - \frac{I_1 - 3}{I_{1,\max}}\Big), \tag{3.201}$$

which involves two temperature-dependent material parameters

$$\mu_{\rm R}(\vartheta) > 0, \qquad I_{1,\max}(\vartheta) > 3. \tag{3.202}$$

In particular, $\mu_{\rm R}$ represents the ground state rubbery shear modulus of the material, and $I_{1,\max}$ represents the upper limit of I_1 (i.e., $I_1 < (3 + I_{1,\max})$), associated with limited chain extensibility of polymeric molecules. For this simple free energy

$$\begin{aligned}\frac{\partial \bar{\psi}^e(\mathbf{C}^e_{\rm dis},\vartheta)}{\partial \mathbf{C}^e_{\rm dis}} &= \tfrac{1}{2}\,\mu_{\rm R}\,\Big(1 - \frac{I_1 - 3}{I_{1,\max}}\Big)^{-1}\frac{\partial I_1}{\partial \mathbf{C}^e_{\rm dis}}\\ &= \tfrac{1}{2}\,\mu_{\rm R}\,\Big(1 - \frac{I_1 - 3}{I_{1,\max}}\Big)^{-1}\mathbf{1}.\end{aligned} \tag{3.203}$$

Using (3.203) in (3.199) gives

$$\mathbf{P}^e = J^{e\,-2/3}\mu_{\rm R}\,\Big(1 - \frac{I_1 - 3}{I_{1,\max}}\Big)^{-1}\left[\mathbf{1} - \frac{1}{3}\Big(\operatorname{tr}\mathbf{C}^e_{\rm dis}\Big)\mathbf{C}^{e\,-1}_{\rm dis}\right]. \tag{3.204}$$

From (3.120),

$$\mathbf{T}^e = J^{e-1}\,\mathbf{F}^e\mathbf{P}^e\mathbf{F}^{e\top} = J^{e-1/3}\,\mathbf{F}^e_{\rm dis}\mathbf{P}^e\mathbf{F}^{e\,\top}_{\rm dis}, \tag{3.205}$$

and hence, using (3.204),

$$\begin{aligned}\mathbf{T}^e &= J^{e\,-1}\mu_{\mathrm{R}}\left(1-\frac{I_1-3}{I_{1,\max}}\right)^{-1}\left[\mathbf{F}^e_{\mathrm{dis}}\mathbf{F}^{e\ \top}_{\mathrm{dis}}-\frac{1}{3}\left(\mathrm{tr}\,\mathbf{C}^e_{\mathrm{dis}}\right)\mathbf{F}^e_{\mathrm{dis}}\mathbf{C}^{e\,-1}_{\mathrm{dis}}\mathbf{F}^{e\ \top}_{\mathrm{dis}}\right],\\ &= J^{e\,-1}\mu_{\mathrm{R}}\left(1-\frac{I_1-3}{I_{1,\max}}\right)^{-1}\left[\mathbf{B}^e_{\mathrm{dis}}-\frac{1}{3}\left(\mathrm{tr}\,\mathbf{B}^e_{\mathrm{dis}}\right)\mathbf{1}\right],\end{aligned}$$

or reinstating the superscript $\alpha = 2$,

$$\mathbf{T}^{e(2)} = J^{-1}\left[\mu_{\mathrm{R}}\left(1-\frac{I_1-3}{I_{1,\max}}\right)^{-1}(\mathbf{B}^{e(2)}_{\mathrm{dis}})_0\right]. \tag{3.206}$$

Further, from (3.122), the Mandel stress is

$$\mathbf{M}^e = \mathbf{C}^e\mathbf{P}^e = J^{2/3}\mathbf{C}^e_{\mathrm{dis}}\mathbf{P}^e, \tag{3.207}$$

and hence, using (3.204),

$$\mathbf{M}^e = \mu_{\mathrm{R}}\left(1-\frac{I_1-3}{I_{1,\max}}\right)^{-1}\left[\mathbf{C}^e_{\mathrm{dis}}-\frac{1}{3}\left(\mathrm{tr}\,\mathbf{C}^e_{\mathrm{dis}}\right)\mathbf{1}\right], \tag{3.208}$$

or reinstating the superscript $\alpha = 2$,

$$\mathbf{M}^{e(2)} = \mu_{\mathrm{R}}\left(1-\frac{I_1-3}{I_{1,\max}}\right)^{-1}(\mathbf{C}^{e\ (2)}_{\mathrm{dis}})_0. \tag{3.209}$$

Note that for $\alpha = 2$ we have ignored a defect energy, and hence there is no back stress.

Flow function. Internal variables

As before, we introduce the definitions of the equivalent shear stress and the equivalent plastic shear strain rate by

$$\bar{\tau}^{(2)} \stackrel{\mathrm{def}}{=} \frac{1}{\sqrt{2}}\,|\mathbf{M}^{e\,(2)}_0|, \qquad \nu^{p\,(2)} \stackrel{\mathrm{def}}{=} \sqrt{2}\,d^{p\,(2)} = \sqrt{2}\,|\mathbf{D}^{p(2)}|\,. \tag{3.210}$$

We consider only one internal variable

$$\boldsymbol{\xi}^{(2)} \quad \rightarrow \quad S^{(2)},$$

with $S^{(2)} > 0$ a positive-valued stress-dimensioned shear resistance, and take the plastic stretching to be given by

$$\mathbf{D}^{p(2)} = \nu^{p\,(2)}\left(\frac{\mathbf{M}^{e\,(2)}_0}{2\,\bar{\tau}^{(2)}}\right), \quad \text{with} \quad \nu^{p\,(2)} = f^{(2)}(\bar{\tau}^{(2)}, \vartheta, S^{(2)}) \geq 0\,. \tag{3.211}$$

For simplicity, we consider a standard, power-law thermally-activated form for the flow function:

$$\nu^{p\,(2)} = \nu_0^{(2)} \exp\left\{-\frac{\Delta F^{(2)}}{k_B\,\vartheta}\right\} \left(\frac{\bar{\tau}^{(2)}}{S^{(2)}}\right)^{1/m^{(2)}} ; \tag{3.212}$$

here the parameters $\nu_0^{(2)}$, $\Delta F^{(2)}$, and $m^{(2)}$ represent a reference strain rate, an activation energy, and a strain rate-sensitivity parameter. The shear deformation resistance S_2 is assumed to be a constant.

3.6 Summary of the specialized constitutive model using two micromechanisms alpha = 1, 2

In this section, we summarize the specialized form of our theory, which should be useful in applications. The underlying constitutive equations relate the following basic fields:

$\mathbf{x} = \boldsymbol{\chi}(\mathbf{X}, t)$,	motion;
$\mathbf{F} = \nabla\boldsymbol{\chi}, \quad J = \det\mathbf{F} > 0$,	deformation gradient;
$\mathbf{F} = \mathbf{F}^{e\,(\alpha)}\mathbf{F}^{p\,(\alpha)}, \quad \alpha = 1, \ldots, M$,	elastic-plastic decomposition of $\mathbf{F}$;
$\mathbf{F}^{p\,(\alpha)}, \quad J^{p\,(\alpha)} = \det\mathbf{F}^{p\,(\alpha)} = 1$,	inelastic distortion;
$\mathbf{F}^{e\,(\alpha)}, \quad J^{e\,(\alpha)} = \det\mathbf{F}^{e\,(\alpha)} = J > 0$,	elastic distortion;
$\mathbf{F}^{e\,(\alpha)} = \mathbf{R}^{e\,(\alpha)}\mathbf{U}^{e\,(\alpha)} = \mathbf{V}^{e\,(\alpha)}\mathbf{R}^{e\,(\alpha)}$,	polar decompositions of $\mathbf{F}^{e\,(\alpha)}$;
$\mathbf{C}^{e\,(\alpha)} = \mathbf{F}^{e\,(\alpha)\top}\mathbf{F}^{e\,(\alpha)}$,	elastic right Cauchy-Green tensors;
$\mathbf{B}^{e\,(\alpha)} = \mathbf{F}^{e\,(\alpha)}\mathbf{F}^{e\,(\alpha)\top}$,	elastic left Cauchy-Green tensors;
$\mathbf{F}^{e\,(\alpha)}_{\text{dis}} \overset{\text{def}}{=} J^{-1/3}\,\mathbf{F}^{e\,(\alpha)}, \quad \det\mathbf{F}^{e\,(\alpha)}_{\text{dis}} = 1$,	distortional part of $\mathbf{F}^{e\,(\alpha)}$;
$\mathbf{C}^{e\,(\alpha)}_{\text{dis}} = (\mathbf{F}^{e\,(\alpha)}_{\text{dis}})^{\top}\mathbf{F}^{e\,(\alpha)}_{\text{dis}}, \quad \mathbf{B}^{e\,(\alpha)}_{\text{dis}} = \mathbf{F}^{e\,(\alpha)}_{\text{dis}}\,(\mathbf{F}^{e\,(\alpha)}_{\text{dis}})^{\top}$	distortional elastic Cauchy-Green strains;
$\mathbf{T}$,	Cauchy stress;
$\mathbf{T} = \sum_{\alpha=1}^{2}\,\mathbf{T}^{e\,(\alpha)}$,	decomposition of Cauchy stress;
$\mathbf{M}^{e\,(\alpha)} = J\mathbf{R}^{e\,(\alpha)\top}\,\mathbf{T}^{e\,(\alpha)}\,\mathbf{R}^{e\,(\alpha)}$,	Mandel stress;
$\psi_{\text{R}} = \sum_{\alpha=1}^{M}\,\bar{\psi}^{(\alpha)}$,	free energy density per unit ref. vol.;
$\eta_{\text{R}} = \sum_{\alpha=1}^{M}\,\bar{\eta}^{(\alpha)}$,	entropy density per unit ref. vol.;
$\boldsymbol{\xi}^{(\alpha)} = (\xi_1^{(\alpha)}, \xi_2^{(\alpha)}, \ldots, \xi_m^{(\alpha)})$	m scalar internal variables for each α;
$\mathbf{A}^{(\alpha)}, \quad \mathbf{A}^{(\alpha)} = \mathbf{A}^{(\alpha)\top}, \quad \det\mathbf{A}^{(\alpha)} = 1$	tensorial internal variables for each α;
$\mathbf{M}^{e\,(\alpha)}_{\text{back}}$,	Back stress;
$\vartheta > 0$,	absolute temperature;
$\nabla\vartheta$,	referential temperature gradient;
$\mathbf{q}_{\text{R}}$,	referential heat flux vector.

The temperature-dependence of the material properties of amorphous polymers depends strongly on the temperature relative to the

- *glass transition temperature* ϑ_g

of the material. It is well-known that the glass transition temperature of such materials is not a constant, but depends strongly on the strain rate to which the material is subjected. Let

$$d \stackrel{\text{def}}{=} \sqrt{2}|\mathbf{D}_0| \tag{3.213}$$

denote the *shear strain rate*, and d^{ref} a *reference strain rate*, we assume that the variation of the glass transition temperature with strain rate may be adequately described by [21, cf. their eq. (10)],

$$\vartheta_g = \begin{cases} \vartheta_g^{\text{ref}} & \text{if} \quad d \le d^{\text{ref}}, \\ \vartheta_g^{\text{ref}} + \left[\dfrac{C_{2g} \times \log_{10}(d/d^{\text{ref}})}{C_{1g} - \log_{10}(d/d^{\text{ref}})}\right] & \text{if} \quad d > d^{\text{ref}}, \end{cases} \tag{3.214}$$

where C_{1g} and C_{2g} are Williams-Landel-Ferry (WLF) parameters [27] relative to the reference glass transition temperature ϑ_g^{ref} .

With the governing fields and the glass transition temperature so defined, we assume the following constitutive equations:

3.6.1 Constitutive equations for alpha=1, intermolecular resistance

1. Free energy:

With

$$\mathbf{C}^{e\,(1)} = \sum_{i=1}^{3} \omega_i \, \mathbf{r}_i^e \otimes \mathbf{r}_i^e, \tag{3.215}$$

denoting the spectral representation of $\mathbf{C}^{e\,(1)}$, and with

$$\mathbf{E}^{e\,(1)} = \sum_{i=1}^{3} E_i^e \, \mathbf{r}_i^e \otimes \mathbf{r}_i^e, \qquad E_i^e = \ln \sqrt{\omega_i^e}, \tag{3.216}$$

denoting a elastic logarithmic strain measure, we consider an elastic free energy of the form

$$\begin{aligned} \psi^{e\,(1)}(\mathbf{C}^{e\,(1)}, \vartheta) = G|\mathbf{E}_0^{e\,(1)}|^2 + \tfrac{1}{2}K(\operatorname{tr}\mathbf{E}^{e\,(1)})^2 \\ - (\vartheta - \vartheta_0)(3\,K\,\alpha)(\operatorname{tr}\mathbf{E}^{e\,(1)}) + c(\vartheta - \vartheta_0) - c\,\vartheta \ln\Big(\frac{\vartheta}{\vartheta_0}\Big). \end{aligned} \tag{3.217}$$

where

$$G(\vartheta) > 0, \quad K(\vartheta) > 0, \quad \alpha(\vartheta), \quad c(\vartheta), \tag{3.218}$$

are *temperature-dependent* shear modulus, bulk modulus, coefficient of thermal expansion, and specific heat, and ϑ_0 is a reference temperature.

With

$$\mathbf{A}^{(1)} = \sum_{i=1}^{3} a_i \, \mathbf{l}_i^d \otimes \mathbf{l}_i^d, \tag{3.219}$$

denoting the spectral representation of $\mathbf{A}^{(1)}$, and with

$$\ln \mathbf{A}^{(1)} = \sum_{i=1}^{3} \ln a_i \, \mathbf{l}_i^d \otimes \mathbf{l}_i^d, \tag{3.220}$$

denoting a defect logarithmic strain measure, we consider a defect free energy of the form

$$\tilde{\psi}^{d\,(1)}(\mathbf{A}^{(1)}, \vartheta) = \frac{1}{4} C(\vartheta) \, \left[(\ln a_1)^2 + (\ln a_2)^2 + (\ln a_3)^2 \right], \tag{3.221}$$

where the positive-valued temperature-dependent parameter

$$C(\vartheta) \geq 0, \tag{3.222}$$

is a back-stress modulus.

2. Mandel stress. Cauchy stress. Back stress. Effective stress:

The Mandel stress is given by

$$\mathbf{M}^{e\,(1)} = 2G\mathbf{E}_0^{e\,(1)} + K \left\{ \operatorname{tr} \mathbf{E}^{e\,(1)} - 3\,\alpha\,(\vartheta - \vartheta_0) \right\} \mathbf{1}. \tag{3.223}$$

The Cauchy stress is given by

$$\mathbf{T}^{e\,(1)} \stackrel{\text{def}}{=} J^{-1}\, \mathbf{R}^{e\,(1)}\, \mathbf{M}^{e\,(1)}\, \mathbf{R}^{e\,(1)\top}. \tag{3.224}$$

The symmetric and deviatoric back stress is

$$\mathbf{M}_{\text{back}}^{(1)} = C \ln \mathbf{A}^{(1)}. \tag{3.225}$$

The driving stress for plastic flow is the effective stress given by

$$\mathbf{M}_{\text{eff}}^{e\,(1)} = \mathbf{M}^{e\,(1)} - \mathbf{M}_{\text{back}}^{(1)}. \tag{3.226}$$

The corresponding *equivalent shear stress* and *mean normal pressure* are given by

$$\bar{\tau}^{(1)} \stackrel{\text{def}}{=} \frac{1}{\sqrt{2}} \, |(\mathbf{M}_{\text{eff}}^{e\,(1)})_0|, \quad \text{and} \quad \bar{p}^{(1)} \stackrel{\text{def}}{=} -\frac{1}{3} \operatorname{tr} \mathbf{M}^{e\,(1)}, \tag{3.227}$$

respectively.

3. Internal variables:

We restrict the list $\boldsymbol{\xi}^{(1)}$ of internal variables to two, positive-valued variables

$$S^{(1)} \geq 0, \qquad \varphi \geq 0$$

that represent aspects of the *intermolecular shear resistance to plastic flow*. The parameter $S^{(1)}$ has dimensions of stress and represents an isotropic resistance to plastic flow, while φ is

a dimensionless order-parameter representing the local *free-volume* (a measure of disorder) of the polymeric glass.

4. Flow rule:

The evolution equation for $\mathbf{F}^{p\,(1)}$ is

$$\left.\begin{aligned}
&\dot{\mathbf{F}}^{p\,(1)} = \mathbf{D}^{p\,(1)}\,\mathbf{F}^{p\,(1)}, \qquad \mathbf{F}^{p\,(1)}(\mathbf{X},0) = \mathbf{1},\\
&\mathbf{D}^{p\,(1)} = \nu^{p\,(1)}\,\Big(\frac{(\mathbf{M}^{e\,(1)}_{\text{eff}})_0}{2\,\bar{\tau}^{(1)}}\Big),\\
&\nu^{p\,(1)} = \begin{cases} 0 & \text{if} \quad \bar{\tau}^{(1)}_{\text{e}} \le 0,\\ \nu^{(1)}_0\,\exp\Big\{-\dfrac{\Delta F^{(1)}}{k_B\,\vartheta}\Big\}\,\Big[\sinh\Big(\dfrac{\bar{\tau}^{(1)}_{\text{e}}\,V}{2k_B\vartheta}\Big)\Big]^{1/m^{(1)}} & \text{if} \quad \bar{\tau}^{(1)}_{\text{e}} > 0\,, \end{cases}
\end{aligned}\right\} \tag{3.228}$$

where

$$\bar{\tau}^{(1)}_{\text{e}} \stackrel{\text{def}}{=} \bar{\tau}^{(1)} - S^{(1)} - \alpha_p\,\bar{p}^{(1)} \tag{3.229}$$

denotes an *effective shear stress*, with $\alpha_p \ge 0$ a *pressure sensitivity parameter*, $\nu^{(1)}_0$ is a pre-exponential factor with units of 1/time, $m^{(1)}$ is a strain rate sensitivity parameter, $\Delta F^{(1)}$ is an *activation energy*, V is a *shear activation volume*, and k_B is Boltzmann's constant.

5. Evolution equations for the internal variables $S^{(1)}$, φ, and $\mathbf{A}^{(1)}$

The evolution equations for $S^{(1)}$ and φ are taken in the coupled form

$$\left.\begin{aligned}
\dot{S}^{(1)} &= h(S^{(1)},\varphi,\vartheta,\nu^{p\,(1)}), \qquad S^{(1)}(\mathbf{X},0) = S^{(1)}_0,\\
\dot{\varphi} &= g(S^{(1)},\varphi,\vartheta,\nu^{p\,(1)}), \qquad \varphi(\mathbf{X},0) = \varphi_0,
\end{aligned}\right\} \tag{3.230}$$

while that for $\mathbf{A}^{(1)}$ is taken as

$$\dot{\mathbf{A}}^{(1)} = \mathbf{D}^{p(1)}\mathbf{A}^{(1)} + \mathbf{A}^{(1)}\mathbf{D}^{p(1)} - \gamma\,\mathbf{A}^{(1)}\,\ln\mathbf{A}^{(1)}\,\nu^{p\,(1)}, \qquad \mathbf{A}^{(1)}(\mathbf{X},0) = \mathbf{1}, \tag{3.231}$$

where $\gamma(\vartheta) \ge 0$ is a constitutive parameter which governs the recovery of $\mathbf{A}^{(1)}$.

3.6.2 Constitutive equations for alpha=2, molecular network resistance

1. Free energy

Let

$$I_1 \stackrel{\text{def}}{=} \operatorname{tr}\mathbf{C}^{e\,(2)}_{\text{dis}} \tag{3.232}$$

denote the first principal invariant of $\mathbf{C}^{e\,(2)}_{\text{dis}}$. We consider following elastic free energy

$$\psi^{e\,(2)} = -\tfrac{1}{2}\mu_{\text{R}}\,I_{1,\max}\,\ln\Big(1 - \frac{I_1 - 3}{I_{1,\max}}\Big), \tag{3.233}$$

where

$$\mu_{\text{R}}(\vartheta) > 0, \qquad I_{1,\max}(\vartheta) > 3 \tag{3.234}$$

are two temperature-dependent material constants. In particular, $\mu_{\rm R}$ represents the ground state rubbery shear modulus of the material, and $I_{1,\max}$ represents the upper limit of I_1 (i.e., $I_1 < (3 + I_{1,\max})$), associated with limited chain extensibility.

2. Mandel stress. Cauchy stress:

The Mandel stress is given by

$$\mathbf{M}^{e\,(2)} = \mu_{\rm R} \left(1 - \frac{I_1 - 3}{I_{1,\max}}\right)^{-1} (\mathbf{C}^{e}_{\rm dis}{}^{(2)})_0. \tag{3.235}$$

The Cauchy stress is given by

$$\mathbf{T}^{e\,(2)} = J^{-1} \left[\mu_{\rm R} \left(1 - \frac{I_1 - 3}{I_{1,\max}}\right)^{-1} (\mathbf{B}^{e\,(2)}_{\rm dis})_0 \right]. \tag{3.236}$$

For $\alpha = 2$ we have neglected a defect energy, and hence there is no back stress. The corresponding *equivalent shear stress* is given by

$$\bar{\tau}^{(2)} \stackrel{\rm def}{=} \frac{1}{\sqrt{2}} |\mathbf{M}^{e\,(2)}_0|, \tag{3.237}$$

3. Internal variables:

We restrict the list $\boldsymbol{\xi}^{(2)}$ of internal variables to a single stress-dimensioned positive-valued variable

$$S^{(2)} > 0$$

that represents a *shear resistance to plastic flow* for molecular relaxation processes.

4. Flow rule:

The evolution equation for $\mathbf{F}^{p(2)}$ is

$$\left.\begin{aligned} \dot{\mathbf{F}}^{p\,(2)} &= \mathbf{D}^{p(2)}\,\mathbf{F}^{p(2)}, \qquad \mathbf{F}^{p(2)}(\mathbf{X},0) = \mathbf{1}, \\ \mathbf{D}^{p(2)} &= \nu^{p\,(2)} \left(\frac{\mathbf{M}^{e\,(2)}_0}{2\,\bar{\tau}^{(2)}}\right), \\ \nu^{p\,(2)} &= \nu^{(2)}_0 \, \exp\left\{-\frac{\Delta F^{(1)}}{k_B\,\vartheta}\right\} \left(\frac{\bar{\tau}^{(2)}}{S^{(2)}}\right)^{1/m^{(2)}} \end{aligned}\right\} \tag{3.238}$$

where $\nu^{(2)}_0$ is a pre-exponential factor with units of 1/time, $\Delta F^{(2)}$ is an *activation energy*, k_B is Boltzmann's constant, and $m^{(2)}$ is a strain rate sensitivity parameter.

5. Evolution equation for $S^{(2)}$

The shear deformation resistance $S^{(2)}$ is assumed to remain constant.

6. Entropy relation. Fourier's Law:

Finally, we have the entropy relation

$$\eta_{\mathrm{R}} = \sum_{\alpha=1}^{M} \eta^{(\alpha)}, \qquad \eta^{(\alpha)} = -\left[\frac{\partial \bar{\psi}^{e\,(\alpha)}(\mathbf{C}^{e\,(\alpha)}, \vartheta)}{\partial \vartheta} + \frac{\partial \bar{\psi}^{d\,(\alpha)}(\mathbf{A}^{(\alpha)}, \vartheta)}{\partial \vartheta}\right], \tag{3.239}$$

together with Fourier's law

$$\mathbf{q}_{\mathrm{R}} = -\kappa\, \nabla \vartheta, \tag{3.240}$$

with $\kappa(\vartheta) > 0$ the thermal conductivity.

3.7 Partial differential equations for the deformation and temperature fields

The partial differential equation for the deformation is obtained from the local force balance:

$$\mathrm{Div}\, \mathbf{T}_{\mathrm{R}} + \mathbf{b}_{0\mathrm{R}} = \rho_{\mathrm{R}}\, \ddot{\boldsymbol{\chi}}. \tag{3.241}$$

The specific heat in the theory is given by

$$c \overset{\mathrm{def}}{=} -\vartheta \left[\sum_{\alpha=1}^{M} \frac{\partial^2 \bar{\psi}^{e\,(\alpha)}(\mathcal{I}_{\mathbf{C}^{e\,(\alpha)}}, \vartheta)}{\partial \vartheta^2} + \sum_{\alpha=1}^{M} \frac{\partial^2 \bar{\psi}^{d\,(\alpha)}(\mathcal{I}_{\mathbf{A}^{(\alpha)}}, \vartheta)}{\partial \vartheta^2}\right]. \tag{3.242}$$

Then, balance of energy gives the following partial differential equation for the temperature

$$\begin{aligned} c\dot{\vartheta} = -\mathrm{Div}\, \mathbf{q}_{\mathrm{R}} + q_{\mathrm{R}} \\ + \sum_{\alpha=1}^{M} \left[|\mathbf{M}^{e\,(\alpha)}_{\mathrm{eff}}{}_0| + \Big(\frac{\partial \tilde{\psi}^{d\,(\alpha)}(\mathcal{I}_{\mathbf{A}^{(\alpha)}}, \vartheta)}{\partial \mathbf{A}^{(\alpha)}} : \mathbf{G}^{(\alpha)}(\boldsymbol{\xi}^{(\alpha)}, \mathbf{A}^{(\alpha)}, \vartheta)\Big)\right] d^{p\,(\alpha)} \\ + \vartheta \sum_{\alpha=1}^{M} \frac{\partial^2 \bar{\psi}^{e\,(\alpha)}(\mathcal{I}_{\mathbf{C}^{e\,(\alpha)}}, \vartheta)}{\partial \vartheta\, \partial \mathbf{C}^{e\,(\alpha)}} : \dot{\mathbf{C}}^{e\,(\alpha)} \\ + \vartheta \sum_{\alpha=1}^{M} \frac{\partial^2 \bar{\psi}^{d\,(\alpha)}(\mathcal{I}_{\mathbf{A}^{(\alpha)}}, \vartheta)}{\partial \vartheta\, \partial \mathbf{A}^{(\alpha)}} : \dot{\mathbf{A}}^{(\alpha)}. \end{aligned} \tag{3.243}$$

Bibliography

[1] C. P. Buckley and D. C. Jones. Glass-rubber constituitive model for amorphous polymers near the glass transition. *Polymer*, 36:3301–3312, 1995. doi: 10.1016/0032-3861(95)99429-X.

[2] P. J. Dooling, C. P. Buckley, S. Rostami, and N. Zahlan. Hot-drawing of poly(methylmethacrylate) and simulation using a glass-rubber constitutive model. *Polymer*, 43:2451–2465, 2002. doi: 10.1016/S0032-3861(01)00799-6.

[3] M. C. Boyce, S. Socrate, and P. G. Llana. Constitutive model for the finite deformation stress strain behavior of poly(ethylene terephthalate) above the glass transition. *Polymer*, 41: 2183–2201, 2000. doi: 10.1016/S0032-3861(99)00406-1.

[4] R. B. Dupaix and M. C. Boyce. Constitutive modeling of the finite strain behavior of amorphous polymers in and above the glass transition. *Mechanics of Materials*, 39:39–52, 2007. doi: 10.1016/j.mechmat.2006.02.006.

[5] E. Kroner. Allgemeine kontinuumstheorie der versetzungen und eigenspannungen. *Archive for Rational Mechanics and Analysis*, 4:273–334, 1960.

[6] E. H. Lee. Elastic plastic deformation at finite strain. *ASME Journal of Applied Mechanics*, 36:1–6, 1969.

[7] M. C. Boyce, D. M. Parks, and A. S. Argon. Large inelastic deformation of glassy polymers. part 1: Rate-dependent constitutive model. *Mechanics of Materials*, 7:15–33, 1998. doi: 10.1016/0167-6636(88)90003-8.

[8] E. M. Arruda and M. C. Boyce. Evolution of plastic anisotropy in amorphous polymers during finite straining. *International Journal of Plasticity*, 9:697–720, 1993. doi: 10.1016/0749-6419(93)90034-N.

[9] P. D. Wu and E. Van der Giessen. On improved network models for rubber elasticity and their applications to orientation hardening of glassy polymers. *Journal of the Mechanics and Physics of Solids*, 41:427–456, 1993. doi: 10.1016/0022-5096(93)90043-F.

[10] L. E. Govaert, P. H. M. Timmermans, and W. A. M. Brekelmans. The influence of intrinsic strain softening on strain localization in polycarbonate: Modeling and experimental validation. *Journal of Engineering Materials and Technology*, 122:177–185, 2000. doi: 10.1115/1.482784.

[11] L. Anand and M. E. Gurtin. A theory of amorphous solids undergoing large deformations, with application to polymeric glasses. *InternationalJournal of Solids and Structures*, 40:1465–1487, 2003. doi: 10.1016/S0020-7683(02)00651-0.

[12] A. Lion. On the large deformation behavior of reinforced rubber at different temperatures. *Journal of the Mechanics and Physics of Solids*, 45:1805–1834, 1997. doi: 10.1016/S0022-5096(97)00028-8.

[13] S. Reese and S. Govindjee. A theory of finite viscoelasticity and numerical aspects. *InternationalJournal of Solids and Structures*, 35:3455–3482, 1998. doi: 10.1016/S0020-7683(97)00217-5.

[14] J. S. Bergström and M. C. Boyce. Large strain time-dependent behavior of filled elastomers. *Mechanics of Materials*, 32:627–644, 2000. doi: 10.1016/S0167-6636(00)00028-4.

[15] C. Miehe and J. Keck. Superimposed finite elastic-viscoelastic-plastoelastic stress response with damage in filled rubbery polymers. experiments, modelling and algorithmic implementation. *Journal of the Mechanics and Physics of Solids*, 48:323–365, 2000. doi: 10.1016/S0022-5096(99)00017-4.

[16] R. C. Lin and U. Schomburg. A finite-elastic-viscoelastic-elastoplastic material law with damage: theoretical and numerical aspects. *Computer Methods in Applied Mechanics and Engineering*, 192:1591–1627, 2003. doi: 10.1016/S0045-7825(02)00649-7.

[17] M. E. Gurtin. A gradient theory of single-crystal viscoplasticity that accounts for geometrically necessary dislocations. *Journal of the Mechanics and Physics of Solids*, 50:5–32, 2002. doi: 10.1016/S0022-5096(01)00104-1.

[18] M. E. Gurtin and L. Anand. The decomposition $\mathbf{F} = \mathbf{F}^e\mathbf{F}^p$, material symmetry, and plastic irrotationality for solids that are isotropic-viscoplastic or amorphous. *International Journal of Plasticity*, 21:1686–1719, 2005. doi: 10.1016/j.ijplas.2004.11.007.

[19] R. B. Dupaix and D. Krishnan. A constitutive model for strain-induced crystallization in poly(ethylene terephthalate) (pet) during finite strain load-hold simulations. *Journal of Engineering Materials and Technology*, 128:28–33, 2006. doi: 10.1115/1.1924564.

[20] J. Richeton, S. Ahzi, K. S. Vecchio, F. C. Jiang, and R. R. Adharapurapu. Influence of temperature and strain rate on the mechanical behavior of three amorphous polymers: Characterization and modeling of the compressive yield stress. *InternationalJournal of Solids and Structures*, 43:2318–2335, 2006. doi: 10.1016/j.ijsolstr.2005.06.040.

[21] J. Richeton, G. Schlatter, K. S. Vecchio, Y. Rémond, and S. Ahzi. A unified model for stiffness modulus of amorphous polymers across transition temperatures and strain rates. *Polymer*, 46:8194–8201, 2006. doi: 10.1016/j.polymer.2005.06.103.

[22] D. G. Fotheringham, B. W. Cherry, and C. Bauwens-Crowet. Comment on "the compression yield behaviour of polymethyl methacrylate over a wide range of temperatures and strain-rates". *Journal of Materials Science*, 11:1368–1371, 1976. doi: 10.1007/BF00545162.

[23] D. G. Fotheringham and B. W. Cherry. The role of recovery forces in the deformation of linear polyethylene. *Journal of Materials Science*, 13:951–964, 1978. doi: 10.1007/BF00544690.

[24] F. Povolo and E. B. Hermida. Phenomenlogical description of strain rate and temperature-dependent yield stress of pmma. *Journal of Applied Polymer Science*, 58:55–68, 1995. doi: 10.1002/app.1995.070580106.

[25] F. Povolo, G. Schwartz, and E. B. Hermida. Temperature and strain rate dependence of the tensile yield stress of pvc. *Journal of Applied Polymer Science*, 61:109–117, 1996. doi: 10.1002/(SICI)1097-4628(19960705)61:1⟨109::AID-APP12⟩3.0.CO;2-2.

[26] A. N. Gent. A new constitutive relation for rubber. *Rubber Chemistry and Technology*, 69:59–61, 1996.

[27] J. D. Ferry. *Viscoelastic properties of polymers*. Wiley, New York, 3rd edition, 1980.

Chapter 4

Application of the theory to PMMA below its glass transition temperature

4.1 Introduction

In this chapter we calibrate the constitutive parameters/functions in the theory developed in the previous chapter for the thermo-mechanical response of PMMA below its glass transition temperature. A summary of this specialized model is presented in Section 4.2 followed by the corresponding calibration procedure for PMMA in Section 4.3. A summary of the key constitutive equations, as well as the material parameters used, for both the one-dimensional and three-dimensional models are shown in Section 4.4.

4.2 Summary of the Specialized Material Model

Based on experience with recent theories of isotropic viscoplasticity of polymeric materials [1–6], we assume that the change in the macroscopic stress response of an amorphous polymer arises due to two basic reasons: (i) changes due to the stretching of intermolecular bonds, and (ii) changes in the configurational entropy due to changes in the molecular conformations. Accordingly, in developing our continuum mechanical theory, we assume two major operative micromechanisms to represent these concepts. Although no real material is composed of springs and dashpots, as a visual aid, Figure 4-1 shows a schematic rheological representation of these micromechanisms. The left micromechanism indexed by $\alpha = 1$ represents contributions to the stress due to intermolecular bond-stretching, and the right micromechanism indexed by $\alpha = 2$ represents contributions to the stress due to entropic changes in molecular conformations.

With such a micromechanical picture in mind, we have developed a rigorous three-dimensional thermo-mechanically coupled large deformation continuum framework for amorphous polymers, details of which were given in Chapter 3. The specialization of this framework to polymer behavior below the glass transition is presented here.

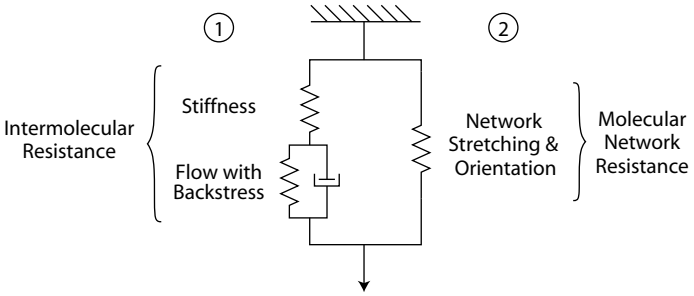

Figure 4-1: One-dimensional rheological representation of the proposed model for temperatures below the glass transition.

4.2.1 Summary of Three-Dimensional Constitutive Equations

This section summarizes a specialized form of our theory which should be useful in modeling the complex finite deformation response of amorphous thermoplastic polymers below their glass transition temperatures. For this case, we neglect plastic deformation in micromechanism $\alpha = 2$ so that

$$\mathbf{F}^{p\,(2)} = \mathbf{1} \tag{4.1}$$

and to ease notation, we introduce

$$\mathbf{F}^{p\,(1)} = \mathbf{F}^{p}, \quad \mathbf{F}^{e\,(1)} = \mathbf{F}^{e}, \quad \mathbf{F}^{e\,(2)} = \mathbf{F}, \tag{4.2}$$

The underlying constitutive equations relate the following basic fields:

$\boldsymbol{\chi}(\mathbf{X}, t)$,	motion;
$\mathbf{F} = \nabla\boldsymbol{\chi},\ J = \det\mathbf{F} > 0$,	deformation gradient;
$\mathbf{F} = \mathbf{F}^{e}\mathbf{F}^{p}$,	elastic-plastic decomposition of $\mathbf{F}$;
$\mathbf{F}^{p}, \quad J^{p} = \det\mathbf{F}^{p} = 1$,	inelastic distortions;
$\mathbf{F}^{e}, \quad J^{e} = \det\mathbf{F}^{e} = J > 0$,	elastic distortions;
$\mathbf{F} = \mathbf{R}\mathbf{U} = \mathbf{V}\mathbf{R}$,	polar decomposition of $\mathbf{F}$;
$\mathbf{F}^{e} = \mathbf{R}^{e}\mathbf{U}^{e} = \mathbf{V}^{e}\mathbf{R}^{e}$,	polar decomposition of $\mathbf{F}^{e}$;
$\mathbf{C} = \mathbf{F}^{\top}\mathbf{F}, \quad \mathbf{C}^{e} = \mathbf{F}^{e\top}\mathbf{F}^{e}$,	right Cauchy-Green strains;
$\mathbf{B} = \mathbf{F}\mathbf{F}^{\top}, \quad \mathbf{B}^{e} = \mathbf{F}^{e}\mathbf{F}^{e\top}$,	left Cauchy-Green strains;
$\mathbf{F}_{\rm dis} \overset{\rm def}{=} J^{-1/3}\mathbf{F}, \quad \det\mathbf{F}_{\rm dis} = 1$,	distortional part of $\mathbf{F}$;
$\mathbf{C}_{\rm dis} = (\mathbf{F}_{\rm dis})^{\top}\mathbf{F}_{\rm dis}, \quad \mathbf{B}_{\rm dis} = \mathbf{F}_{\rm dis}(\mathbf{F}_{\rm dis})^{\top}$,	distortional Cauchy-Green strains;
$\mathbf{T}$,	Cauchy stress;
$\mathbf{T} = \sum_{\alpha=1}^{2}\mathbf{T}^{e\,(\alpha)}$,	decomposition of Cauchy stress;
$\mathbf{M}^{e\,(1)} = J\mathbf{R}^{e\top}\mathbf{T}^{e\,(1)}\mathbf{R}^{e}$,	Mandel stress for $\alpha = 1$;
$\mathbf{M}^{e\,(2)} = J\mathbf{R}^{\top}\mathbf{T}^{e\,(2)}\mathbf{R}$,	Mandel stress for $\alpha = 2$;
$\psi_{\rm R} = \sum_{\alpha=1}^{2}\bar{\psi}^{(\alpha)}$,	free energy density per unit reference volume;
$\eta_{\rm R} = \sum_{\alpha=1}^{2}\bar{\eta}^{(\alpha)}$,	entropy density per unit reference volume;
$\boldsymbol{\xi} = (\xi_1, \xi_2, \ldots, \xi_m)$,	scalar internal variables;
$\mathbf{A}, \quad \mathbf{A} = \mathbf{A}^{\top}, \quad \det\mathbf{A} = 1$,	tensorial internal variable;
$\mathbf{M}^{e}_{\rm back}$,	back stress;
$\vartheta > 0$,	absolute temperature;

$\nabla\vartheta$,	referential temperature gradient;
$\mathbf{q}_{\mathrm{R}}$,	referential heat flux vector.

Temperature dependence

The temperature-dependence of the material properties of amorphous polymers depends strongly on the temperature relative to the glass transition temperature ϑ_g of the material. It is well-known that the glass transition temperature of such materials is not a constant, but depends strongly on the strain rate to which the material is subjected. Let

$$d \stackrel{\text{def}}{=} \sqrt{2}|\mathbf{D}_0| \tag{4.3}$$

denote the macroscopic effective shear strain rate, and d^{ref} a reference strain rate. We assume that the variation of the glass transition temperature with strain rate may be adequately described by [5, cf. their eq. (10)]

$$\vartheta_g = \begin{cases} \vartheta_g^{\text{ref}} & \text{if} \quad d \leq d^{\text{ref}}, \\ \vartheta_g^{\text{ref}} + \left[\dfrac{C_{2g} \times \log_{10}(d/d^{\text{ref}})}{C_{1g} - \log_{10}(d/d^{\text{ref}})}\right] & \text{if} \quad d > d^{\text{ref}}, \end{cases} \tag{4.4}$$

where C_{1g} and C_{2g} are Williams-Landel-Ferry (WLF) parameters [7] relative to the reference glass transition temperature ϑ_g^{ref}.

For this specialization of the model below the glass transition, we choose a temperature ϑ_* below the glass transition which we will use to define the temperature dependence of our material parameters. We assume that it varies identically to the glass transition temperature such that

$$\vartheta_* = \begin{cases} \vartheta_*^{\text{ref}} & \text{if} \quad d \leq d^{\text{ref}}, \\ \vartheta_*^{\text{ref}} + \left[\dfrac{C_{2g} \times \log_{10}(d/d^{\text{ref}})}{C_{1g} - \log_{10}(d/d^{\text{ref}})}\right] & \text{if} \quad d > d^{\text{ref}}, \end{cases} \tag{4.5}$$

where ϑ_*^{ref} is the reference value of the temperature. With the governing fields so defined, we assume the following constitutive equations for the two micromechanisms $\alpha = 1, 2$.

1. **Free energy**:

   For micromechanism $\alpha = 1$, with

   $$\mathbf{C}^e = \sum_{i=1}^{3} \omega_i \, \mathbf{r}_i^e \otimes \mathbf{r}_i^e, \tag{4.6}$$

   denoting the spectral representation of $\mathbf{C}^e$, and with

   $$\mathbf{E}^e = \sum_{i=1}^{3} E_i^e \, \mathbf{r}_i^e \otimes \mathbf{r}_i^e, \qquad E_i^e = \ln \sqrt{\omega_i^e}, \tag{4.7}$$

denoting an elastic logarithmic strain measure, we consider an elastic free energy of the form

$$\psi^{e\,(1)}(\mathbf{C}^e,\vartheta) = G|\mathbf{E}^e_0|^2 + \tfrac{1}{2}K(\operatorname{tr}\mathbf{E}^e)^2 \\ - 3\,K\,\alpha^{\mathrm{th}}(\,\vartheta-\vartheta_0)\operatorname{tr}\mathbf{E}^e + c(\vartheta-\vartheta_0) - c\,\vartheta\ln\Big(\frac{\vartheta}{\vartheta_0}\Big). \quad (4.8)$$

where $G(\vartheta) > 0$ is the temperature-dependent shear modulus, $K > 0$ is the bulk modulus, $\alpha^{\mathrm{th}} > 0$ is the coefficient of thermal expansion, $c > 0$ is the specific heat, and ϑ_0 is a reference temperature. The shear modulus is assumed to decrease linearly with increasing temperature such that

$$G(\vartheta) = G^{\mathrm{ref}} - X_G(\vartheta - \vartheta_*), \quad (4.9)$$

where G^{ref} is the value of the shear modulus at a chosen reference temperature ϑ^{ref}, and X_G describes the variation of the shear modulus with temperature.

With

$$\mathbf{A} = \sum_{i=1}^{3} a_i\,\mathbf{l}^d_i \otimes \mathbf{l}^d_i, \quad (4.10)$$

denoting the spectral representation of $\mathbf{A}$, and with

$$\ln\mathbf{A} = \sum_{i=1}^{3} \ln a_i\,\mathbf{l}^d_i \otimes \mathbf{l}^d_i, \quad (4.11)$$

denoting a defect logarithmic strain measure, we consider a defect free energy of the form

$$\tilde{\psi}^d(\mathbf{A},\vartheta) = \frac{1}{4}C(\vartheta)\,\left[(\ln a_1)^2 + (\ln a_2)^2 + (\ln a_3)^2\right], \quad (4.12)$$

where $C(\vartheta) \geq 0$ is a backstress modulus chosen to decrease linearly with temperature following the form of the internal stress used by Fotheringham et al. [8], Povolo and Hermida [9] and Richeton et al. [10]. So that

$$C(\vartheta) = \begin{cases} -X_C(\vartheta - \vartheta_C) & \text{if } \ \vartheta \leq \vartheta_C, \\ 0 & \text{if } \ \vartheta > \vartheta_C, \end{cases} \quad (4.13)$$

where $X_C > 0$ is a material parameter and ϑ_C is the temperature near the material's glass transition where $C(\vartheta)$ vanishes.

For micromechanism $\alpha = 2$, let

$$I_1 \stackrel{\mathrm{def}}{=} \operatorname{tr}\mathbf{C}_{\mathrm{dis}} \quad (4.14)$$

denote the first principal invariant of $\mathbf{C}_{\mathrm{dis}}$. We consider following elastic free energy

$$\psi^{e\,(2)} = -\tfrac{1}{2}\mu_{\mathrm{R}}\,I_{1,\max}\,\ln\Big(1 - \frac{I_1 - 3}{I_{1,\max}}\Big), \quad (4.15)$$

where $\mu_{\mathrm{R}}(\vartheta) > 0$ and $I_{1,\max} > 3$ are two material parameters. In particular, μ_{R} represents the ground state rubbery shear modulus of the material, and $I_{1,\max}$ represents the upper limit

of I_1 (i.e., $I_1 < (3 + I_{1,\max})$), associated with limited chain extensibility. We assume that $\mu_{\rm R}$ decreases linearly with increasing temperature such that

$$\mu_{\rm R}(\vartheta) = \mu_{\rm R}^{\rm ref} - X_\mu(\vartheta - \vartheta_*), \tag{4.16}$$

where $\mu_{\rm R}^{\rm ref}$ is the value of $\mu_{\rm R}$ at a chosen reference temperature $\vartheta^{\rm ref}$ and X_μ describes the variation of $\mu_{\rm R}$ with temperature.

2. Mandel stress. Cauchy stress. Back stress. Effective stress:

For micromechanism $\alpha = 1$, the Mandel stress is given by

$$\mathbf{M}^{e\,(1)} = 2G\mathbf{E}_0^e + K\left\{\operatorname{tr}\mathbf{E}^e - 3\,\alpha^{\rm th}\,(\vartheta - \vartheta_0)\right\}\mathbf{1}, \tag{4.17}$$

and the corresponding Cauchy stress is then

$$\mathbf{T}^{e\,(1)} \stackrel{\rm def}{=} J^{-1}\,\mathbf{R}^e\,\mathbf{M}^{e\,(1)}\,\mathbf{R}^{e\top}. \tag{4.18}$$

The symmetric and deviatoric back stress is

$$\mathbf{M}_{\rm back} = C\ln\mathbf{A}, \tag{4.19}$$

and the driving stress for plastic flow is the effective stress given by

$$\mathbf{M}_{\rm eff}^{e\,(1)} = \mathbf{M}^{e\,(1)} - \mathbf{M}_{\rm back}. \tag{4.20}$$

The corresponding *equivalent shear stress* and *mean normal pressure* are given by

$$\bar\tau \stackrel{\rm def}{=} \frac{1}{\sqrt{2}}\,|(\mathbf{M}_{\rm eff}^{e\,(1)})_0|, \quad \text{and} \quad \bar p \stackrel{\rm def}{=} -\frac{1}{3}\operatorname{tr}\mathbf{M}^{e\,(1)}, \tag{4.21}$$

respectively.

For micromechanism $\alpha = 2$, the Mandel stress is given by

$$\mathbf{M}^{e(2)} = \mu_{\rm R}\left(1 - \frac{I_1 - 3}{I_{1,\max}}\right)^{-1}(\mathbf{C}_{\rm dis})_0, \tag{4.22}$$

and the corresponding Cauchy stress is then

$$\mathbf{T}^{e(2)} = J^{-1}\left[\mu_{\rm R}\left(1 - \frac{I_1 - 3}{I_{1,\max}}\right)^{-1}(\mathbf{B}_{\rm dis})_0\right]. \tag{4.23}$$

3. Internal variables:

We restrict the list $\boldsymbol{\xi}$ of internal variables to two, positive-valued variables

$$S \geq 0, \qquad \varphi \geq 0$$

that represent aspects of the *intermolecular shear resistance to plastic flow*. The parameter S has dimensions of stress and represents an *isotropic resistance to plastic flow*, while φ is a dimensionless parameter representing the local *free-volume* of the polymeric glass.

4. **Flow rule**: The evolution equation for $\mathbf{F}^p$ is assumed to follow the "cooperative model" of Fotheringham et al. [8], Povolo and Hermida [9] and Richeton et al. [10]. The equations are

$$\left.\begin{aligned} &\dot{\mathbf{F}}^p = \mathbf{D}^p\,\mathbf{F}^p, \qquad \mathbf{F}^p(\mathbf{X},0) = \mathbf{1}, \\ &\mathbf{D}^p = \nu^p\left(\frac{(\mathbf{M}^{e\,(1)}_{\text{eff}})_0}{2\,\bar{\tau}}\right), \\ &\nu^p = \begin{cases} 0 & \text{if} \quad \bar{\tau}^{(1)}_{\text{e}} \le 0, \\ \nu_0\,\exp\left\{-\dfrac{\Delta F}{k_B\,\vartheta}\right\}\left[\sinh\left(\dfrac{\bar{\tau}^{(1)}_{\text{e}}\,V}{2k_B\vartheta}\right)\right]^{1/m} & \text{if} \quad \bar{\tau}^{(1)}_{\text{e}} > 0\,, \end{cases} \end{aligned}\right\} \tag{4.24}$$

where

$$\bar{\tau}^{(1)}_{\text{e}} \stackrel{\text{def}}{=} \bar{\tau} - S - \alpha_p\,\bar{p} \tag{4.25}$$

denotes an *effective shear stress*, with $\alpha_p \ge 0$ a *pressure sensitivity parameter*, ν_0 is a pre-exponential factor with units of 1/time, m is a strain rate sensitivity parameter, ΔF is an *activation energy*, V is a *shear activation volume*, and k_B is Boltzmann's constant.

5. **Evolution equations for the internal variables S, φ, and $\mathbf{A}$**

We assume that the material disorders and is accompanied by a microscale dilatation as plastic deformation occurs resulting in an increase of the free volume φ. This increase leads to a fluctuation in the isotropic resistance S causing a transient rise in the flow stress of the material as plastic deformation proceeds. We therefore assume that the evolution of the free volume φ is coupled to the evolution of the isotropic resistance S in order to reproduce the typical yield peak observed in the stress-strain response of amorphous polymers below the glass transition temperature ϑ_g. The coupling is introduced through this special set of equations:

$$\left.\begin{aligned} \dot{\varphi} &= g\;(\varphi^* - \varphi)\;\nu^p, \qquad \varphi(\mathbf{X},0) = \varphi_i > 0, \\ \dot{S} &= h\;(S^* - S)\;\nu^p, \qquad S(\mathbf{X},0) = S_i \ge 0, \\ S^* &= S_i + b\;(\varphi^* - \varphi)\,, \end{aligned}\right\} \tag{4.26}$$

where the material parameter $\varphi^* \ge \varphi_i$ represents a saturation value of the free volume φ.[1]

The material parameters/functions $g(\vartheta) > 0$, $h > 0$, and $b(\vartheta, \nu^p) \ge 0$ describe the initial hardening, subsequent rate of softening, and magnitude of the yield peak. We assume the following particular functions to describe the temperature and rate-dependence of g and b:

$$\left.\begin{aligned} g &= g_1 + g_2\vartheta, \\ b &= b_1\;\left(\vartheta^2 + b_2\vartheta + b_3\right)\;\left(\frac{\nu^p}{\nu_{\text{ref}}}\right)^{b_4}, \end{aligned}\right\} \tag{4.27}$$

[1] The saturation value φ^* is in general expected to be a function of the temperature ϑ and the strain-rate ν^p, but there is insufficient experimental information to be more precise about such variations at this time

where the list $\{g_1,\, g_2,\, b_1,\, b_2,\, b_3,\, b_4\}$ are material parameters and ν_{ref} is a reference strain-rate. These functions for b and g are empirical and have been chosen to fit experimental data.

The evolution equation for $\mathbf{A}$ is taken as

$$\dot{\mathbf{A}} = \mathbf{D}^p\mathbf{A} + \mathbf{A}\mathbf{D}^p - \gamma\left(\mathbf{A}\,\ln\mathbf{A}\right)\nu^p, \qquad \mathbf{A}(\mathbf{X},0) = \mathbf{1}, \tag{4.28}$$

where $\gamma \geq 0$ is a constitutive parameter which governs the dynamic recovery of $\mathbf{A}$.

6. Entropy relation. Fourier's Law:

Finally, we have the entropy relation

$$\eta_{\text{R}} = -\left[\frac{\partial\bar{\psi}^{e\,(1)}(\mathbf{C}^e,\vartheta)}{\partial\vartheta} + \frac{\partial\bar{\psi}^{e\,(2)}(\mathbf{C},\vartheta)}{\partial\vartheta} + \frac{\partial\bar{\psi}^{d}(\mathbf{A},\vartheta)}{\partial\vartheta}\right], \tag{4.29}$$

together with Fourier's law

$$\mathbf{q}_{\text{R}} = -\kappa\,\nabla\vartheta, \tag{4.30}$$

where $\kappa(\vartheta) > 0$ is the thermal conductivity and

$$\left.\begin{aligned}
\frac{\partial\bar{\psi}^{e\,(1)}(\mathbf{C}^e,\vartheta)}{\partial\vartheta} &= \frac{\partial G}{\partial\vartheta}|\mathbf{E}^e_0|^2 - 3\,K\alpha^{\text{th}}(\text{tr}\,\mathbf{E}^e) - c\ln\left(\frac{\vartheta}{\vartheta_0}\right),\\
\frac{\partial\bar{\psi}^{e\,(2)}(\mathbf{C},\vartheta)}{\partial\vartheta} &= \frac{1}{2}\,\frac{\partial\mu_{\text{R}}}{\partial\vartheta}\,I_{1,\max}\,\ln\left(1-\frac{I_1-3}{I_{1,\max}}\right),\\
\frac{\partial\bar{\psi}^{d}(\mathbf{A},\vartheta)}{\partial\vartheta} &= \frac{1}{4}\,\frac{\partial C}{\partial\vartheta}\,\left[(\ln a_1)^2 + (\ln a_2)^2 + (\ln a_3)^2\right].
\end{aligned}\right\} \tag{4.31}$$

We have assumed that K, α^{th}, c, and $I_{1,\max}$ are temperature-independent below the glass transition.

7. Partial differential equations for the temperature field

The specific heat in the theory is given by

$$c \overset{\text{def}}{=} -\vartheta\left[\frac{\partial^2\bar{\psi}^{e\,(1)}(\mathcal{I}_{\mathbf{C}^e},\vartheta)}{\partial\vartheta^2} + \frac{\partial^2\bar{\psi}^{e\,(2)}(\mathcal{I}_{\mathbf{C}},\vartheta)}{\partial\vartheta^2} + \frac{\partial^2\bar{\psi}^{d}(\mathcal{I}_{\mathbf{A}},\vartheta)}{\partial\vartheta^2}\right], \tag{4.32}$$

and balance of energy gives the following partial differential equation for the temperature

$$\begin{aligned}
c\dot{\vartheta} = -\text{Div}\,\mathbf{q}_{\text{R}} + q_{\text{R}} &+ \underbrace{\left[|(\mathbf{M}^{e\,(1)}_{\text{eff}})_0| + \frac{\partial\tilde{\psi}^{d}(\mathcal{I}_{\mathbf{A}},\vartheta)}{\partial\mathbf{A}} : \mathbf{G}(\mathbf{A})\right] d^p}_{\text{rate of plastic dissipation}}\\
&+ \underbrace{\vartheta\left[\frac{\partial^2\bar{\psi}^{e\,(1)}(\mathcal{I}_{\mathbf{C}^e},\vartheta)}{\partial\vartheta\,\partial\mathbf{C}^e} : \dot{\mathbf{C}}^e + \frac{\partial^2\bar{\psi}^{e\,(2)}(\mathcal{I}_{\mathbf{C}},\vartheta)}{\partial\vartheta\,\partial\mathbf{C}} : \dot{\mathbf{C}} + \frac{\partial^2\bar{\psi}^{d}(\mathcal{I}_{\mathbf{A}},\vartheta)}{\partial\vartheta\,\partial\mathbf{A}} : \dot{\mathbf{A}}\right]}_{\text{“thermoelastic coupling” terms due to variation of } \mathbf{C}^e,\ \mathbf{C},\text{ and } \mathbf{A}}
\end{aligned} \tag{4.33}$$

Table 4.1: Summary of the five terms in the heat equation of (4.35)

Term	Description
$\bar{\tau}\,\nu^p$	Plastic dissipation
$\frac{1}{2}\,C\,\gamma\,\lvert\ln\mathbf{A}\rvert^2\,\nu^p$	Backstress dissipation
$\vartheta\,\dfrac{\partial\mathbf{M}^{e\,(1)}}{\partial\vartheta}:[\mathbf{F}^{e\top}\,\mathbf{D}^e\,\mathbf{F}^{e-\top}]$	Thermoelastic storage
$\frac{1}{2}\,\vartheta\,\dfrac{\partial C}{\partial\vartheta}\,\big[(\ln\mathbf{A})\mathbf{A}^{-1}\big]:\dot{\mathbf{A}}$	Backstress storage
$\vartheta\,\dfrac{\partial\mathbf{M}^{e\,(2)}}{\partial\vartheta}:[\mathbf{F}^{\top}\,\mathbf{D}\,\mathbf{F}^{-\top}]$	Gent storage

where

$$\left.\begin{aligned}\mathbf{G}(\mathbf{A}) &= \frac{1}{\sqrt{2}}\,\gamma\,\mathbf{A}\ln\mathbf{A},\\ \frac{\partial\tilde{\psi}^d(\mathcal{I}_{\mathbf{A}},\vartheta)}{\partial\mathbf{A}} &= \frac{1}{2}\,C\,(\ln\mathbf{A})\mathbf{A}^{-1},\\ \frac{\partial^2\bar{\psi}^{e\,(1)}(\mathcal{I}_{\mathbf{C}^e},\vartheta)}{\partial\vartheta\,\partial\mathbf{C}^e} &= \frac{\partial}{\partial\vartheta}\left[\frac{1}{2}\,\mathbf{C}^{e\,-1}\,\mathbf{M}^{e\,(1)}\right],\\ \frac{\partial^2\bar{\psi}^{e\,(2)}(\mathcal{I}_{\mathbf{C}},\vartheta)}{\partial\vartheta\,\partial\mathbf{C}} &= \frac{\partial}{\partial\vartheta}\left[\frac{1}{2}\,\mathbf{C}^{-1}\,\mathbf{M}^{e\,(2)}\right].\end{aligned}\right\}\tag{4.34}$$

Using the symmetry of $\mathbf{A}$, $\mathbf{M}^{e\,(\alpha)}$, $\mathbf{C}^e$ and $\mathbf{C}$, (4.33) can be rewritten as

$$\begin{aligned}c\dot{\vartheta} = -\mathrm{Div}\,\mathbf{q}_{\mathrm{R}} + q_{\mathrm{R}} + \underbrace{\left[\bar{\tau}+\frac{1}{2}\,C\,\gamma\,\lvert\ln\mathbf{A}\rvert^2\right]\,\nu^p}_{\text{rate of plastic dissipation}}\\ + \underbrace{\vartheta\left[\frac{\partial\mathbf{M}^{e\,(1)}}{\partial\vartheta}:\big[\mathbf{F}^{e\top}\,\mathbf{D}^e\,\mathbf{F}^{e-\top}\big]+\frac{\partial\mathbf{M}^{e\,(2)}}{\partial\vartheta}:\big[\mathbf{F}^{\top}\,\mathbf{D}\,\mathbf{F}^{-\top}\big]+\frac{1}{2}\,\frac{\partial C}{\partial\vartheta}\,\big[(\ln\mathbf{A})\mathbf{A}^{-1}\big]:\dot{\mathbf{A}}\right]}_{\text{“thermoelastic coupling” terms}}\end{aligned}\tag{4.35}$$

where

$$\left.\begin{aligned}\frac{\partial\mathbf{M}^{e\,(1)}}{\partial\vartheta} &= 2\,\frac{\partial G}{\partial\vartheta}\,\mathbf{E}^e_0 - 3\,K\alpha^{\mathrm{th}}\mathbf{1},\\ \frac{\partial\mathbf{M}^{e\,(2)}}{\partial\vartheta} &= \frac{\partial\mu_{\mathrm{R}}}{\partial\vartheta}\Big(1-\frac{I_1-3}{I_{1,\max}}\Big)^{-1}\,(\mathbf{C}_{\mathrm{dis}})_0.\end{aligned}\right\}\tag{4.36}$$

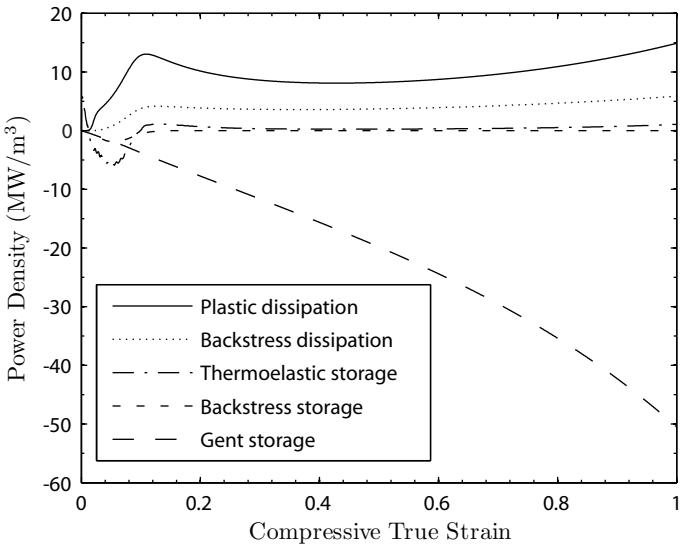

Figure 4-2: Contributions of the various terms of the the heat equation of (4.35) during a one-element adiabatic ABAQUS calculation at a strain-rate of 10^{-1}/s at 25 C. The specific form of each term is summarized in Table 4.1.

At this stage of the development of the theory, the "thermoelastic-coupling" terms which give rise to a temperature change due to variations of $\mathbf{C}^e$, $\mathbf{C}$ and $\mathbf{A}$ with deformation are not well-characterized. To demonstrate this, in Figure 4-2 we plot the contribution of all terms of the plastic dissipation and thermoelastic-coupling to the heat equation for a simple compression simulation at 25 C. The five terms are summarized in Table 4.1. As the test progresses, the contribution from the Gent storage term begins to contribute significantly to the cooling of the specimen at large deformations. It is not immediately clear why this contribution is physically unrealistic; it is likely that some of the large strain hardening is dissipated and not fully stored. Accordingly, as an approximation, we neglect these terms and assume instead that only a fraction $0 \lessapprox \beta \lessapprox 1$ of the rate of plastic dissipation is dissipated as heat

$$c\dot{\vartheta} = -\mathrm{Div}\,\mathbf{q}_{\mathrm{R}} + q_{\mathrm{R}} + \beta\left(\bar{\tau} + \frac{1}{2}\,C\,\gamma\,|\ln\mathbf{A}|^2\right)\nu^p \tag{4.37}$$

where β is the fraction of inelastic work that is dissipated, and we have used

4.2.2 Summary of One-Dimensional Constitutive Equations

In this section we present an approximate one-dimensional version of the model which substantially aids in the calibration of material properties from experimental data. The underlying constitutive equations relate the following basic fields:

$U > 0$,	stretch,
U^p,	plastic stretch,
$U^e = UU^{p-1}$,	elastic part of the stretch,
$\epsilon = \ln U$,	logarithmic strain,
$\epsilon^e = \ln U^e$,	logarithmic elastic strain,
$\boldsymbol{\xi} = \big(V, \varphi\big)$	scalar internal variables,
$A > 0$,	squared stretch-like internal variable,
$\vartheta > 0$,	absolute temperature,
$\psi = \psi^{e\,(1)}\big(U^e, \vartheta\big) + \psi^{e\,(2)}\big(U, \vartheta\big) + \psi^d\big(A, \vartheta\big)$,	free energy density,
$\sigma = \sum_{\alpha=1}^{2} \sigma^{e(\alpha)}$,	decomposition of the Cauchy stress.

Temperature dependence

The temperature-dependence of the material properties of amorphous polymers depends strongly on the temperature relative to the glass transition temperature ϑ_g of the material. It is well-known that the glass transition temperature of such materials is not a constant, but depends strongly on the strain-rate to which the material is subjected. Let

$$\dot{\epsilon} \stackrel{\text{def}}{=} \frac{\partial \epsilon}{\partial t} \tag{4.38}$$

denote the axial strain-rate, and $\dot{\epsilon}^{\text{ref}}$ a reference strain-rate. We assume that the variation of the glass transition temperature with strain-rate may be adequately described by [5, cf. their eq. (10)]

$$\vartheta_g = \begin{cases} \vartheta_g^{\text{ref}} & \text{if} \quad \dot{\epsilon} \leq \dot{\epsilon}^{\text{ref}}, \\ \vartheta_g^{\text{ref}} + \left[\dfrac{C_{2g} \times \log_{10}(\dot{\epsilon}/\dot{\epsilon}^{\text{ref}})}{C_{1g} - \log_{10}(\dot{\epsilon}/\dot{\epsilon}^{\text{ref}})}\right] & \text{if} \quad \dot{\epsilon} > \dot{\epsilon}^{\text{ref}}, \end{cases} \tag{4.39}$$

where C_{1g} and C_{2g} are Williams-Landel-Ferry (WLF) parameters [7] relative to the reference glass transition temperature ϑ_g^{ref}. With the governing fields and the glass transition temperature so defined, we assume the following constitutive equations for the two micromechanisms $\alpha = 1, 2$.

For this specialization of the model below the glass transition, we choose a temperature ϑ_* below the glass transition which we will use to define the temperature dependence of our material parameters. We assume that it varies identically to the glass transition temperature such that

$$\vartheta_* = \begin{cases} \vartheta_*^{\text{ref}} & \text{if} \quad \dot{\epsilon} \leq \dot{\epsilon}^{\text{ref}}, \\ \vartheta_*^{\text{ref}} + \left[\dfrac{C_{2g} \times \log_{10}(\dot{\epsilon}/\dot{\epsilon}^{\text{ref}})}{C_{1g} - \log_{10}(\dot{\epsilon}/\dot{\epsilon}^{\text{ref}})}\right] & \text{if} \quad \dot{\epsilon} > \dot{\epsilon}^{\text{ref}}, \end{cases} \tag{4.40}$$

where ϑ_*^{ref} is the reference value of the temperature. With the governing fields so defined, we assume the following constitutive equations for the two micromechanisms $\alpha = 1, 2$.

1. **Free Energy**: For $\psi^{e(1)}$ we use a simple linear elastic form for the free energy

$$\psi^{e\,(1)} = \tfrac{1}{2}\, E\, |\epsilon^e|^2, \tag{4.41}$$

where $E(\vartheta) > 0$ is the temperature-dependent Young's modulus. The modulus is assumed to decrease linearly with increasing temperature such that

$$E(\vartheta) = E^{\text{ref}} - X_E(\vartheta - \vartheta_*), \tag{4.42}$$

where E^{ref} is the value of the modulus at a chosen reference temperature ϑ^{ref} and X_E describes the variation of the modulus with temperature.

For ψ^d we use a simple defect free energy of the form[2]

$$\psi^{d\,(1)} = \tfrac{3}{8}\, C\, (\ln A)^2, \tag{4.43}$$

where $C(\vartheta) \geq 0$ is a back-stress modulus chosen to decrease linearly with temperature following the form of the internal stress used by Povolo and Hermida [9], Fotheringham and Cherry [11], and Richeton et al. [10]

$$C(\vartheta) = \begin{cases} -X_C(\vartheta - \vartheta_C) & \text{if} \quad \vartheta \leq \vartheta_C, \\ 0 & \text{if} \quad \vartheta > \vartheta_C, \end{cases} \tag{4.44}$$

where X_C is a material parameter and ϑ_C is the temperature near the material's glass transition where $C(\vartheta)$ vanishes.

For $\psi^{(2)}$ we use the first invariant of the stretch[3]

[2] Let (a_1, a_2, a_3) denote the set of a principal stretches of a symmetric positive definite unimodular tensor $\mathbf{A}$ in three dimensions representing a squared stretch tensor. Since $\det \mathbf{A} = 1$, the a_i satisfy $a_1 a_2 a_3 = 1$. Assuming a corresponding defect free energy of the form

$$\psi^d = \tfrac{1}{4}\, C\, \big[(\ln a_1)^2 + (\ln a_2)^2 + (\ln a_3)^2\big],$$

then in one-dimension, with $A \overset{\text{def}}{=} a_1$, $a_2 = a_3 = A^{-\frac{1}{2}}$, the defect free energy can be written as

$$\psi^d = \tfrac{3}{8}\, C\, (\ln A)^2,$$

[3] Let $(\lambda_1, \lambda_2, \lambda_3)$ denote the set of a principal stretches of a symmetric positive definite tensor $\mathbf{U}$ in three dimensions representing a stretch tensor. For incompressibility of such a stretch, the λ_i satisfy $\lambda_1 \lambda_2 \lambda_3 = 1$. The first invariant I_1 of the stretch is defined by

$$I_1 \overset{\text{def}}{=} \lambda_1^2 + \lambda_2^2 + \lambda_3^2.$$

In one-dimension, with $\lambda \overset{\text{def}}{=} \lambda_1$, $\lambda_2 = \lambda_3 = \lambda^{-\frac{1}{2}}$,

$$I_1 = \lambda^2 + 2\, \lambda^{-1}.$$

$$I_1 \equiv U + 2U^{-1}, \tag{4.45}$$

and adopt the Gent [12] form of the free energy

$$\psi^{e\,(2)} = -\tfrac{1}{2}\,\mu_{\rm R}\,I_{1,\max}\,\ln\left(1 - \frac{I_1 - 3}{I_{1,\max}}\right) \tag{4.46}$$

where $\mu_{\rm R}(\vartheta) > 0$ and $I_{1,\max} > 3$ are two material parameters. In particular, $\mu_{\rm R}$ represents the ground state rubbery shear modulus of the material, and $I_{1,\max}$ represents the upper limit of I_1 (i.e., $I_1 < (3 + I_{1,\max})$), associated with limited chain extensibility. We assume that $\mu_{\rm R}$ decreases linearly with increasing temperature such that

$$\mu_{\rm R}(\vartheta) = \mu_{\rm R}^{\rm ref} - X_\mu(\vartheta - \vartheta_*), \tag{4.47}$$

where $\mu_{\rm R}^{\rm ref}$ is the value of $\mu_{\rm R}$ at a chosen reference temperature $\vartheta^{\rm ref}$ and X_μ describes the variation of $\mu_{\rm R}$ with temperature.

2. Equation for the stress: The elastic stress in mechanism $\alpha = 1$ is given by

$$\sigma^{e\,(1)} = E\,\epsilon^e \tag{4.48}$$

and the back-stress relation is[4]

$$\sigma_{\rm back} = \tfrac{3}{2}\,C\,\ln A. \tag{4.49}$$

such that the driving stress for plastic flow is the effective stress given by

$$\sigma_{\rm eff}^{(1)} = \sigma^{e\,(1)} - \sigma_{\rm back} \tag{4.50}$$

[4]Given a free energy function of the form

$$\psi = \hat{\psi}(A),$$

the engineering stress S is defined by

$$S = 2\frac{\partial \psi}{\partial A}.$$

Also, assuming incompressibility, the Cauchy stress σ can then be represented as

$$\sigma = SA = 2A\frac{\partial \hat{\psi}}{\partial A},$$

The stress in mechanism $\alpha = 2$ is given by[5]

$$\sigma^{e(2)} = \mu_{\mathrm{R}} \left(1 - \frac{I_1 - 3}{I_{1,\max}}\right)^{-1} \left(U^2 - U^{-1}\right) \tag{4.51}$$

3. Internal variables:

The list $\boldsymbol{\xi}$ of internal variables is

$$S \geq 0, \qquad \varphi \geq 0,$$

that represent aspects of the *intermolecular shear resistance to plastic flow*. The parameter S has dimensions of stress and represents an *isotropic resistance to plastic flow*, while φ is a dimensionless parameter representing the local *free-volume* of the polymeric glass.

4. Flow rule: The evolution equation for U^p is

$$\left.\begin{aligned}
&\dot{U}^p = D^p U^p, \qquad U^p(0) = 1, \\
&D^p = \dot{\epsilon}^p \operatorname{sign}(\sigma^{e(1)}) \\
&\bar{\sigma} \stackrel{\text{def}}{=} |\sigma^{(1)}_{\text{eff}}| - S - \alpha_p \bar{p}, \qquad \bar{p} \stackrel{\text{def}}{=} -\tfrac{1}{3}\,\sigma^{e(1)} \\
&\dot{\epsilon}^p = \begin{cases} \dot{\epsilon}_0 \exp\left(-\dfrac{\Delta F}{k_B \vartheta}\right) \left[\sinh\left(\dfrac{\bar{\sigma} V}{2\, k_B \vartheta}\right)\right]^{1/m} & \text{if} \quad \bar{\sigma} > 0, \\ 0 & \text{if} \quad \bar{\sigma} \leq 0. \end{cases}
\end{aligned}\right\} \tag{4.52}$$

The quantity $\dot{\epsilon}^p$ is the plastic strain-rate and follows the form of the "cooperative model" used by Richeton et al. [10], where $\bar{\sigma}$ denotes an effective stress with $\alpha_p \geq 0$ a pressure sensitivity parameter and $\bar{p}$ a pressure. Additionally, $\dot{\epsilon}_0$ is a pre-exponential factor with units of 1/time, ΔF is an activation energy, m is a strain rate sensitivity parameter, V represents a tensile activation volume, and k_B is Boltzmann's constant.

5. Evolution equations for the internal variables S, φ, and A

We assume that the material disorders and is accompanied by a microscale dilatation as plastic deformation occurs resulting in an increase of the free volume φ. This increase leads to a fluctuation in the isotropic resistance S causing a transient rise in the flow stress of the material as plastic deformation proceeds. We therefore assume that the evolution of the

[5] Given a free energy function of the form

$$\psi = \hat{\psi}\,(I_1)\,, \qquad I_1 = \lambda^2 + 2\lambda^{-1},$$

the engineering stress S is defined by

$$S = \frac{\partial \psi}{\partial \lambda} = \frac{\partial \hat{\psi}}{\partial I_1} \frac{\partial I_1}{\partial \lambda}.$$

Also, assuming incompressibility

$$a_0 = a\lambda,$$

where a_0 is the original cross-sectional area and a is the current cross-sectional area. The Cauchy stress σ can then be represented as

$$\sigma = S\lambda = \lambda \frac{\partial \hat{\psi}}{\partial I_1} \frac{\partial I_1}{\partial \lambda},$$

free volume φ is coupled to the evolution of the isotropic resistance S in order to reproduce the typical yield peak observed in the stress-strain response of amorphous polymers below the glass transition temperature ϑ_g. The coupling is introduced through this special set of equations:

$$\left.\begin{aligned} \dot{\varphi} &= g\ (\varphi^* - \varphi)\ \dot{\epsilon}^p, \qquad \varphi(0) = \varphi_i > 0, \\ \dot{S} &= h\ (S^* - S)\ \dot{\epsilon}^p, \qquad S(0) = S_i \geq 0, \\ S^* &= S_i + b\ (\varphi^* - \varphi)\,, \end{aligned}\right\} \tag{4.53}$$

where the material parameter $\varphi^* \geq \varphi_i$ represents a saturation value of the free volume φ. The material parameters/functions $g(\vartheta) > 0$, $h > 0$, and $b(\vartheta, \dot{\epsilon}^p) \geq 0$ describe the initial hardening, subsequent rate of softening, and magnitude of the yield peak. We assume the following particular functions to describe the temperature and rate-dependence of g and b

$$\left.\begin{aligned} g &= g_1 + g_2\vartheta, \\ b &= b_1\ \left(\vartheta^2 + b_2\vartheta + b_3\right)\ \left(\frac{\dot{\epsilon}^p}{\dot{\epsilon}_{\text{ref}}}\right)^{b_4}, \end{aligned}\right\} \tag{4.54}$$

where the list $\{g_1,\, g_2,\, b_1,\, b_2,\, b_3,\, b_4\}$ are material parameters and $\dot{\epsilon}_{\text{ref}}$ is a reference strain-rate. These functions for b and g are empirical and have been chosen to fit experimental data.

The evolution equation for A is taken as

$$\dot{A} = 2\, D^p A - \gamma(A \ln A)\, \dot{\epsilon}^p, \qquad A(0) = 1, \tag{4.55}$$

where $\gamma > 0$ is a constitutive parameter that governs the dynamic recovery of A.

4.3 Material Parameter Calibration Below the Glass Transition

With the full three-dimensional and simplified one-dimensional version of the theory in place, we are in position to determine the material parameters/functions appearing in the theory by curve-fitting the experimental data for PMMA. We start with the one-dimensional calibration procedure using MATLAB in Section 4.3.1 followed by the appropriate adjustments necessary to complete calibration of the three-dimensional model in the finite element program ABAQUS/Explicit in Section 4.3.2.

Once the three-dimensional isothermal model is calibrated, a set of multi-element fully-coupled calculations is performed in ABAQUS/Explicit to calibrate the internal heating response of the material. These calculations and results are summarized in 4.3.3.

4.3.1 One-Dimensional Model Calibration Procedure

We have implemented the one-dimensional model of Section 4.2.2 in MATLAB using an explicit integration scheme, and we use it to calibrate the material parameters from the experiments described in Chapter 2. The one-dimensional calibration process consists of five sequential steps which are outlined in detail in this section. The five steps cover calibration of these aspects of the stress-strain response: (1) initial yield stress, (2) back stress, (3) elastic modulus, (4) large strain behavior, and (5) yield peak shape.

Initial Yield Stress

We have chosen to use the cooperative model [6, 9, 11] to describe the rate and temperature dependence of the yield stress of PMMA below the glass transition. One important difference between our implementation and that of the earlier authors is that we have replaced their scalar internal stress with a stretch-dependent back stress (4.49). The reasoning is that the internal stress must be conjugate to a stretch measure so that it can be accounted for in the total internal energy of the system, and therefore in the partial differential equation governing the temperature field. However, for the purposes of finding material parameters, we start with the earlier form using the scalar internal stress, and then we replace it with a suitable stretch-dependent back stress later in the calibration procedure.

From (4.52), for simple *compression*, during fully-developed flow when $\dot{\epsilon}^p \approx \dot{\epsilon}$ (taken to be positive) the expression for yield stress σ_y as a function of temperature ϑ and strain rate $\dot{\epsilon}$ is given by

$$\left(1 - \frac{\alpha_p}{3}\right) |\sigma_y| = r(\vartheta) + \frac{2k_B\vartheta}{V} \sinh^{-1}\left[\left(\frac{\dot{\epsilon}}{\dot{\epsilon}^*(\vartheta)}\right)^m\right] \tag{4.56}$$

where α_p is a pressure sensitivity parameter, r is a temperature dependent internal stress, k_B is the Boltzmann constant, V is an activation volume, $\dot{\epsilon}^*$ is a thermally activated characteristic strain rate, and m is a strain rate sensitivity parameter. Because of (4.44), the "internal stress" r follows a linear relationship with temperature such that

$$r = \begin{cases} r_1(\vartheta_r - \vartheta) & : \vartheta \leq \vartheta_r, \\ 0 & : \vartheta > \vartheta_r, \end{cases} \tag{4.57}$$

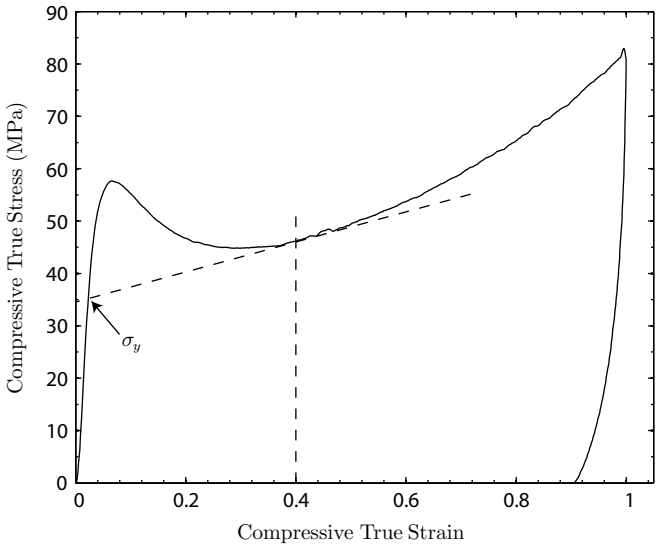

Figure 4-3: Schematic showing yield stress determined by the intersection of the initial loading path with the tangent of the stress-strain curve at 0.4 strain

where ϑ_r describes the temperature at which the internal stress vanishes and r_1 is a material parameter. The characteristic strain rate $\dot{\epsilon}^*$ is assumed to follow an Arrhenius-type temperature dependence

$$\dot{\epsilon}^* = \dot{\epsilon}_0 \exp\left(-\frac{\Delta F}{k_B \vartheta}\right) \tag{4.58}$$

where $\dot{\epsilon}_0$ is a reference strain rate and ΔF is an activation energy. To summarize, from (4.56), (4.57), and (4.58), there is a list of six material parameters that must be calibrated with the experimental yield data

$$\{\, V, m, r_1, \vartheta_r, \dot{\epsilon}_0, \Delta F \,\} \tag{4.59}$$

At this point in the calibration procedure we ignore the effects of the yield peak and define the yield stress as the intersection of the initial loading path with the tangent of the stress-strain curve at approximately 0.4 strain; this is shown schematically in Figure 4-3.[6] Following this approach, yield stress values have been extracted from the PMMA compression experiments in the temperature range 25 C to 110 C at four strain-rates. The ratio of these yield stresses to test temperature are shown in Figure 4-4 as a function of the logarithm of strain-rate. Estimated isotherms have been drawn to visually connect the yield points for a given testing temperature.

Unfortunately, for a given temperature we have only four data points spanning a relatively narrow strain-rate range which makes fitting the flow function (4.56) very difficult. By utilizing the yield stress superposition principle [10, 13], however, we can form a master curve of all 24 data points at a single reference temperature that covers a much wider range of strain rates. To obtain the master curve, the experimental data is shifted along both axes by temperature-dependent shift

[6]This is a non-standard definition of the yield stress for polymeric materials. In most previous studies the yield stress is identified with the yield-peak in the compressive stress-strain curve.

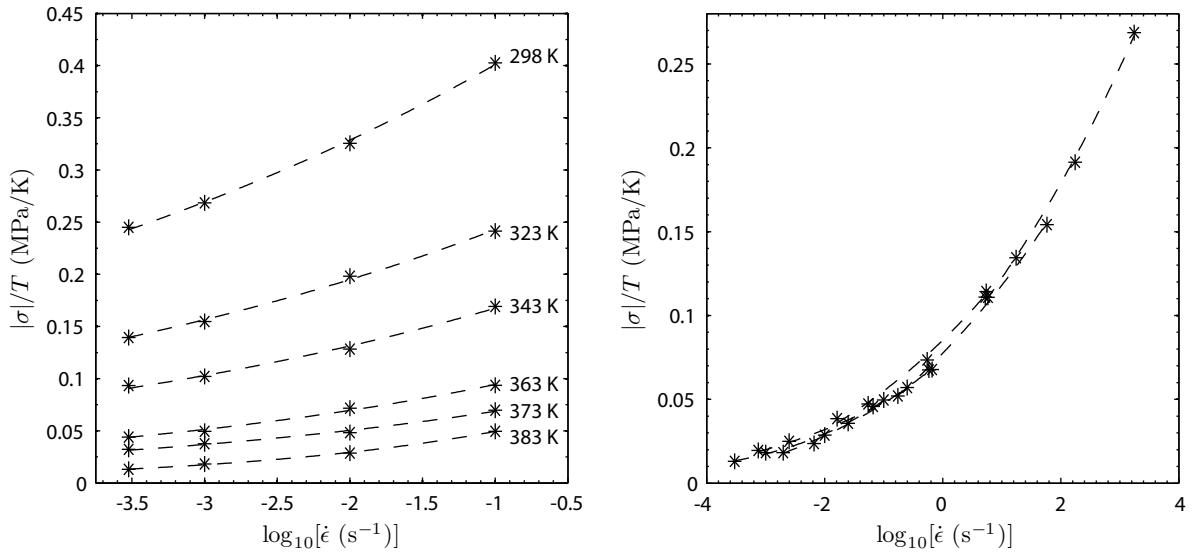

Figure 4-4: Ratio of compressive yield stress to temperature as a function of the logarithm of strain rate. (*) indicates experimental results, (- -) indicates estimated isotherms. The right figure shows the master curve constructed at 383 K from the data in the left figure.

factors that follow a linearized Arrhenius law

$$\left.\begin{aligned} \text{Horizontal shift:} \qquad \Delta(\log_{10}\dot{\epsilon}) &= H\left(\frac{1}{\vartheta}-\frac{1}{\vartheta_{\mathrm{ref}}}\right), \\ \text{Vertical shift:} \qquad \Delta\left(\frac{\sigma_y}{\vartheta}\right) &= B\left(\frac{1}{\vartheta}-\frac{1}{\vartheta_{\mathrm{ref}}}\right), \end{aligned}\right\} \tag{4.60}$$

where ϑ is the temperature of the experiment, ϑ_{ref} is the temperature that the data will be shifted to, and H and B are material parameters. Povolo and Hermida [9] and Richeton et al. [10] reasoned that these shift factors could be equated with the material parameters used in the cooperative model such that

$$\left.\begin{aligned} H &= \frac{\Delta F}{k_B \ln 10}, \\ B &= -r(\vartheta=0) = -r_1\theta_r, \end{aligned}\right\} \tag{4.61}$$

This gives some physical significance to the values of the shift factors that are chosen. We have used Richeton's [10] value of ΔF to establish the H shift factor, and then selected B to match our data; the values are listed in Table 4.2. Figure 4-4 shows the master curve constructed at $\vartheta_{\mathrm{ref}} =$ 383 K using these shift factors.

To complete the fitting of the flow function (4.56) to the master curve, we introduce the assumptions:

- The pressure sensitivity parameter α_p is set equal to 0.353 [14].
- The internal stress r vanishes at the glass transition temperature [11]; that is $\vartheta_r = \vartheta_g$, and $r(\vartheta_g) = 0$.

Table 4.2: PMMA material parameters for yield point calibration below ϑ_g

Parameter	Value
H (s^{-1} K^{-1})	5.7×10^3
B (MPa)	-180
V (m^3)	2.11×10^{-28}
m	0.218
$\dot{\epsilon}_0$ (s^{-1})	1.15×10^{16}
ΔF (kJ mol^{-1})	109
r_1 (MPa K^{-1})	0.47
ϑ_r (K)	383

- The glass transition is assumed to occur at a single temperature independent of both strain-rate and pressure. For the purposes of fitting the yield point, we assume $\vartheta_g = 383$ K.

- The initial value of the isotropic resistance S_i is equal to zero, and the isotropic resistance S does not evolve; that is $\dot{S} = 0$ and $S = S_i = 0$.

Therefore, for a master curve constructed at $\vartheta_{\text{ref}} = \vartheta_g = 383$ K, the internal stress term drops out of the flow function (4.56) resulting in

$$\frac{|\sigma_y|}{\vartheta_g} = \frac{2k_B}{V}\left(1 - \frac{\alpha_p}{3}\right)^{-1} \sinh^{-1}\left[\left(\frac{\dot{\epsilon}}{\dot{\epsilon}^*(\vartheta_g)}\right)^m\right] \tag{4.62}$$

with the list of unknown parameters reduced to: $\{V,\, \dot{\epsilon}^*(\vartheta_g),\, m\}$. A non-linear least-squares fitting method was used in MATLAB to obtain these parameters from the shifted experimental data. Subsequently, by considering (4.57), (4.58), and (4.61), the values of r_1 and $\dot{\epsilon}_0$ are easily determined. The complete set of parameters is listed in Table 4.2. The resulting fit to the 383 K master curve is shown in Figure 4-5 along with the corresponding result for the unshifted experimental data.

Back Stress

Once the yield data has been satisfactorily calibrated, the internal stress $r(\vartheta)$ in the flow function needs to be replaced with the stretch-dependent back stress σ_{back}. To begin, we note that for *compression*

$$D^p = -\dot{\epsilon}^p, \tag{4.63}$$

and we may then rewrite the evolution equation for A (4.55) as

$$\dot{A} = -(2 + \gamma \ln A)\, A\, \dot{\epsilon}^p. \tag{4.64}$$

It follows then that the saturation value of A in *compression* is

$$A^* = \exp\left(-\frac{2}{\gamma}\right). \tag{4.65}$$

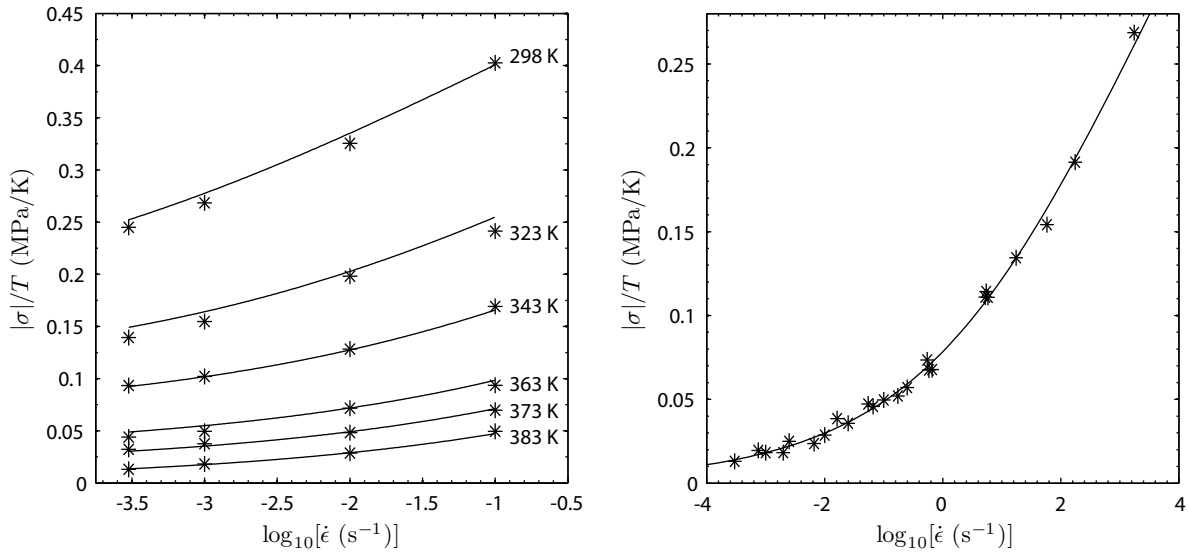

Figure 4-5: Fit of flow function for compressive yield stress normalized by temperature versus strain rate. (*) indicates experimental results, (-) indicates model. Fit of flow function to master curve at 383 K.

Combining this result with the equation for the back stress (4.49) gives the saturation value of the back stress as a function of the material parameters $C(\vartheta)$ and γ

$$\sigma^*_{\text{back}}(\vartheta) = 3\,\frac{C(\vartheta)}{\gamma}\,. \tag{4.66}$$

Equating the back stress saturation value with the internal stress r results in these relations between the back stress parameters and those for the internal stress

$$\left.\begin{aligned} \vartheta_C &= \vartheta_r, \\ \frac{X_C}{\gamma} &= \frac{r_1}{3}\,. \end{aligned}\right\} \tag{4.67}$$

To determine γ, we note that it controls the rate of saturation of the back stress. This is highlighted in Figure 4-6 where the back stress and total stress response are shown with varying values of γ but with a constant ratio of C/γ (and therefore constant σ^*_{back}. As γ increases, the rate of saturation of the back stress increases. Similarly, γ is also related to the viscoelastic response of the material. Therefore, γ should be chosen such that the creep and total stress-strain response of the material is calibrated suitably throughout the temperature range of interest. Since we do not have a complete set of creep data for our entire temperature range, we select (γ = constant) and fit it to room-temperature creep data from Anand and Ames [14] in Figure 4-7 and also choose it such that the unloading curvature at room temperature is suitably fit. The values of all the back stress parameters are shown in Table 4.6.

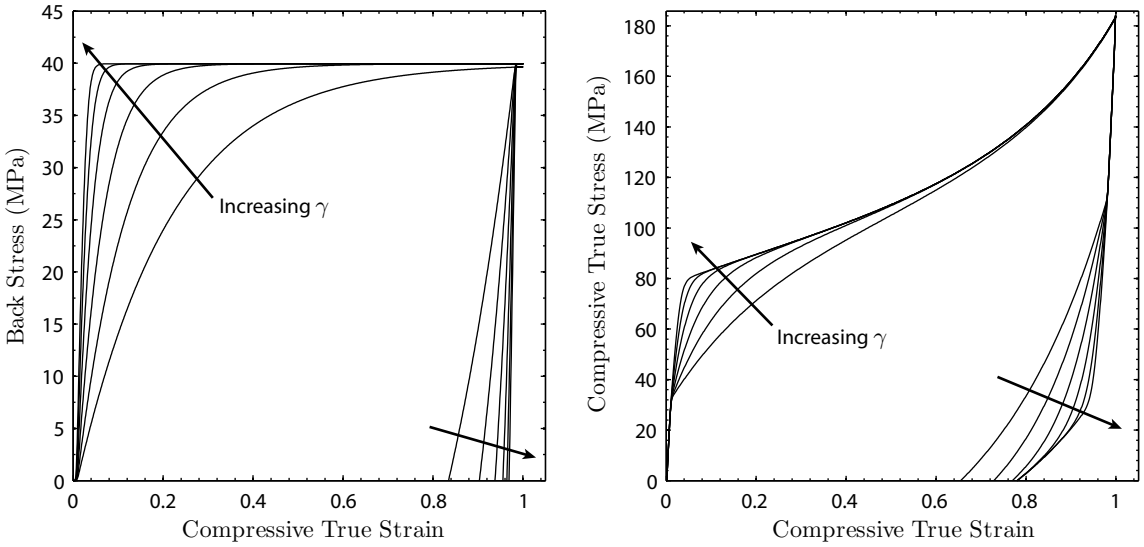

Figure 4-6: Effect of sequentially doubling the the material parameter γ from 5 to 160 on the back stress (left) and complete stress-strain response (right) for a constant ratio of C/γ.

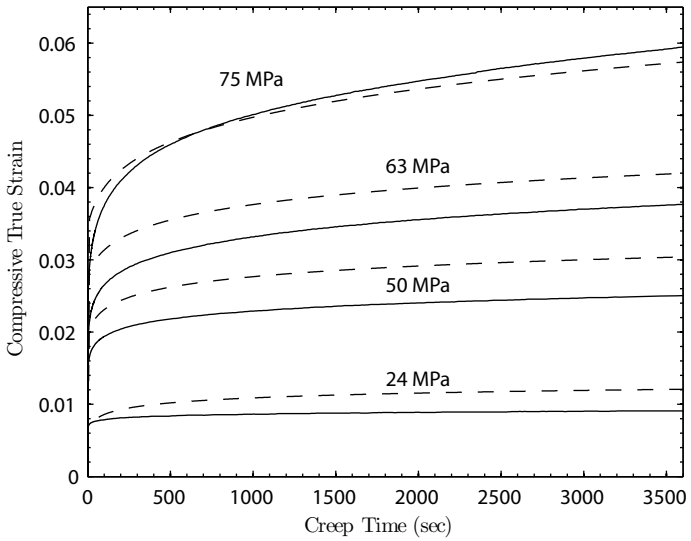

Figure 4-7: One-dimensional MATLAB simulations (- -) and simple compressive creep tests (–) at four pre-yield stress levels.

Elastic Modulus

The elastic modulus is assumed to decrease linearly with temperature and be rate-independent in the temperature range of interest. The initial modulus was estimated from stress-strain data and fit to (4.42). The resulting material parameters are shown in Table 4.6.

Large Strain Behavior

To calibrate the large strain behavior of PMMA, the complete one-dimensional model is implemented in MATLAB with all material parameters that have been determined up to this step. By iterating in MATLAB, values for μ_R and $I_{1,\max}$ are chosen to match the lowest strain-rate data sets (3×10^{-4}/s) throughout the temperature range. To do this, we note that the parameter μ_R controls the initial slope of the post-yield hardening and $I_{1,\max}$ controls the "locking stretch", the stretch at which rapid hardening sets in and the stress appears to go to infinity. The chosen values for μ_R are fit to (4.47) to determine $\mu_{\mathrm{R}}^{\mathrm{ref}}$ and X_μ. It is difficult to estimate $I_{1,\max}$ from our experimental data because our data does not extend to strains that are large enough to observe "locking". We therefore assume a reasonable constant value for $I_{1,\max}$. The resulting material parameters for the large strain behavior are listed in Table 4.6.

The stress-strain curves at this stage of the calibration procedure are shown in Figures 4-8 and 4-9. The fit to room-temperature creep data from Anand and Ames [14] is shown in Figure 4-7. For the lower strain-rates of 3×10^{-4}/s and 10^{-3}/s, the simulations correlate with the experimental data very well. However, for the higher strain-rates of 10^{-2}/s and 10^{-1}/s, there is an excessive discrepancy in the large strain behavior between the experiments and simulations. This discrepancy is caused by thermal softening in the material due to inelastic dissipation, and at this point we are using an isothermal version of the model that does not account for internal heating. Later, in Section 4.3.3, we add thermo-mechanical coupling to the model in order to capture the internal heating effect.

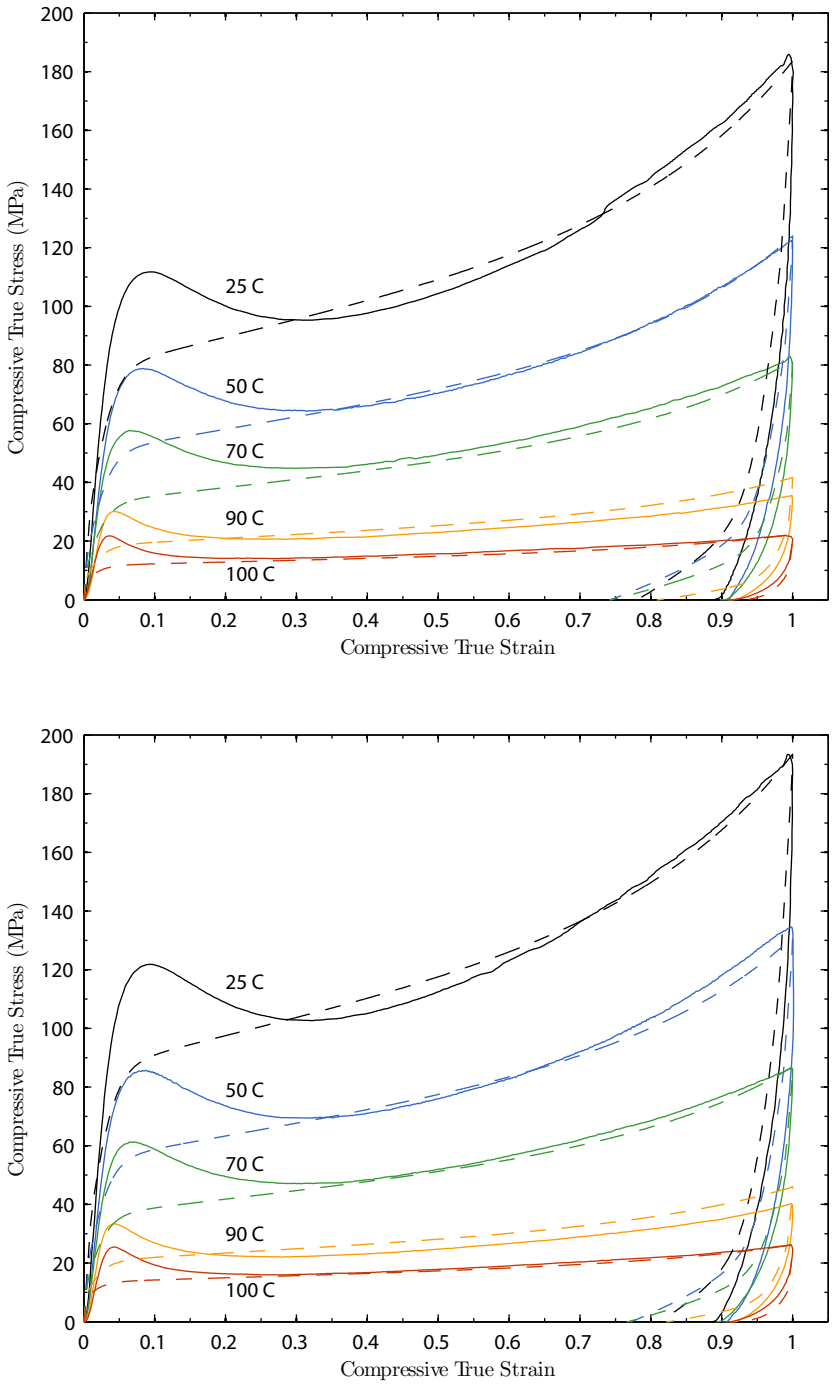

Figure 4-8: One-dimensional MATLAB simulations (- -) and simple compression tests (–) at strain-rates of 3×10^{-4}/s (top) and 10^{-3}/s (bottom) at temperatures ranging from room temperature through 100 C. Simulation excludes yield-peak ($\dot{S}=0$).

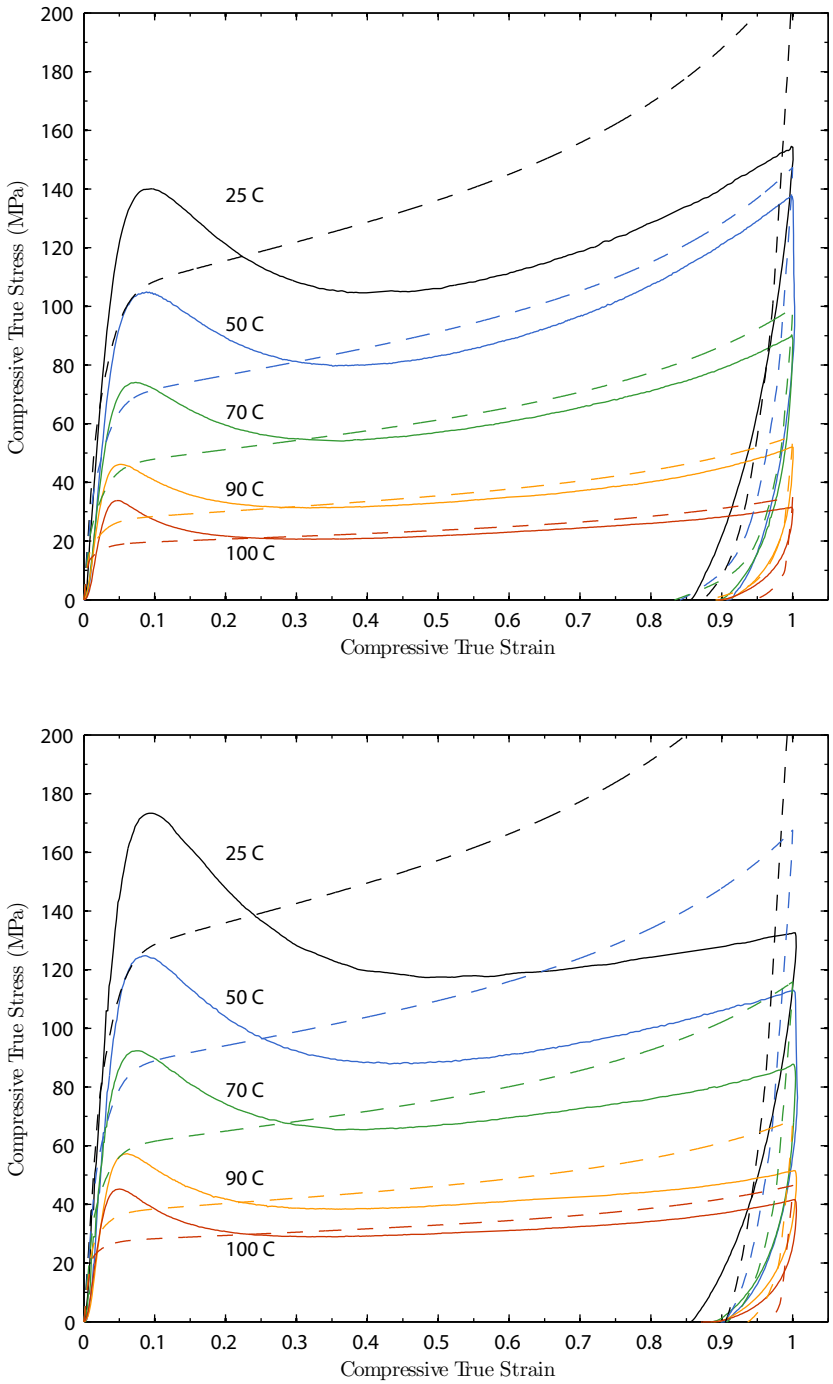

Figure 4-9: One-dimensional MATLAB simulations (- -) and simple compression tests (–) at strain-rates of 10^{-2}/s (top) and 10^{-1}/s (bottom) at temperatures ranging from room temperature through 100 C. Simulation excludes yield-peak ($\dot{S} = 0$).

Yield Peak

To calibrate the yield peak, we must determine the list of parameters which guide the evolution of S and φ: $\{\varphi_i, \varphi^*, S_i, b, g, h\}$.

Below the glass-transition we assume the free volume parameters to be $\varphi_i = 0$ and $\varphi^* = 0.001$. While these values should depend on strain-rate and temperature, we do not have the appropriate data to be specific about any such dependencies. Further, we assume the initial value of the isotropic resistance to be $S_i = 0$.

To find $\{b, g, h\}$, several simulations are performed using different values of these parameters to obtain the correct shape of the yield peak at the various strain-rates and temperatures. In order to aid the iterative curve-fitting procedure, Figure 4-10 can be used as a guide to illustrate how these parameters affect the shape of the yield-peak. Once $\{b, g, h\}$ are determined for each stress-strain curve, they were found to match the functional forms given in (4.54); the parameters for these functions are listed in Table 4.6. The final stress-strain curves using the one-dimensional model in MATLAB including the yield peak calibration are shown in Figures 4-11 and 4-12.

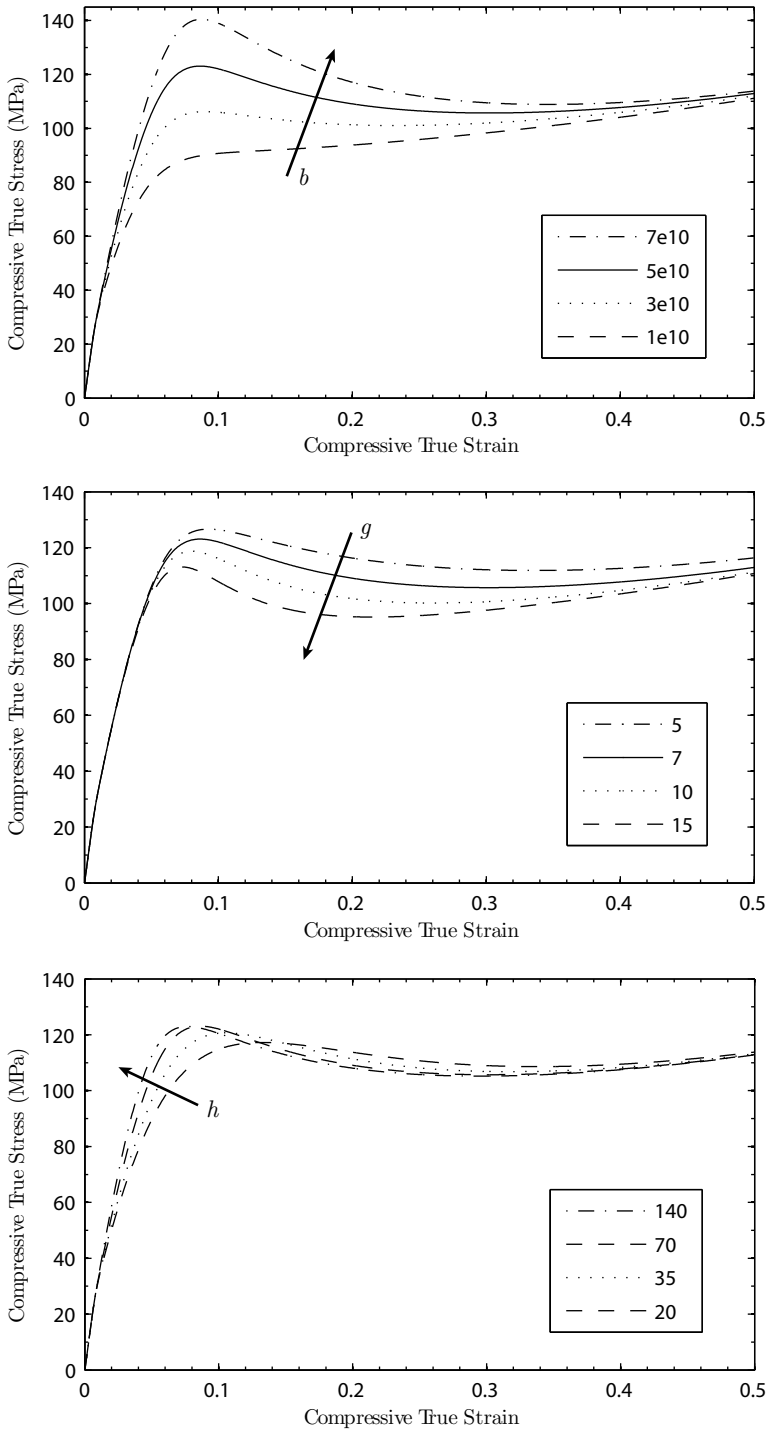

Figure 4-10: Schematic of the effect of the material parameters $\{b,\ g,\ h\}$ on the shape of the yield peak of the stress-strain curve. Arrows indicate an increase of the parameter: (top) b, (middle) g, (bottom) h.

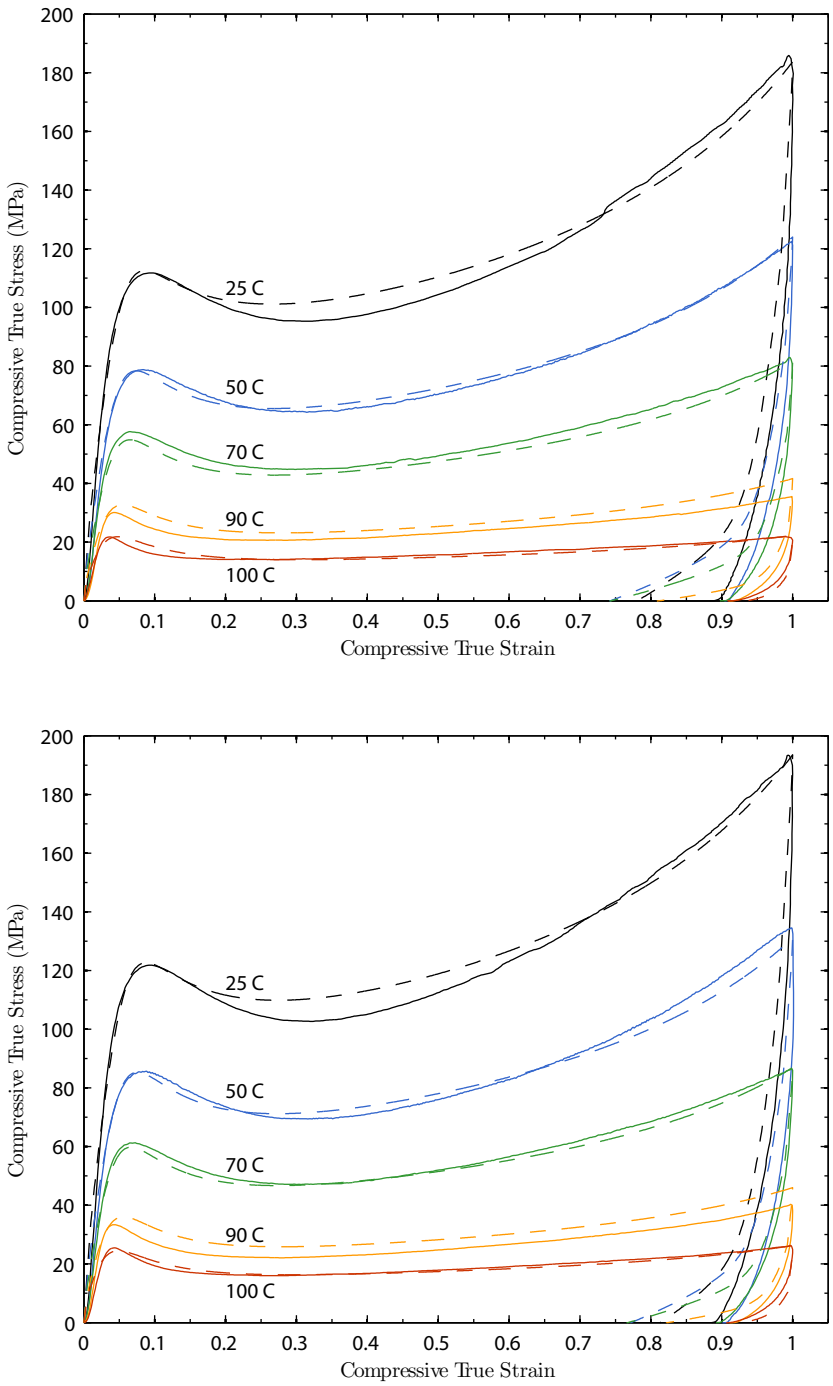

Figure 4-11: One-dimensional MATLAB simulations (- -) and simple compression tests (–) at strain-rates of 3×10^{-4}/s (top) and 10^{-3}/s (bottom) at temperatures ranging from room temperature through 100 C.

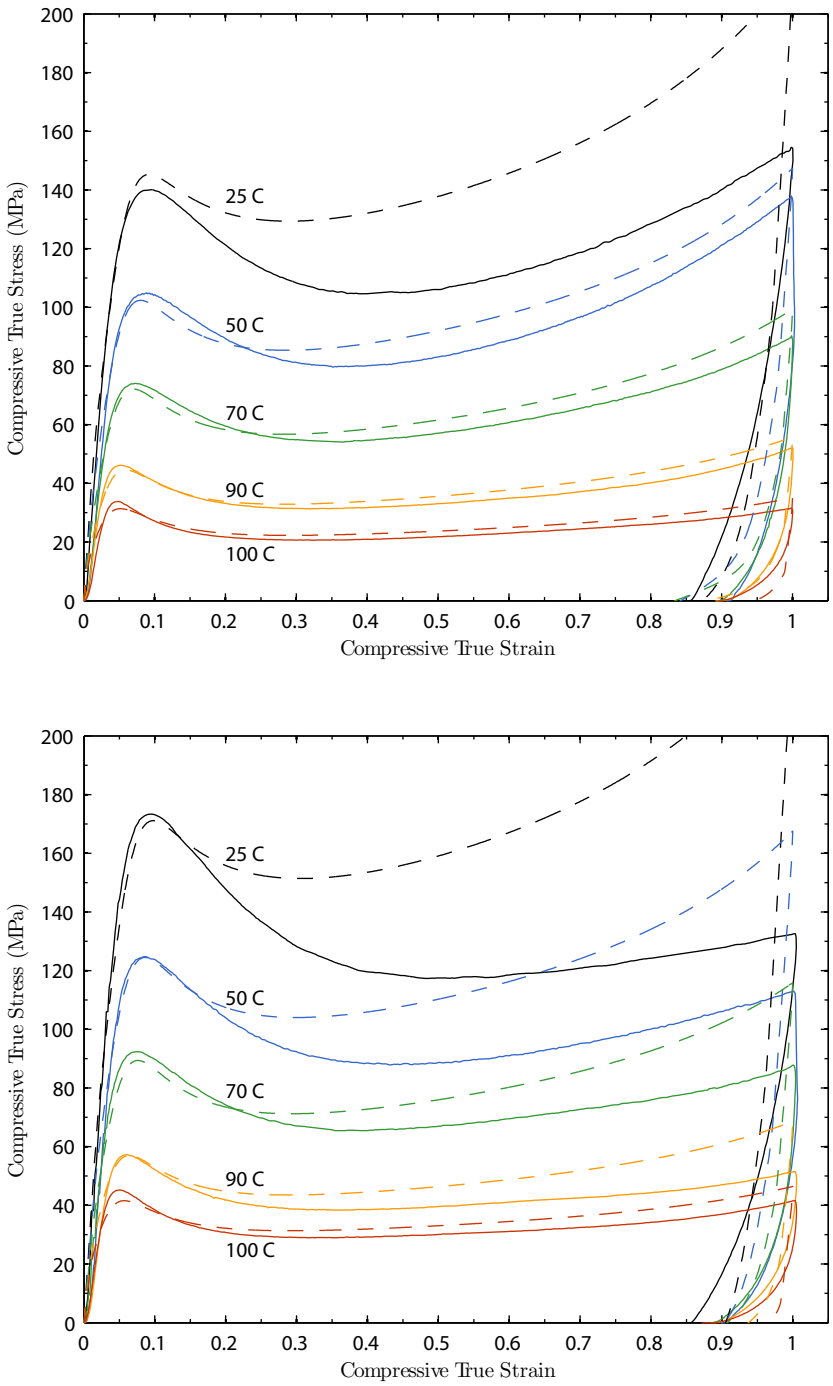

Figure 4-12: One-dimensional MATLAB simulations (- -) and simple compression tests (–) at strain-rates of 10^{-2}/s (top) and 10^{-1}/s (bottom) at temperatures ranging from room temperature through 100 C.

4.3.2 Three-Dimensional Model Calibration Procedure

Except for the list of parameters $\{\alpha_p,\ \nu_0,\ V,\ S_i,\ b,\ g,\ h,\ \gamma\}$, the values of the one-dimensional material parameters are unchanged when used in the three-dimensional equations. Noting that

$$\tau\nu = \sigma\dot{\epsilon}, \quad \sigma = \sqrt{3}\tau, \quad \dot{\epsilon} = \frac{\nu}{\sqrt{3}} \tag{4.68}$$

the list of parameters $\{\alpha_p, \nu_0, V, S_i, b, g, h, \gamma\}$ may be converted from the one-dimensional tension form to the three-dimensional shear form using

$$\left.\begin{aligned} \dot{\epsilon}_0 &= \tfrac{1}{\sqrt{3}}\,\nu_0\,, \\ \alpha_p^{\text{tension}} &= \sqrt{3}\,\alpha_p^{\text{shear}}\,, \\ S_i^{\text{tension}} &= \sqrt{3}\,S_i^{\text{shear}}\,, \\ V^{\text{tension}} &= \tfrac{1}{\sqrt{3}}\,V^{\text{shear}}\,, \\ b_1^{\text{tension}} &= \sqrt{3}\,b_1^{\text{shear}}\,, \\ g_1^{\text{tension}} &= \sqrt{3}\,g_1^{\text{shear}}\,, \\ g_2^{\text{tension}} &= \sqrt{3}\,g_2^{\text{shear}}\,, \\ h^{\text{tension}} &= \sqrt{3}\,h^{\text{shear}}\,, \\ \gamma^{\text{tension}} &= \sqrt{3}\,\gamma^{\text{shear}}\,. \end{aligned}\right\} \tag{4.69}$$

Further, assuming a value of $\nu_{\text{poi}} = 0.35$ as Poisson's ratio, we may use the standard relations for converting the elastic modulus E to the shear and bulk moduli (G, K).

Figure 4-13 shows the results of using these conversion factors with the parameters determined from the one-dimensional calibration procedure. We see that the three-dimensional single-element result from ABAQUS/Explicit agrees fairly well with the one-dimensional MATLAB results. A slight adjustment of $\mu_{\text{R}}^{\text{ref}}$ in ABAQUS brings the simulations into even closer agreement. The final stress-strain curves from the ABAQUS calculations are shown in Figures 4-14 and 4-15. The complete list of material parameters used in the ABAQUS calculations is in Table 4.7.

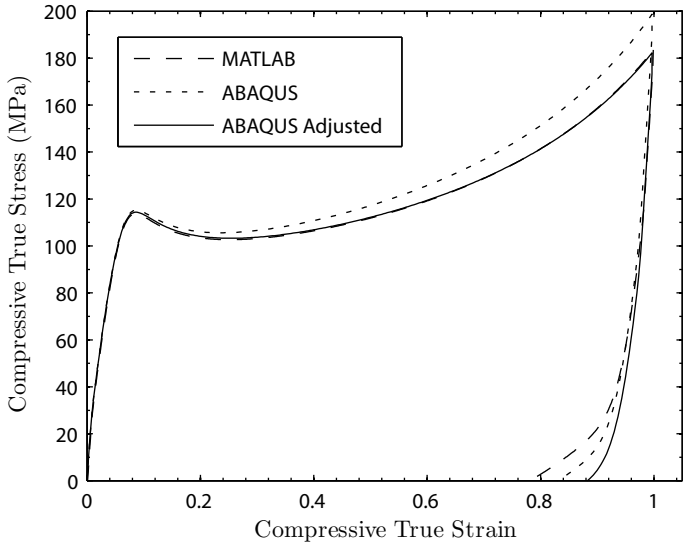

Figure 4-13: Comparison of one-dimensional MATLAB simulation (- -) to three-dimensional one-element ABAQUS simulation ($\cdots$) with material parameter conversion between the two models using only the relations in (4.69). Further adjustment of $\mu_{\mathrm{R}}^{\mathrm{ref}}$ and X_μ in ABAQUS (–) gives an even better match to the MATLAB results.

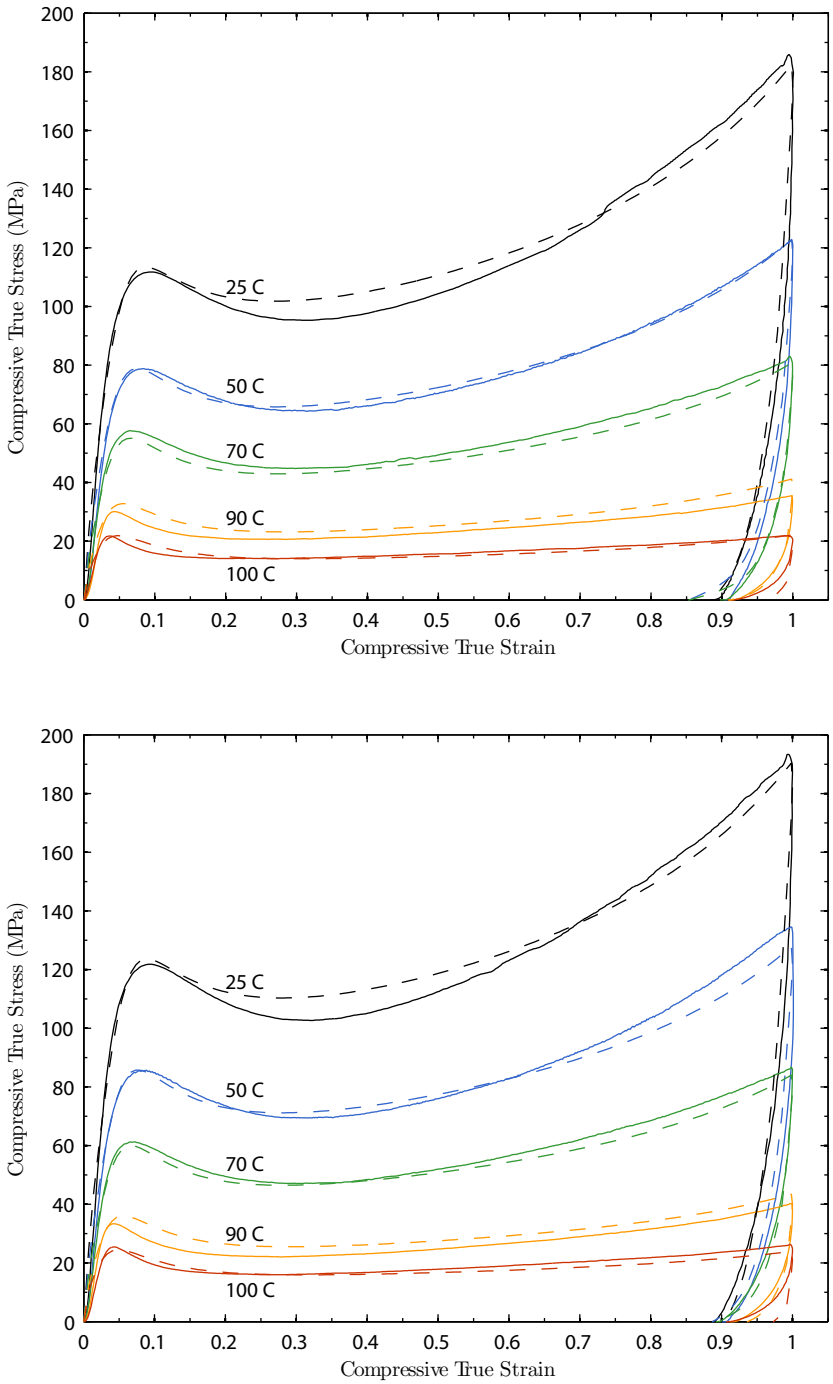

Figure 4-14: Three-dimensional one-element isothermal ABAQUS simulations (- -) and simple compression tests (–) at strain-rates of 3×10^{-4}/s (top) and 10^{-3}/s (bottom) at temperatures ranging from room temperature through 100 C.

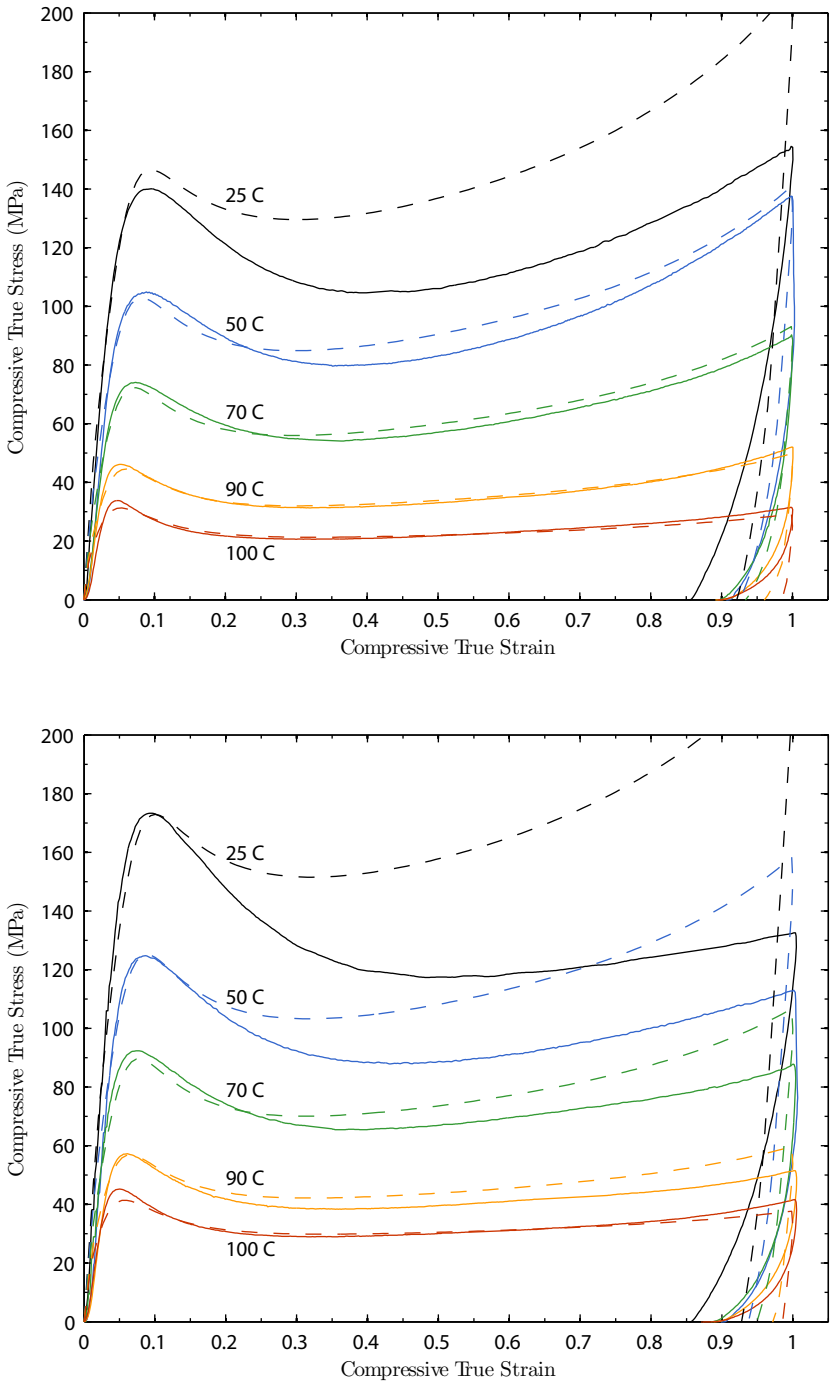

Figure 4-15: Three-dimensional one-element isothermal ABAQUS simulations (- -) and simple compression tests (–) at strain-rates of 10^{-2}/s (top) and 10^{-1}/s (bottom) at temperatures ranging from room temperature through 100 C.

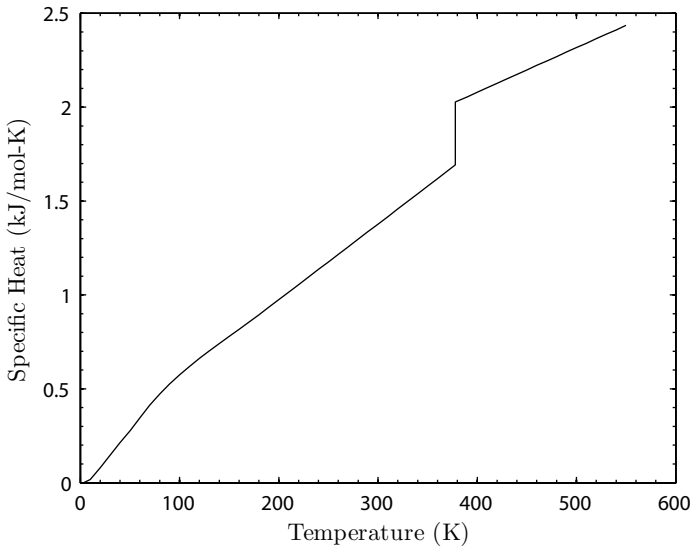

Figure 4-16: Specific heat of PMMA versus temperature. Reproduced from Gaur et al. [16]

4.3.3 Internal Heating

While the model works very well for the low strain-rates where the material behaves nearly isothermally (cf. Figure 4-14), there is a large discrepancy between the model and experiment at the higher strain rates of 10^{-2}/s and 10^{-1}/s (cf. Figure 4-15). This discrepancy is due to the thermal softening of the material caused by inelastic dissipation coupled with the low thermal diffusivity of PMMA [15]. In order to capture this internal heating, we must introduce a thermo-mechanical coupling in our finite element implementation using the heat equation of (4.37)

$$c\dot{\vartheta} = -\mathrm{Div}\,\mathbf{q}_{\mathrm{R}} + q_{\mathrm{R}} + \beta\left(\bar{\tau}^{(1)}\,\nu^{p} + \frac{1}{2}\,C\,\gamma\,|\ln\mathbf{A}|^{2}\right) \tag{4.70}$$

where the factor β is the fraction of inelastic work that is dissipated. To complete thermo-mechanical coupling, we must also specify two additional material parameters: the specific heat c, and the thermal conductivity κ. The temperature dependence of these parameters is taken from the literature [16, 17] and reproduced in Figures 5-27 and 5-28 respectively.

Multi-Element Model

In order to accurately predict the temperature rise for intermediate strain-rates where isothermal or adiabatic approximations do not suffice, we must setup a realistic finite element model of our experimental apparatus that includes thermal interactions between the specimen and its environment [15]. Because our specimens are cylindrical, we have chosen to model the compression experiment as an axisymmetric problem with additional symmetry about the horizontal axis. A schematic of this model is shown in Figure 4-18. For the steel platen, we assume a basic thermoelastic material model whose material parameters are listed in Table 4.3. For the surface film coefficient between the specimen sidewall and air, we assume $h_1 = 40$ (W/m^2-K). We create a heat sink on the top

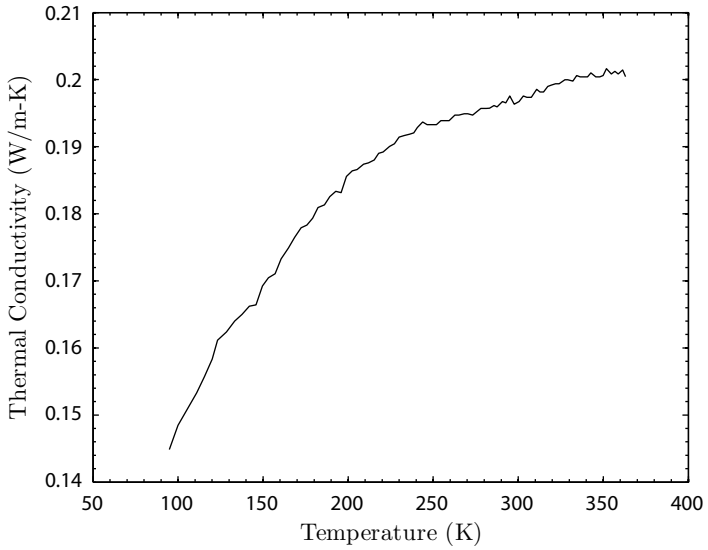

Figure 4-17: Thermal conductivity of PMMA versus temperature. Reproduced from Eiermann and Hellwege [17]

Table 4.3: Steel material parameters for thermo-mechanically coupled three-dimensional model

Parameter	Value
Young's Modulus, E (GPa)	200
Poisson's Ratio, ν	0.3
Density, ρ (kg m^{-3})	7833
Thermal Conductivity, κ (W m^{-1} K^{-1})	52
Specific Heat, c (J kg^{-1} K^{-1})	586

of the steel platen by fixing the nodes at the ambient temperature T_∞. At the interface between the PMMA specimen and the steel platen we assume frictionless contact. To assure excellent heat transfer at this interface, we use a thermal conductance of $k = 1000$ (W/m^2-K). The ambient temperature of each simulation T_∞ is initially constant throughout the specimen and platen. A true strain-rate velocity profile is applied to the top surface of the steel platen to impose deformation on the specimen.

The final stress-strain curves using this multi-element fully coupled calculation are shown in Figures 4-19 and 4-20 for the various strain-rates and temperatures using a factor of $\beta = 0.8$ in the heat equation of (4.70).

Figure 4-21 shows the contours of nodal temperature rise at a strain of -1.0 for the room temperature (25 C) multi-element fully-coupled ABAQUS simulation at a strain-rate of 10^{-1}/s. As others have shown, there is a large gradient in temperature throughout the height and diameter of the specimen. Figure 4-22 shows experimental measurements of surface temperature rise from Mulliken [18] under a test of similar conditions compared with surface midpoint temperature measurements from our simulations. While the results do not match perfectly, the general trend of the experiments does seem to be well reproduced in the simulation, namely a large temperature

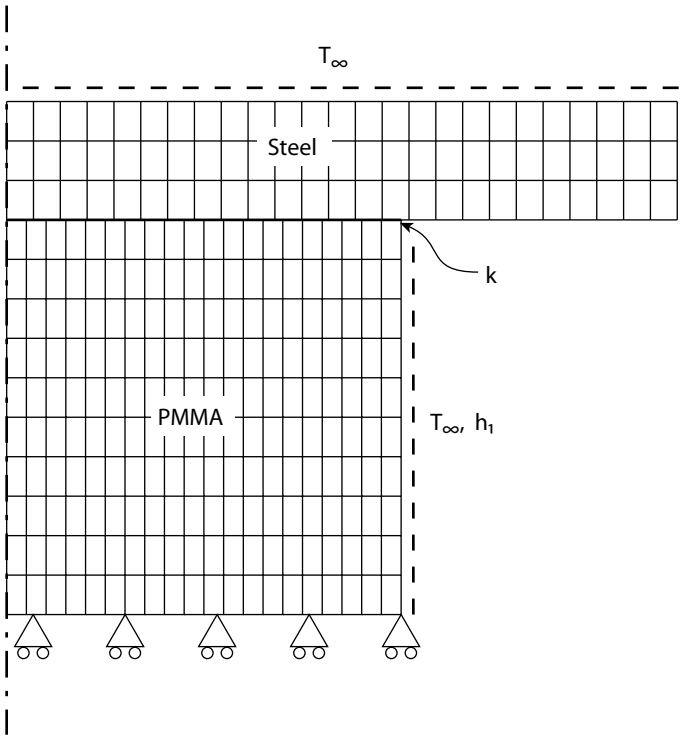

Figure 4-18: Axisymmetric finite element geometry for thermo-mechanically coupled compression simulations.

rise for the high-rate nearly adiabatic case and a negligible temperature rise for the low-rate nearly isothermal case. Arruda et al. [15] saw similar results for their experiments and simulations.

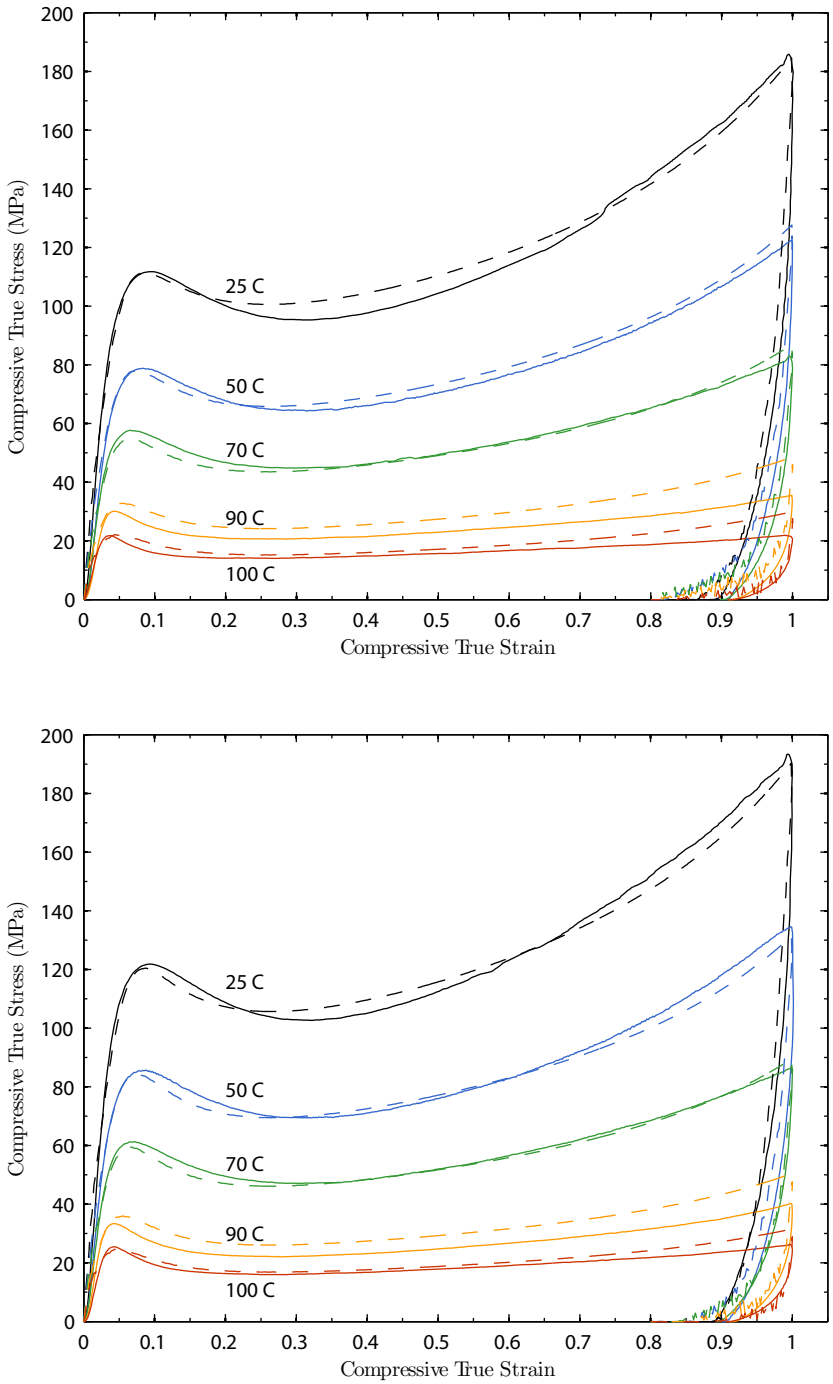

Figure 4-19: Three-dimensional multi-element full-coupled ABAQUS simulations (- -) and simple compression tests (–) at strain-rates of 3×10^{-4}/s (top) and 10^{-3}/s (bottom) at temperatures ranging from room temperature through 100 C. A factor of $\beta = 0.8$ is used in the heat equation of (4.70).

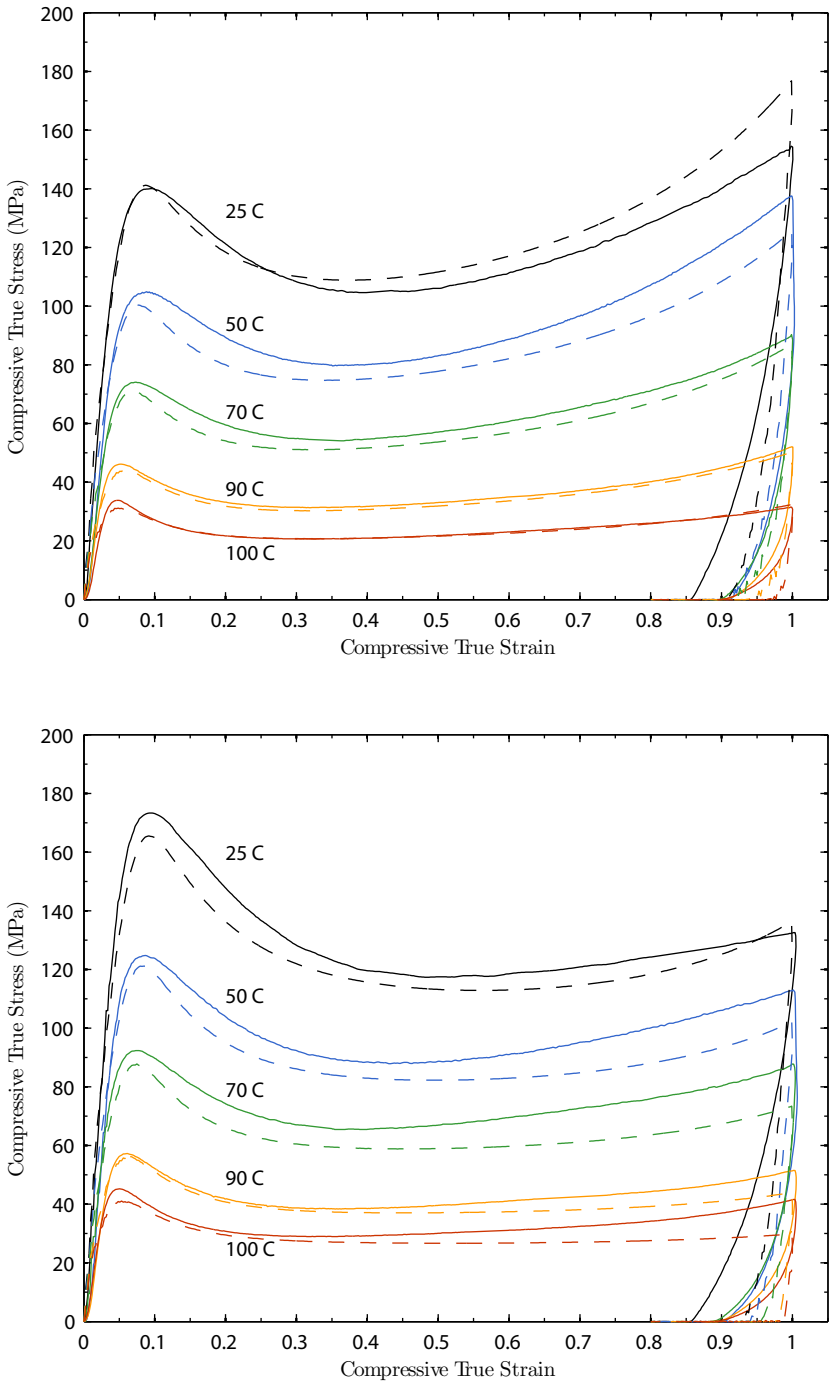

Figure 4-20: Three-dimensional multi-element fully-coupled ABAQUS simulations (- -) and simple compression tests (–) at strain-rates of 10^{-2}/s (top) and 10^{-1}/s (bottom) at temperatures ranging from room temperature through 100 C. A factor of $\beta = 0.8$ is used in the heat equation of (4.70).

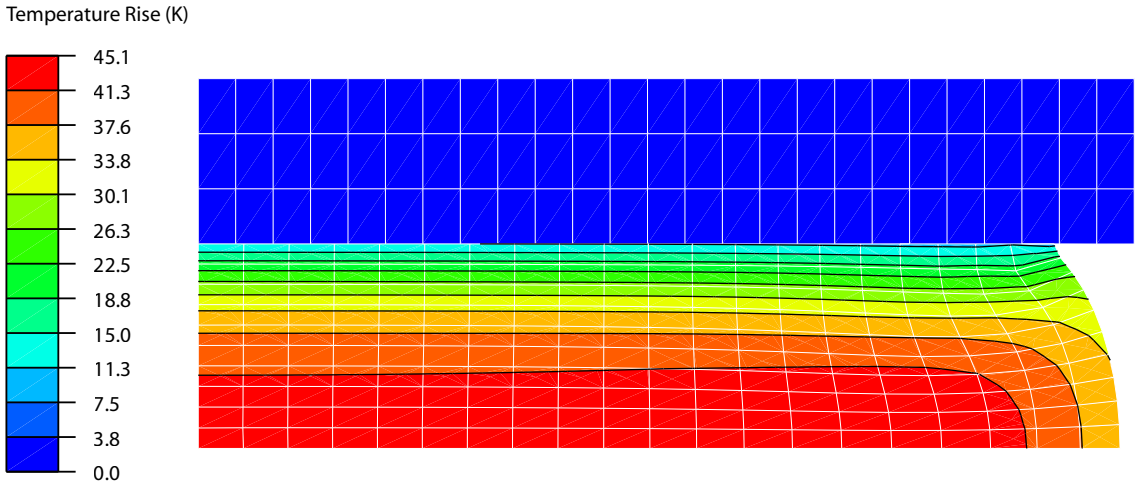

Figure 4-21: Contours of nodal temperature rise at a strain of -1.0 for the room temperature (25 C) multi-element fully-coupled ABAQUS simulation at a strain-rate of $10^{-1}/\text{s}$.

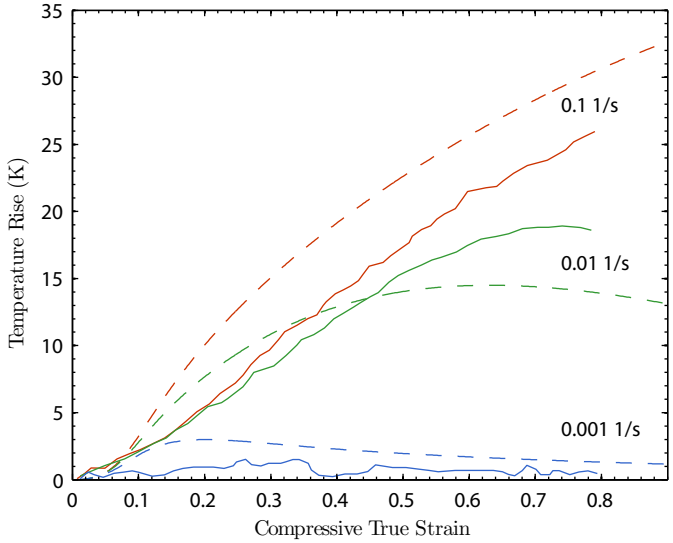

Figure 4-22: ABAQUS surface midpoint temperature measurements (- -) for three strain rates at room temperature. Experimental data is from Mulliken [18] for a similarly sized specimen.

4.4 Summary of Equations and Parameters

The equations and associated parameters for the one-dimensional and full three-dimensional constitutive theory are briefly summarized here for convenience. For a more detailed summary, refer to Section 4.2.

Table 4.4: Summary of the the one-dimensional equations

Term	Description
$\sigma = \sigma^{e\,(1)} + \sigma^{e\,(2)}$	Total stress
$\sigma^{e\,(1)} = E\,\epsilon^e = E\,(\epsilon - \epsilon^p)$	Elastic stress in $\alpha = 1$
$E = E^{\mathrm{ref}} - X_E(\vartheta - \vartheta_*)$	Modulus temperature dependence
$\sigma_{\mathrm{back}} = \frac{3}{2}\,C\,\ln A$	Backstress in $\alpha = 1$
$C = \begin{cases} X_C(\vartheta_C - \vartheta) & : \vartheta \le \vartheta_C \\ 0 & : \vartheta > \vartheta_C \end{cases}$	Modulus temperature dependence
$\dot{A} = 2\,D^p A - \gamma A \ln A\,\dot{\epsilon}^p, \qquad A(0) = 1$	Backstress stretch evolution
$\sigma^{e(2)} = \mu_{\mathrm{R}} \left(1 - \dfrac{I_1 - 3}{I_{1,\max}}\right)^{-1} \left(U^2 - U^{-1}\right)$	Stress in $\alpha = 2$
$\mu_{\mathrm{R}}(\vartheta) = \mu_{\mathrm{R}}^{\mathrm{ref}} - X_\mu(\vartheta - \vartheta_*)$	Modulus temperature dependence
$\dot{\epsilon}^p = \dot{\epsilon}_0 \exp\left(-\dfrac{\Delta F}{k_B \vartheta}\right) \left[\sinh\left(\dfrac{\bar{\sigma} V}{2\,k_B \vartheta}\right)\right]^{1/m}$	Flow rule
$\bar{\sigma} = \lvert\sigma^{e\,(1)} - \sigma_{\mathrm{back}}\rvert - S - \alpha_p\,\bar{p}$	Driving stress
$\bar{p} = -\frac{1}{3}\,\sigma^{e(1)}$	Pressure
$\dot{\varphi} = g\,(\varphi^* - \varphi)\,\dot{\epsilon}^p, \qquad \varphi(0) = \varphi_i > 0$	Free volume evolution
$\dot{S} = h\,(S^* - S)\,\dot{\epsilon}^p, \qquad S(0) = S_i \ge 0$	Isotropic resistance evolution
$S^* = S_i + b\,(\varphi^* - \varphi)$	Saturation value of S
$g = g_1 + g_2 \vartheta$	Temperature dependence of g
$b = b_1\,\left(\vartheta^2 + b_2 \vartheta + b_3\right) \left(\dfrac{\dot{\epsilon}^p}{\dot{\epsilon}_{\mathrm{ref}}}\right)^{b_4}$	Temperature and rate dependence of b

Table 4.5: Summary of the the three-dimensional equations

Term	Description
$\mathbf{T} = \mathbf{T}^{e\,(1)} + \mathbf{T}^{e\,(2)}$	Total Cauchy stress
$\mathbf{T}^{e\,(1)} = J^{-1}\mathbf{R}^{e}\,\mathbf{M}^{e\,(1)}\,\mathbf{R}^{e\top}$	Cauchy stress for $\alpha = 1$
$\mathbf{T}^{e\,(2)} = J^{-1}\mathbf{R}\,\mathbf{M}^{e\,(2)}\,\mathbf{R}^{\top}$	Cauchy stress for $\alpha = 2$
$\mathbf{M}^{e(1)} = 2G\mathbf{E}^{e}_{0} + K\left\{\mathrm{tr}\,\mathbf{E}^{e} - 3\,\alpha^{\mathrm{th}}\,(\vartheta - \vartheta_0)\right\}\mathbf{1}$	Mandel stress for $\alpha = 1$
$G = G^{\mathrm{ref}} - X_G(\vartheta - \vartheta_*)$	Modulus temperature dependence
$\mathbf{M}_{\mathrm{back}} = C\ln\mathbf{A}$	Backstress for $\alpha = 1$
$C = \begin{cases} -X_C(\vartheta - \vartheta_C) & : \vartheta \le \vartheta_C \\ 0 & : \vartheta > \vartheta_C \end{cases}$	Modulus temperature dependence
$\dot{\mathbf{A}} = \mathbf{D}^{p}\mathbf{A} + \mathbf{A}\mathbf{D}^{p} - \gamma\,\mathbf{A}\ln\mathbf{A}\,\nu^{p}, \qquad \mathbf{A}(\mathbf{X},0) = \mathbf{1}$	Backstress stretch evolution
$\mathbf{M}^{e(2)} = \mu_{\mathrm{R}}\left(1 - \dfrac{I_1 - 3}{I_{1,\max}}\right)^{-1}(\mathbf{C}_{\mathrm{dis}})_0$	Mandel stress for $\alpha = 2$
$\mu_{\mathrm{R}}(\vartheta) = \mu_{\mathrm{R}}^{\mathrm{ref}} - X_\mu(\vartheta - \vartheta_*)$	Modulus temperature dependence
$\nu^{p} = \nu_0\,\exp\left\{-\dfrac{\Delta F}{k_B\,\vartheta}\right\}\left[\sinh\left(\dfrac{\bar{\tau}_{\mathrm{e}}^{(1)}\,V}{2k_B\vartheta}\right)\right]^{1/m}$	Flow rule
$\bar{p} = -\frac{1}{3}\mathrm{tr}\,\mathbf{M}^{e\,(1)}$	Pressure
$\mathbf{M}^{e\,(1)}_{\mathrm{eff}} = \mathbf{M}^{e\,(1)} - \mathbf{M}_{\mathrm{back}}$	Driving stress
$\bar{\tau} = \frac{1}{\sqrt{2}}\,\lvert(\mathbf{M}^{e\,(1)}_{\mathrm{eff}})_0\rvert$	Equivalent shear stress
$\bar{\tau}_{\mathrm{e}}^{(1)} = \bar{\tau} - S - \alpha_p\,\bar{p}$	Effective shear stress
$\dot{\varphi} = g\,(\varphi^{*} - \varphi)\,\nu^{p}, \qquad \varphi(\mathbf{X},0) = \varphi_i > 0$	Free volume evolution
$\dot{S} = h\,(S^{*} - S)\,\nu^{p}, \qquad S(\mathbf{X},0) = S_i \ge 0$	Activation volume evolution
$S^{*} = S_i + b\,(\varphi^{*} - \varphi)$	Saturation value of S
$g = g_1 + g_2\vartheta$	Temperature dependence of g
$b = b_1\,\left(\vartheta^2 + b_2\vartheta + b_3\right)\,\left(\dfrac{\nu^{p}}{\nu_{\mathrm{ref}}}\right)^{b_4}$	Temperature and rate dependence of b

Table 4.6: PMMA material parameters for one-dimensional model

Parameter	Value
ρ (kg m^{-3})	1200
$\dot{\epsilon}_{\mathrm{ref}}$ (s^{-1})	3×10^{-4}
${\vartheta^{\mathrm{ref}}}_*$ (K)	298
C_{1g}	11
C_{2g} (K)	36
E^{ref} (GPa)	3.5
X_E (MPa K^{-1})	20
$\mu_{\mathrm{R}}^{\mathrm{ref}}$ (MPa)	23
X_μ (MPa K^{-1})	0.26
$I_{1,\max}$	5.5
X_C (MPa K^{-1})	9.4
ϑ_C (K)	383
γ	60
V (m^3)	2.11×10^{-28}
m	0.218
$\dot{\epsilon}_0$ (s^{-1})	1.15×10^{16}
ΔF (kJ mol^{-1})	109
α_p	0.353
φ_i	0
φ^*	0.001
S_i	0
b_1 (Pa K^{-2})	-3.16×10^6
b_2 (K)	-562
b_3 (K^2)	6.62×10^4
b_4	0.054
g_1	-8.52
g_2 (K^{-1})	5.48×10^{-2}
h (s)	70

Table 4.7: PMMA material parameters for three-dimensional model

Parameter	Value
ρ (kg m^{-3})	1200
ν_{ref} (s^{-1})	5×10^{-4}
${\vartheta^{\mathrm{ref}}}_*$ (K)	298
C_{1g}	11
C_{2g} (K)	36
G^{ref} (GPa)	1.3
X_G (MPa K^{-1})	7.4
K (GPa)	3.9
α^{th} (K^{-1})	7×10^{-5}
$\mu_{\mathrm{R}}^{\mathrm{ref}}$ (MPa)	20
X_μ (MPa K^{-1})	0.22
$I_{1,\max}$	5.5
X_C (MPa K^{-1})	9.4
ϑ_C (K)	383
γ	34.64
V (m^3)	3.65×10^{-28}
m	0.218
ν_0 (s^{-1})	2×10^{16}
ΔF (kJ mol^{-1})	109
α_p	0.204
φ_i	0
φ^*	0.001
S_i (Pa)	0
b_1 (Pa K^{-2})	-1.82×10^6
b_2 (K)	-562
b_3 (K^2)	6.62×10^4
b_4	0.054
g_1	-4.92
g_2 (K^{-1})	3.16×10^{-2}
h (s)	40.4

Bibliography

[1] C. P. Buckley and D. C. Jones. Glass-rubber constituitive model for amorphous polymers near the glass transition. *Polymer*, 36:3301–3312, 1995. doi: 10.1016/0032-3861(95)99429-X.

[2] P. J. Dooling, C. P. Buckley, S. Rostami, and N. Zahlan. Hot-drawing of poly(methylmethacrylate) and simulation using a glass-rubber constitutive model. *Polymer*, 43:2451–2465, 2002. doi: 10.1016/S0032-3861(01)00799-6.

[3] M. C. Boyce, S. Socrate, and P. G. Llana. Constitutive model for the finite deformation stress strain behavior of poly(ethylene terephthalate) above the glass transition. *Polymer*, 41: 2183–2201, 2000. doi: 10.1016/S0032-3861(99)00406-1.

[4] R. B. Dupaix and M. C. Boyce. Constitutive modeling of the finite strain behavior of amorphous polymers in and above the glass transition. *Mechanics of Materials*, 39:39–52, 2007. doi: 10.1016/j.mechmat.2006.02.006.

[5] J. Richeton, G. Schlatter, K. S. Vecchio, Y. Rémond, and S. Ahzi. A unified model for stiffness modulus of amorphous polymers across transition temperatures and strain rates. *Polymer*, 46: 8194–8201, 2006. doi: 10.1016/j.polymer.2005.06.103.

[6] J. Richeton, S. Ahzi, K. S. Vecchio, F. C. Jiang, and R. R. Adharapurapu. Influence of temperature and strain rate on the mechanical behavior of three amorphous polymers: Characterization and modeling of the compressive yield stress. *InternationalJournal of Solids and Structures*, 43:2318–2335, 2006. doi: 10.1016/j.ijsolstr.2005.06.040.

[7] J. D. Ferry. *Viscoelastic properties of polymers*. Wiley, New York, 3rd edition, 1980.

[8] D. G. Fotheringham, B. W. Cherry, and C. Bauwens-Crowet. Comment on "the compression yield behaviour of polymethyl methacrylate over a wide range of temperatures and strain-rates". *Journal of Materials Science*, 11:1368–1371, 1976. doi: 10.1007/BF00545162.

[9] F. Povolo and E. B. Hermida. Phenomenlogical description of strain rate and temperature-dependent yield stress of pmma. *Journal of Applied Polymer Science*, 58:55–68, 1995. doi: 10.1002/app.1995.070580106.

[10] J. Richeton, S. Ahzi, L. Daridon, and Y. Rémond. A formulation of the cooperative model for the yield stress of amorphous polymers for a wide range of strain rates and temperatures. *Polymer*, 46:6035–6043, 2005. doi: 10.1016/j.polymer.2005.05.079.

[11] D. G. Fotheringham and B. W. Cherry. The role of recovery forces in the deformation of linear polyethylene. *Journal of Materials Science*, 13:951–964, 1978. doi: 10.1007/BF00544690.

[12] A. N. Gent. A new constitutive relation for rubber. *Rubber Chemistry and Technology*, 69: 59–61, 1996.

[13] C. Bauwens-Crowet, J. C. Bauwens, and G. Homés. Tensile yield-stress behavior of glassy polymers. *Journal of Polymer Science: Part A-2*, 7:735–742, 1969. doi: 10.1002/pol.1969.160070411.

[14] L. Anand and N. M. Ames. On modeling the micro-indentation response of an amorphous polymer. *International Journal of Plasticity*, 22:1123–1170, 2006. doi: 10.1016/j.ijplas.2005.07.006.

[15] E. M. Arruda, M. C. Boyce, and R. Jayachandran. Effects of strain rate, temperature and thermomechanical coupling on the finite strain deformation of glassy polymers. *Mechanics of Materials*, 19:193–212, 1995. doi: 10.1016/0167-6636(94)00034-E.

[16] U. Gaur, S.-F. Lau, B. B. Wunderlich, and B. Wunderlich. Heat capacity and other thermodynamic properties of linear macromolecules. vi. acrylic polymers. *Journal of Physical and Chemical Reference Data*, 11:1065–1089, 1982.

[17] K. Eiermann and K.-H. Hellwege. Thermal conductivity of high polymers from -180c to 90c. *Journal of Polymer Science*, 57:99–106, 1962. doi: 10.1002/pol.1962.1205716508.

[18] A. D. Mulliken. *Mechanics of Amorphous Polymers and Polymer Nanocomposites during High Rate Deformation*. PhD thesis, Massachusetts Institute of Technology, September 2006.

Chapter 5

Application of the theory to PMMA through its glass transition temperature

5.1 Introduction

As shown in the previous chapter, the continuum-mechanical framework developed in Chapter 3 works well in capturing the material response of PMMA below the glass transition. In this chapter we specialize the constitutive equations further to be able to capture the material response of PMMA not only below the glass transition, but continuously through it to temperatures above the glass transition. A summary of this specialized model is presented in Section 5.2 followed by the corresponding calibration procedure for PMMA in Section 5.3. A summary of the key constitutive equations, as well as the material parameters used, for both the one-dimensional and three-dimensional models are given in Section 5.4.

5.2 Summary of the Specialized Material Model

Based on experience with recent theories of isotropic viscoplasticity of polymeric materials [1–6], we assume that the change in the macroscopic stress response of an amorphous polymer arises due to two basic reasons: (i) changes due to the stretching of intermolecular bonds, and (ii) changes in the configurational entropy due to changes in the molecular conformations. Accordingly, in developing our continuum mechanical theory, we assume two major operative micromechanisms to represent these concepts. Although no real material is composed of springs and dashpots, as a visual aid, Figure 5-1 shows a schematic rheological representation of these micromechanisms. The left micromechanism indexed by $\alpha = 1$ represents contributions to the stress due to intermolecular bond-stretching, and the right micromechanism indexed by $\alpha = 2$ represents contributions to the stress due to entropic changes in molecular conformations, but this time allowing for chain-slippage at mechanical crosslinks – the additional dashpot in the branch $\alpha = 2$.

With such a micromechanical picture in mind, we have developed a rigorous three-dimensional thermo-mechanically coupled large deformation continuum framework for amorphous polymers,

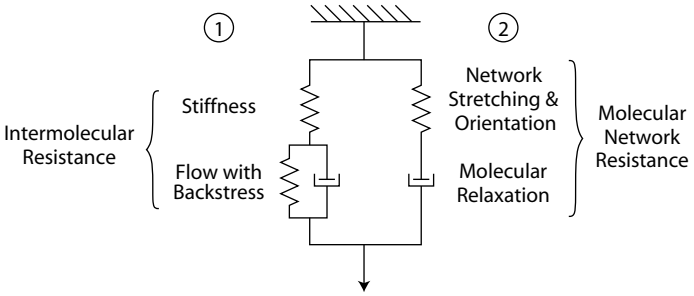

Figure 5-1: One-dimensional rheological representation of the proposed model for temperatures below the glass transition.

details of which are given later in Chapter 3. The specialization of this framework to polymer behavior through the glass transition is presented here.

5.2.1 Summary of Three-Dimensional Constitutive Equations

This section summarizes a specialized form of our theory which should be useful in modeling the complex finite deformation response of amorphous thermoplastic polymers through their glass transition.

The underlying constitutive equations relate the following basic fields:

$\mathbf{x} = \boldsymbol{\chi}(\mathbf{X}, t)$,	motion;
$\mathbf{F} = \nabla\boldsymbol{\chi},\ J = \det\mathbf{F} > 0$,	deformation gradient;
$\mathbf{F} = \mathbf{F}^{e\,(\alpha)}\mathbf{F}^{p\,(\alpha)},\ \alpha = 1, 2$,	elastic-plastic decompositions of $\mathbf{F}$;
$\mathbf{F}^{p\,(\alpha)}, \quad J^{p\,(\alpha)} = \det\mathbf{F}^{p\,(\alpha)} = 1$,	inelastic distortions;
$\mathbf{F}^{e\,(\alpha)}, \quad J^{e\,(\alpha)} = \det\mathbf{F}^{e\,(\alpha)} = J > 0$,	elastic distortions;
$\mathbf{F}^{e\,(\alpha)} = \mathbf{R}^{e\,(\alpha)}\mathbf{U}^{e\,(\alpha)} = \mathbf{V}^{e\,(\alpha)}\mathbf{R}^{e\,(\alpha)}$,	polar decompositions of $\mathbf{F}^{e\,(\alpha)}$;
$\mathbf{C}^{e\,(\alpha)} = \mathbf{F}^{e\,(\alpha)\top}\mathbf{F}^{e\,(\alpha)}$,	elastic right Cauchy-Green tensors;
$\mathbf{B}^{e\,(\alpha)} = \mathbf{F}^{e\,(\alpha)}\mathbf{F}^{e\,(\alpha)\top}$,	elastic left Cauchy-Green tensors;
$\mathbf{F}^{e\,(\alpha)}_{\rm dis} \stackrel{\rm def}{=} J^{-1/3}\,\mathbf{F}^{e\,(\alpha)}, \quad \det\mathbf{F}^{e\,(\alpha)}_{\rm dis} = 1$,	distortional part of $\mathbf{F}^{e\,(\alpha)}$,
$\mathbf{C}^{e\,(\alpha)}_{\rm dis} = (\mathbf{F}^{e\,(\alpha)}_{\rm dis})^{\top}\,\mathbf{F}^{e\,(\alpha)}_{\rm dis}, \quad \mathbf{B}^{e\,(\alpha)}_{\rm dis} = \mathbf{F}^{e\,(\alpha)}_{\rm dis}\,(\mathbf{F}^{e\,(\alpha)}_{\rm dis})^{\top}$,	distortional elastic Cauchy-Green strains;
$\mathbf{T}$,	Cauchy stress;
$\mathbf{T} = \sum_{\alpha=1}^{2}\mathbf{T}^{e\,(\alpha)}$,	decomposition of Cauchy stress;
$\mathbf{M}^{e\,(\alpha)} = J\mathbf{R}^{e\,(\alpha)\top}\,\mathbf{T}^{e\,(\alpha)}\,\mathbf{R}^{e\,(\alpha)}$,	Mandel stress;
$\psi_{\rm R} = \sum_{\alpha=1}^{M}\bar{\psi}^{(\alpha)}$,	free energy density per unit reference volume;
$\eta_{\rm R} = \sum_{\alpha=1}^{M}\bar{\eta}^{(\alpha)}$,	entropy density per unit reference volume;
$\boldsymbol{\xi}^{(\alpha)} = (\xi_1^{(\alpha)}, \xi_2^{(\alpha)}, \ldots, \xi_m^{(\alpha)})$	m scalar internal variables for each α;
$\mathbf{A}^{(1)}, \quad \mathbf{A}^{(1)} = \mathbf{A}^{(1)\top}, \quad \det\mathbf{A}^{(1)} = 1$	tensorial internal variable;
$\mathbf{M}^{e\,(1)}_{\rm back}$,	Back stress;
$\vartheta > 0$,	absolute temperature;
$\nabla\vartheta$,	referential temperature gradient;
$\mathbf{q}_{\rm R}$,	referential heat flux vector.

Glass transition

The temperature-dependence of the material properties of amorphous polymers depends strongly on the temperature relative to the glass transition temperature ϑ_g of the material. It is well-known that the glass transition temperature of such materials is not a constant, but depends strongly on the strain rate to which the material is subjected. Let

$$d \stackrel{\text{def}}{=} \sqrt{2}|\mathbf{D}_0| \tag{5.1}$$

denote the macroscopic effective shear strain rate, and d^{ref} a reference strain rate. We assume that the variation of the glass transition temperature with strain rate may be adequately described by [5, cf. their eq. (10)]

$$\vartheta_g = \begin{cases} \vartheta_g^{\text{ref}} & \text{if} \quad d \le d^{\text{ref}}, \\ \vartheta_g^{\text{ref}} + \left[\dfrac{C_{2g} \times \log_{10}(d/d^{\text{ref}})}{C_{1g} - \log_{10}(d/d^{\text{ref}})}\right] & \text{if} \quad d > d^{\text{ref}}, \end{cases} \tag{5.2}$$

where C_{1g} and C_{2g} are Williams-Landel-Ferry (WLF) parameters [7] relative to the reference glass transition temperature ϑ_g^{ref}. With the governing fields and the glass transition temperature so defined, we assume the following constitutive equations for the two micromechanisms $\alpha = 1, 2$.

Constitutive equations for alpha=1, intermolecular resistance

1. **Free energy:**

   With

   $$\mathbf{C}^{e\,(1)} = \sum_{i=1}^{3} \omega_i \, \mathbf{r}_i^e \otimes \mathbf{r}_i^e, \tag{5.3}$$

   denoting the spectral representation of $\mathbf{C}^{e\,(1)}$, and with

   $$\mathbf{E}^{e\,(1)} = \sum_{i=1}^{3} E_i^e \, \mathbf{r}_i^e \otimes \mathbf{r}_i^e, \qquad E_i^e = \ln \sqrt{\omega_i^e}, \tag{5.4}$$

   denoting an elastic logarithmic strain measure, we consider an elastic free energy of the form

   $$\begin{aligned} \psi^{e\,(1)}(\mathbf{C}^{e\,(1)}, \vartheta) = G|\mathbf{E}_0^{e\,(1)}|^2 + \tfrac{1}{2}K(\operatorname{tr}\mathbf{E}^{e\,(1)})^2 \\ - (\vartheta - \vartheta_0)(3\,K\,\alpha^{th})(\operatorname{tr}\mathbf{E}^{e\,(1)}) + c(\vartheta - \vartheta_0) - c\,\vartheta \ln\Big(\frac{\vartheta}{\vartheta_0}\Big). \end{aligned} \tag{5.5}$$

   where

   $$G(\vartheta) > 0, \quad K(\vartheta) > 0, \quad \alpha^{th}(\vartheta), \quad c(\vartheta), \tag{5.6}$$

   are the *temperature-dependent* shear modulus, bulk modulus, coefficient of thermal expansion, and specific heat, and ϑ_0 is a reference temperature.

   For polymeric materials the magnitude of the elastic shear modulus decreases drastically as the temperature increases through the glass transition temperature ϑ_g of the material.

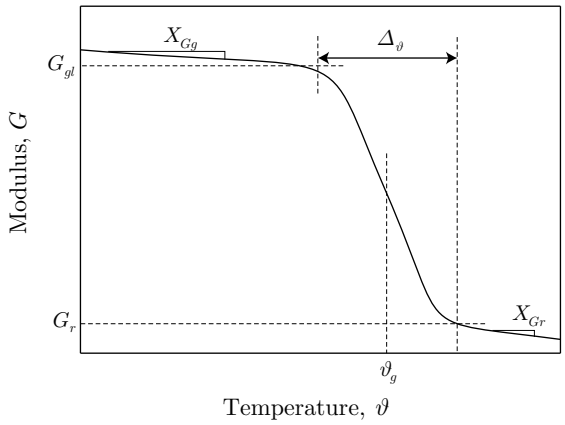

Figure 5-2: Schematic of the phenomenological temperature dependence of the shear modulus G.

Following Dupaix and Boyce [4], we assume that the temperature-dependence of the shear modulus may be adequately approximated by a phenomenological function of the form

$$G(\vartheta) = \tfrac{1}{2}(G_{gl} + G_r) - \tfrac{1}{2}(G_{gl} - G_r)\tanh\left(\frac{1}{\Delta_\vartheta}(\vartheta - \vartheta_g)\right) + X_G(\vartheta - \vartheta_g), \tag{5.7}$$

where ϑ_g is the glass transition temperature, G_{gl} and G_r are representative modulii in the glassy and rubbery regions, Δ_ϑ is a parameter denoting the temperature range across which the glass transition occurs, and X_g represents the slope of the temperature variation beyond the transition region (cf. Figure 5-2), where

$$X_G = \begin{cases} X_{Gg} & : \quad \vartheta \leq \vartheta_g \\ X_{Gr} & : \quad \vartheta > \vartheta_g \end{cases} \tag{5.8}$$

For the temperature-dependence of Poisson's ratio ν_{poi} we also assume

$$\nu_{\text{poi}}(\vartheta) = \tfrac{1}{2}(\nu_{gl} + \nu_r) - \tfrac{1}{2}(\nu_{gl} - \nu_r)\tanh\left(\frac{1}{\Delta_\vartheta}(\vartheta - \vartheta_g)\right), \tag{5.9}$$

with ν_{gl} and ν_r representative values of Poisson's ratio below and above the material's glass transition temperature respectively. The bulk modulus K can then be found from the standard relation

$$K = G \times \frac{2(1 + \nu_{\text{poi}})}{3(1 - 2\nu_{\text{poi}})} \tag{5.10}$$

With

$$\mathbf{A}^{(1)} = \sum_{i=1}^{3} a_i \, \mathbf{l}_i^d \otimes \mathbf{l}_i^d, \tag{5.11}$$

denoting the spectral representation of $\mathbf{A}^{(1)}$, and with

$$\ln \mathbf{A}^{(1)} = \sum_{i=1}^{3} \ln a_i \, \mathbf{l}_i^d \otimes \mathbf{l}_i^d, \tag{5.12}$$

denoting a defect logarithmic strain measure, we consider a defect free energy of the form

$$\tilde{\psi}^{d\,(1)}(\mathbf{A}^{(1)}, \vartheta) = \frac{1}{4} C(\vartheta) \, \left[(\ln a_1)^2 + (\ln a_2)^2 + (\ln a_3)^2 \right], \tag{5.13}$$

where the positive-valued temperature-dependent parameter

$$C(\vartheta) \geq 0, \tag{5.14}$$

is a back-stress modulus chosen to decrease linearly with temperature following the form of the internal stress used by Fotheringham et al. [8], Povolo and Hermida [9] and Richeton et al. [10]. So that

$$C(\vartheta) = \begin{cases} X_C(\vartheta_C - \vartheta) & \text{if} \quad \vartheta \leq \vartheta_C, \\ 0 & \text{if} \quad \vartheta > \vartheta_C, \end{cases} \tag{5.15}$$

where $X_C > 0$ is a material parameter and ϑ_C is the temperature near the material's glass transition where $C(\vartheta)$ vanishes.

2. **Mandel stress. Cauchy stress. Back stress. Effective stress:** The Mandel stress is given by

$$\mathbf{M}^{e\,(1)} = 2G\mathbf{E}_0^{e\,(1)} + K \left\{ \operatorname{tr} \mathbf{E}^{e\,(1)} - 3\,\alpha^{th}\,(\vartheta - \vartheta_0) \right\} \mathbf{1}, \tag{5.16}$$

and the corresponding Cauchy stress is

$$\mathbf{T}^{e\,(1)} \stackrel{\text{def}}{=} J^{-1}\, \mathbf{R}^{e\,(1)}\, \mathbf{M}^{e\,(1)}\, \mathbf{R}^{e\,(1)\top}. \tag{5.17}$$

The symmetric and deviatoric back stress is

$$\mathbf{M}^{(1)}_{\text{back}} = C \ln \mathbf{A}^{(1)}. \tag{5.18}$$

and the driving stress for plastic flow is the effective stress given by

$$\mathbf{M}^{e\,(1)}_{\text{eff}} \stackrel{\text{def}}{=} \mathbf{M}^{e\,(1)} - \mathbf{M}^{(1)}_{\text{back}}. \tag{5.19}$$

The corresponding *equivalent shear stress* and *mean normal pressure* are given by

$$\bar{\tau}^{(1)} \stackrel{\text{def}}{=} \frac{1}{\sqrt{2}} \, |(\mathbf{M}^{e\,(1)}_{\text{eff}})_0|, \quad \text{and} \quad \bar{p}^{(1)} \stackrel{\text{def}}{=} -\frac{1}{3} \operatorname{tr} \mathbf{M}^{e\,(1)}, \tag{5.20}$$

respectively.

3. **Internal variables:** We restrict the list $\boldsymbol{\xi}^{(1)}$ of internal variables to two, positive-valued variables

$$S^{(1)} \geq 0, \qquad \varphi \geq 0$$

that represent aspects of the *intermolecular shear resistance to plastic flow*. The parameter $S^{(1)}$ has dimensions of stress and represents an *isotropic resistance to plastic flow*, while φ is a dimensionless order-parameter representing the local *free-volume* (a measure of disorder) of the polymeric glass.

4. **Flow rule:** The evolution equation for $\mathbf{F}^{p(1)}$ is

$$\left.\begin{aligned}
&\dot{\mathbf{F}}^{p\,(1)} = \mathbf{D}^{p(1)}\,\mathbf{F}^{p(1)}, \qquad \mathbf{F}^{p(1)}(\mathbf{X},0) = \mathbf{1},\\
&\mathbf{D}^{p(1)} = \nu^{p\,(1)}\,\left(\frac{(\mathbf{M}_{\text{eff}}^{e\,(1)})_0}{2\,\bar{\tau}^{(1)}}\right),\\
&\bar{\tau}_{\text{e}}^{(1)} \stackrel{\text{def}}{=} \bar{\tau}^{(1)} - S^{(1)} - \alpha_p\,\bar{p}^{(1)}\\
&\nu^{p\,(1)} = \begin{cases} 0 & \text{if} \quad \bar{\tau}_{\text{e}}^{(1)} \le 0,\\ \nu^*\,\left[\sinh\left(\dfrac{\bar{\tau}_{\text{e}}^{(1)}\,V}{2k_B\vartheta}\right)\right]^{1/m^{(1)}} & \text{if} \quad \bar{\tau}_{\text{e}}^{(1)} > 0\,, \end{cases}
\end{aligned}\right\} \tag{5.21}$$

The quantity $\nu^{p\,(1)}$ is a plastic strain-rate and follows the form of the "cooperative model" used by Richeton et al. [10], where $\bar{\sigma}^{(1)}$ denotes an effective stress with $\alpha_p \ge 0$ a pressure sensitivity parameter, and $\bar{p}^{(1)}$ a pressure. Additionally, $m^{(1)}$ is a strain-rate sensitivity parameter, V is a shear activation volume, k_B is Boltzmann's constant, and ν^* is a characteristic thermally-activated strain-rate

$$\nu^*(\vartheta) = \begin{cases} \nu_0^{(1)}\,\exp\left(-\dfrac{\Delta F^{(1)}}{k_B\vartheta}\right) & \text{if} \quad \vartheta < \vartheta_g,\\ \nu_0^{(1)}\,\exp\left(-\dfrac{\Delta F^{(1)}}{k_B\vartheta_g}\right)\,\exp\left(\dfrac{\ln 10 \times c_1^*(\vartheta-\vartheta_g)}{c_2^*+\vartheta-\vartheta_g}\right) & \text{if} \quad \vartheta \ge \vartheta_g. \end{cases} \tag{5.22}$$

where $\nu_0^{(1)}$ is a pre-exponential factor with units of 1/time, $\Delta F^{(1)}$ is an activation energy, and c_1^* and c_2^* are WLF parameters which govern the drastic increase of the characteristic strain-rate through the glass transition region.

5. **Evolution equations for the internal variables $S^{(1)}$, φ, and $\mathbf{A}^{(1)}$**

We assume that the material disorders and is accompanied by a microscale dilatation as plastic deformation occurs resulting in an increase of the free volume φ. This increase leads to a fluctuation in the isotropic resistance $S^{(1)}$ causing a transient rise in the flow stress of the material as plastic deformation proceeds. We therefore assume that the evolution of the free volume φ is coupled to the evolution of the isotropic resistance S in order to reproduce the typical yield peak observed in the stress-strain response of amorphous polymers below the glass transition temperature ϑ_g. The coupling is introduced through this special set of equations:

$$\left.\begin{aligned}
&\dot{\varphi} = g\,(\varphi^* - \varphi)\,\nu^{p\,(1)}, \qquad \varphi(\mathbf{X},0) = \varphi_i > 0,\\
&\dot{S}^{(1)} = h\,\left(S^* - S^{(1)}\right)\,\nu^{p\,(1)}, \qquad S^{(1)}(\mathbf{X},0) = S_i \ge 0,\\
&S^* = S_i + b\,(\varphi^* - \varphi)\,,
\end{aligned}\right\} \tag{5.23}$$

where the material parameter $\varphi^*(\vartheta, \nu^{p\,(1)}) \geq \varphi_i$ represents the saturation value of the free volume φ.

We expect that the difference between the initial φ_i and saturation φ^* values of the free volume φ goes to zero as the material transitions into its rubbery regime above the glass transition. Therefore, we assign a hyperbolic tangent function to the value of φ^* to smoothly change its value at the glass transition along with the elastic modulus. For the rubbery region we choose $\varphi^* = \varphi_i$, and in the glass region we choose $\varphi^* = \varphi_g^*$, resulting in this function for φ^*:

$$\varphi^* = \tfrac{1}{2}(\varphi_g^* + \varphi_i) - \tfrac{1}{2}(\varphi_g^* - \varphi_i) \tanh\left(\frac{1}{\Delta_\vartheta}(\vartheta - \vartheta_g)\right). \tag{5.24}$$

Note that the width Δ_ϑ and temperature ϑ_g of this transition are identical to the values used for the elastic modulus.

The material parameters $h > 0$, $g(\vartheta) > 0$, and $b(\vartheta, \nu^{p\,(1)}) \geq 0$ describe the initial hardening, subsequent rate of softening, and magnitude of the yield peak. We have assumed the following functions to describe their temperature and rate-dependence

$$\left.\begin{aligned} g &= g_1 + g_2\vartheta, \\ b &= b_1\,\left(\vartheta^2 + b_2\vartheta + b_3\right)\,\left(\frac{\nu^{p\,(1)}}{\nu_{\text{ref}}}\right)^{b_4}, \end{aligned}\right\} \tag{5.25}$$

where the list $\{g_1,\, g_2,\, b_1,\, b_2,\, b_3,\, b_4\}$ are material parameters and ν_{ref} is a reference strain-rate. The functions for b and g are empirical and the forms given in (5.25) have been chosen to fit experimental data.

The evolution equation for for $\mathbf{A}^{(1)}$ is taken as

$$\left.\begin{aligned} \dot{\mathbf{A}}^{(1)} &= \mathbf{D}^{p(1)}\mathbf{A}^{(1)} + \mathbf{A}^{(1)}\mathbf{D}^{p(1)} - \sqrt{2}\,\mathbf{G}\,\nu^{p\,(1)}, \qquad \mathbf{A}^{(1)}(\mathbf{X}, 0) = \mathbf{1}, \\ \mathbf{G} &= \tfrac{1}{\sqrt{2}}\,\gamma\,\mathbf{A}^{(1)}\,\ln\mathbf{A}^{(1)}, \end{aligned}\right\} \tag{5.26}$$

where $\gamma(\vartheta) \geq 0$ is a constitutive parameter which governs the recovery of $\mathbf{A}^{(1)}$.

Constitutive equations for alpha=2, molecular network resistance

1. **Free energy** Let

$$I_1 \stackrel{\text{def}}{=} \operatorname{tr}\mathbf{C}_{\text{dis}}^{e\,(2)} \tag{5.27}$$

denote the first principal invariant of $\mathbf{C}_{\text{dis}}^{e\,(2)}$. We then consider following elastic free energy

$$\psi^{e\,(2)} = -\tfrac{1}{2}\mu_{\text{R}}\, I_{1,\max}\, \ln\Big(1 - \frac{I_1 - 3}{I_{1,\max}}\Big), \tag{5.28}$$

where

$$\mu_{\text{R}}(\vartheta) > 0, \qquad I_{1,\max}(\vartheta) > 3 \tag{5.29}$$

are two temperature-dependent material parameters. In particular, μ_{R} represents the ground state rubbery shear modulus of the material, and $I_{1,\max}$ represents the upper limit of I_1

(i.e., $I_1 < (3 + I_{1,\max})$), associated with limited chain extensibility. We assume that $\mu_{\rm R}$ decreases with increasing temperature and $I_{1,\max}$ increases. Empirical functions which fit the experimental temperature dependence of these parameters are

$$\mu_{\rm R}(\vartheta) = \tfrac{1}{2}(\mu_{\rm R}^a + \mu_{\rm R}^b) - \tfrac{1}{2}(\mu_{\rm R}^a - \mu_{\rm R}^b)\tanh\left(\frac{1}{\Delta_\mu}(\vartheta - \vartheta_\mu)\right) + X_\mu(\vartheta - \vartheta_\mu) \tag{5.30}$$

$$I_{1,\max}(\vartheta) = \tfrac{1}{2}(I_1^a + I_1^b) - \tfrac{1}{2}(I_1^a - I_1^b)\tanh\left(\frac{1}{\Delta_I}(\vartheta - \vartheta_I)\right). \tag{5.31}$$

where we note that the transition of these parameters is not necessarily related to the transition of the elastic moduli in micromechanism $\alpha = 1$.

2. Mandel stress. Cauchy stress:

The Mandel stress is given by

$$\mathbf{M}^{e\,(2)} = \mu_{\rm R}\left(1 - \frac{I_1 - 3}{I_{1,\max}}\right)^{-1}(\mathbf{C}^{e}_{\rm dis}{}^{(2)})_0. \tag{5.32}$$

and the Cauchy stress is then

$$\mathbf{T}^{e\,(2)} = J^{-1}\left[\mu_{\rm R}\left(1 - \frac{I_1 - 3}{I_{1,\max}}\right)^{-1}(\mathbf{B}^{e\,(2)}_{\rm dis})_0\right]. \tag{5.33}$$

For $\alpha = 2$ we have neglected a defect energy, and hence there is no back stress. The corresponding *equivalent shear stress* is given by

$$\bar{\tau}^{(2)} \stackrel{\rm def}{=} \frac{1}{\sqrt{2}}\,|\mathbf{M}_0^{e\,(2)}|, \tag{5.34}$$

3. Internal variables:

We restrict the list $\boldsymbol{\xi}^{(2)}$ of internal variables to a single stress-dimensioned positive-valued variable

$$S^{(2)} > 0$$

that represents a *shear resistance to plastic flow* for molecular relaxation processes.

4. Flow rule:

The evolution equation for $\mathbf{F}^{p(2)}$ is

$$\left.\begin{aligned}
\dot{\mathbf{F}}^{p\,(2)} &= \mathbf{D}^{p(2)}\,\mathbf{F}^{p(2)}, \qquad \mathbf{F}^{p(2)}(\mathbf{X},0) = \mathbf{1},\\
\mathbf{D}^{p(2)} &= \nu^{p\,(2)}\left(\frac{\mathbf{M}_0^{e\,(2)}}{2\,\bar{\tau}^{(2)}}\right),\\
\nu^{p\,(2)} &= \nu_0^{(2)}\,\exp\left\{-\frac{\Delta F^{(2)}}{k_B\,\vartheta}\right\}\left(\frac{\bar{\tau}^{(2)}}{S^{(2)}}\right)^{1/m^{(2)}}
\end{aligned}\right\} \tag{5.35}$$

where $\nu_0^{(2)}$ is a pre-exponential factor with units of 1/time, $\Delta F^{(2)}$ is an *activation energy*, k_B is Boltzmann's constant, and $m^{(2)}$ is a strain rate sensitivity parameter.

5. Evolution equation for S_2

The shear deformation resistance $S^{(2)}$ is assumed to remain constant.

Entropy relation. Fourier's Law:

Finally, we have the entropy relation

$$\eta_{\mathrm{R}} = -\left[\frac{\partial \bar{\psi}^{e\,(1)}(\mathbf{C}^{e(1)},\vartheta)}{\partial\vartheta} + \frac{\partial \bar{\psi}^{e\,(2)}(\mathbf{C}^{e(2)},\vartheta)}{\partial\vartheta} + \frac{\partial \bar{\psi}^{d\,(1)}(\mathbf{A}^{(1)},\vartheta)}{\partial\vartheta}\right], \tag{5.36}$$

together with Fourier's law

$$\mathbf{q}_{\mathrm{R}} = -\kappa\,\nabla\vartheta, \tag{5.37}$$

with $\kappa(\vartheta) > 0$ the thermal conductivity.

Partial differential equations for the deformation and temperature fields

The partial differential equation for the deformation is obtained from the local force balance:

$$\mathrm{Div}\,\mathbf{T}_{\mathrm{R}} + \mathbf{b}_{0\mathrm{R}} = \rho_{\mathrm{R}}\,\ddot{\boldsymbol{\chi}}. \tag{5.38}$$

The specific heat in the theory is given by

$$c \overset{\mathrm{def}}{=} -\vartheta\left[\frac{\partial^2 \bar{\psi}^{e\,(1)}(\mathcal{I}_{\mathbf{C}^{e\,(1)}},\vartheta)}{\partial\vartheta^2} + \frac{\partial^2 \bar{\psi}^{e\,(2)}(\mathcal{I}_{\mathbf{C}^{e\,(2)}},\vartheta)}{\partial\vartheta^2} + \frac{\partial^2 \bar{\psi}^{d\,(1)}(\mathcal{I}_{\mathbf{A}^{(1)}},\vartheta)}{\partial\vartheta^2}\right]. \tag{5.39}$$

Balance of energy gives the following partial differential equation for the temperature

$$\begin{aligned} c\dot{\vartheta} = -\mathrm{Div}\,\mathbf{q}_{\mathrm{R}} + q_{\mathrm{R}} + \sum_{\alpha=1}^{M} \underbrace{\left[|\mathbf{M}^{e\,(\alpha)}_{\mathrm{eff}}{}_0|\,d^{p\,(\alpha)}\right] + \left[\frac{\partial \tilde{\psi}^{d\,(1)}(\mathcal{I}_{\mathbf{A}^{(1)}},\vartheta)}{\partial \mathbf{A}^{(1)}} : \mathbf{G}^{(1)}(\boldsymbol{\xi}^{(1)},\mathbf{A}^{(1)},\vartheta)\right] d^{p\,(1)}}_{\text{rate of plastic dissipation}} \\ \underbrace{+\,\vartheta\left[\frac{\partial^2 \bar{\psi}^{e\,(1)}(\mathcal{I}_{\mathbf{C}^{e\,(1)}},\vartheta)}{\partial\vartheta\,\partial\mathbf{C}^{e\,(1)}} : \dot{\mathbf{C}}^{e\,(1)} + \frac{\partial^2 \bar{\psi}^{e\,(2)}(\mathcal{I}_{\mathbf{C}^{e\,(2)}},\vartheta)}{\partial\vartheta\,\partial\mathbf{C}^{e\,(2)}} : \dot{\mathbf{C}}^{e\,(2)} + \frac{\partial^2 \bar{\psi}^{d\,(1)}(\mathcal{I}_{\mathbf{A}^{(1)}},\vartheta)}{\partial\vartheta\,\partial\mathbf{A}^{(1)}} : \dot{\mathbf{A}}^{(1)}\right]}_{\text{“thermoelastic-coupling” terms}}. \end{aligned} \tag{5.40}$$

As argued in the previous chapter, we neglect the "thermoelastic-coupling" terms and assume instead that only a fraction of the inelastic work is dissipated so that our final heat equation become

$$c\dot{\vartheta} = -\mathrm{Div}\,\mathbf{q}_{\mathrm{R}} + q_{\mathrm{R}} + \beta\left(\bar{\tau}^{(1)}\,\nu^{p\,(1)} + \tfrac{1}{2}\,C\,\gamma\,|\ln\mathbf{A}^{(1)}|^2\,\nu^{p\,(1)} + \bar{\tau}^{(2)}\,\nu^{p\,(2)}\right) \tag{5.41}$$

where β is the fraction of inelastic work that is dissipated, and we have used

$$\left.\begin{aligned} \mathbf{G}(\mathbf{A}) &= \frac{1}{\sqrt{2}}\,\gamma\,\mathbf{A}\ln\mathbf{A}, \\ \frac{\partial\tilde{\psi}^{d}(\mathcal{I}_{\mathbf{A}^{(1)}},\vartheta)}{\partial\mathbf{A}^{(1)}} &= \frac{1}{2}\,C\,(\ln\mathbf{A}^{(1)})\mathbf{A}^{(1)\,-1}. \end{aligned}\right\} \tag{5.42}$$

5.2.2 Summary of One-Dimensional Constitutive Equations

In this section we present an approximate one-dimensional version of the model which substantially aids in the calibration of material properties from experimental data. The underlying constitutive equations relate the following basic fields:

$U > 0$,	stretch,
$U^{p(\alpha)}$,	plastic stretch,
$U^{e(\alpha)} = UU^{p(\alpha)-1}$,	elastic part of the stretch,
$\epsilon = \ln U$,	logarithmic strain,
$\epsilon^{e(\alpha)} = \ln U^{e(\alpha)}$,	logarithmic elastic strains,
$\boldsymbol{\xi}^{(\alpha)} = \big(\xi_1^{(\alpha)}, \xi_2^{(\alpha)}, \ldots, \xi_m^{(\alpha)}\big)$	scalar internal variables,
$A > 0$,	squared stretch-like internal variable,
$\vartheta > 0$,	absolute temperature,
$\psi = \sum_{\alpha=1}^{2} \psi^{e\,(\alpha)}\big(U^{e\,(\alpha)},\vartheta\big) + \psi^{d\,(1)}\big(A,\vartheta\big)$,	free energy density,
$\sigma = \sum_{\alpha=1}^{2} \sigma^{e(\alpha)}$,	decomposition of the Cauchy stress.

Glass transition

The temperature-dependence of the material properties of amorphous polymers depends strongly on the temperature relative to the glass transition temperature ϑ_g of the material. It is well-known that the glass transition temperature of such materials is not a constant, but depends strongly on the strain-rate to which the material is subjected. Let

$$\dot{\epsilon} \stackrel{\text{def}}{=} \frac{\partial\epsilon}{\partial t} \tag{5.43}$$

denote the axial strain-rate, and $\dot{\epsilon}^{\text{ref}}$ a reference strain-rate. We assume that the variation of the glass transition temperature with strain-rate may be adequately described by [5, cf. their eq. (10)]

$$\vartheta_g = \begin{cases} \vartheta_g^{\text{ref}} & \text{if} \quad \dot{\epsilon} \le \dot{\epsilon}^{\text{ref}}, \\ \vartheta_g^{\text{ref}} + \left[\dfrac{C_{2g} \times \log_{10}(\dot{\epsilon}/\dot{\epsilon}^{\text{ref}})}{C_{1g} - \log_{10}(\dot{\epsilon}/\dot{\epsilon}^{\text{ref}})}\right] & \text{if} \quad \dot{\epsilon} > \dot{\epsilon}^{\text{ref}}, \end{cases} \tag{5.44}$$

where C_{1g} and C_{2g} are Williams-Landel-Ferry (WLF) parameters [7] relative to the reference glass transition temperature ϑ_g^{ref}. With the governing fields and the glass transition temperature so defined, we assume the following constitutive equations for the two micromechanisms $\alpha = 1, 2$.

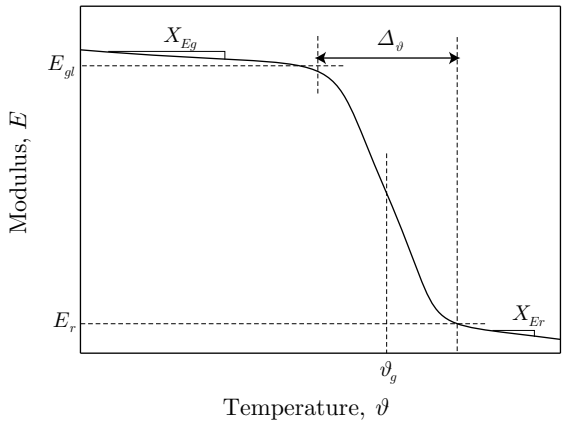

Figure 5-3: Schematic of the phenomenological temperature dependence of the elastic modulus E.

Constitutive equations for alpha=1

1. **Free Energy**: For $\psi^{e(1)}$ we use a simple linear elastic form for the free energy

$$\psi^{e(1)} = \tfrac{1}{2}\, E\, |\epsilon^{e(1)}|^2, \tag{5.45}$$

where $E(\vartheta) > 0$ is the Young's modulus. Following Dupaix and Boyce [4], we assume that the temperature-dependence of the elastic modulus may be adequately approximated by a phenomenological function of the form

$$E(\vartheta) = \tfrac{1}{2}(E_{gl} + E_r) - \tfrac{1}{2}(E_{gl} - E_r)\tanh\left(\frac{1}{\Delta_\vartheta}(\vartheta - \vartheta_g)\right) + X_E(\vartheta - \vartheta_g), \tag{5.46}$$

where E_{gl} and E_r are representative modulii in the glassy and rubbery regions, Δ_ϑ is a parameter denoting the temperature range across which the glass transition occurs, and the constant X_E represents the change in modulus with temperature outside of the glass transition region (cf. Figure 5-3), where

$$X_E = \begin{cases} X_{Eg} & : \quad \vartheta \le \vartheta_g \\ X_{Er} & : \quad \vartheta > \vartheta_g \end{cases} \tag{5.47}$$

For $\psi^{d(1)}$ we use a simple defect free energy of the form[1]

$$\psi^{d\,(1)} = \tfrac{3}{8}\,C\,(\ln A)^2, \tag{5.48}$$

where $C(\vartheta) \geq 0$ is a back-stress modulus chosen to decrease linearly with temperature following the form of the internal stress used by Povolo and Hermida [9], Fotheringham and Cherry [11], and Richeton et al. [10]

$$C(\vartheta) = \begin{cases} X_C(\vartheta_C - \vartheta) & \text{if} \quad \vartheta \leq \vartheta_C, \\ 0 & \text{if} \quad \vartheta > \vartheta_C. \end{cases} \tag{5.49}$$

Here X_C is a material parameter and ϑ_C is the temperature near the material's glass transition where $C(\vartheta)$ vanishes.

2. **Equation for the stress**: The elastic stress is given by

$$\sigma^{e\,(1)} = E\,\epsilon^{e(1)} \tag{5.50}$$

and the back-stress relation is[2]

$$\sigma^{(1)}_{\text{back}} = \tfrac{3}{2}\,C\,\ln A. \tag{5.51}$$

such that the driving stress for plastic flow is the effective stress given by

$$\sigma^{(1)}_{\text{eff}} = \sigma^{e\,(1)} - \sigma^{(1)}_{\text{back}} \tag{5.52}$$

3. **Internal variables**: We restrict the list $\boldsymbol{\xi}^{(1)}$ of internal variables to two, positive-valued variables

$$S^{(1)} \geq 0, \qquad \varphi \geq 0$$

[1] Let (a_1, a_2, a_3) denote the set of a principal stretches of a symmetric positive definite unimodular tensor $\mathbf{A}$ in three dimensions representing a squared stretch tensor. For incompressibility of such a stretch, the a_i satisfy $a_1 a_2 a_3 = 1$. Assuming a corresponding defect free energy of the form

$$\psi^d = \tfrac{1}{4}\,C\left[(\ln a_1)^2 + (\ln a_2)^2 + (\ln a_3)^2\right],$$

then in one-dimension, with $A \overset{\text{def}}{=} a_1$, $a_2 = a_3 = A^{-\frac{1}{2}}$, the defect free energy can be written as

$$\psi^d = \tfrac{3}{8}\,C\,(\ln A)^2,$$

[2] Given a free energy function of the form

$$\psi = \hat{\psi}(A),$$

the engineering stress S is defined by

$$S = 2\frac{\partial \psi}{\partial A}.$$

Also, assuming incompressibility, the Cauchy stress σ can then be represented as

$$\sigma = SA = 2A\frac{\partial \hat{\psi}}{\partial A},$$

that represent aspects of the *intermolecular shear resistance to plastic flow*. The parameter $S^{(1)}$ has dimensions of stress and represents an *isotropic resistance to plastic flow*, while φ is a dimensionless parameter representing the local *free-volume* of the polymeric glass.

4. Flow rule: The evolution equation for $U^{p\,(1)}$ is

$$\dot{U}^{p\,(1)} = D^{p\,(1)} U^{p\,(1)}, \qquad U^{p\,(1)}(0) = 1, \tag{5.53}$$

$$D^{p\,(1)} = \dot{\epsilon}^{p\,(1)}\,\mathrm{sign}(\sigma^{e\,(1)}) \tag{5.54}$$

$$\bar{\sigma}^{(1)} \stackrel{\text{def}}{=} |\sigma^{(1)}_{\text{eff}}| - S^{(1)} - \alpha_p\,\bar{p}, \qquad \bar{p} \stackrel{\text{def}}{=} -\tfrac{1}{3}\,\sigma^{e\,(1)} \tag{5.55}$$

$$\dot{\epsilon}^{p\,(1)} = \begin{cases} \dot{\epsilon}^*(\vartheta)\left[\sinh\left(\dfrac{\bar{\sigma}^{(1)} V}{2\,k_B \vartheta}\right)\right]^{1/m^{(1)}} & \text{if} \quad \bar{\sigma}^{(1)} > 0, \\ 0 & \text{if} \quad \bar{\sigma}^{(1)} \le 0. \end{cases} \tag{5.56}$$

The quantity $\dot{\epsilon}^{p\,(1)}$ is a plastic strain-rate and follows the form of the "cooperative model" used by Richeton et al. [10], where $\bar{\sigma}^{(1)}$ denotes a pressure modified effective stress with $\alpha_p \ge 0$ a pressure sensitivity parameter, and $\bar{p}^{(1)}$ a pressure. Additionally, $m^{(1)}$ is a strain-rate sensitivity parameter, V is a tensile activation volume, k_B is Boltzmann's constant, and $\dot{\epsilon}^*$ is a characteristic thermally-activated strain-rate

$$\dot{\epsilon}^*(\vartheta) = \begin{cases} \dot{\epsilon}_0^{(1)} \exp\left(-\dfrac{\Delta F^{(1)}}{k_B \vartheta}\right) & \text{if} \quad \vartheta < \vartheta_g, \\ \dot{\epsilon}_0^{(1)} \exp\left(-\dfrac{\Delta F^{(1)}}{k_B \vartheta_g}\right) \exp\left(\dfrac{\ln 10 \times c_1^*(\vartheta - \vartheta_g)}{c_2^* + \vartheta - \vartheta_g}\right) & \text{if} \quad \vartheta \ge \vartheta_g. \end{cases} \tag{5.57}$$

where $\dot{\epsilon}_0^{(1)}$ is a pre-exponential factor with units of 1/time, $\Delta F^{(1)}$ is an activation energy, and c_1^* and c_2^* are WLF parameters which govern the drastic increase of the characteristic strain-rate through the glass transition region.

5. Evolution equations for the internal variables $S^{(1)}$, φ, and A

We assume that the material disorders and is accompanied by a microscale dilatation as plastic deformation occurs resulting in an increase of the free volume φ. This increase leads to a fluctuation in the isotropic resistance $S^{(1)}$ causing a transient rise in the flow stress of the material as plastic deformation proceeds. We therefore assume that the evolution of the free volume φ is coupled to the evolution of the isotropic resistance S in order to reproduce the typical yield peak observed in the stress-strain response of amorphous polymers below the glass transition temperature ϑ_g. The coupling is introduced through this special set of equations:

$$\left.\begin{aligned} \dot{\varphi} &= g\,(\varphi^* - \varphi)\,\dot{\epsilon}^{p\,(1)}, \qquad \varphi(0) = \varphi_i > 0, \\ \dot{S}^{(1)} &= h\left(S^* - S^{(1)}\right)\dot{\epsilon}^{p\,(1)}, \qquad S^{(1)}(0) = S_i \ge 0, \\ S^* &= S_i + b\,(\varphi^* - \varphi)\,, \end{aligned}\right\} \tag{5.58}$$

where the material parameter $\varphi(\vartheta, \dot{\epsilon}^{p\,(1)})^* \geq \varphi_i$ represents the saturation value of the free volume φ.

We expect that the difference between the initial φ_i and saturation φ^* values of the free volume φ goes to zero as the material transitions into its rubbery regime above the glass transition. Therefore, we assign a hyperbolic tangent function to the value of φ^* to smoothly change its value at the glass transition along with the elastic modulus. For the rubbery region we choose $\varphi^* = \varphi_i$, and in the glass region we choose $\varphi^* = \varphi_g^*$, resulting in this function for φ^*:

$$\varphi^* = \tfrac{1}{2}(\varphi_g^* + \varphi_i) - \tfrac{1}{2}(\varphi_g^* - \varphi_i) \tanh\left(\frac{1}{\Delta_\vartheta}(\vartheta - \vartheta_g)\right). \tag{5.59}$$

Note that the width Δ_ϑ and temperature ϑ_g of this transition are identical to the values used for the elastic modulus.

The material parameters $h > 0$, $g(\vartheta) > 0$, and $b(\vartheta, \dot{\epsilon}^{p\,(1)}) \geq 0$ describe the initial hardening, subsequent rate of softening, and magnitude of this yield peak. We have assumed the following functions to describe their temperature and rate-dependence

$$\left.\begin{aligned} g &= g_1 + g_2\vartheta, \\ b &= b_1\,\left(\vartheta^2 + b_2\vartheta + b_3\right)\,\left(\frac{\dot{\epsilon}^{p\,(1)}}{\dot{\epsilon}_{\text{ref}}}\right)^{b_4}, \end{aligned}\right\} \tag{5.60}$$

where the list $\{g_1,\, g_2,\, b_1,\, b_2,\, b_3,\, b_4\}$ are material parameters and $\dot{\epsilon}_{\text{ref}}$ is a reference strain-rate. The functions for b and g are purely empirical and the forms given in (5.60) have been chosen to fit experimental data.

The evolution equation for A is taken as

$$\left.\begin{aligned} \dot{A} &= 2\,D^{p\,(1)}A - G\,\dot{\epsilon}^{p\,(1)}, \qquad A(0) = 1, \\ G &= \gamma A \ln A, \end{aligned}\right\} \tag{5.61}$$

where $\gamma > 0$ is a constitutive parameter that governs the dynamic recovery of A.

Constitutive equations for alpha=2

1. **Free energy**: For $\psi^{(2)}$ we use the first invariant of the stretch[3]

$$I_1 \equiv \left(U^{e(2)}\right)^2 + 2U^{e(2)-1}, \tag{5.62}$$

[3]Let $(\lambda_1, \lambda_2, \lambda_3)$ denote the set of a principal stretches of a symmetric positive definite tensor $\mathbf{U}$ in three dimensions representing a stretch tensor. For incompressibility of such a stretch, the λ_i satisfy $\lambda_1\lambda_2\lambda_3 = 1$. The first invariant I_1 of the stretch is defined by

$$I_1 \stackrel{\text{def}}{=} \lambda_1^2 + \lambda_2^2 + \lambda_3^2.$$

In one-dimension, with $\lambda \stackrel{\text{def}}{=} \lambda_1$, $\lambda_2 = \lambda_3 = \lambda^{-\frac{1}{2}}$,

$$I_1 = \lambda^2 + 2\,\lambda^{-1}.$$

and adopt the Gent [12] form of the free energy

$$\psi^{(2)} = -\tfrac{1}{2}\,\mu_{\rm R}\,I_{1,\max}\,\ln\left(1-\frac{I_1-3}{I_{1,\max}}\right) \tag{5.63}$$

where $\mu_{\rm R}(\vartheta) > 0$ and $I_{1,\max}(\vartheta) > 3$ are two temperature-dependent material parameters. In particular, $\mu_{\rm R}$ represents the ground state rubbery shear modulus of the material, and $I_{1,\max}$ represents the upper limit of I_1 (i.e., $I_1 < (3 + I_{1,\max})$), associated with limited chain extensibility. We assume that $\mu_{\rm R}$ decreases with increasing temperature and $I_{1,\max}$ increases. Empirical functions which fit the experimental temperature dependence of these parameters are

$$\mu_{\rm R}(\vartheta) = \tfrac{1}{2}(\mu_{\rm R}^a + \mu_{\rm R}^b) - \tfrac{1}{2}(\mu_{\rm R}^a - \mu_{\rm R}^b)\tanh\left(\frac{1}{\Delta_\mu}(\vartheta-\vartheta_\mu)\right) + X_\mu(\vartheta-\vartheta_\mu) \tag{5.64}$$

$$I_{1,\max}(\vartheta) = \tfrac{1}{2}(I_1^a + I_1^b) - \tfrac{1}{2}(I_1^a - I_1^b)\tanh\left(\frac{1}{\Delta_I}(\vartheta-\vartheta_I)\right). \tag{5.65}$$

where we note that the transition of these parameters is not necessarily related to the transition of the elastic moduli in micromechanism $\alpha = 1$.

2. **Equation for the stress**:[4] The stress in micromechanism $\alpha = 2$ is

$$\sigma^{e\,(2)} = \mu_{\rm R}\left(1-\frac{I_1-3}{I_{1,\max}}\right)^{-1}\left(\left(U^{e\,(2)}\right)^2 - U^{e\,(2)-1}\right) \tag{5.66}$$

3. **Internal variables**: We restrict the list $\boldsymbol{\xi}^{(2)}$ of internal variables to a single, stress-dimensioned positive-valued variable

$$S^{(2)} > 0 \tag{5.67}$$

that represents a resistance to plastic flow for molecular relaxation processes.

[4] Given a free energy function of the form

$$\psi = \hat{\psi}\,(I_1)\,, \qquad I_1 = \lambda^2 + 2\lambda^{-1},$$

the engineering stress S is defined by

$$S = \frac{\partial\psi}{\partial\lambda} = \frac{\partial\hat{\psi}}{\partial I_1}\frac{\partial I_1}{\partial\lambda}.$$

Also, assuming incompressibility

$$a_0 = a\lambda,$$

where a_0 is the original cross-sectional area and a is the current cross-sectional area. The Cauchy stress σ can then be represented as

$$\sigma = S\lambda = \lambda\frac{\partial\hat{\psi}}{\partial I_1}\frac{\partial I_1}{\partial\lambda},$$

4. **Flow rule**: The evolution equation for $U^{p\,(2)}$ is

$$\dot{U}^{p\,(2)} = D^{p\,(2)} U^{p\,(2)}, \qquad U^{p\,(2)}(0) = 1, \tag{5.68}$$

$$D^{p\,(2)} = \dot{\epsilon}^{p\,(2)}\,\mathrm{sign}(\sigma^{e\,(2)}) \tag{5.69}$$

$$\dot{\epsilon}^{p\,(2)} = \dot{\epsilon}_0^{(2)} \exp\left\{-\frac{\Delta F^{(2)}}{k_B \vartheta}\right\} \left(\frac{|\sigma^{e\,(2)}|}{S^{(2)}}\right)^{1/m^{(2)}} \tag{5.70}$$

where $\dot{\epsilon}_0^{(2)}$ is a pre-exponential factor with units of 1/time, $m^{(2)}$ is a strain-rate sensitivity parameter, $\Delta F^{(2)}$ is an activation energy, and k_B is Boltzmann's constant.

5. **Evolution equation for the internal variable** $S^{(2)}$

We assume that the internal variable $S^{(2)}$ is constant.

5.3 Material Parameter Calibration Through the Glass Transition

With the full three-dimensional and simplified one-dimensional version of the theory in place, we can now determine the material parameters required by the theory. We start with the one-dimensional calibration procedure using MATLAB in Section 5.3.1, followed by the appropriate adjustments necessary to complete calibration of the three-dimensional model in the finite element program ABAQUS/Explicit in Section 5.3.2.

Once the three-dimensional isothermal model is calibrated, a set of multi-element fully-coupled calculations is performed in ABAQUS/Explicit to calibrate the internal heating response of the material. These calculations and results are summarized in 5.3.3.

5.3.1 One-Dimensional Material Parameter Calibration Procedure

We have implemented the one-dimensional model of Section 5.2.2 in MATLAB using an explicit integration scheme, and we use it to calibrate the material parameters from the experiments described in Chapter 2. The one-dimensional calibration process consists of six sequential steps which are outlined in detail in this section. The six steps cover calibration of these aspects of the stress-strain response: (1) initial yield stress, (2) back stress, (3) elastic modulus, (4) large strain behavior, (5) high-temperature network slipping, and (6) yield peak shape.

Initial Yield Stress

We have chosen to use the cooperative model [6, 9, 11] to describe the rate and temperature dependence of the yield stress of PMMA below the glass transition. One important difference between our implementation and that of the earlier authors is that we have replaced their scalar internal stress with a stretch-dependent back stress (5.51). The reasoning is that the internal stress must be conjugate to a stretch measure so that it can be accounted for in the total internal energy of the system, and accordingly in the partial differential equation governing the temperature field. However, for the purposes of finding material parameters, we start with the earlier form using the scalar internal stress, and then we replace it with a suitable stretch-dependent back stress later in the calibration procedure.

For uniaxial *compression*, the expression for yield stress σ_y as a function of temperature ϑ and strain-rate $\dot{\epsilon}$ is given by

$$\left(1-\frac{\alpha_p}{3}\right)|\sigma_y| = r(\vartheta) + \frac{2k_B\vartheta}{V}\sinh^{-1}\left[\left(\frac{\dot{\epsilon}}{\dot{\epsilon}^*(\vartheta)}\right)^m\right] \tag{5.71}$$

where α_p is a pressure sensitivity parameter, r is a temperature dependent internal stress, k_B is the Boltzmann constant, V is an activation volume, $\dot{\epsilon}^*$ is a thermally-activated characteristic strain-rate, and m is a strain-rate sensitivity parameter. The internal stress r follows a linear relationship with temperature such that

$$r = \begin{cases} r_1(\vartheta_r - \vartheta) & : \vartheta \leq \vartheta_r, \\ 0 & : \vartheta > \vartheta_r, \end{cases} \tag{5.72}$$

where ϑ_r describes the temperature at which the internal stress vanishes and r_1 is a material parameter. The characteristic strain-rate $\dot{\epsilon}^*$ is assumed to follow an Arrhenius-type temperature

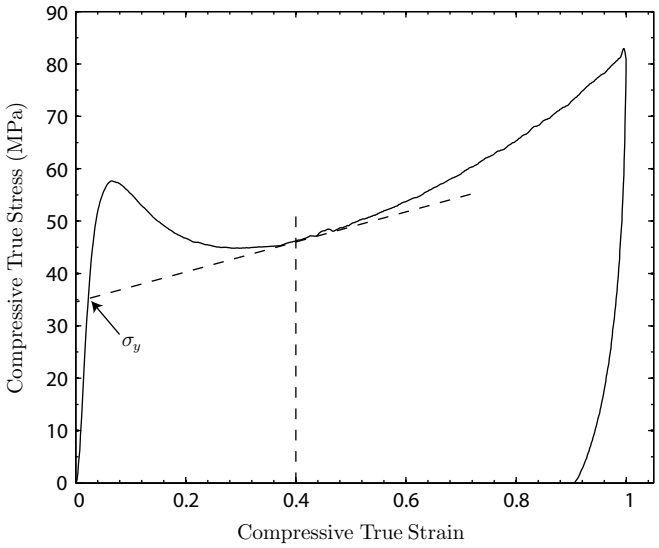

Figure 5-4: Schematic showing yield stress determined by the intersection of the initial loading path with the tangent of the stress-strain curve at 0.4 strain

dependence

$$\dot{\epsilon}^* = \dot{\epsilon}_0 \exp\left(-\frac{\Delta F}{k_B \vartheta}\right) \tag{5.73}$$

where $\dot{\epsilon}_0$ is a reference strain-rate and ΔF is an activation energy. To summarize, from (5.71), (5.72), and (5.73), there is a list of six material parameters that must be calibrated with the experimental yield data

$$\{\, V, m, r_1, \vartheta_r, \dot{\epsilon}_0, \Delta F \,\} \tag{5.74}$$

At this point in the calibration procedure we ignore the effects of the yield peak and define the yield stress as the intersection of the initial loading path with the tangent of the stress-strain curve at approximately 0.4 strain; this is shown schematically in Figure 5-4. Following this approach, yield stress values have been extracted from the PMMA compression experiments in the temperature range 25 C to 110 C at all four strain-rates. The ratio of these yield stresses to test temperature are shown in Figure 5-5 as a function of the logarithm of strain-rate. Estimated isotherms have been drawn to visually connect the yield points for a given testing temperature.

Unfortunately, for a given temperature we have only four data points spanning a relatively narrow strain-rate range which makes fitting the flow function (5.71) very difficult. By utilizing the yield stress superposition principle [10, 13], however, we can form a master curve of all 24 data points at a single reference temperature that covers a much wider range of strain-rates. To obtain the master curve, the experimental data is shifted along both axes by temperature-dependent shift factors that follow a linearized Arrhenius law

$$\left.\begin{aligned} \Delta(\log_{10}\dot{\epsilon}) &= H\left(\frac{1}{\vartheta} - \frac{1}{\vartheta_{\text{ref}}}\right) \\ \Delta\left(\frac{\sigma_y}{\vartheta}\right) &= B\left(\frac{1}{\vartheta} - \frac{1}{\vartheta_{\text{ref}}}\right) \end{aligned}\right\} \tag{5.75}$$

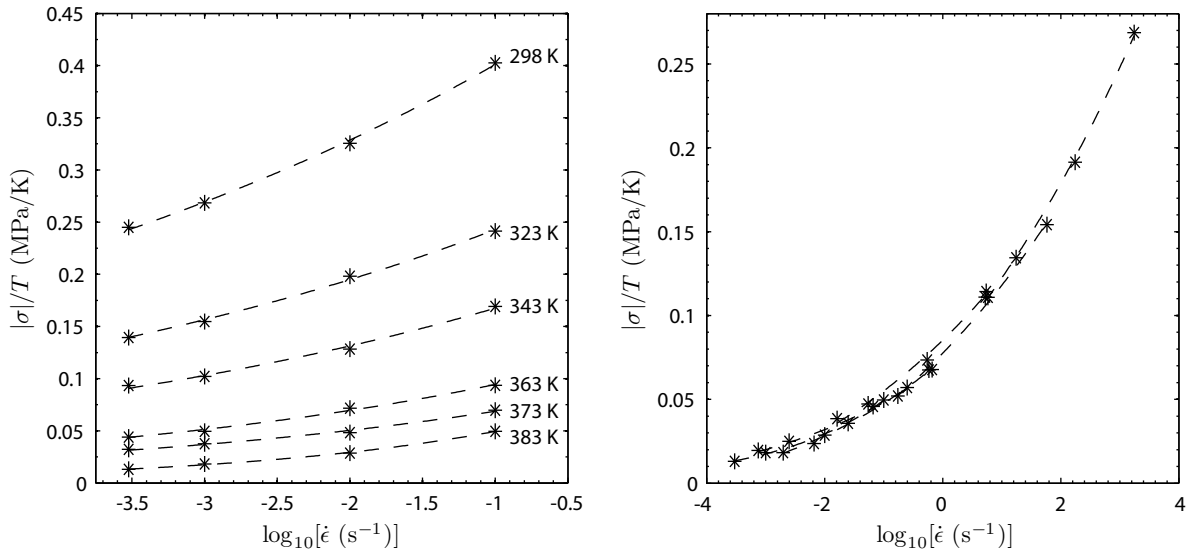

Figure 5-5: Ratio of compressive yield stress to temperature as a function of the logarithm of strain-rate. (*) indicates experimental results, (- -) indicates estimated isotherms. The right figure shows the master curve constructed at 383 K from the data in the left figure.

where ϑ is the temperature of the experiment, ϑ_{ref} is the temperature that the data will be shifted to, and H and B are material parameters. Povolo and Hermida [9] and Richeton et al. [10] reasoned that these shift factors could be equated with the material parameters used in the cooperative model such that

$$\left.\begin{aligned} H &= \frac{\Delta F}{k_B \ln 10} \\ B &= -r(\vartheta = 0) = -r_1\, \theta_r \end{aligned}\right\} \tag{5.76}$$

This gives some physical significance to the values of the shift factors that are chosen. We have used Richeton's [10] value of ΔF to establish the H shift factor, and then selected B to match our data; the values are listed in Table 5.1. Figure 5-5 shows the master curve constructed at $\vartheta_{\mathrm{ref}} =$ 383 K using these shift factors.

To complete the fitting of the flow function (5.71) to the master curve, we introduce three assumptions:

- The pressure sensitivity parameter α_p is set equal to 0.353 [14].
- The internal stress r vanishes at the glass transition temperature [11]; that is $\vartheta_r = \vartheta_g$, and $r(\vartheta_g) = 0$.
- The glass transition is assumed to occur at a single temperature independent of both strain-rate and pressure. For the purposes of fitting the yield point, we assume $\vartheta_g = 383$ K.
- The initial value of the isotropic resistance $S_i^{(1)}$ is equal to zero, and the isotropic resistance $S^{(1)}$ does not evolve; that is $\dot{S}^{(1)} = 0$ and $S^{(1)} = S_i^{(1)} = 0$.

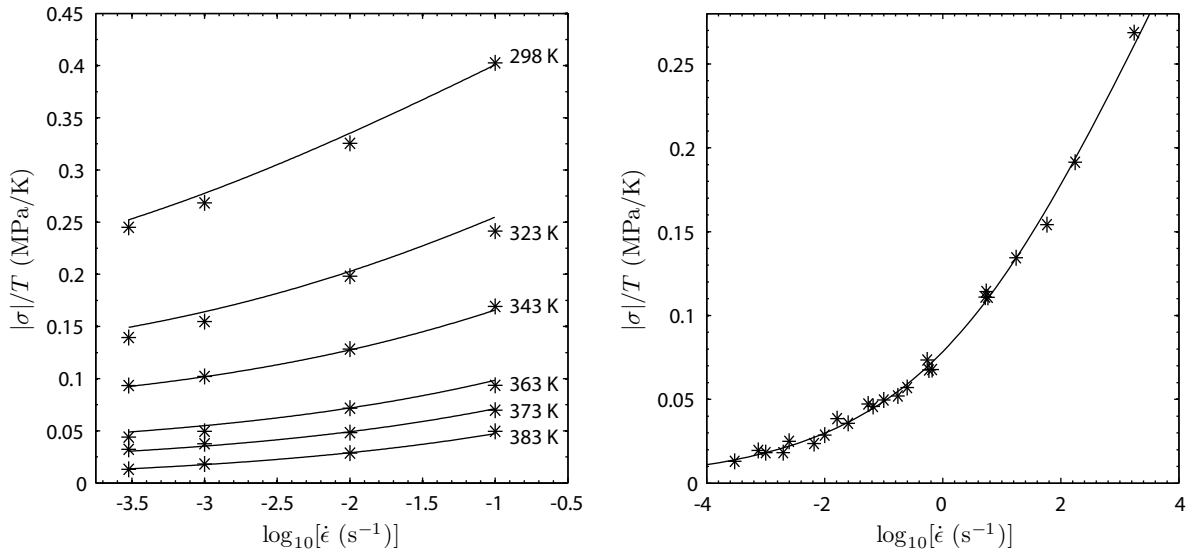

Figure 5-6: Fit of flow function for compressive yield stress normalized by temperature versus strain-rate. (*) indicates experimental results, (-) indicates model. Fit of flow function to master curve at 383 K.

Therefore, for a master curve constructed at $\vartheta_{\mathrm{ref}} = \vartheta_g = 383$ K, the internal stress term drops out of the flow function (5.71) resulting in

$$\frac{|\sigma_y|}{\vartheta_g} = \frac{2k_B}{V}\left(1 - \frac{\alpha_p}{3}\right)^{-1} \sinh^{-1}\left[\left(\frac{\dot{\epsilon}}{\dot{\epsilon}^*(\vartheta_g)}\right)^m\right] \tag{5.77}$$

with the list of unknown parameters reduced to: $\{V,\, \dot{\epsilon}^*(\vartheta_g),\, m\}$. A non-linear least-squares fitting method was used in MATLAB to obtain these parameters from the shifted experimental data. Subsequently, by considering (5.72), (5.73), and (5.76), the values of r_1 and $\dot{\epsilon}_0$ are easily determined. The complete set of parameters is listed in Table 5.1. The resulting fit to the 383 K master curve is shown in Figure 5-6 along with the corresponding result for the unshifted experimental data.

In the glass transition region, the yield stress drops off to zero very rapidly and has been shown to follow a WLF-like trend. Therefore, for temperatures above ϑ_g the temperature dependence of $\dot{\epsilon}^*$ becomes [10]

$$\dot{\epsilon}^* = \dot{\epsilon}_0^{(1)} \exp\left(-\frac{\Delta F^{(1)}}{k_B \vartheta_g}\right) \exp\left(\frac{\ln 10 \times c_1^*(\vartheta - \vartheta_g)}{c_2^* + \vartheta - \vartheta_g}\right) \quad \text{if} \quad \vartheta \geq \vartheta_g. \tag{5.78}$$

where c_1^* and c_2^* are WLF parameters which govern the change of the characteristic strain-rate through the glass transition region. To determine these two material parameters, the complete one-dimensional model is implemented in MATLAB and values for $\dot{\epsilon}^*$ are chosen for each of the experiments at temperatures greater than ϑ_g. The selected values of $\dot{\epsilon}^*$ are shown in Figure 5-7 along with a fit to the function (5.78). The material parameters used to obtain this fit are listed in Table 5.1.

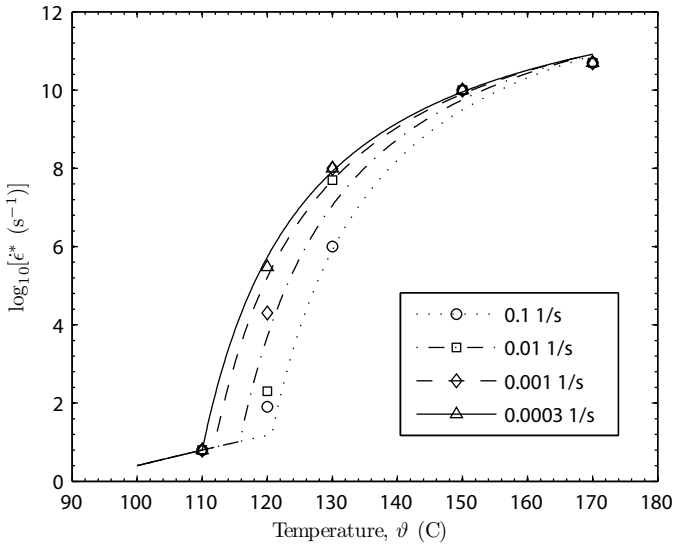

Figure 5-7: WLF fit of characteristic strain-rate $\dot{\epsilon}^*$ versus temperature above the glass transition temperature ϑ_g. Symbols indicate selected value for fitting one-dimensional MATLAB model, lines indicate fit of function given in (5.78).

Table 5.1: PMMA material parameters for yield point calibration

Parameter	Value
H (s^{-1} K^{-1})	5.7×10^3
B (MPa)	-180
V (m^3)	2.11×10^{-28}
m	0.218
$\dot{\epsilon}_0$ (s^{-1})	1.15×10^{16}
ΔF (kJ mol^{-1})	109
r_1 (MPa K^{-1})	0.47
ϑ_r (K)	383
c_1^*	13
c_2^* (K)	16

Back Stress

Once the yield data has been satisfactorily calibrated, the internal stress $r(\vartheta)$ in the flow function can be replaced with the stretch-dependent back stress σ_{back}. To begin, we note that for *compression*

$$D^p = -\dot{\epsilon}^p, \tag{5.79}$$

and we may then rewrite the evolution equation for A (5.61) in *compression* as

$$\dot{A} = -(2 + \gamma \ln A)\, A\, \dot{\epsilon}^p. \tag{5.80}$$

It follows then that the saturation value of A in *compression* is

$$A^* = \exp\left(-\frac{2}{\gamma}\right). \tag{5.81}$$

Combining this result with the equation for the back stress (5.51) gives the saturation value of the back stress as a function of the material parameters $C(\vartheta)$ and γ

$$\sigma^*_{\text{back}}(\vartheta) = 3\,\frac{C(\vartheta)}{\gamma}\,. \tag{5.82}$$

Equating the back stress saturation value with the internal stress r gives these relations between the back stress moduli and the internal stress parameters

$$\left.\begin{aligned} \vartheta_C &= \vartheta_r, \\ \frac{X_C}{\gamma} &= \frac{r_1}{3}\,. \end{aligned}\right\} \tag{5.83}$$

To determine γ, we note that it controls the rate of saturation of the back stress. This is highlighted in Figure 5-8 where the back stress and total stress response are shown with varying values of γ but with a constant ratio of C/γ (and therefore constant σ^*_{back}. As γ increases, the rate of saturation of the back stress increases. Similarly, γ is also related to the viscoelastic response of the material. Therefore, γ should be chosen such that the creep and total stress-strain response of the material is calibrated suitably throughout the temperature range of interest. Since we do not have a complete set of creep data for our entire temperature range, we select (γ = constant) and fit it to room-temperature creep data from Anand and Ames [14] in Figure 5-9 and also choose it such that the unloading curvature at room temperature is suitably fit. The values of all the back stress parameters are shown in Table 5.5.

Elastic Modulus

The elastic modulus is assumed to decrease linearly with temperature according to (5.46) and acquires rate-dependence through the rate-sensitivity of the glass transition (5.44). The initial modulus was estimated from stress-strain data for all our data sets and then fit to (5.46) and (5.44) as seen in Figure 5-10. The resulting material parameters are shown in Table 5.5.

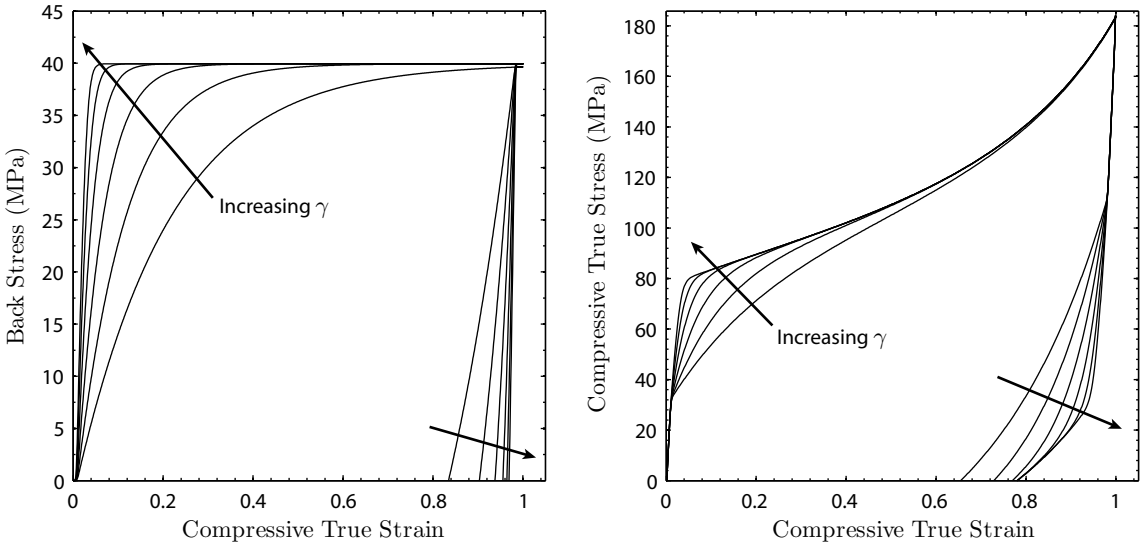

Figure 5-8: Effect of sequentially doubling the the material parameter γ from 5 to 160 on the back stress (left) and complete stress-strain response (right) for a constant ratio of C/γ.

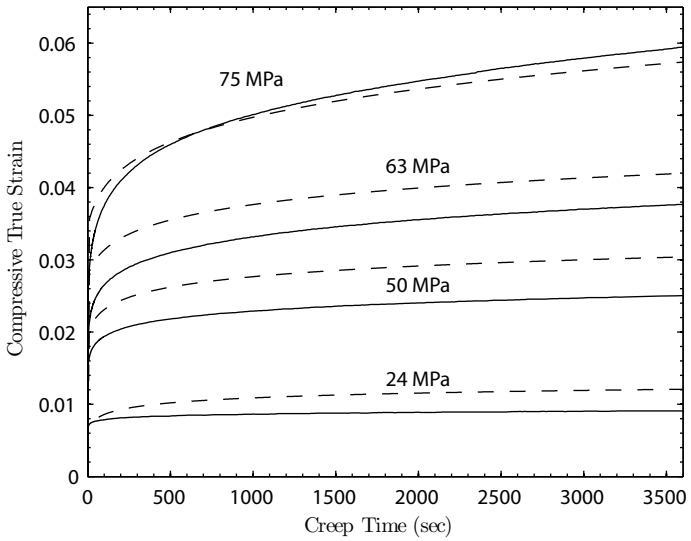

Figure 5-9: One-dimensional MATLAB simulations (- -) and uniaxial compressive creep tests (–) at four pre-yield stress levels.

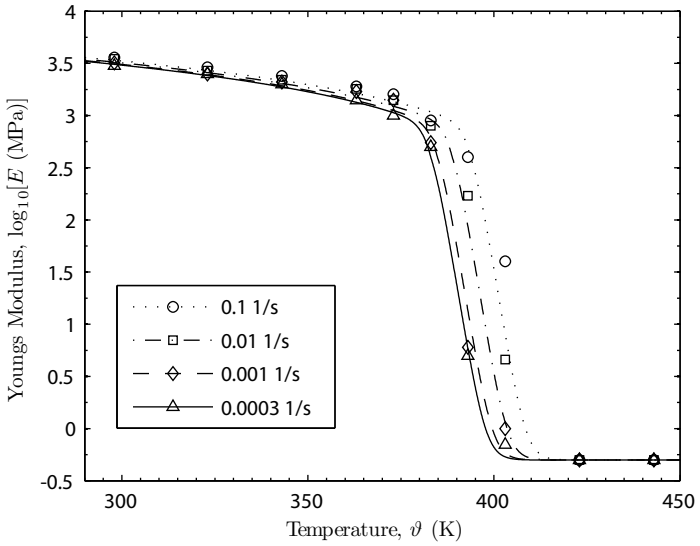

Figure 5-10: Fit of elastic modulus to phenomenological functions (5.46) and (5.44).

Large Strain Behavior

To calibrate the large strain behavior of PMMA, the complete one-dimensional model is implemented in MATLAB and the following assumptions are made:

- There is no inelastic deformation associated with slipping of the molecular network; that is $\dot{\epsilon}^{p\,(2)} = 0$.
- The large strain hardening behavior of PMMA is rate-independent; that is μ_{R} and $I_{1,\max}$ are rate-independent.

Following these assumptions, values for μ_{R} and $I_{1,\max}$ are chosen for each testing temperature at the lowest strain-rate (3×10^{-4}/s). To do this, we note that the parameter μ_R controls the initial slope of the post-yield hardening and $I_{1,\max}$ controls the "locking stretch", the stretch at which rapid hardening sets in and the stress appears to go to infinity. The selected values for μ_{R} are shown in Figure 5-11 along with a fit to the phenomenological function (5.64). It is difficult to estimate $I_{1,\max}$ from our experimental data however. This is because our data does not extend to strains that are large enough to observe a substantial change in the hardening slope. We therefore assume a suitable constant value below ϑ_g and allow it to transition smoothly to a higher value above the glass transition using the phenomenological function of (5.65). The selected values of $I_{1,\max}$ are shown in Figure 5-12 along with the functional fit. The material parameters used to describe μ_{R} and $I_{1,\max}$ are shown in Table 5.5.

High-Temperature Network Slipping

We have very little experimental data to calibrate the high-temperature network slipping parameters, however, we can complete a rough calibration given some additional assumptions:

- In order to allow for inelastic deformation associated with slipping of the molecular network, $\dot{\epsilon}^{p\,(2)}$ is no longer restricted.

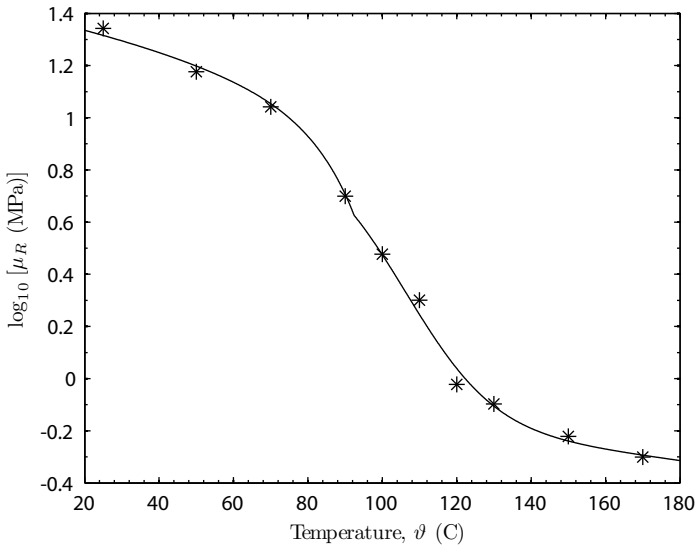

Figure 5-11: Fit of Gent modulus versus temperature. (*) indicates selected value for the given temperature at a strain-rate of 3×10^{-4}, (–) indicates fit of phenomenological function given in (5.64).

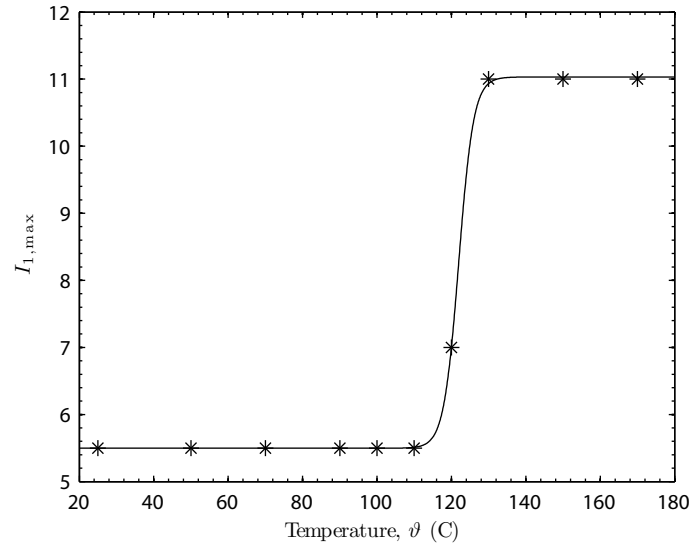

Figure 5-12: Fit of Gent locking parameter versus temperature. (*) indicates selected value for the given temperature at a strain-rate of 3×10^{-4}, (–) indicates fit of phenomenological function given in (5.65).

- The activation energy for network slipping is equivalent to the activation energy for the intermolecular resistance below the glass transition; that is $\Delta F^{(1)} = \Delta F^{(2)}$.
- The deformation resistance $S^{(2)}$ does not evolve with strain and is independent of temperature.

Recall that the flow function for $\dot{\epsilon}^{p\,(2)}$ is given by

$$\dot{\epsilon}^{p(2)} = \dot{\epsilon}_0^{(2)} \exp\left\{\frac{-\Delta F^{(2)}}{k_B \vartheta}\right\} \left(\frac{|\sigma_y|}{S^{(2)}}\right)^{1/m^{(2)}} . \tag{5.84}$$

At yield, for a given strain-rate $\dot{\epsilon}$ and temperature ϑ, we assume that $S^{(2)} = \sigma_y$ and approximate the flow function as

$$\dot{\epsilon}_0^{(2)} = \dot{\epsilon} \exp\left\{\frac{\Delta F^{(2)}}{k_B \vartheta}\right\} , \tag{5.85}$$

so that a value for $\dot{\epsilon}_0^{(2)}$ can be obtained. We observe obvious slipping in our experimental data for the test at 170 C at a strain-rate of 3×10^{-4}/s and use these values to choose $\dot{\epsilon}_0^{(2)}$. Values for $S^{(2)}$ and $m^{(2)}$ are then chosen to provide a good fit for the data in the temperature region above the glass transition. The material parameters used to obtain this fit are shown in Table 5.5.

The resulting stress-strain curves at this stage of the calibration procedure are shown in Figures 5-13, 5-14, 5-15 and 5-16. For the lower strain-rates of 3×10^{-4}/s and 10^{-3}/s, the simulations correlate with the experimental data very well, yet for the higher strain-rates of 10^{-2}/s and 10^{-1}/s, there is an excessive discrepancy in the large strain behavior between the experiments and simulations. This discrepancy is caused by thermal softening in the material due to inelastic dissipation, and at this point we are using an isothermal version of the model that does not account for internal heating. Later, in Section 5.3.3, we add thermo-mechanical coupling to the model in order to capture the internal heating effect.

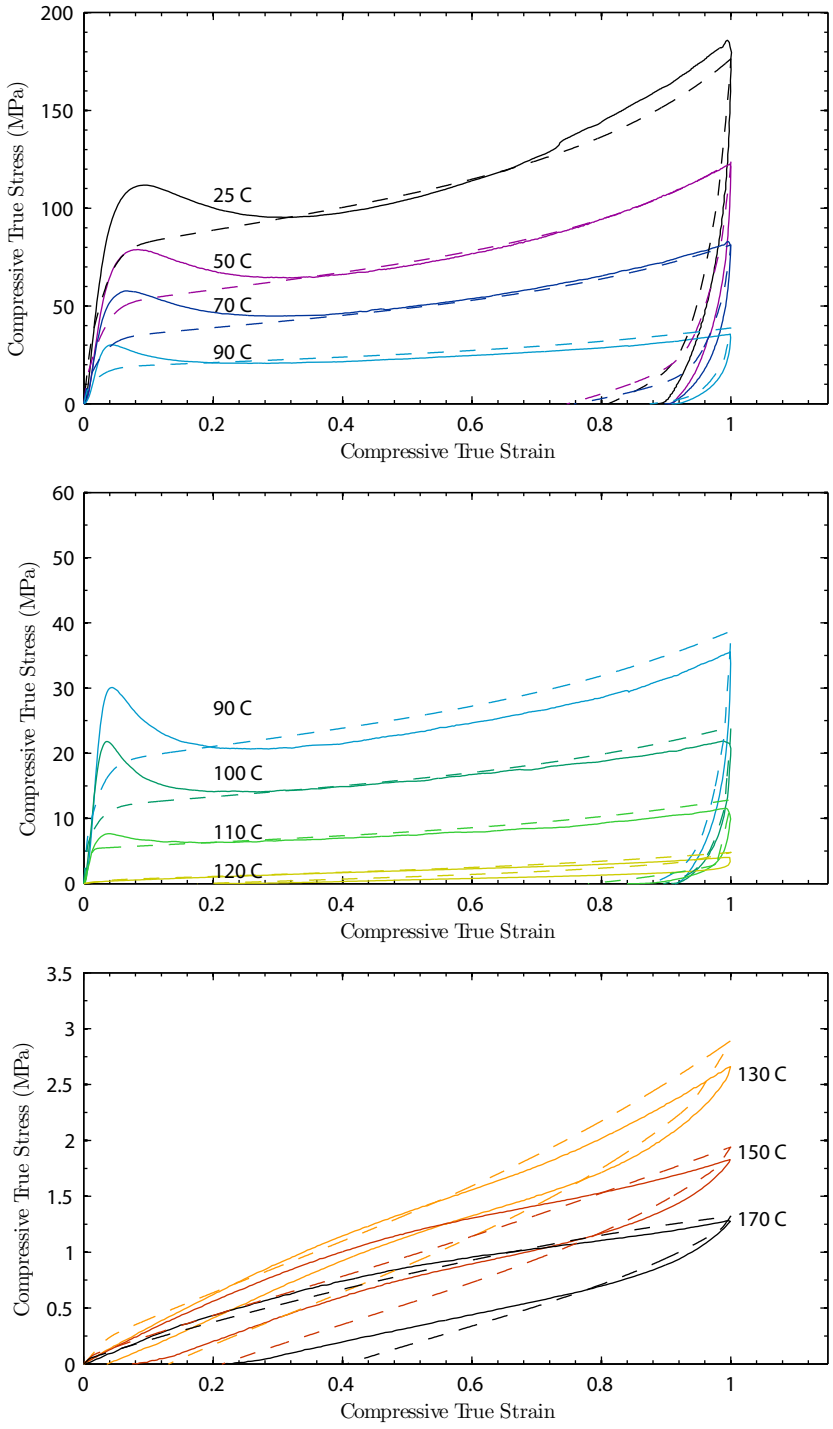

Figure 5-13: One-dimensional MATLAB simulation (- -) and uniaxial compression tests (–) at a strain-rate of 3×10^{-4}/s and various temperatures ranging from room temperature through 170 C. Simulation includes yield-point and large strain calibrations only.

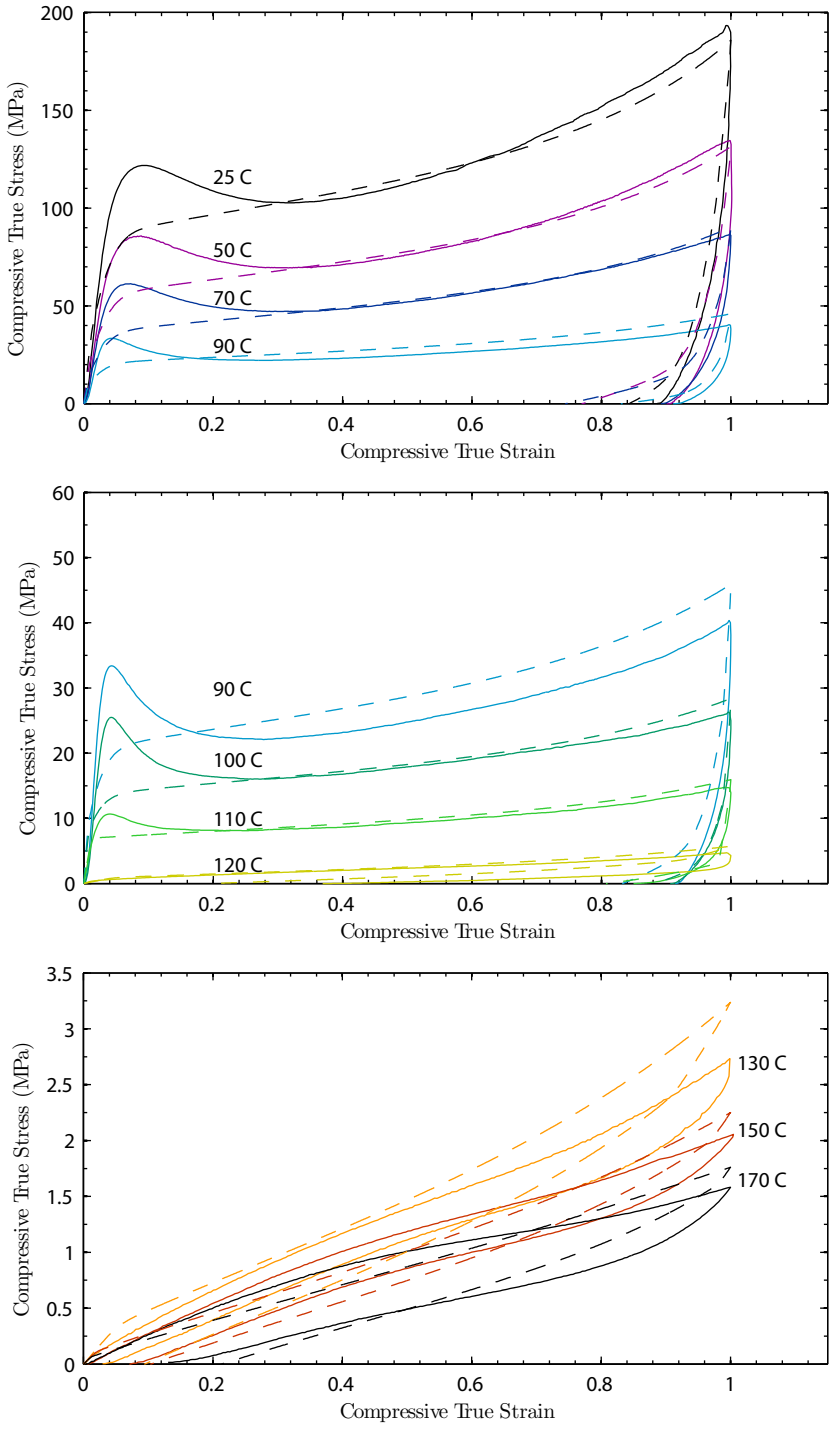

Figure 5-14: One-dimensional MATLAB simulation (- -) and uniaxial compression tests (–) at a strain-rate of 10^{-3}/s and various temperatures ranging from room temperature through 170 C. Simulation includes yield-point and large strain calibrations only.

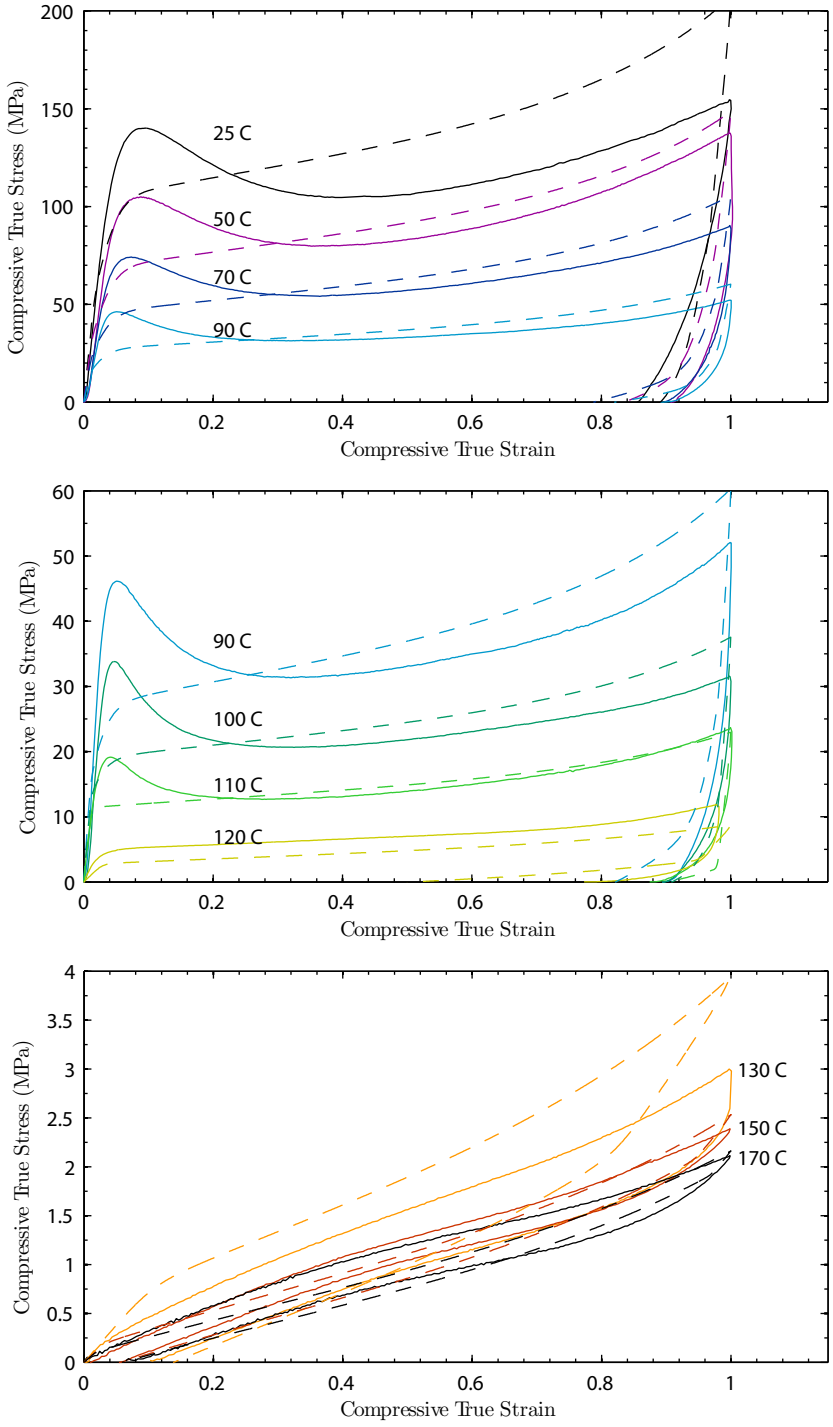

Figure 5-15: One-dimensional MATLAB simulation (- -) and uniaxial compression tests (–) at a strain-rate of 10^{-2}/s and various temperatures ranging from room temperature through 170 C. Simulation includes yield-point and large strain calibrations only.

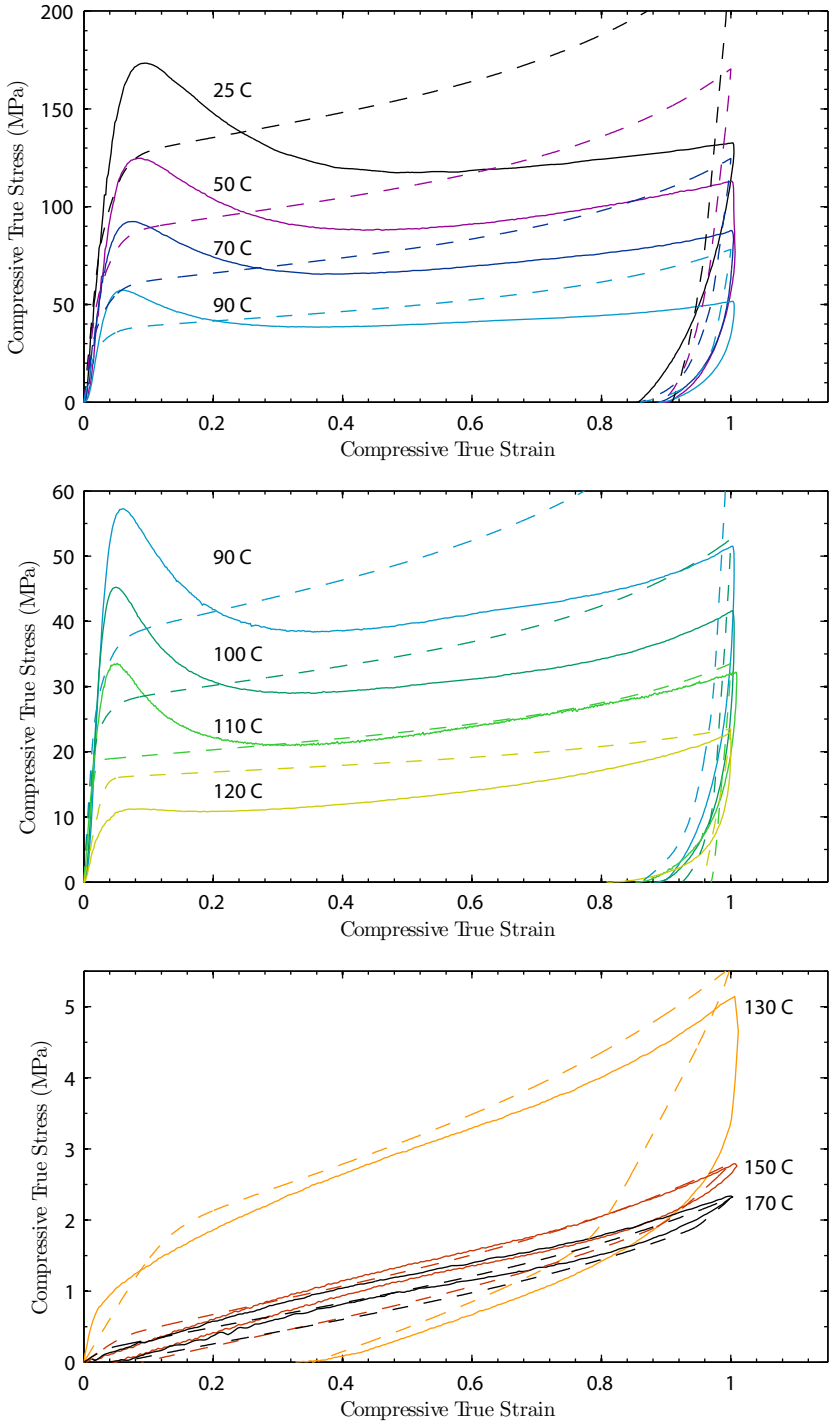

Figure 5-16: One-dimensional MATLAB simulation (- -) and uniaxial compression tests (–) at a strain-rate of 10^{-1}/s and various temperatures ranging from room temperature through 170 C. Simulation includes yield-point and large strain calibrations only.

Yield Peak

To calibrate the yield peak, we must determine the list of parameters which guide the evolution of $S^{(1)}$ and φ: $\{\varphi_i, \varphi^*, g, b, h\}$.

While the initial and saturation values of the free-volume should depend on strain-rate and temperature, we do not have the appropriate data to choose these values accordingly. Therefore, below the glass-transition we assume these parameters to be $\varphi_i = 0$ and $\varphi_g^* = 0.001$. Above the glass transition, we assume $\varphi^* = \varphi_i = 0$ and we use a hyperbolic-tangent function (5.59) to smoothly interpolate φ^* within the glass transition. Note that rate-dependence in the glass transition region is introduced by use of the rate-dependent glass transition temperature ϑ_g in (5.59).

Next, several simulations using different values of $\{b, g, h\}$ must be performed to obtain the correct shape of the yield peak at the various strain-rates and temperatures. Figure 5-17 shows how these parameters affect the shape of the yield-peak in order to aid the iterative curve-fitting procedure. Once these parameters are determined for each stress-strain curve, they were found to fit the functional forms given in (5.60); the parameters for these functions are listed in Table 5.5. The final stress-strain curves including the yield peak calibration are shown in Figures 5-18, 5-19, 5-20 and 5-21.

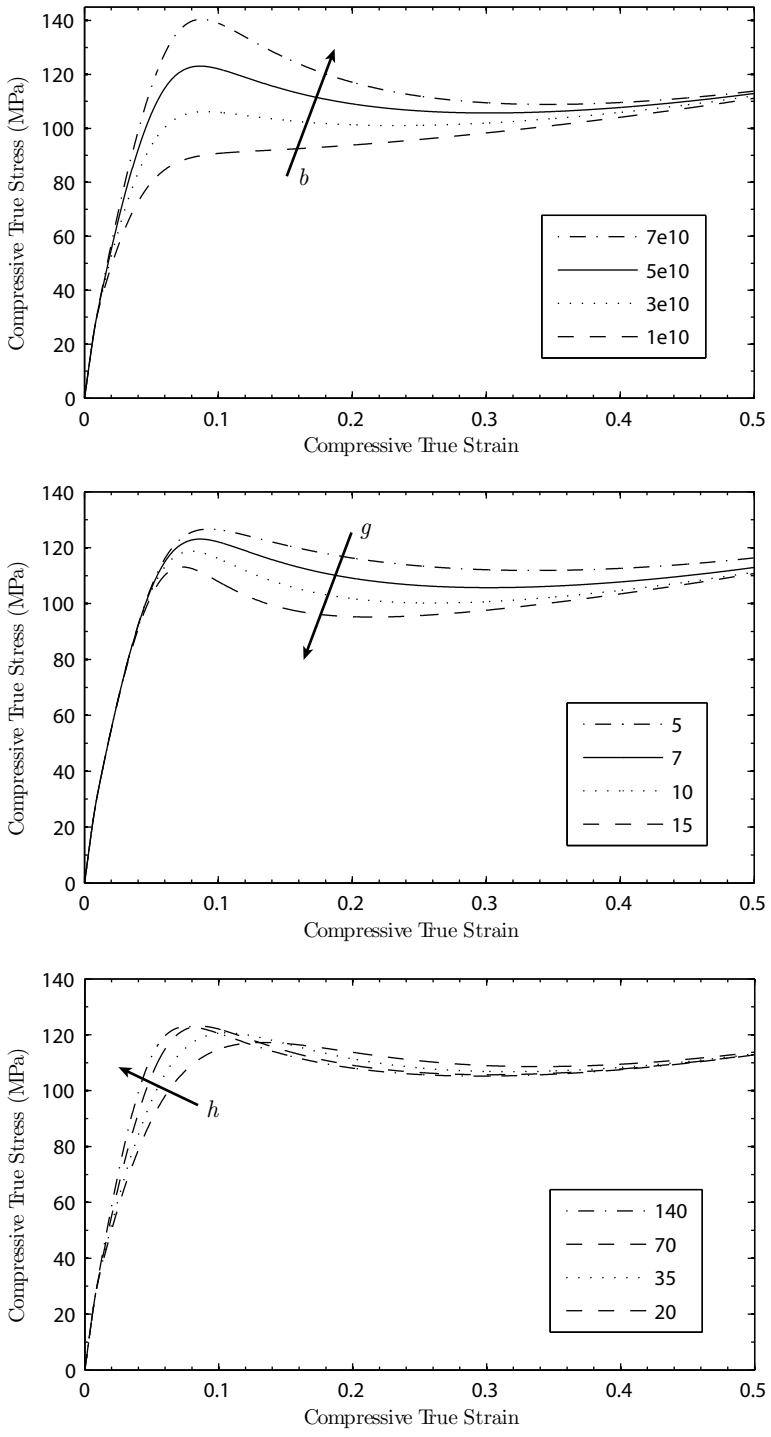

Figure 5-17: Schematic of the effect of the material parameters $\{b,\ g,\ h\}$ on the shape of the yield peak of the stress-strain curve. Arrows indicate an increase of the parameter: (top) b, (middle) g, (bottom) h.

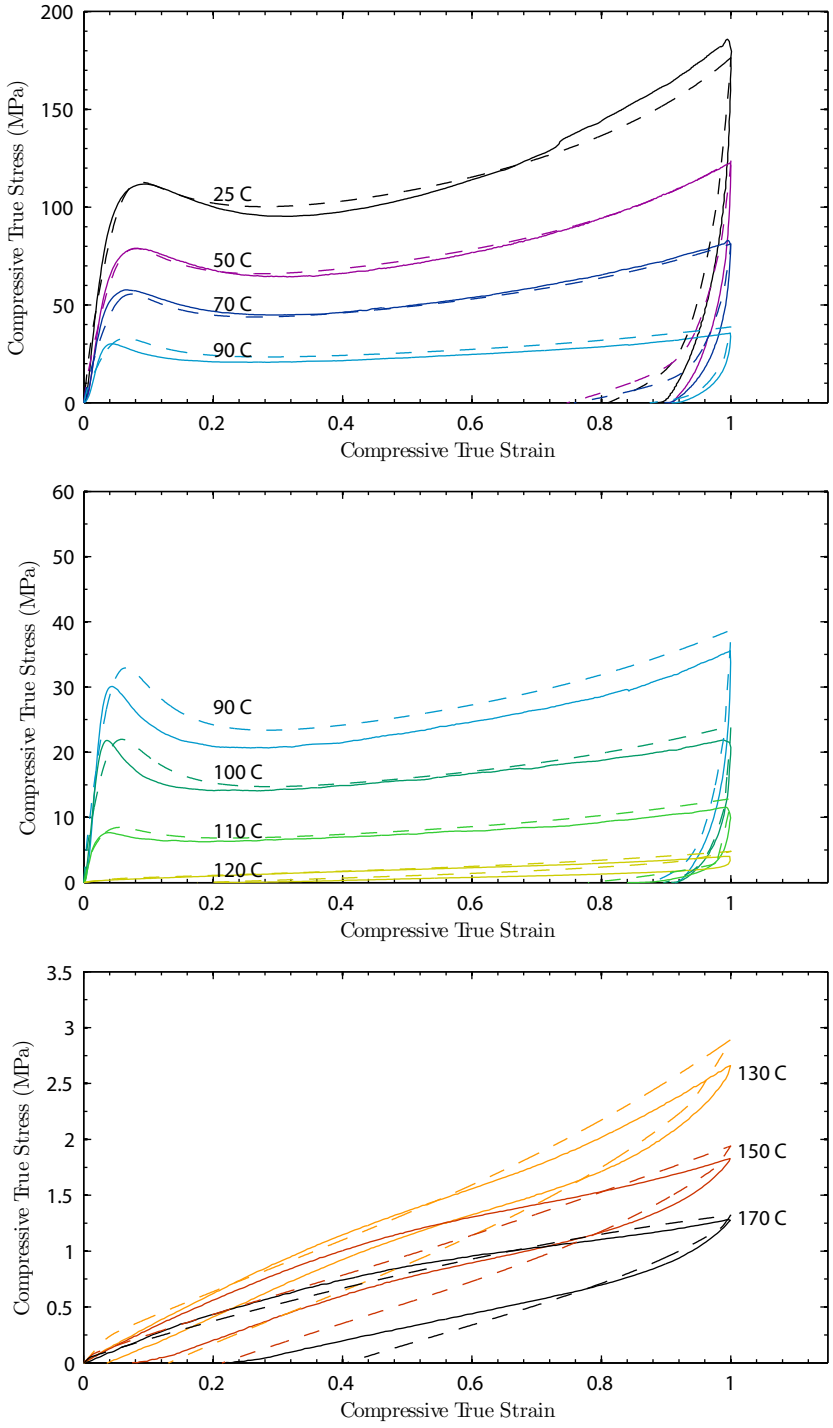

Figure 5-18: One-dimensional MATLAB simulation (- -) and uniaxial compression tests (–) at a strain-rate of 3×10^{-4}/s and various temperatures ranging from room temperature through 170 C.

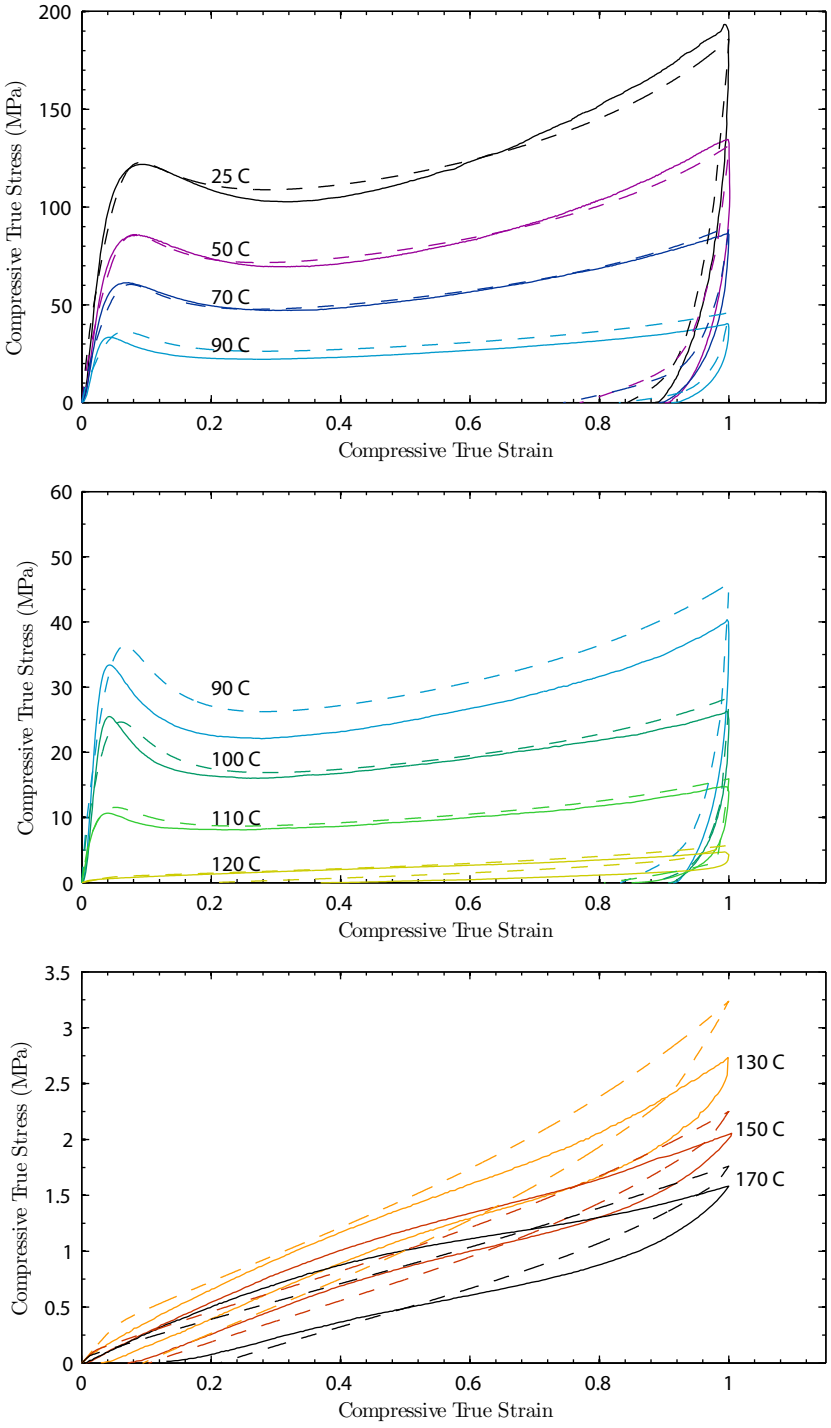

Figure 5-19: One-dimensional MATLAB simulation (- -) and uniaxial compression tests (–) at a strain-rate of 10^{-3}/s and various temperatures ranging from room temperature through 170 C.

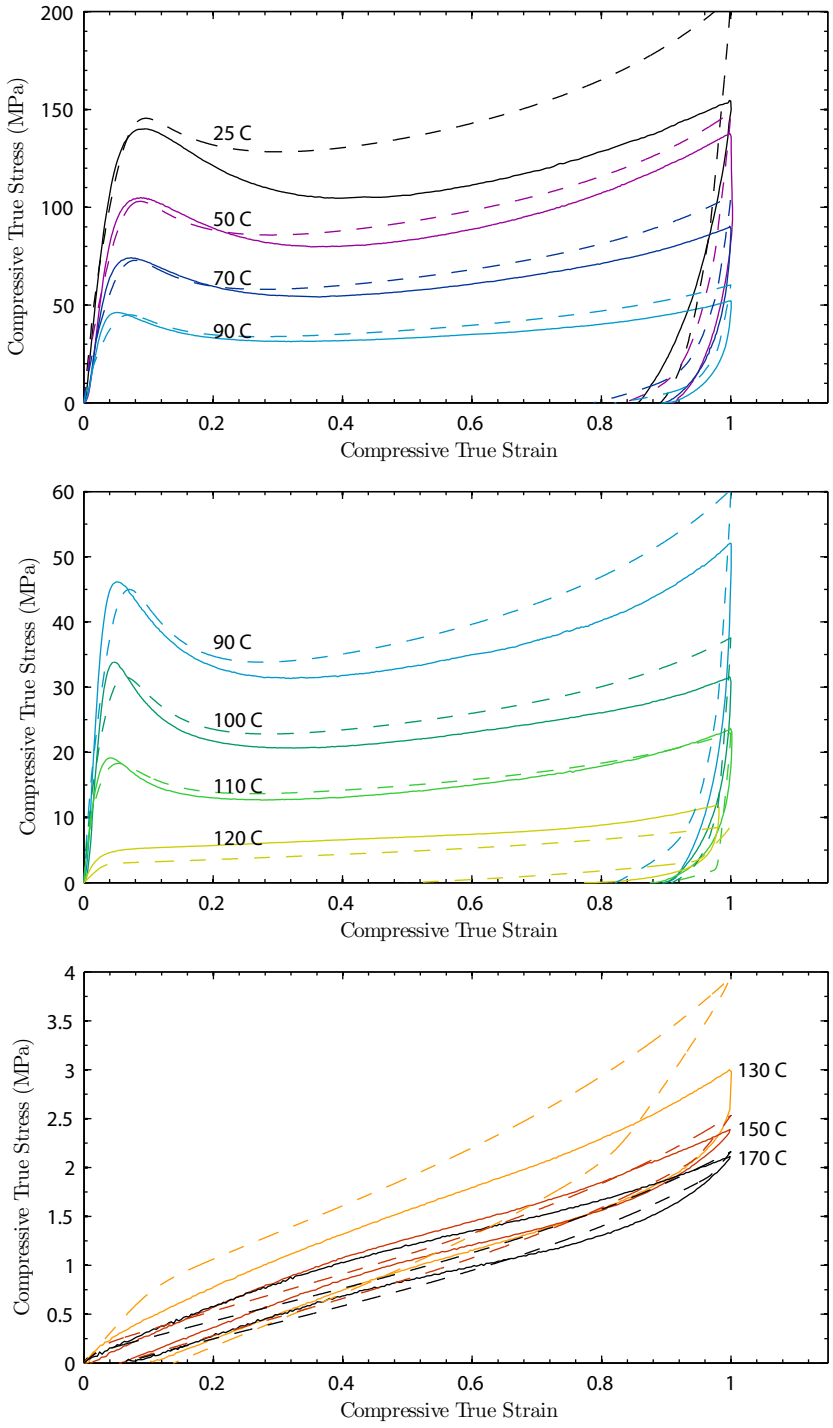

Figure 5-20: One-dimensional MATLAB simulation (- -) and uniaxial compression tests (–) at a strain-rate of 10^{-2}/s and various temperatures ranging from room temperature through 170 C.

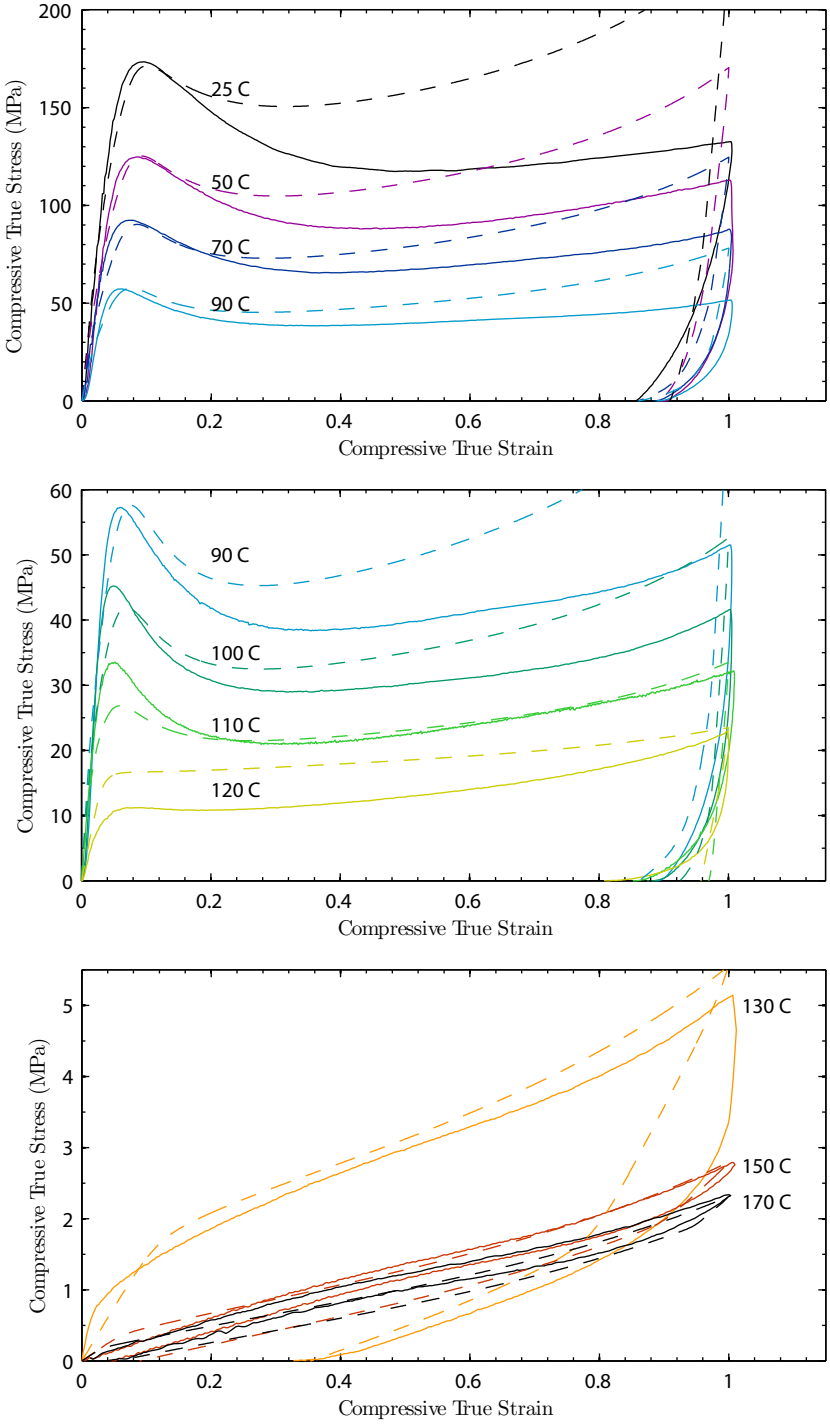

Figure 5-21: One-dimensional MATLAB simulation (- -) and uniaxial compression tests (–) at a strain-rate of 10^{-1}/s and various temperatures ranging from room temperature through 170 C.

5.3.2 Three-Dimensional Model Calibration Procedure

Except for the list of parameters $\{\alpha_p,\, \nu_0,\, V,\, S_i^{(1)},\, b,\, g,\, h,\, \gamma,\, S^{(2)}\}$, the values of the one-dimensional material parameters are unchanged when used in the three-dimensional equations. Noting that

$$\tau\nu = \sigma\dot{\epsilon}, \quad \sigma = \sqrt{3}\tau, \quad \dot{\epsilon} = \frac{\nu}{\sqrt{3}} \tag{5.86}$$

the list of parameters $\{\alpha_p,\, \nu_0,\, V,\, S_i^{(1)},\, b,\, g,\, h,\, \gamma\}$ may be converted from the one-dimensional tension form to the three-dimensional shear form using

$$\left.\begin{aligned}
\dot{\epsilon}_0 &= \tfrac{1}{\sqrt{3}}\,\nu_0\,, \\
\alpha_p^{\text{tension}} &= \sqrt{3}\,\alpha_p^{\text{shear}}\,, \\
S_i^{(1)\,\text{tension}} &= \sqrt{3}\,S_i^{(1)\,\text{shear}}\,, \\
V^{\text{tension}} &= \tfrac{1}{\sqrt{3}}\,V^{\text{shear}}\,, \\
b_1^{\text{tension}} &= \sqrt{3}\,b_1^{\text{shear}}\,, \\
g_1^{\text{tension}} &= \sqrt{3}\,g_1^{\text{shear}}\,, \\
g_2^{\text{tension}} &= \sqrt{3}\,g_2^{\text{shear}}\,, \\
h^{\text{tension}} &= \sqrt{3}\,h^{\text{shear}}\,, \\
\gamma^{\text{tension}} &= \sqrt{3}\,\gamma^{\text{shear}}\,, \\
S^{(2)\,\text{tension}} &= \sqrt{3}\,S^{(2)\,\text{shear}}\,.
\end{aligned}\right\} \tag{5.87}$$

Further, assuming a value of Poisson's ratio

$$\nu_{\text{poi}} = \begin{cases} 0.35 & : \quad \vartheta \le \vartheta_g \\ 0.495 & : \quad \vartheta > \vartheta_g \end{cases} \tag{5.88}$$

we may use the standard relations for converting the elastic modulus E to the shear modulus G.

Figure 5-22 shows the results of using these conversion factors with the parameters determined from the one-dimensional calibration procedure. We see that the three-dimensional single-element result from ABAQUS/Explicit agrees fairly well with the one-dimensional MATLAB results. A slight adjustment of μ_{R} in ABAQUS brings the simulations into even closer agreement. The final stress-strain curves from the ABAQUS calculations are shown in Figures 5-23, 5-24, 5-25 and 5-26. The complete list of material parameters used in the ABAQUS calculations is in Table 5.6.

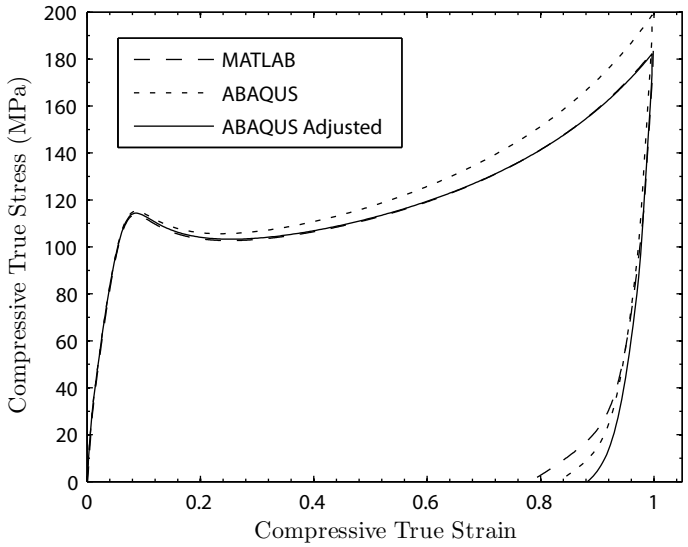

Figure 5-22: Comparison of one-dimensional MATLAB simulation (- -) to three-dimensional one-element ABAQUS simulation ($\cdots$) with material parameter conversion between the two models using only the relations in (5.87). Further adjustment of $\mu_{\mathrm{R}}^{\mathrm{ref}}$ and X_μ in ABAQUS (–) gives a better match to the MATLAB results.

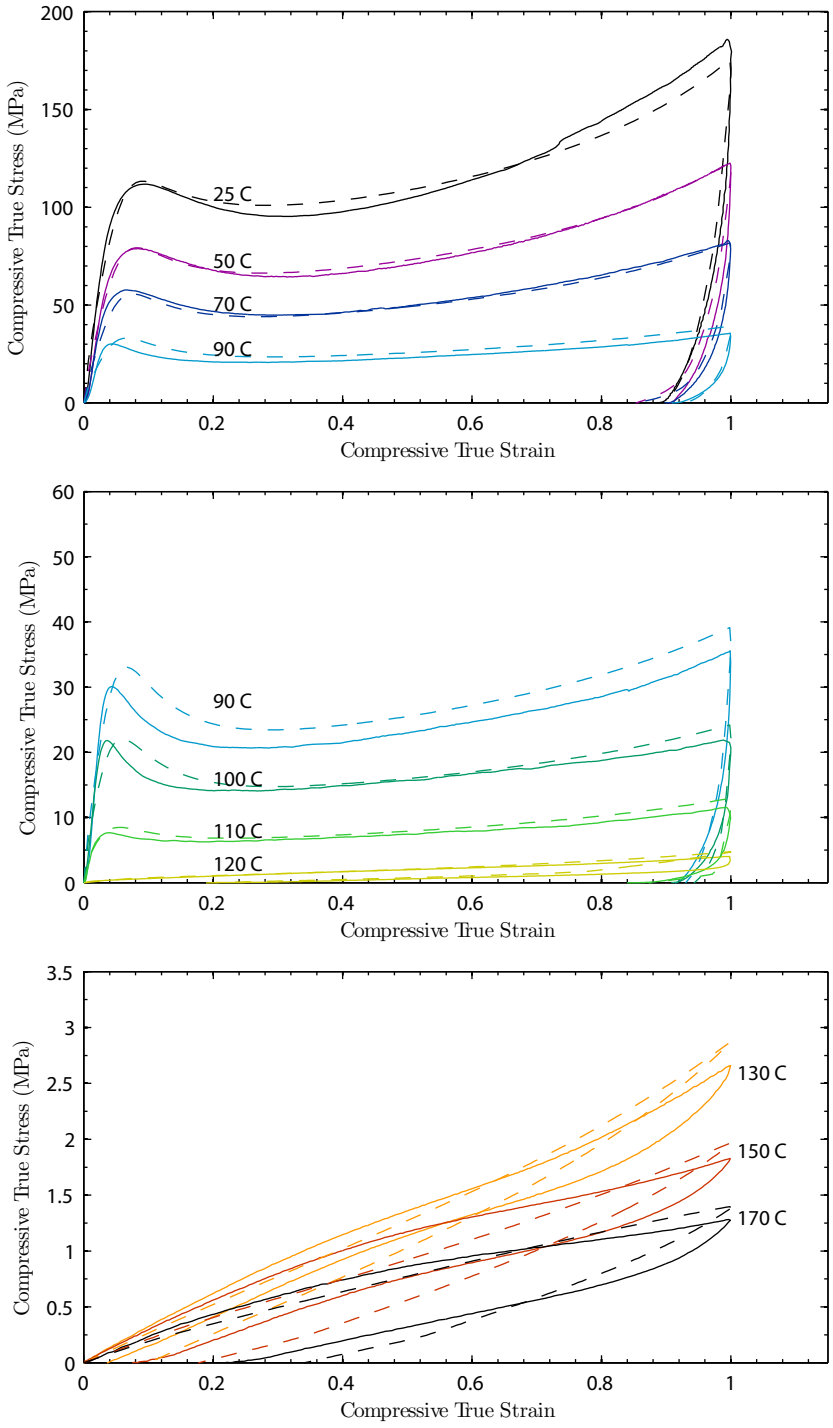

Figure 5-23: Three-dimensional one-element isothermal ABAQUS simulations (- -) and uniaxial compression tests (–) at strain-rates of 3×10^{-4}/s at temperatures ranging from room temperature through 170 C.

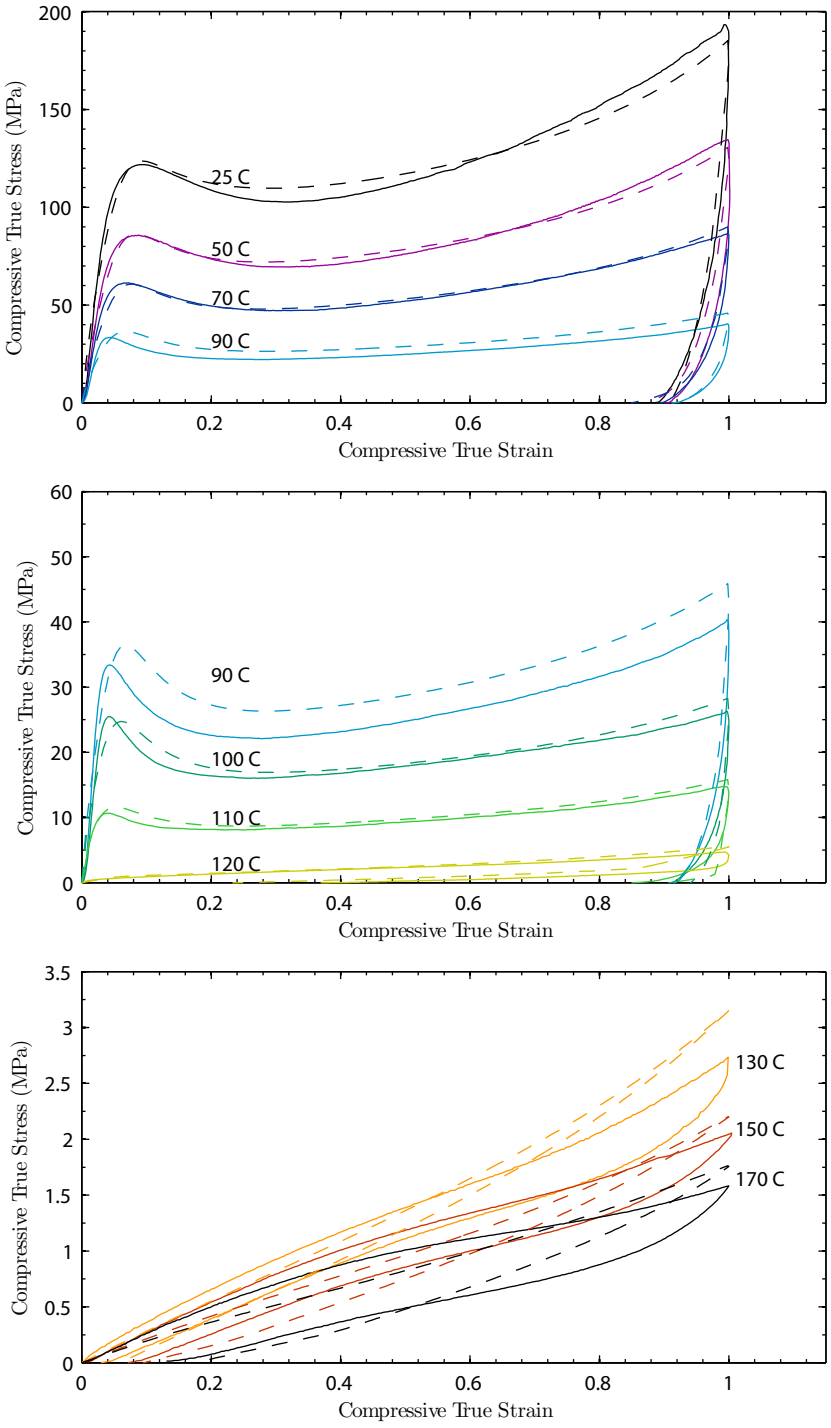

Figure 5-24: Three-dimensional one-element isothermal ABAQUS simulations (- -) and uniaxial compression tests (–) at strain-rates of 10^{-3}/s at temperatures ranging from room temperature through 170 C.

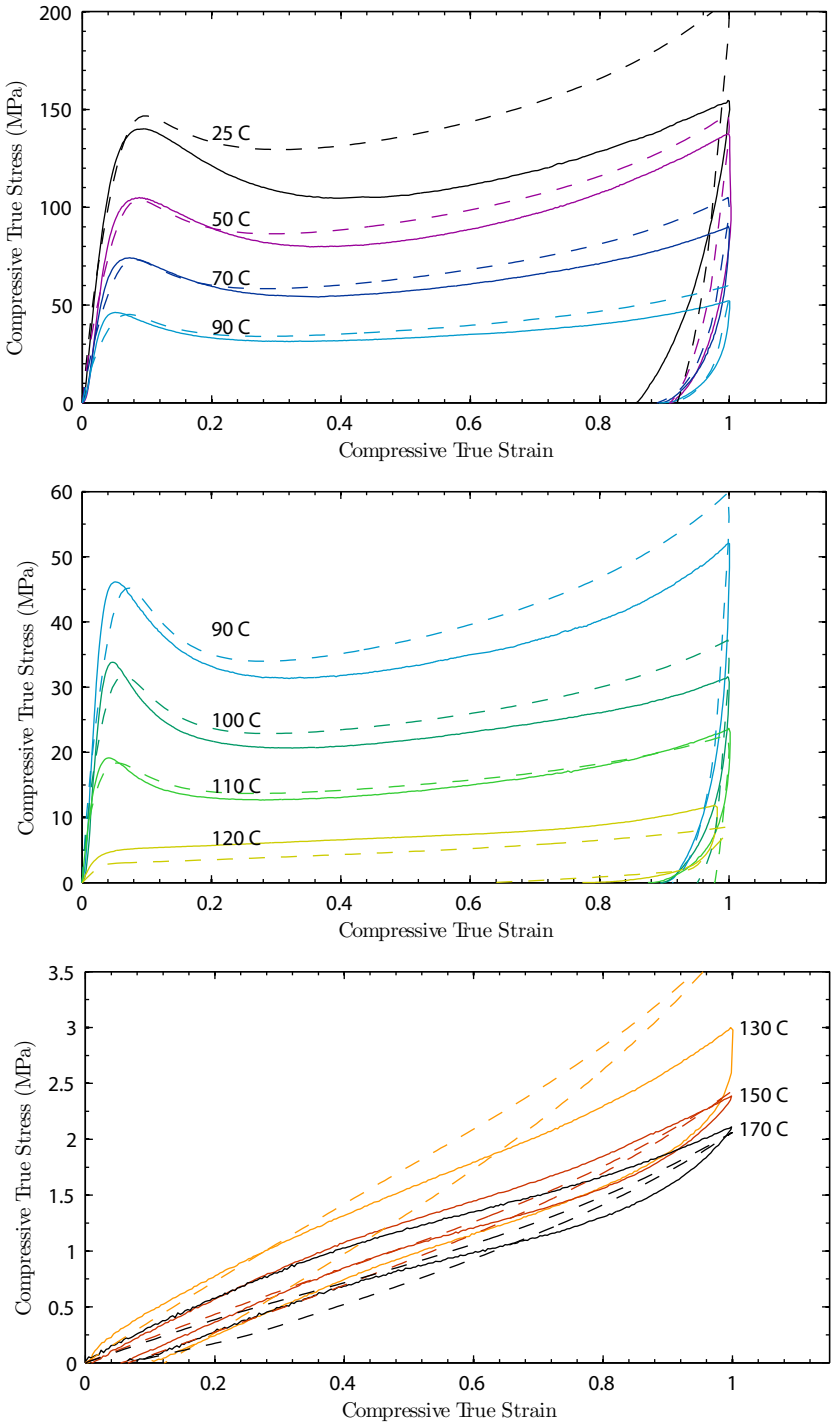

Figure 5-25: Three-dimensional one-element isothermal ABAQUS simulations (- -) and uniaxial compression tests (–) at strain-rates of 10^{-2}/s at temperatures ranging from room temperature through 170 C.

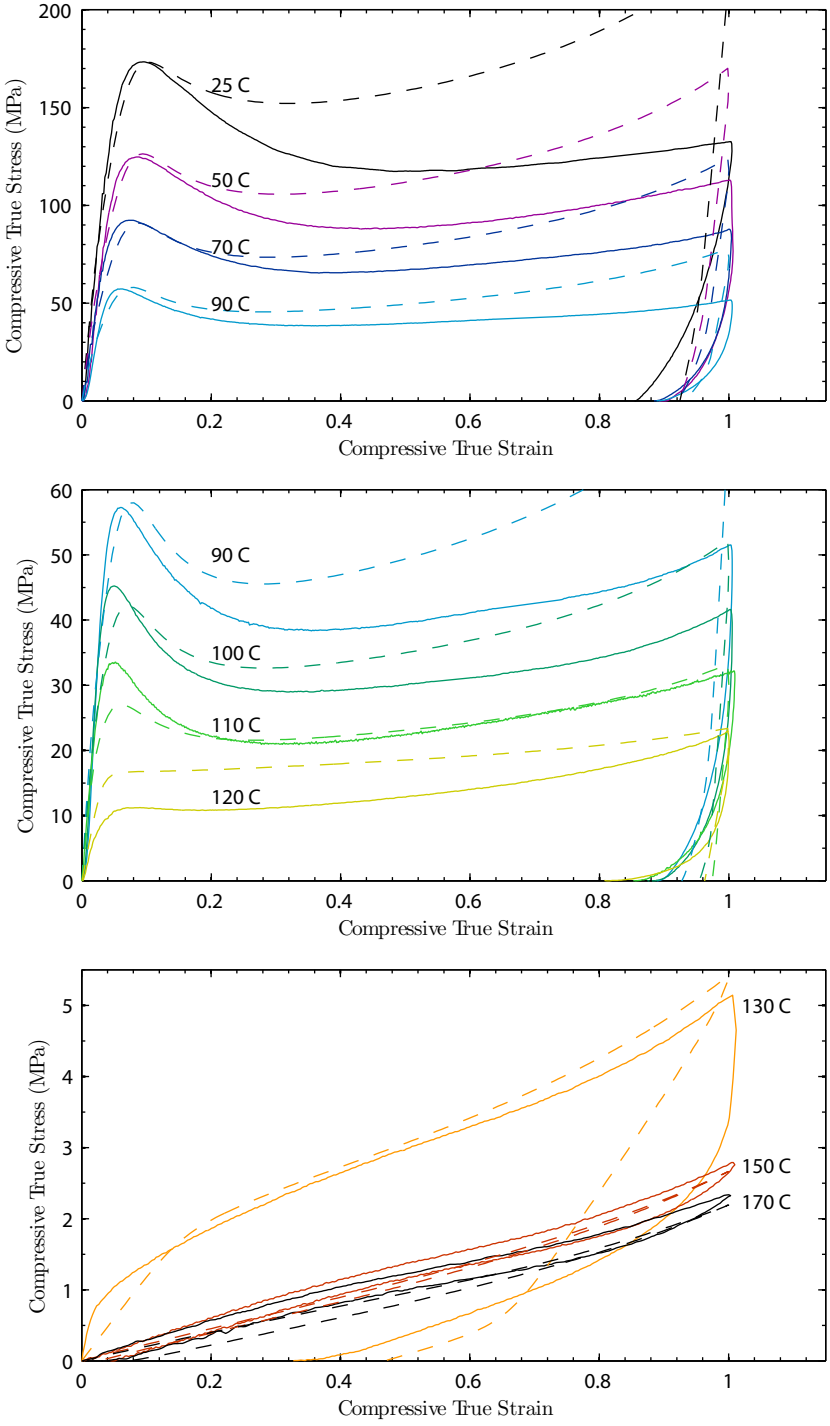

Figure 5-26: Three-dimensional one-element isothermal ABAQUS simulations (- -) and uniaxial compression tests (–) at strain-rates of 10^{-1}/s at temperatures ranging from room temperature through 170 C.

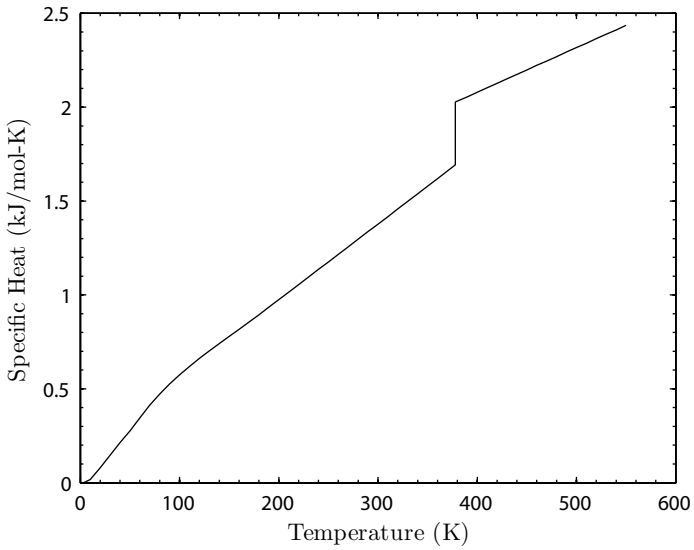

Figure 5-27: Specific heat of PMMA versus temperature. Reproduced from Gaur et al. [16]

5.3.3 Internal Heating

While the model works very well for the low strain-rates where the material behaves nearly isothermally (cf. Figures 5-23 and 5-24), there is a large discrepancy between the model and experiment at the higher strain rates of 10^{-2}/s and 10^{-1}/s (cf. Figures 5-25 and 5-26). This discrepancy is due to the thermal softening of the material caused by inelastic dissipation coupled with the low thermal diffusivity of PMMA [15]. In order to capture this internal heating, we must introduce a thermo-mechanical coupling in our finite element implementation using the heat equation of (5.41)

$$c\dot{\vartheta} = -\mathrm{Div}\,\mathbf{q}_{\mathrm{R}} + q_{\mathrm{R}} + \beta\left(\bar{\tau}^{(1)}\,\nu^{p\,(1)} + \bar{\tau}^{(2)}\,\nu^{p\,(2)} + \frac{1}{2}\,C\,\gamma\,|\ln\mathbf{A}|^2\right) \tag{5.89}$$

where the factor β is the fraction of inelastic work that is dissipated. To complete the thermo-mechanical coupling, we must also specify two additional material parameters: the specific heat c, and the thermal conductivity κ. The temperature dependence of these parameters is taken from the literature [16, 17] and reproduced in Figures 5-27 and 5-28 respectively.

Multi-Element Model

In order to accurately predict the temperature rise for intermediate strain-rates where isothermal or adiabatic approximations do not suffice, we must setup a realistic finite element model of our experimental apparatus that includes thermal interactions between the specimen and its environment [15]. Because our specimens are cylindrical, we have chosen to model the compression experiment as an axisymmetric problem with additional symmetry about the horizontal axis. A schematic of this model is shown in Figure 5-29. For the steel platen, we assume a basic thermoelastic material model whose material parameters are listed in Table 5.2. For the surface film coefficient between the specimen sidewall and air, we assume $h_1 = 40$ (W/m^2-K). We create a heat sink on the top

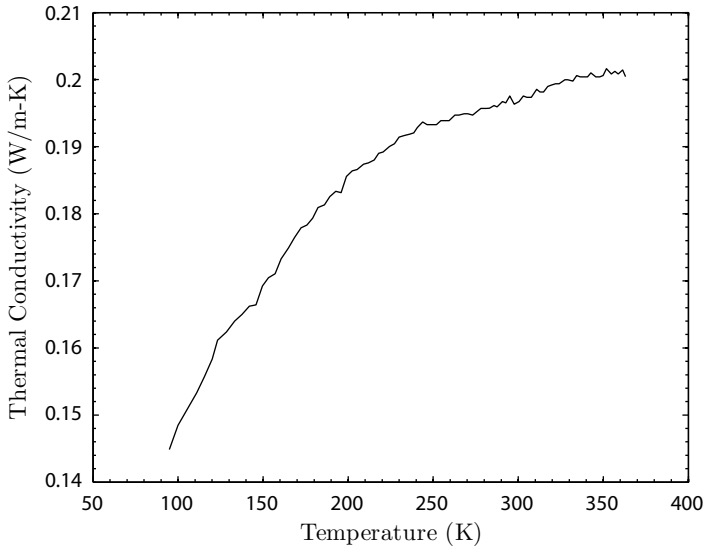

Figure 5-28: Thermal conductivity of PMMA versus temperature. Reproduced from Eiermann and Hellwege [17]

Table 5.2: Steel material parameters for thermo-mechanically coupled three-dimensional model

Parameter	Value
Young's Modulus, E (GPa)	200
Poisson's Ratio, ν	0.3
Density, ρ (kg m^{-3})	7833
Thermal Conductivity, κ (W m^{-1} K^{-1})	52
Specific Heat, c (J kg^{-1} K^{-1})	586

of the steel platen by fixing the nodes at the ambient temperature T_∞. At the interface between the PMMA specimen and the steel platen we assume frictionless contact. To assure excellent heat transfer at this interface, we use a thermal conductance of $k = 1000$ (W/m^2-K). The ambient temperature of each simulation T_∞ is initially constant throughout the specimen and platen. A true strain-rate velocity profile is applied to the top surface of the steel platen to impose deformation on the specimen.

The final stress-strain curves using this multi-element fully-coupled calculation in ABAQUS/Explicit are shown in Figures 5-30, 5-31, 5-32 and 5-33 for the various strain-rates and temperatures. An inelastic heat fraction of $\beta = 0.80$ was used in the heat equation (5.89) to obtain these results.

Figure 5-34 shows the contours of nodal temperature rise at a strain of -1.0 for the room temperature (25 C) simulation conducted at a strain-rate of 10^{-1}/s. As others have shown, there is a large gradient in temperature throughout the height and diameter of the specimen. Figure 5-35 shows experimental measurements of surface temperature rise from Mulliken [18] under a test of similar conditions compared with surface midpoint temperature measurements from our simulations. While the results do not match perfectly, the general trend of the experiments does seem to be well reproduced in the simulation, namely a large temperature rise for the high-rate

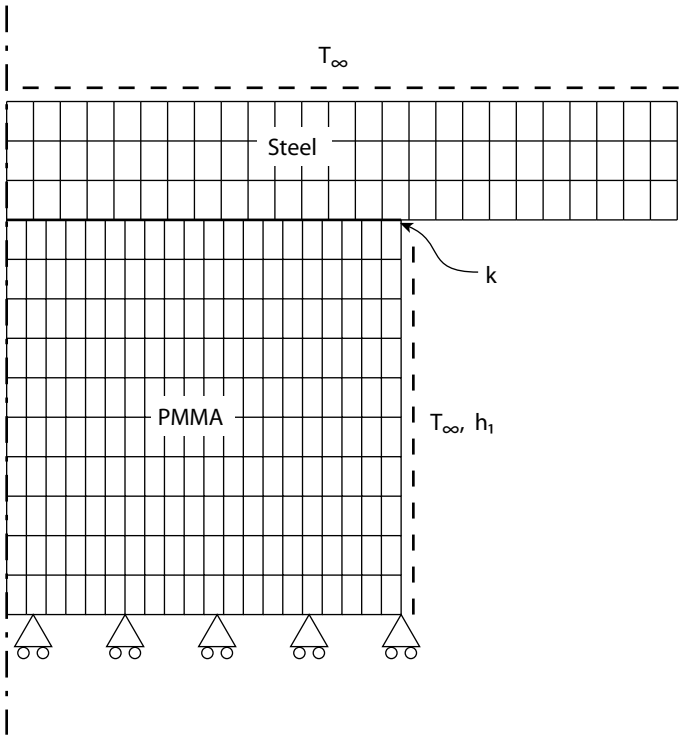

Figure 5-29: Axisymmetric finite element geometry for thermo-mechanically coupled compression simulations.

nearly adiabatic case and a negligible temperature rise for the low-rate nearly isothermal case. Arruda et al. [15] saw similar results for their experiments and simulations.

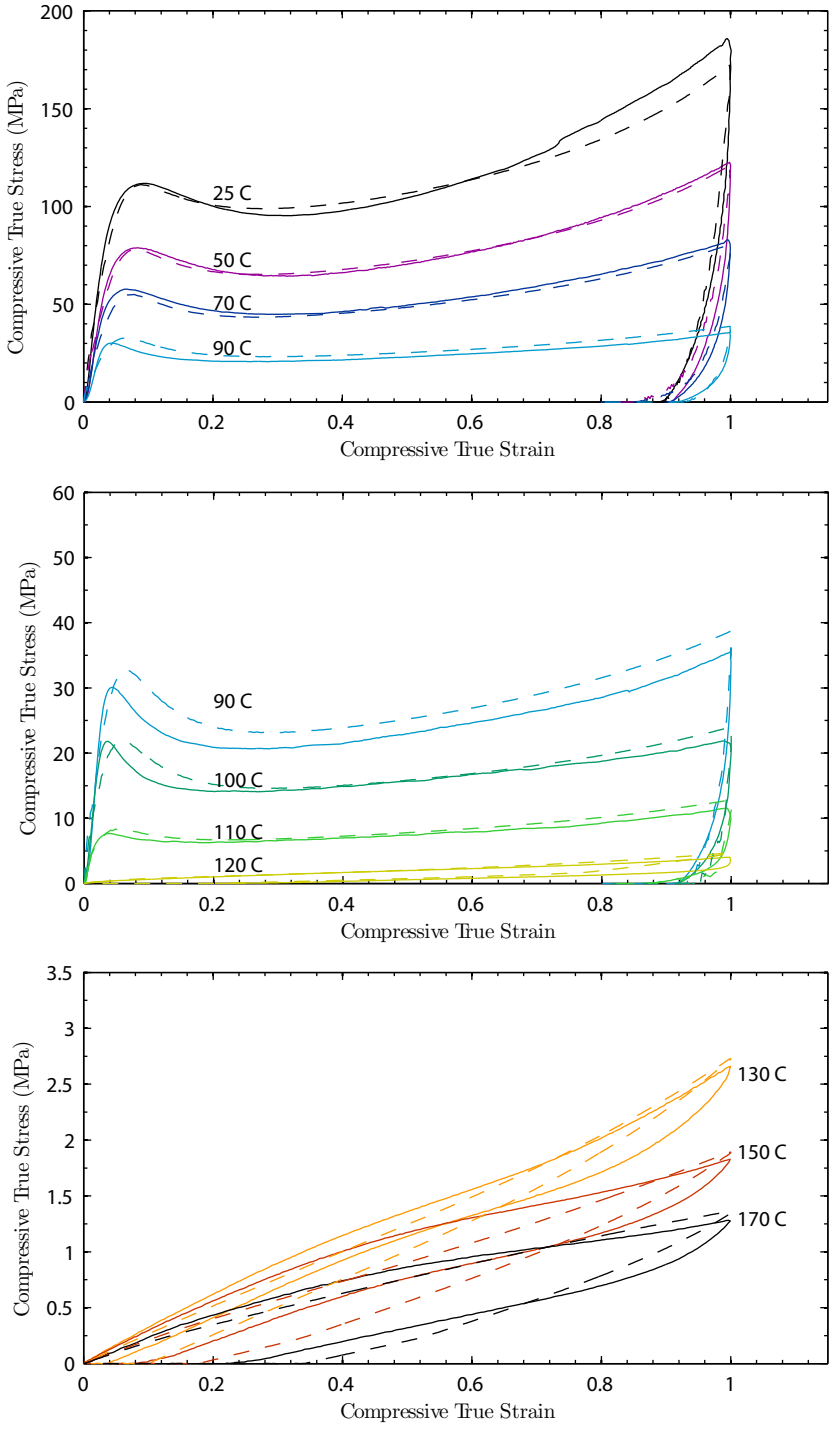

Figure 5-30: Three-dimensional multi-element fully-coupled ABAQUS simulations (- -) and uniaxial compression experiments (–) at a strain-rate of 3×10^{-4}/s and temperatures ranging from room temperature through 170 C.

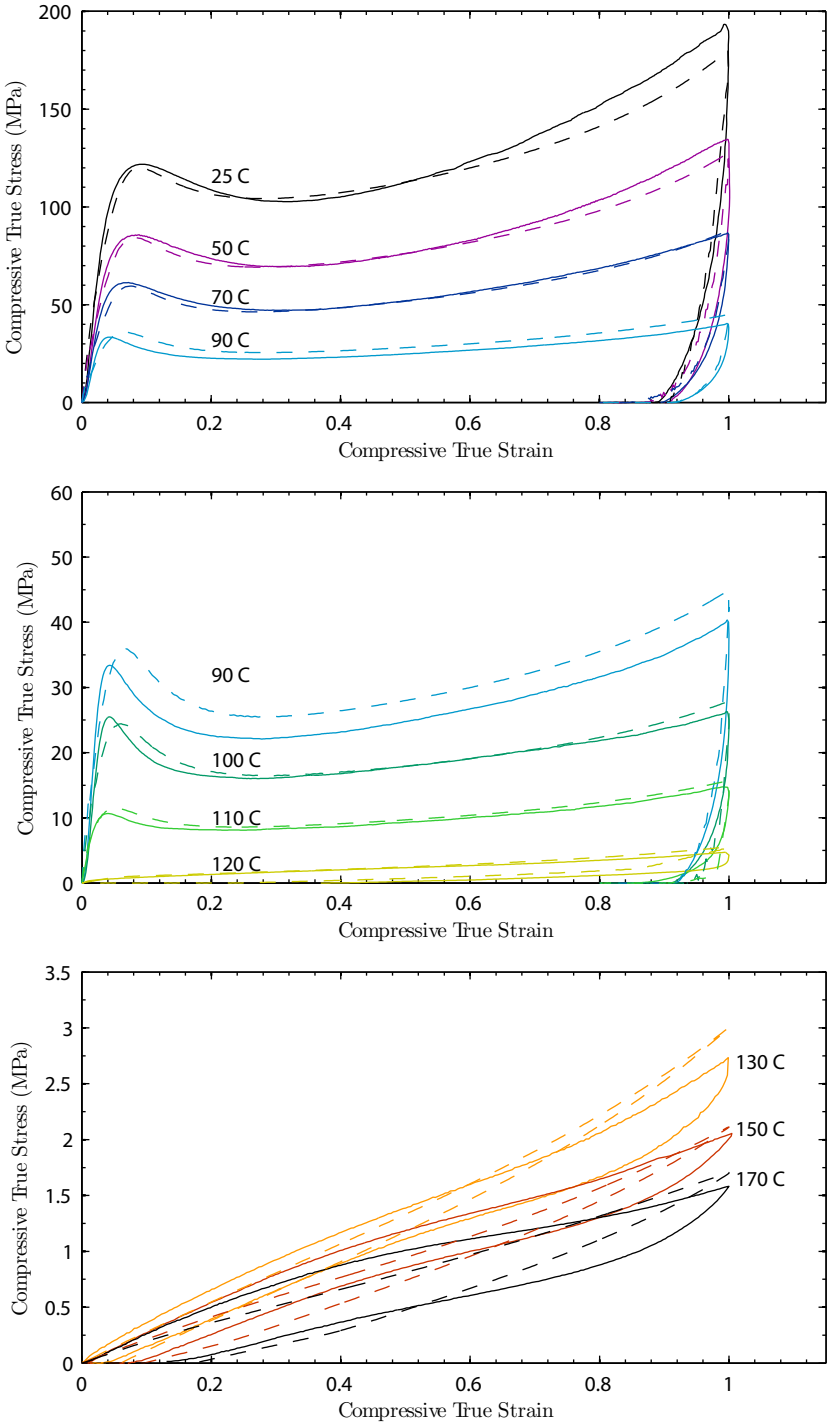

Figure 5-31: Three-dimensional multi-element fully-coupled ABAQUS simulations (- -) and uniaxial compression experiments (–) at a strain-rate of 10^{-3}/s and temperatures ranging from room temperature through 170 C.

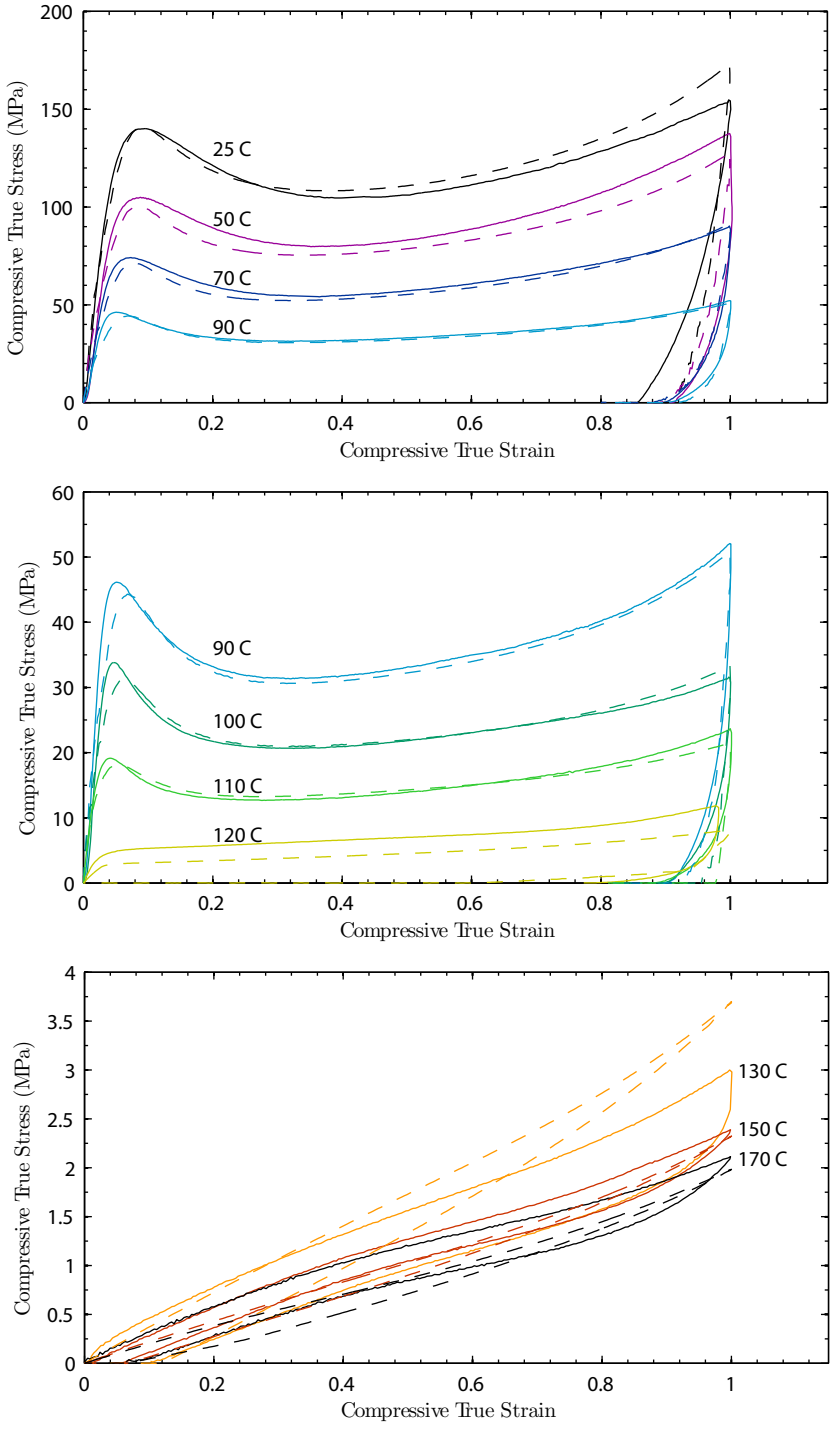

Figure 5-32: Three-dimensional multi-element fully-coupled ABAQUS simulations (- -) and uniaxial compression experiments (–) at a strain-rate of 10^{-2}/s and temperatures ranging from room temperature through 170 C.

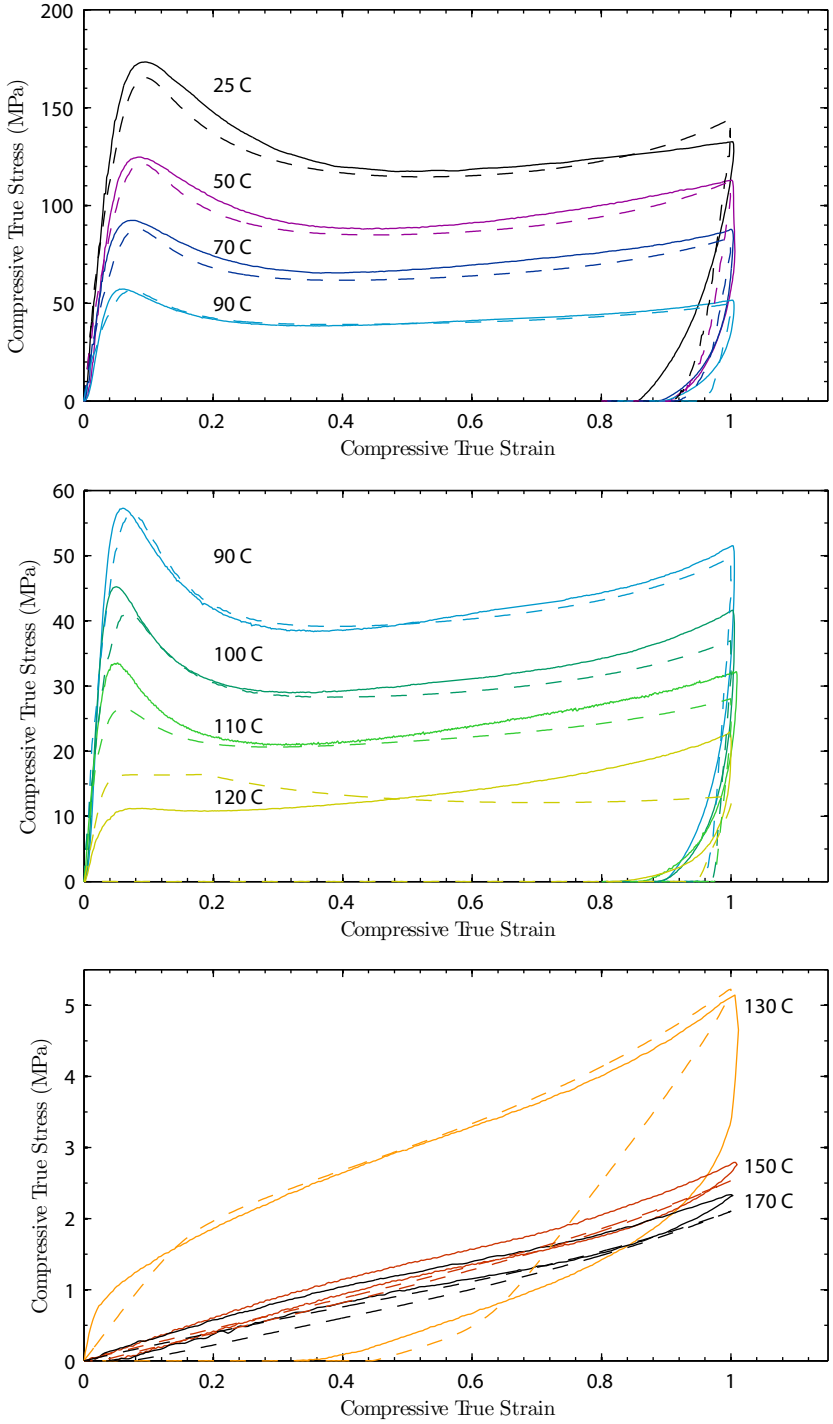

Figure 5-33: Three-dimensional multi-element fully-coupled ABAQUS simulations (- -) and uniaxial compression experiments (–) at a strain-rate of 10^{-1}/s and temperatures ranging from room temperature through 170 C.

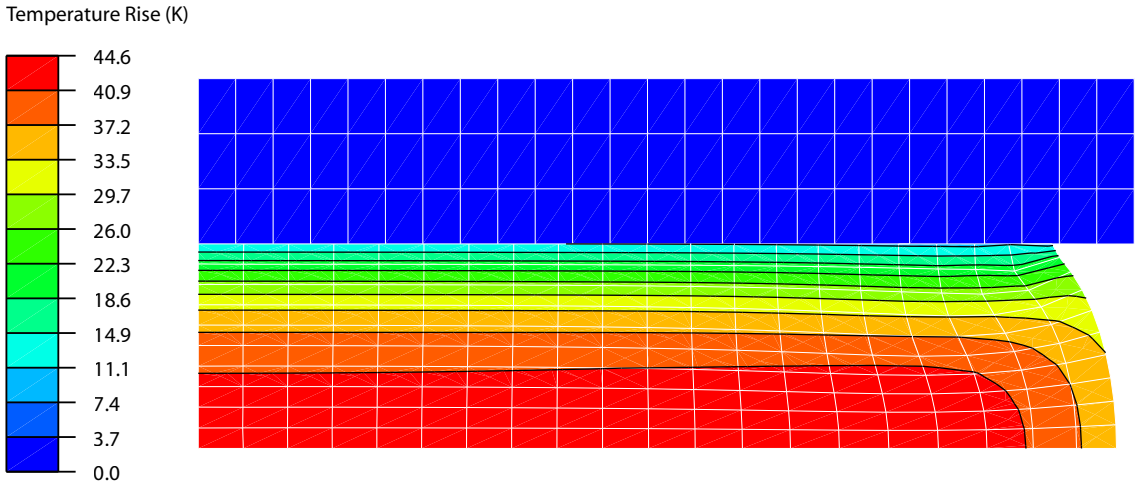

Figure 5-34: Contours of nodal temperature rise at a strain of -1.0 for the room temperature (25 C) multi-element fully-coupled ABAQUS simulation at a strain-rate of $10^{-1}/\text{s}$.

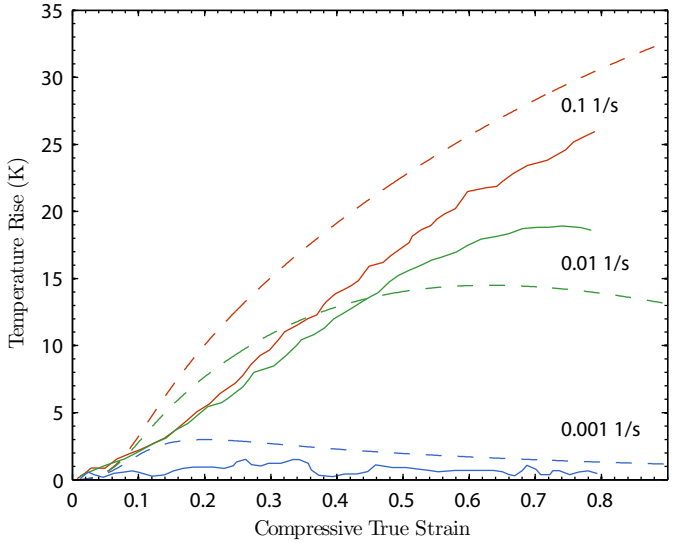

Figure 5-35: ABAQUS surface midpoint temperature measurements (- -) for three strain rates at room temperature (25 C). Experimental data (–) is from Mulliken [18] for a similarly sized specimen.

5.4 Summary of Equations and Parameters

The equations and associated parameters for the one-dimensional and full three-dimensional constitutive theory are briefly summarized here for convenience. For a more detailed summary, refer to Section 5.2.

Table 5.3: Summary of the the one-dimensional equations

Term	Description
$\sigma = \sigma^{e\,(1)} + \sigma^{e\,(2)}$	Total stress
$\sigma^{e\,(1)} = E\,\epsilon^{e\,(1)}$	Elastic stress in $\alpha = 1$
$E = \frac{1}{2}(E_{gl} + E_r) - \frac{1}{2}(E_{gl} - E_r)\tanh\left(\frac{1}{\Delta_\vartheta}(\vartheta - \vartheta_g)\right) + X_E(\vartheta - \vartheta_g)$	Elastic modulus
$\vartheta_g = \vartheta_g^{\text{ref}} + \left[\frac{C_{2g} \times \log_{10}(\dot\epsilon/\dot\epsilon_{\text{ref}})}{C_{1g} - \log_{10}(\dot\epsilon/\dot\epsilon_{\text{ref}})}\right]$	Glass transition
$\sigma^{(1)}_{\text{back}} = \frac{3}{2}\,C\,\ln A$	Backstress in $\alpha = 1$
$C = \begin{cases} -X_C(\vartheta - \vartheta_C) & : \vartheta \le \vartheta_C \\ 0 & : \vartheta > \vartheta_C \end{cases}$	Backstress modulus
$\dot A = 2\,D^{p\,(1)}A - \gamma A \ln A\,\dot\epsilon^{p\,(1)}, \qquad A(0) = 1$	Backstress stretch evolution
$\sigma^{e\,(2)} = \mu_{\text{R}}\left(1 - \frac{I_1 - 3}{I_{1,\max}}\right)^{-1}\left(\left(U^{e\,(2)}\right)^2 - U^{e\,(2)-1}\right)$	Stress in $\alpha = 2$
$\mu_{\text{R}} = \frac{1}{2}(\mu^a_{\text{R}} + \mu^b_{\text{R}}) - \frac{1}{2}(\mu^a_{\text{R}} - \mu^b_{\text{R}})\tanh\left(\frac{1}{\Delta_\mu}(\vartheta - \vartheta_\mu)\right) + X_\mu(\vartheta - \vartheta_\mu)$	Gent modulus
$I_{1,\max} = \frac{1}{2}(I_1^a + I_1^b) - \frac{1}{2}(I_1^a - I_1^b)\tanh\left(\frac{1}{\Delta_I}(\vartheta - \vartheta_I)\right)$	Gent parameter
$\dot\epsilon^{p\,(1)} = \dot\epsilon^*\left[\sinh\left(\frac{\bar\sigma V}{2\,k_B\vartheta}\right)\right]^{1/m^{(1)}}$	Flow rule for $\alpha = 1$
$\dot\epsilon^* = \begin{cases} \dot\epsilon_0^{(1)}\exp\left(-\frac{\Delta F^{(1)}}{k_B\vartheta}\right) & : \vartheta < \vartheta_g, \\ \dot\epsilon_0^{(1)}\exp\left(-\frac{\Delta F^{(1)}}{k_B\vartheta_g}\right)\exp\left(\frac{\ln 10 \times c_1^*(\vartheta - \vartheta_g)}{c_2^* + \vartheta - \vartheta_g}\right) & : \vartheta \ge \vartheta_g \end{cases}$	
$\bar p = -\frac{1}{3}\,\sigma^{e\,(1)}$	Pressure
$\bar\sigma^{(1)} = \lvert\sigma^{e\,(1)} - \sigma^{(1)}_{\text{back}}\rvert - S^{(1)} - \alpha_p\,\bar p$	Driving stress
$\dot\varphi = g\,(\varphi^* - \varphi)\,\dot\epsilon^{p\,(1)}, \qquad \varphi(0) = \varphi_i > 0$	Free volume evolution
$\dot S^{(1)} = h\left(S^* - S^{(1)}\right)\dot\epsilon^{p\,(1)}, \qquad S^{(1)}(0) = S_i^{(1)} \ge 0$	Isotropic resistance
$S^* = S_i^{(1)} + b\,(\varphi^* - \varphi)$	Saturation value of $S^{(1)}$
$g = g_1 + g_2\vartheta$	
$b = b_1\,\left(\vartheta^2 + b_2\vartheta + b_3\right)\left(\frac{\dot\epsilon^{p\,(1)}}{\dot\epsilon_{\text{ref}}}\right)^{b_4}$	
$\varphi^* = \frac{1}{2}(\varphi_g^* + \varphi_i) - \frac{1}{2}(\varphi_g^* - \varphi_i)\tanh\left(\frac{1}{\Delta_\vartheta}(\vartheta - \vartheta_g)\right)$	
$\dot\epsilon^{p\,(2)} = \dot\epsilon_0^{(2)}\exp\left\{-\frac{\Delta F^{(2)}}{k_B\vartheta}\right\}\left(\frac{\lvert\sigma^{e\,(2)}\rvert}{S^{(2)}}\right)^{1/m^{(2)}}$	Flow rule for $\alpha = 2$

Table 5.4: Summary of the the three-dimensional equations

Term	Description
$\mathbf{T} = \mathbf{T}^{e\,(1)} + \mathbf{T}^{e\,(2)}$	Total Cauchy stress
$\mathbf{T}^{e\,(1)} = J^{-1}\mathbf{R}^{e\,(1)}\,\mathbf{M}^{e\,(1)}\,\mathbf{R}^{e\,(1)\top}$	Cauchy stress for $\alpha = 1$
$\mathbf{T}^{e\,(2)} = J^{-1}\mathbf{R}^{e\,(2)}\,\mathbf{M}^{e\,(2)}\,\mathbf{R}^{e\,(2)\top}$	Cauchy stress for $\alpha = 2$
$\mathbf{M}^{e\,(1)} = 2G\mathbf{E}_0^e + K\left\{\operatorname{tr}\mathbf{E}^e - 3\,\alpha^{\mathrm{th}}\,(\vartheta - \vartheta_0)\right\}\mathbf{1}$	Mandel stress for $\alpha = 1$
$G = \frac{1}{2}(G_{gl} + G_r) - \frac{1}{2}(G_{gl} - G_r)\tanh\left(\frac{1}{\Delta_\vartheta}(\vartheta - \vartheta_g)\right) + X_G(\vartheta - \vartheta_g)$	Shear modulus
$\vartheta_g = \vartheta_g^{\mathrm{ref}} + \left[\frac{C_{2g} \times \log_{10}(d/d^{\mathrm{ref}})}{C_{1g} - \log_{10}(d/d^{\mathrm{ref}})}\right]$	Glass transition
$\nu_{\mathrm{poi}} = \frac{1}{2}(\nu_{gl} + \nu_r) - \frac{1}{2}(\nu_{gl} - \nu_r)\tanh\left(\frac{1}{\Delta_\vartheta}(\vartheta - \vartheta_g)\right)$	Poisson's ratio
$\mathbf{M}^{(1)}_{\mathrm{back}} = C\ln\mathbf{A}^{(1)}$	Backstress for $\alpha = 1$
$C = \begin{cases} -X_C(\vartheta - \vartheta_C) & : \vartheta \le \vartheta_C \\ 0 & : \vartheta > \vartheta_C \end{cases}$	Backstress modulus
$\dot{\mathbf{A}}^{(1)} = \mathbf{D}^{p\,(1)}\mathbf{A}^{(1)} + \mathbf{A}^{(1)}\mathbf{D}^{p\,(1)} - \gamma\,\mathbf{A}^{(1)}\ln\mathbf{A}^{(1)}\,\nu^{p\,(1)}, \quad \mathbf{A}(\mathbf{X},0) = \mathbf{1}$	Backstress stretch evolution
$\mathbf{M}^{e\,(2)} = \mu_{\mathrm{R}}\left(1 - \frac{I_1 - 3}{I_{1,\max}}\right)^{-1}(\mathbf{C}^{e}_{\mathrm{dis}}{}^{(2)})_0$	Mandel stress for $\alpha = 2$
$\mu_{\mathrm{R}} = \frac{1}{2}(\mu^a_{\mathrm{R}} + \mu^b_{\mathrm{R}}) - \frac{1}{2}(\mu^a_{\mathrm{R}} - \mu^b_{\mathrm{R}})\tanh\left(\frac{1}{\Delta_\mu}(\vartheta - \vartheta_\mu)\right) + X_\mu(\vartheta - \vartheta_\mu)$	Gent modulus
$I_{1,\max} = \frac{1}{2}(I_1^a + I_1^b) - \frac{1}{2}(I_1^a - I_1^b)\tanh\left(\frac{1}{\Delta_I}(\vartheta - \vartheta_I)\right)$	Gent parameter
$\nu^{p\,(1)} = \nu^*\,\exp\left\{-\frac{\Delta F^{(1)}}{k_B\,\vartheta}\right\}\left[\sinh\left(\frac{\bar{\tau}^{(1)}_{\mathrm{e}}\,V}{2k_B\vartheta}\right)\right]^{1/m^{(1)}}$	Flow rule for $\alpha = 1$
$\nu^* = \begin{cases} \nu_0^{(1)}\exp\left(-\frac{\Delta F^{(1)}}{k_B\vartheta}\right) & : \vartheta < \vartheta_g, \\ \nu_0^{(1)}\exp\left(-\frac{\Delta F^{(1)}}{k_B\vartheta_g}\right)\exp\left(\frac{\ln 10 \times c_1^*(\vartheta - \vartheta_g)}{c_2^* + \vartheta - \vartheta_g}\right) & : \vartheta \ge \vartheta_g \end{cases}$	
$\bar{p}^{(1)} = -\frac{1}{3}\operatorname{tr}\mathbf{M}^{e\,(1)}$	Pressure
$\mathbf{M}^{e\,(1)}_{\mathrm{eff}} = \mathbf{M}^{e\,(1)} - \mathbf{M}^{(1)}_{\mathrm{back}}$	Driving stress
$\bar{\tau}^{(1)} = \frac{1}{\sqrt{2}}\,\lvert(\mathbf{M}^{e\,(1)}_{\mathrm{eff}})_0\rvert$	Equivalent shear stress
$\bar{\tau}^{(1)}_{\mathrm{e}} = \bar{\tau}^{(1)} - S^{(1)} - \alpha_p\,\bar{p}^{(1)}$	Effective shear stress
$\dot{\varphi} = g\,(\varphi^* - \varphi)\,\nu^{p\,(1)}, \qquad \varphi(\mathbf{X},0) = \varphi_i > 0$	Free volume evolution
$\dot{S}^{(1)} = h\left(S^* - S^{(1)}\right)\nu^{p\,(1)}, \qquad S^{(1)}(\mathbf{X},0) = S_i^{(1)} \ge 0$	Isotropic resistance evolution
$S^* = S_i^{(1)} + b\,(\varphi^* - \varphi)$	Saturation value of $S^{(1)}$
$g = g_1 + g_2\vartheta$	
$b = b_1\,\left(\vartheta^2 + b_2\vartheta + b_3\right)\left(\frac{\nu^{p\,(1)}}{\nu_{\mathrm{ref}}}\right)^{b_4}$	
$\varphi^* = \frac{1}{2}(\varphi_g^* + \varphi_i) - \frac{1}{2}(\varphi_g^* - \varphi_i)\tanh\left(\frac{1}{\Delta_\vartheta}(\vartheta - \vartheta_g)\right)$	
$\nu^{p\,(2)} = \nu_0^{(2)}\,\exp\left\{-\frac{\Delta F^{(2)}}{k_B\,\vartheta}\right\}\left(\frac{\bar{\tau}^{(2)}}{S^{(2)}}\right)^{1/m^{(2)}}$	Flow rule for $\alpha = 2$
$\bar{\tau}^{(2)} = \frac{1}{\sqrt{2}}\,\lvert\mathbf{M}_0^{e\,(2)}\rvert$	Equivalent shear stress

Table 5.5: PMMA material parameters for one-dimensional model

Parameter	Value
ρ (kg m^{-3})	1200
$\dot{\epsilon}_{\mathrm{ref}}$ (s^{-1})	3×10^{-4}
$\vartheta_g^{\mathrm{ref}}$ (K)	383
C_{1g}	11
C_{2g} (K)	36
E_{gl} (MPa)	800
E_r (MPa)	0.5
Δ_ϑ (K)	4
X_E (MPa K^{-1})	$\begin{cases} 27 & : \quad \vartheta \leq \vartheta_g \\ 0 & : \quad \vartheta > \vartheta_g \end{cases}$
μ_{R}^a (MPa)	7.8
μ_{R}^b (MPa)	0.78
Δ_μ (K)	21
ϑ_μ (K)	$\vartheta_g - 18$
X_μ (kPa K^{-1})	$\begin{cases} 190 & : \quad \vartheta \leq \vartheta_\mu \\ 2.1 & : \quad \vartheta > \vartheta_\mu \end{cases}$
I_1^a	5.5
I_1^b	11
Δ_I (K)	4
ϑ_I (K)	395
X_C (MPa K^{-1})	9.4
ϑ_C (K)	383
γ	60
V (m^3)	2.11×10^{-28}
$m^{(1)}$	0.218
$\dot{\epsilon}_0^{(1)}$ (s^{-1})	1.15×10^{16}
$\Delta F^{(1)}$ (kJ mol^{-1})	109
c_1^*	13
c_2^* (K)	16
α_p	0.353
φ_i	0
φ_g^*	0.001
$S_i^{(1)}$ (Pa)	0
b_1 (Pa K^{-2})	-3.16×10^6
b_2 (K)	-562
b_3 (K^2)	6.62×10^4
b_4	0.054
g_1	-8.52
g_2 (K^{-1})	5.48×10^{-2}
h (s)	70
$\Delta F^{(2)}$ (kJ/mol)	109
$m^{(2)}$	0.5
$\dot{\epsilon}_0^{(2)}$ (s^{-1})	2×10^9
$S^{(2)}$ (MPa)	1.5

Table 5.6: PMMA material parameters for three-dimensional model

Parameter	Value
ρ (kg m^{-3})	1200
ν_{ref} (s^{-1})	5×10^{-4}
$\vartheta_g^{\mathrm{ref}}$ (K)	383
C_{1g}	11
C_{2g} (K)	36
α_{gl} (K^{-1})	7×10^{-5}
α_r (K^{-1})	16×10^{-5}
G_{gl} (MPa)	296
G_r (MPa)	0.168
Δ_ϑ (K)	4
X_G (MPa K^{-1})	$\begin{cases} 10 & : \quad \vartheta \leq \vartheta_g \\ 0 & : \quad \vartheta > \vartheta_g \end{cases}$
ν_{gl}	0.35
ν_r	0.495
μ_{R}^a (MPa)	6.7
μ_{R}^b (MPa)	0.67
Δ_μ (K)	21
ϑ_μ (K)	$\vartheta_g - 18$
X_μ (kPa K^{-1})	$\begin{cases} 165 & : \quad \vartheta \leq \vartheta_\mu \\ 2.1 & : \quad \vartheta > \vartheta_\mu \end{cases}$
I_1^a	5.5
I_1^b	11
Δ_I (K)	4
ϑ_I (K)	395
X_C (MPa K^{-1})	9.4
ϑ_C (K)	383
γ	34.64
V_i (m^3)	3.65×10^{-28}
$m^{(1)}$	0.218
$\nu_0^{(1)}$ (s^{-1})	2×10^{16}
$\Delta F^{(1)}$ (kJ mol^{-1})	109
c_1^*	13
c_2^* (K)	16
α_p	0.204
φ_i	0
φ_g^*	0.001
$S_i^{(1)}$ (Pa)	0
b_1 (Pa K^{-2})	-1.82×10^6
b_2 (K)	-562
b_3 (K^2)	6.62×10^4
b_4	0.054
g_1	-4.92
g_2 (K^{-1})	3.16×10^{-2}
h (s)	40.4
$\Delta F^{(2)}$ (kJ/mol)	109
$m^{(2)}$	0.5
$\nu_0^{(2)}$ (s^{-1})	3.46×10^9
$S^{(2)}$ (MPa)	0.866

Bibliography

[1] C. P. Buckley and D. C. Jones. Glass-rubber constituitive model for amorphous polymers near the glass transition. *Polymer*, 36:3301–3312, 1995. doi: 10.1016/0032-3861(95)99429-X.

[2] P. J. Dooling, C. P. Buckley, S. Rostami, and N. Zahlan. Hot-drawing of poly(methylmethacrylate) and simulation using a glass-rubber constitutive model. *Polymer*, 43:2451–2465, 2002. doi: 10.1016/S0032-3861(01)00799-6.

[3] M. C. Boyce, S. Socrate, and P. G. Llana. Constitutive model for the finite deformation stress strain behavior of poly(ethylene terephthalate) above the glass transition. *Polymer*, 41: 2183–2201, 2000. doi: 10.1016/S0032-3861(99)00406-1.

[4] R. B. Dupaix and M. C. Boyce. Constitutive modeling of the finite strain behavior of amorphous polymers in and above the glass transition. *Mechanics of Materials*, 39:39–52, 2007. doi: 10.1016/j.mechmat.2006.02.006.

[5] J. Richeton, G. Schlatter, K. S. Vecchio, Y. Rémond, and S. Ahzi. A unified model for stiffness modulus of amorphous polymers across transition temperatures and strain rates. *Polymer*, 46: 8194–8201, 2006. doi: 10.1016/j.polymer.2005.06.103.

[6] J. Richeton, S. Ahzi, K. S. Vecchio, F. C. Jiang, and R. R. Adharapurapu. Influence of temperature and strain rate on the mechanical behavior of three amorphous polymers: Characterization and modeling of the compressive yield stress. *InternationalJournal of Solids and Structures*, 43:2318–2335, 2006. doi: 10.1016/j.ijsolstr.2005.06.040.

[7] J. D. Ferry. *Viscoelastic properties of polymers*. Wiley, New York, 3rd edition, 1980.

[8] D. G. Fotheringham, B. W. Cherry, and C. Bauwens-Crowet. Comment on "the compression yield behaviour of polymethyl methacrylate over a wide range of temperatures and strain-rates". *Journal of Materials Science*, 11:1368–1371, 1976. doi: 10.1007/BF00545162.

[9] F. Povolo and E. B. Hermida. Phenomenlogical description of strain rate and temperature-dependent yield stress of pmma. *Journal of Applied Polymer Science*, 58:55–68, 1995. doi: 10.1002/app.1995.070580106.

[10] J. Richeton, S. Ahzi, L. Daridon, and Y. Rémond. A formulation of the cooperative model for the yield stress of amorphous polymers for a wide range of strain rates and temperatures. *Polymer*, 46:6035–6043, 2005. doi: 10.1016/j.polymer.2005.05.079.

[11] D. G. Fotheringham and B. W. Cherry. The role of recovery forces in the deformation of linear polyethylene. *Journal of Materials Science*, 13:951–964, 1978. doi: 10.1007/BF00544690.

[12] A. N. Gent. A new constitutive relation for rubber. *Rubber Chemistry and Technology*, 69: 59–61, 1996.

[13] C. Bauwens-Crowet, J. C. Bauwens, and G. Homés. Tensile yield-stress behavior of glassy polymers. *Journal of Polymer Science: Part A-2*, 7:735–742, 1969. doi: 10.1002/pol.1969.160070411.

[14] L. Anand and N. M. Ames. On modeling the micro-indentation response of an amorphous polymer. *International Journal of Plasticity*, 22:1123–1170, 2006. doi: 10.1016/j.ijplas.2005.07.006.

[15] E. M. Arruda, M. C. Boyce, and R. Jayachandran. Effects of strain rate, temperature and thermomechanical coupling on the finite strain deformation of glassy polymers. *Mechanics of Materials*, 19:193–212, 1995. doi: 10.1016/0167-6636(94)00034-E.

[16] U. Gaur, S.-F. Lau, B. B. Wunderlich, and B. Wunderlich. Heat capacity and other thermodynamic properties of linear macromolecules. vi. acrylic polymers. *Journal of Physical and Chemical Reference Data*, 11:1065–1089, 1982.

[17] K. Eiermann and K.-H. Hellwege. Thermal conductivity of high polymers from -180c to 90c. *Journal of Polymer Science*, 57:99–106, 1962. doi: 10.1002/pol.1962.1205716508.

[18] A. D. Mulliken. *Mechanics of Amorphous Polymers and Polymer Nanocomposites during High Rate Deformation*. PhD thesis, Massachusetts Institute of Technology, September 2006.

Chapter 6

Hot Embossing of PMMA

6.1 Introduction

Numerical simulation of micro-hot-embossing processes for amorphous polymers are in their infancy. Most previously published attempts [1–17] have been hampered by a lack of suitable thermo-mechanical constitutive model and its numerical implementation in a finite element program. In this chapter we validate our recently developed visco-elastic-plastic, thermo-mechanically-coupled, large-deformation theory for amorphous polymers and its numerical implementation in Abaqus/Explicit [18] by carrying out representative hot-embossing simulations, and comparing aspects of the results from such simulations against corresponding experimental results. Once validated, our model and its numerical implementation should be useful for both optimizing the hot-embossing process cycle as well as determining the mechanical properties of the final part.

A schematic of a typical force and temperature profile used in a hot embossing process cycle is shown in Figure 6-1. The basic process proceeds as follows:

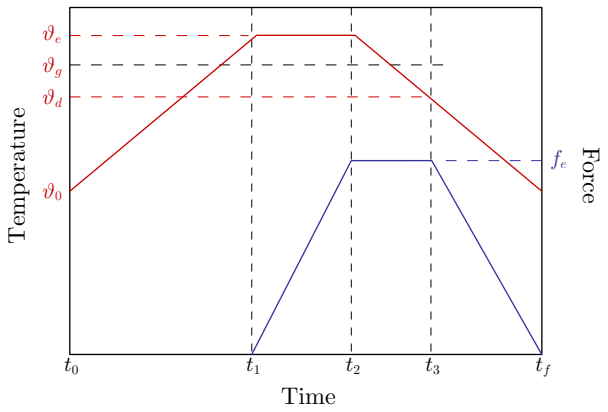

Figure 6-1: Schematic of typical force and temperature profiles used in a hot embossing process cycle.

1. A polymer substrate is placed on a rigid platen and is brought into physical contact with a rigid tool from above. A slight pre-load may be applied. (t_0)

2. The tool and platen are heated up to the embossing temperature ϑ_e and time is allowed for thermal equilibrium to be reached. This temperature is typically above the polymer's glass transition temperature ϑ_g, however, there is also interest in embossing at lower temperatures. ($t_0 \rightarrow t_1$)

3. The embossing force f_e is then gradually applied to the tool, causing its features to be impressed on the polymer substrate. ($t_1 \rightarrow t_2$)

4. The tool and platen are then cooled while still under load until the demolding temperature ϑ_d is reached. This temperature is typically below the polymer's glass transition temperature ϑ_g, however, there is also interest in demolding at higher temperatures. ($t_2 \rightarrow t_3$)

5. Finally, the tool is unloaded and removed from the polymer substrate. ($t_3 \rightarrow t_f$)

In this chapter, we present our hot embossing experiments and simulations on PMMA. We have conducted these experiments with tool features at two different length scales. The first tool has millimeter sized features and we refer to this as our "macro-embossing" tool. The second tool has micrometer sized features and we refer to it as our "micro-embossing" tool. We first present the experimental results and comparisons to numerical simulations for the case of macro-embossing followed by similar discussions for the case of micro-embossing.

6.2 Macro-embossing

6.2.1 Experiments

Procedures

The polymer substrate used in the macro-embossing experiments is the same grade of cast PMMA used earlier in the compression experiments of Chapter 2. The as-received sheet stock has nominal width and length dimensions of 12 in, and a nominal thicknesses of 3 mm. Disks were cut out of the polymer sheet prior to annealing using a standard hole saw of nominal outside dimension of 1.75 in, resulting in a polymer disk core of a smaller dimension. The polymer disks were then annealed at 150 C and slow cooled to room temperature before testing. After the annealing step, the dimensions were found to change.

The axisymmetric tool used is shown in Figure 6-2. It consists of two concentric ring features having 2 mm width and 0.5 mm height. We chose an axisymmetric design so that we can more easily simulate the setup in a finite element program. This tool is installed in the hot embossing assembly that was designed by Vikas Srivastava and is pictured in Figure 6-3. As in the compression setup discussed earlier, the assembly is inserted into the Instron grips and is heated by the same cartridge heaters and controllers. To maintain good alignment between the embossing tool and the polymer substrate, the tool is attached to a spherical seat at the upper end and a tight clearance is maintained between the tool shaft and its heated collar. The polymer substrate fits snugly into the heated collar and is sandwiched between a 3 mm thick glass plate and the embossing tool. The substrate is thus highly constrained in order to promote die filling instead of lateral expansion

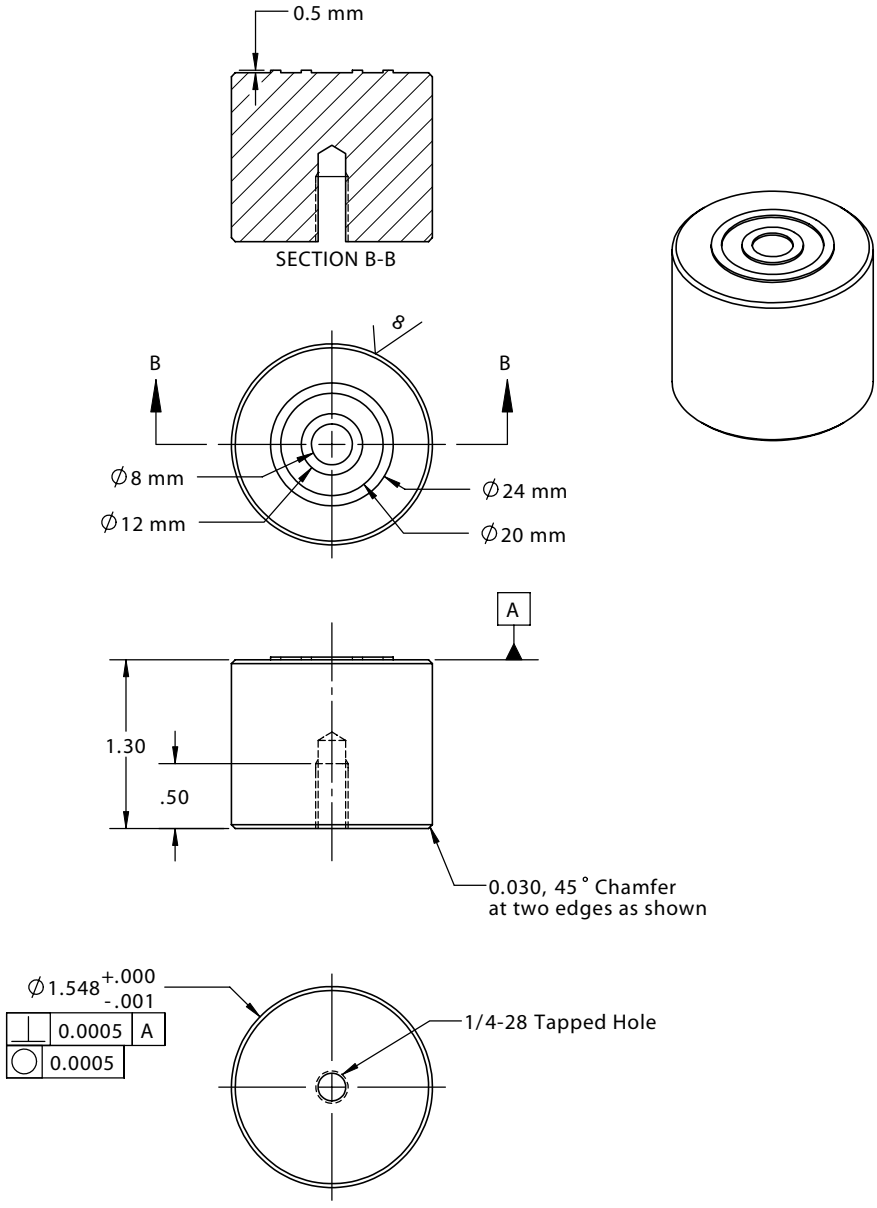

Figure 6-2: Drawing of axisymmetric embossing tool. All dimension are in inches unless otherwise noted.

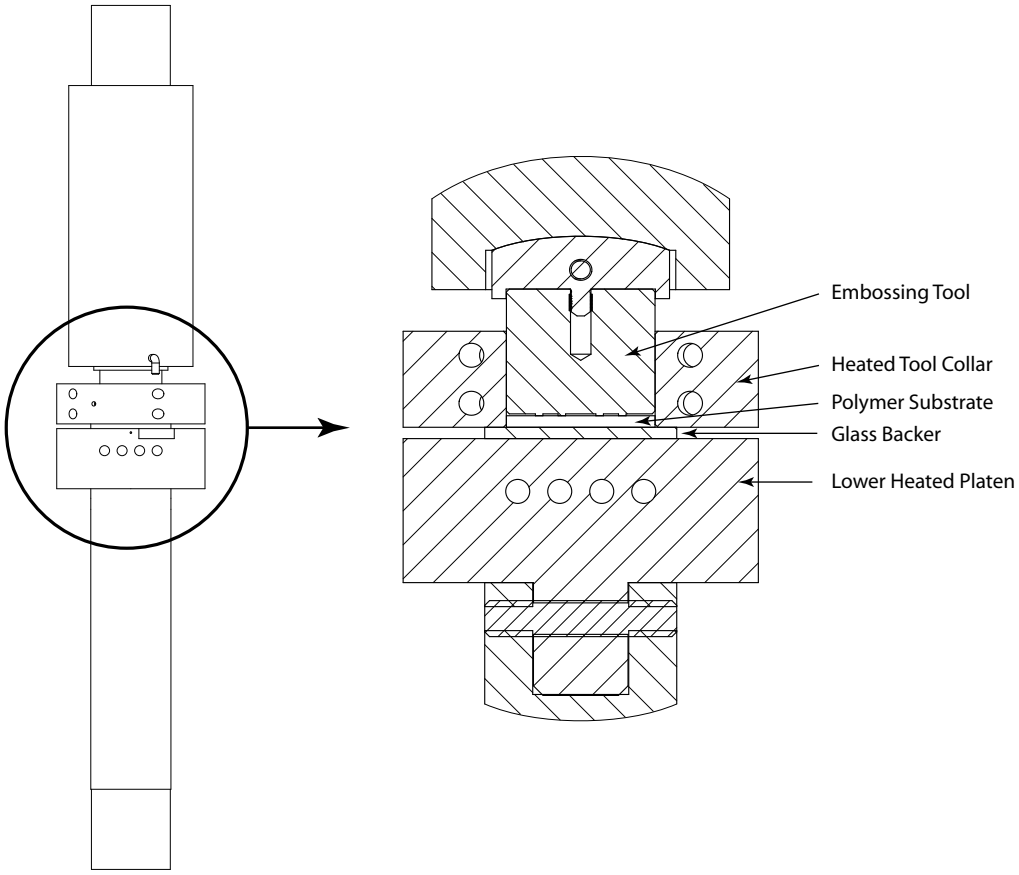

Figure 6-3: Drawing of embossing assembly designed by Vikas Srivastava.

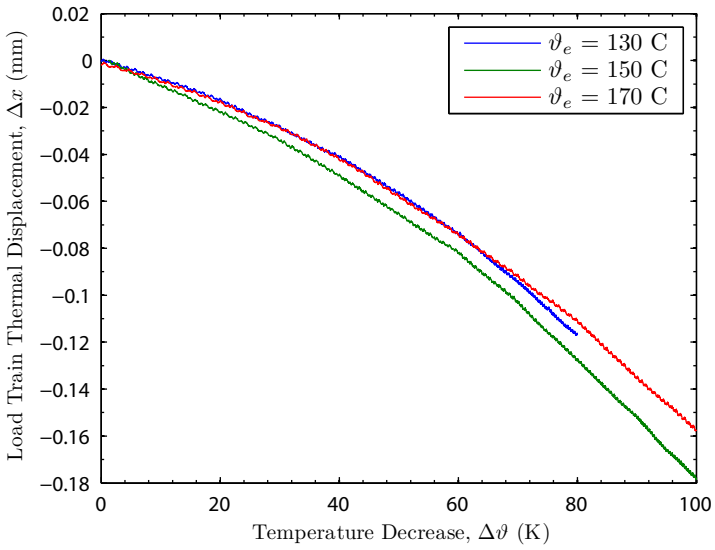

Figure 6-4: Load train thermal contraction for three different initial temperatures of 130 C, 150 C, 170 C. While the relation between load train contraction and temperature change is non-linear, it appears to be independent of initial temperature.

when the tool is impressed into it. The glass plate is used to maintain the smooth surface finish of the back of the polymer disk. Without its use, the poor surface finish of the steel platen would be transferred to the the polymer disk during the embossing procedure.

We followed the basic process cycle outlined earlier. Three different embossing temperatures (130 C, 150 C, 170 C) above the glass transition of PMMA were used in combination with three different demolding temperatures (50 C, 70 C, 90 C) below the glass transition of PMMA. Also, as a reference, one additional part was both embossed and demolded below the glass transition at 100 C. For each test, the system was brought up to the embossing temperature and allowed to equilibrate for 15 min. Next, the force was ramped up at a rate of 0.04 kN/sec to the embossing force of 5 kN (120 kN for the 100 C embossing). Once at load, the cartridge heaters were turned off and the oven fan was used to circulate room temperature air around the setup to speed cooling. Once at the demolding temperature, the force was quickly removed and the part was taken out of the setup.

Displacement during the embossing experiment was recorded from the Instron actuator displacement signal which is located far from the embossing setup and therefore isolated from the larger thermal fluctuations of the embossing process. However, the thermal contraction of the entire load train during the embossing cycle would be included in this displacement measurement. To compensate for this, three tests were conducted with a flat featureless tool pressing directly against the glass backing plate with no polymer substrate in between. The load was ramped up to the embossing force of 5 kN and displacement was measured during cooling for the three embossing temperatures of 130 C, 150 C, and 170 C. The results are shown in Figure 6-4. We see that the load train thermal contraction during cooling is not linearly related with temperature change, however, it appears to be independent of initial temperature. This thermal contraction can be used to isolate the creep and thermal contraction of the polymer in the Instron displacement signal.

Results

There did not appear to be any remarkable differences among the embossed parts subject to the nine different experimental conditions which are the result of the combination of the three different embossing temperatures (130 C, 150 C, 170 C) with the three different demolding temperatures (50 C, 70 C, 90 C). As such, only the results for the part embossed at 170 C and demolded at 50 C will be shown along with the reference part which was embossed and demolded at 100 C.

Figure 6-5 shows the height contour of a section across the diameter of the PMMA parts. The data is captured using a Zygo optical profilometer. As a comparison, the height contours of the steel tool are also shown. For further clarification, the height profile of a cross-section of the part is shown in Figure 6-6 with respect to the tool profile. The tool profile has been inverted in both figures for ease of comparison. We see that the part embossed at 170 C and allowed to cool to 50 C before unloading has replicated the tool feature heights very well. The part embossed and demolded at 100 C, however, shows very poor replication of the tool feature height. We attribute this to the difference in time spent under pressure. The 170 C part pressurized for about 15 mins during cooling, which allows the material to creep into the recesses of the tool. The 100 C part, however, was subjected to the molding force for only a few seconds before it was unloaded and recovered elastically.

Because the Zygo cannot capture the fine details of mold filling near the feature walls, we also took an SEM image of the 170 C part which is shown in Figure 6-7. It is clear from this image that the channel features are not well-filled in the PMMA part even though the feature height is well replicated.

Figure 6-8 shows the resulting birefringence patterns in the part embossed at 170 C and demolded at 50 C, and the part embossed and demolded both at 100 C. To produce the birefringence patterns, the polymer disk was sandwiched between two circular polarizing filters, each with its quarter-wave plate on the side facing the polymer disk. The sandwich was transmissively illuminated with white light and the image was captured at 4600 dpi using an Epson V100 Photo scanner. The birefringence patterns clearly show that there is a much higher residual stress state in the part embossed at 100 C versus the one at 170 C.

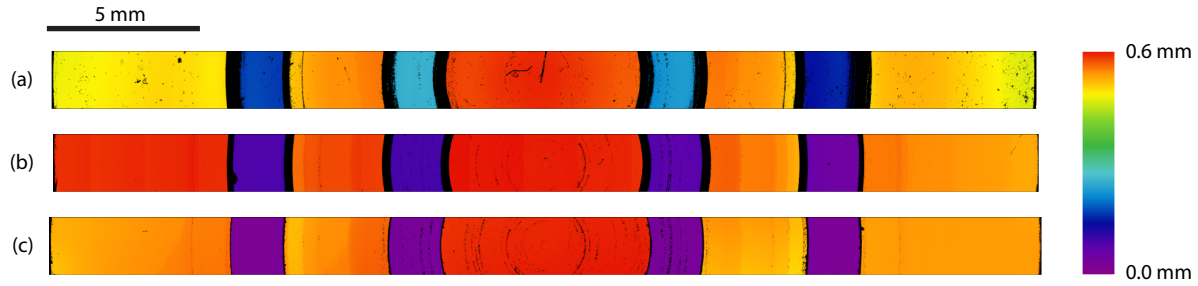

Figure 6-5: Height contours of section across the diameter of (a) macro-embossed axisymmetric PMMA part embossed and demolded at 100 C, (b) macro-embossed axisymmetric PMMA part embossed at 170 C and demolded at 50 C, (c) steel tool. The tool height has been inverted to show agreement with the embossed part. Black color in the contours indicate areas of missing data which is indicative of an area of high curvature.

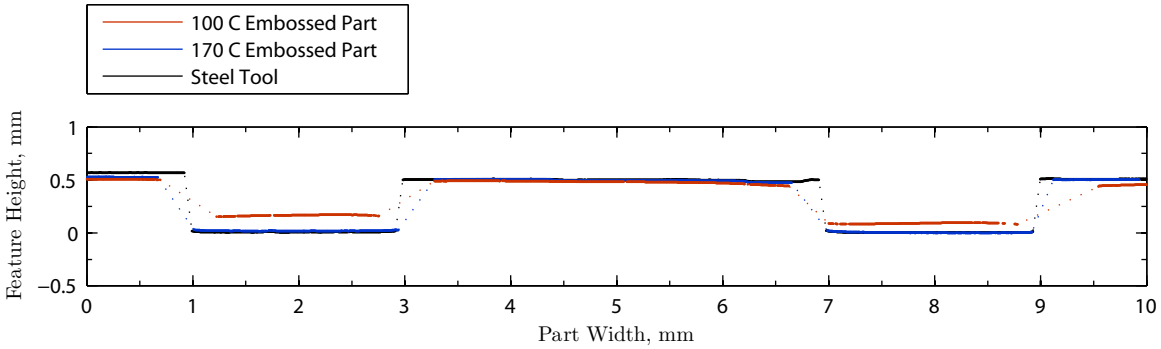

Figure 6-6: Height profiles of cross-section of macro-embossed axisymmetric PMMA parts and the steel tool. The cross-sections are taken from the right half of the data shown in Figure 6-5. Solid lines indicate measured data, while the dotted lines indicate areas of missing data which is indicative of an area of high curvature.

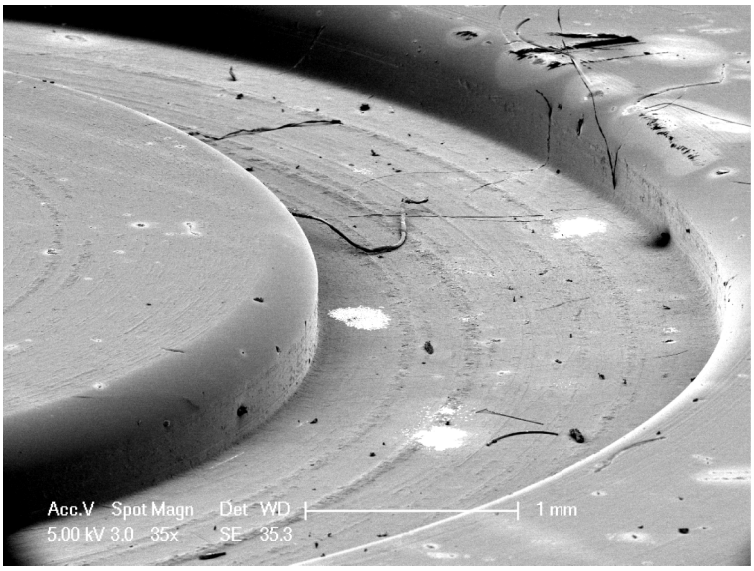

Figure 6-7: SEM image of macro-embossed PMMA part embossed at 170 C and demolded at 50 C. The image is from the outer most ring feature which is the feature shown on the right of Figure 6-6. Notice the region of high curvature at the top of the feature wall that corresponds to the missing data in Figures 6-5 and 6-6. Image courtesy of Hayden Taylor.

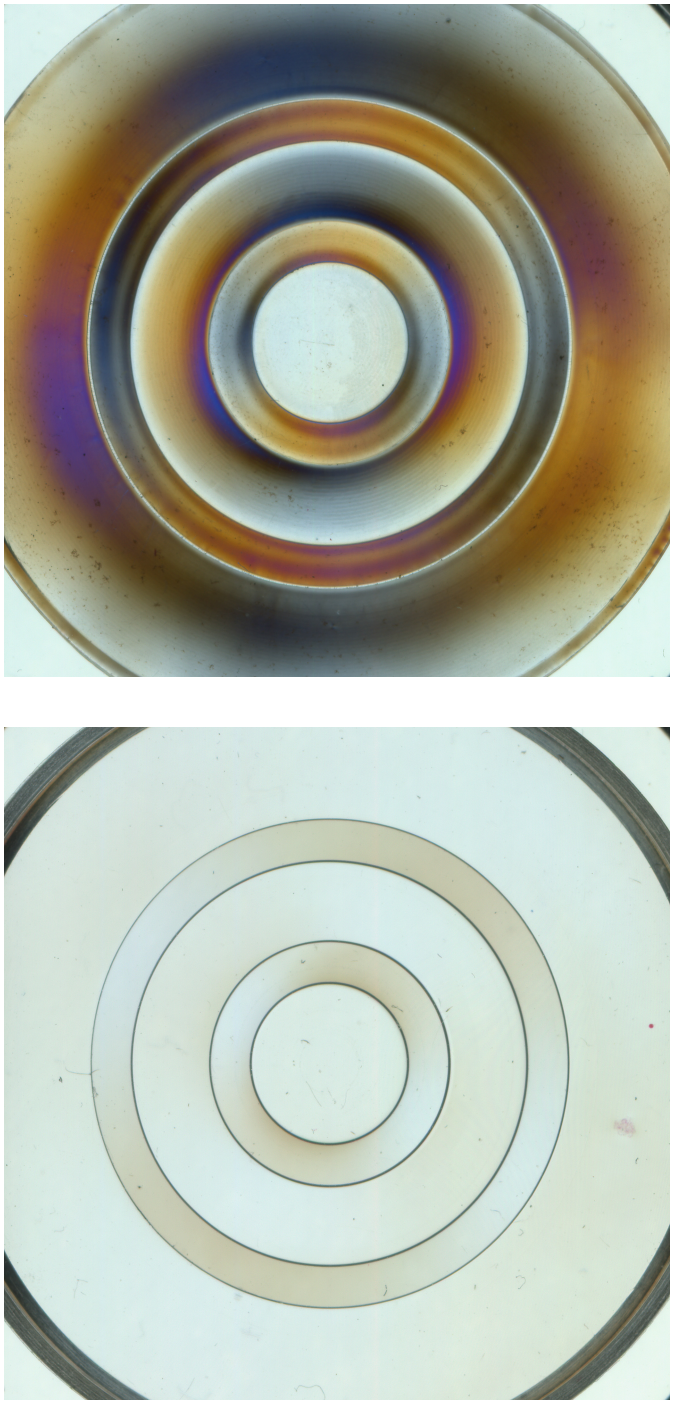

Figure 6-8: Birefringence patterns in PMMA disks (top) embossed and demolded at 100 C at a force of 120 kN, and (bottom) embossed at 170 C at a force of 5 kN and demolded at 50 C. To produce the birefringence patterns, the polymer disks were each sandwiched between two circular polarizing filters, each with its quarter-wave plate on the side facing the polymer disk. The sandwich was transmissively illuminated with white light and the image was captured at 4600 dpi using an Epson V100 Photo scanner. Images courtesy of Hayden Taylor.

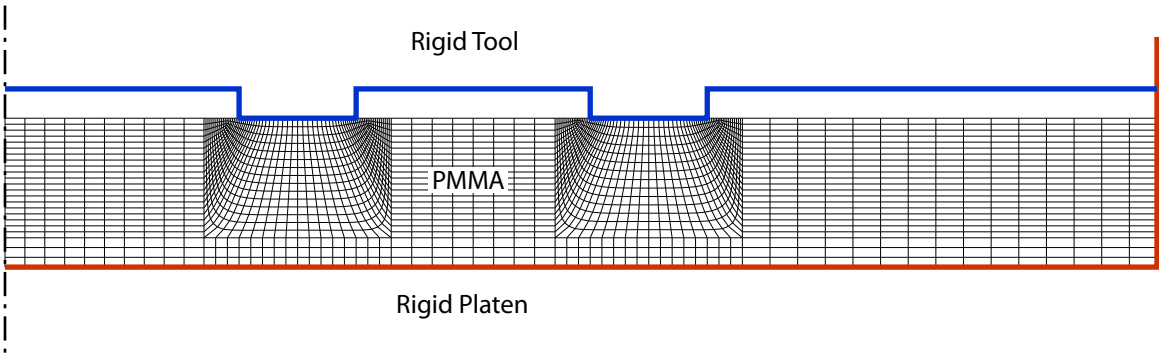

Figure 6-9: Axisymmetric finite element geometry for isothermal embossing simulations. The PMMA substrate is constrained between the fixed rigid platen shown in red and the movable rigid tool shown in blue.

6.2.2 Axisymmetric Simulations

The schematic of the finite element setup is shown in Figure 6-9. Because the tool and PMMA part are circular, we assume that axisymmetric conditions are satisfied. We model the tool, the heated collar, and the lower platen as rigid parts. We assume the interface between the PMMA and both the heated collar and lower platen are frictionless, while the interface between the PMMA and the tool approaches no-slip by using a friction coefficient of 0.5.

For the case of the part embossed and demolded at 100 C, we use isothermal conditions in the simulation. A comparison of the experimental part profile versus the corresponding isothermal simulation is shown in Figure 6-10. The simulation shows that areas of high curvature near the feature walls correspond to missing data from the optical profilometer measurements of the experimental part. Unfortunately, the simulation shows a final feature depth of approximately 0.4 mm, while the embossed part features are closer to 0.3 mm. This indicates that the simulation did not recover enough after the load was removed.

For the case of the part embossed at 170 C and demolded at 50 C, we conducted a complete thermo-mechanically coupled analysis. The temperature of the rigid parts is controlled during the simulation, and a very high conductance is assigned at the interface between the PMMA part and the rigid parts. A comparison of the experimental part profile versus the corresponding thermo-mechanically coupled simulation is shown in Figure 6-11. As in the 100 C embossing, areas of high curvature near the feature walls correspond to missing data from the optical profilometer measurements of the experimental part. Additionally, the final feature height has not been well predicted. In this case, the simulation predicts a final feature height of about 0.41 mm, but the embossed part features are very near the tool feature height of 0.5 mm. We believe the mismatch in feature height is because there is too much elastic recovery during the cooling phase of the simulation. In order to remedy this discrepancy, more work needs to be done to investigate the response of PMMA as it cools through the glass transition under load.

Contour plots of residual stress after cooling to room temperature for both embossed parts are shown in Figures 6-12 and 6-13. While the residual stress in the part is approximately the same for each case, the stresses are much more uniform in the 170 C part as compared with the 100 C part. Further conclusions and comparisons with the experimental birefringence results are inconclusive.

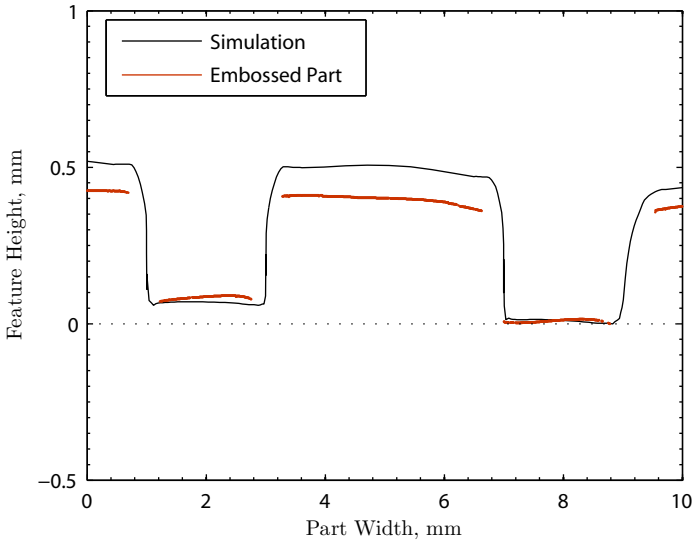

Figure 6-10: Comparison of the experimental part profile versus the corresponding isothermal simulation for the part embossed and demolded at 100 C.

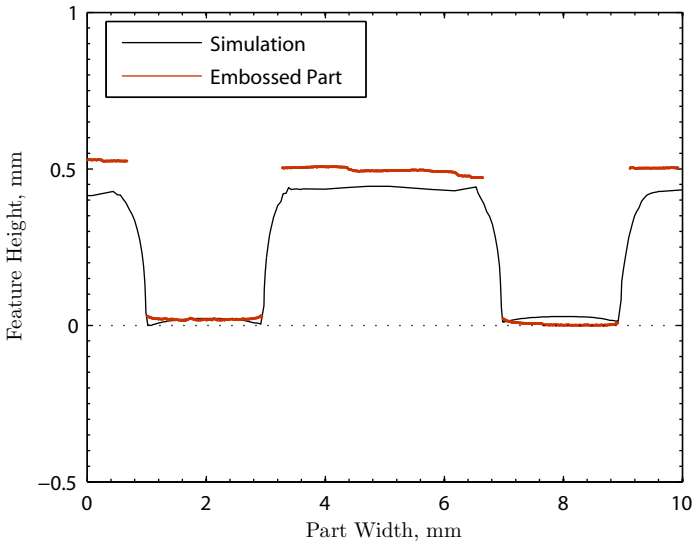

Figure 6-11: Comparison of the experimental part profile versus the corresponding isothermal simulation for the part embossed at 170 C and demolded at 50 C.

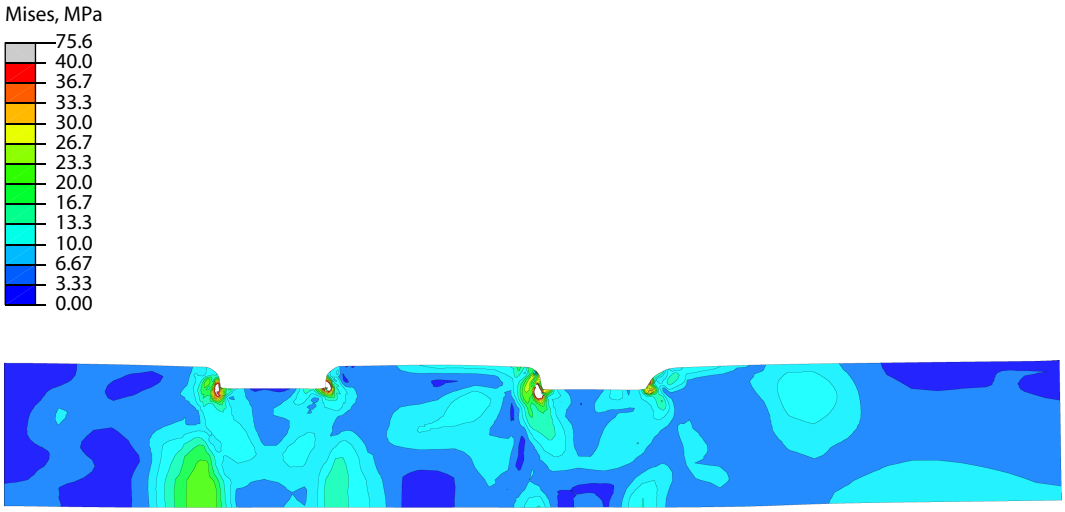

Figure 6-12: Simulation residual stresses in PMMA disk embossed and demolded at 100 C.

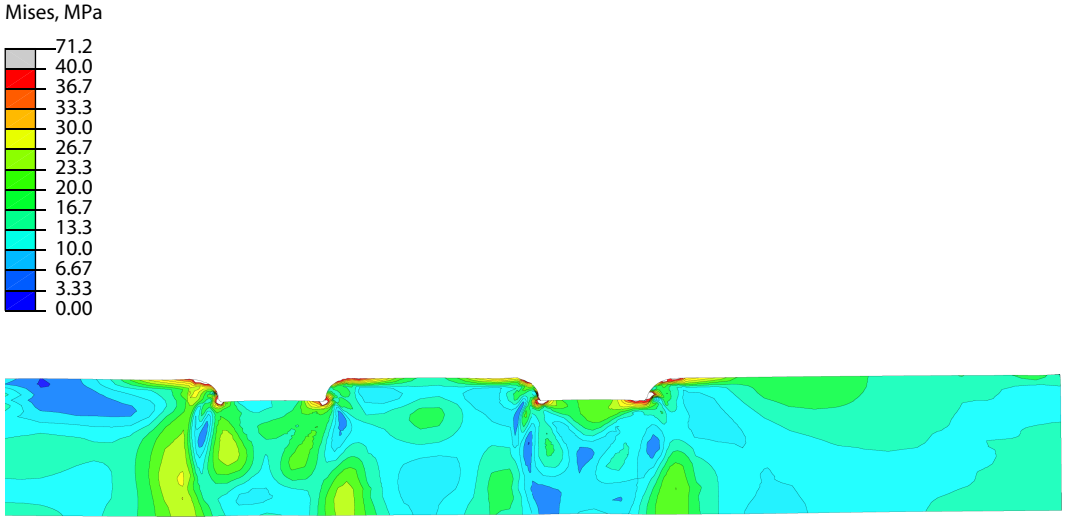

Figure 6-13: Simulation residual stresses in PMMA disk embossed at 170 C and demolded at 50 C.

6.3 Micro-embossing

6.3.1 Experiments

Procedures

The polymer substrate used in the micro-embossing experiments is the same as that used for the macro-embossing experiments except that it has a smaller nominal thicknesses of 1.5 mm. Square test specimens of approximately 25 mm length and width were produced by scoring the polymer sheet and snapping the sheet along the score mark. The polymer samples were not annealed prior to testing.

A silicon tool courtesy of Hayden Taylor was used in the micro-embossing experiments [19]. To manufacture the tool, a 100 mm diameter (100) silicon wafer was spin-coated with a 10 μm thick layer of AZ4620 positive photoresist (Shipley, Newton, MA). The resist was photolithographically patterned with an array of long, parallel rectangular openings that were 65 μm wide and on a pitch of 120 μm. The photoresist served as a mask for the subsequent deep reactive ion etching of the underlying silicon. The silicon was etched to a depth of approximately 30 μm, using a fluorine-based inductively coupled plasma in a machine manufactured by Surface Technology Systems of Newport, UK. After etching, the photoresist was stripped from the wafer by exposure to an oxygen plasma for 2 hours. SEM images of the tool are shown in Figure 6-14 along with Zygo interferometer measurements of the feature height contours and the cross-section profile.

The micro-embossing was conducted using a setup in Professor Dave Hardt's laboratory with the aid of Matthew Dirckx [20]. The machine is capable of rapid heating and cooling as compared to the setup used in our macro-embossing experiments. It also has better force and displacement control in our range of interest.

We followed the basic embossing process cycle as outlined earlier and chose to emboss at 130 C and demold at 90 C. For each test, the polymer substrate was placed on the lower machine platen and the silicon tool was then rested on the top surface of the polymer. The platens were then brought close together without applying pressure to the polymer while the system was brought up to the embossing temperature. After allowing the system to equilibrate for 5 min, a displacement ramp of 0.02 mm/sec was applied until the embossing force was reached. Seven different embossing forces were used: 0.3 kN, 0.5 kN, 0.7 kN, 1.0 kN, 1.5 kN, 2.0 kN, and 2.5 kN. Once the desired load was reached, it was held while the system was cooled at a rate of about 0.5 degrees/sec to the demolding temperature. To demold, the force was quickly removed and the part was taken out of the setup and manually separated from the tool.

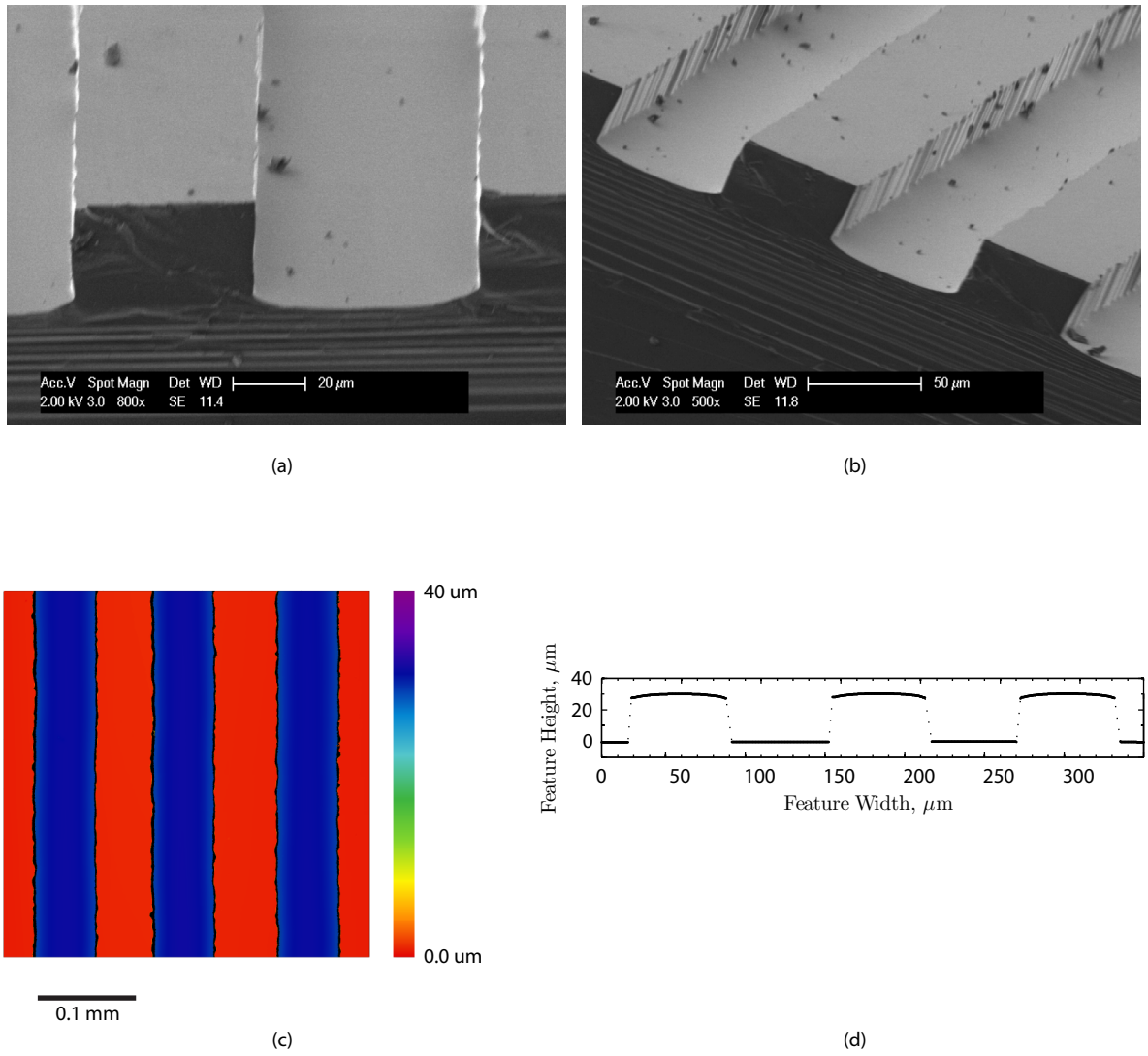

Figure 6-14: Images of Hayden Taylor's silicon tool used for micro-embossing experiments: (a and b) SEM images courtesy of Hayden Taylor, (c) Zygo height contour, (d) Zygo height profile. In the contour plot, black indicates area of missing data. In the height profile, solid lines indicate measured data, while the dotted lines indicate areas of missing data.

Results

Results of the micro-embossing of PMMA are shown in the following figures. Figure 6-15 shows height contours of sections of the PMMA parts for four of the different loading conditions. The data is captured using a Zygo optical profilometer. For further clarification, height profiles of sections of the parts and the silicon tool are shown in Figure 6-16. The tool profile has been inverted for ease of comparison. What we see is that as the load is increased from 0.3 kN to 2.5 kN, the tool feature is gradually filled.

One item of note is that there appears to be about a 3 μm discrepancy in the PMMA feature height and tool feature height, even at a large force of 2.5 kN. It is unclear what the source of this discrepancy is. Its possible that the PMMA features shrank during cooling. Also, the tool features may not have a uniform depth across the tool, such that the features that were measured were deeper than the ones that were actually performing the embossing.

We also took SEM images of our parts in order to look at the details near the feature walls that cannot be envisioned with the Zygo profilometer. The images are shown in Figure 6-17 for the various loading conditions. To capture the images, the PMMA parts were scored and snapped in half and then sputtered with gold. The images are taken along the snapped edge, which should be near the center of the molded part. A red line has been sketched on the SEM images to clarify the feature profile.

A major problem encountered during the micro-embossing experiments was tool failure. For embossing loads greater than 1 kN, it was impossible to separate the silicon tool from the PMMA part without breaking it. Figure 6-18 shows SEM images of the broken tool embedded in a PMMA part that was embossed at 2 kN. It is clear that better tooling needs to be developed in order to continue similar experimental endeavors.

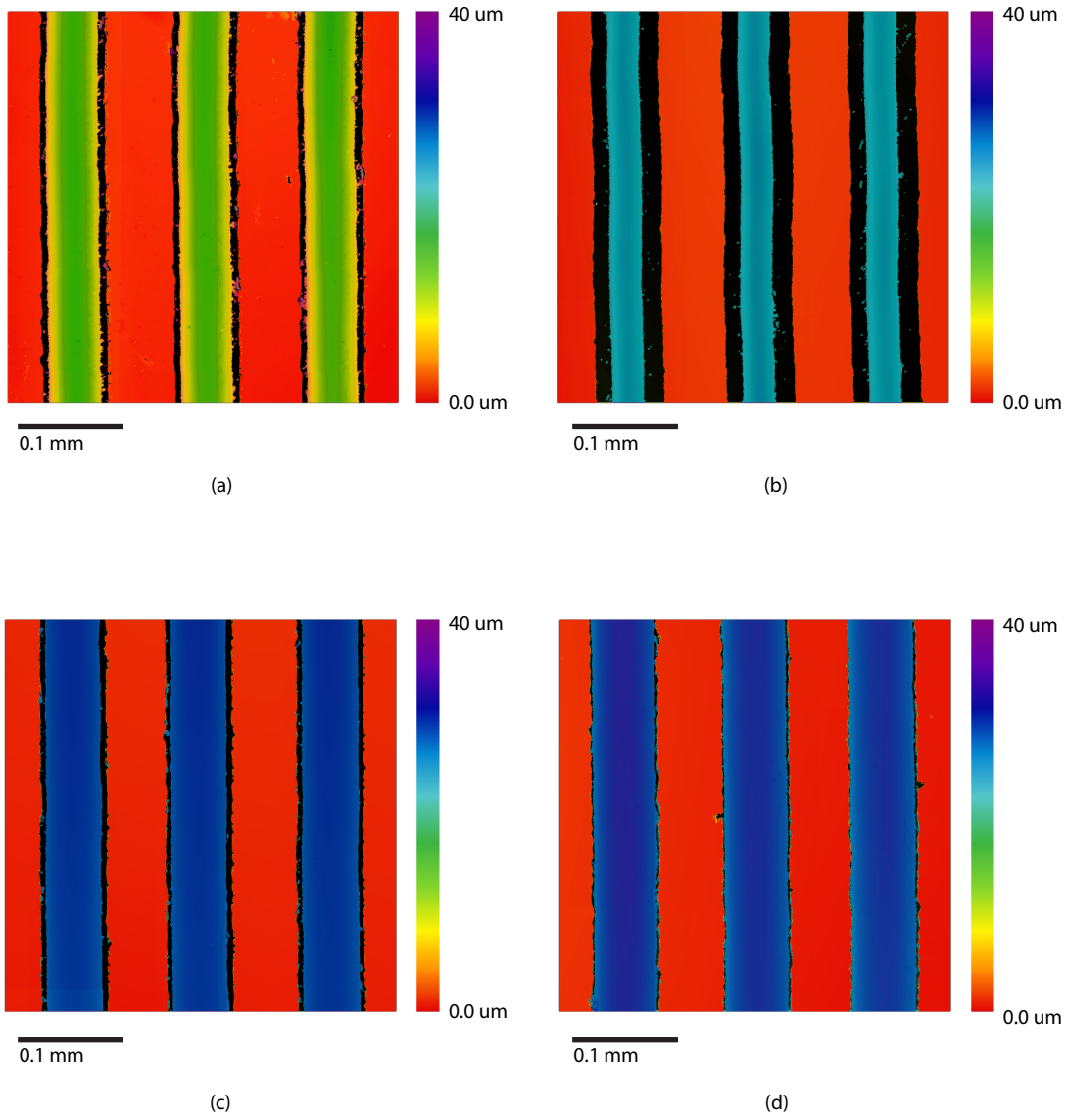

Figure 6-15: Zygo interferometer height contours of selected micro-embossed PMMA parts for different embossing forces: (a) 0.3 kN, (b) 0.5 kN, (c) 1.0 kN, (d) 2.5 kN. Black indicates areas of missing data which is indicative of an area of high curvature.

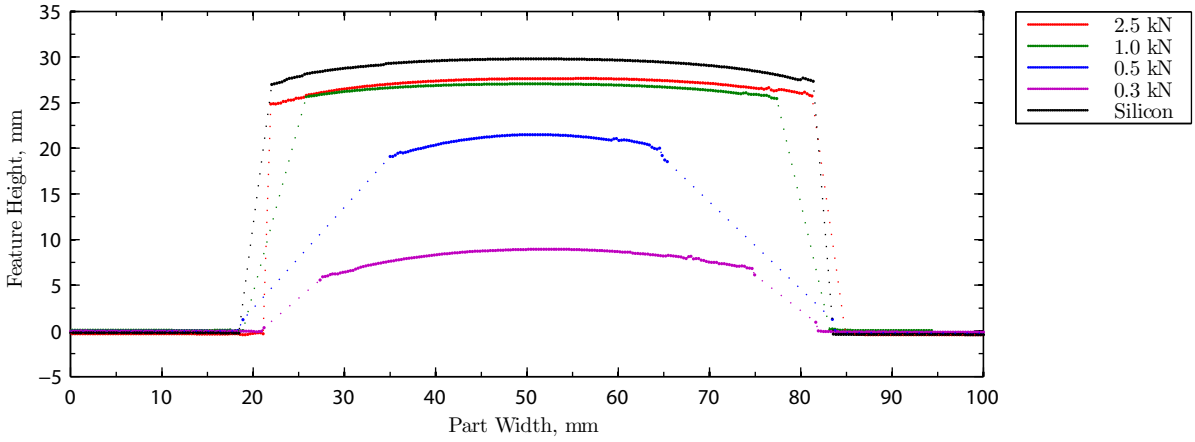

Figure 6-16: Zygo interferometer height profiles of selected micro-embossed PMMA part features for different embossing forces (0.3 kN, 0.5 kN, 1.0 kN, 2.5 kN) compared with the height profile of the silicon tool. Solid lines indicate measured data, while the dotted lines indicate areas of missing data which is indicative of an area of high curvature.

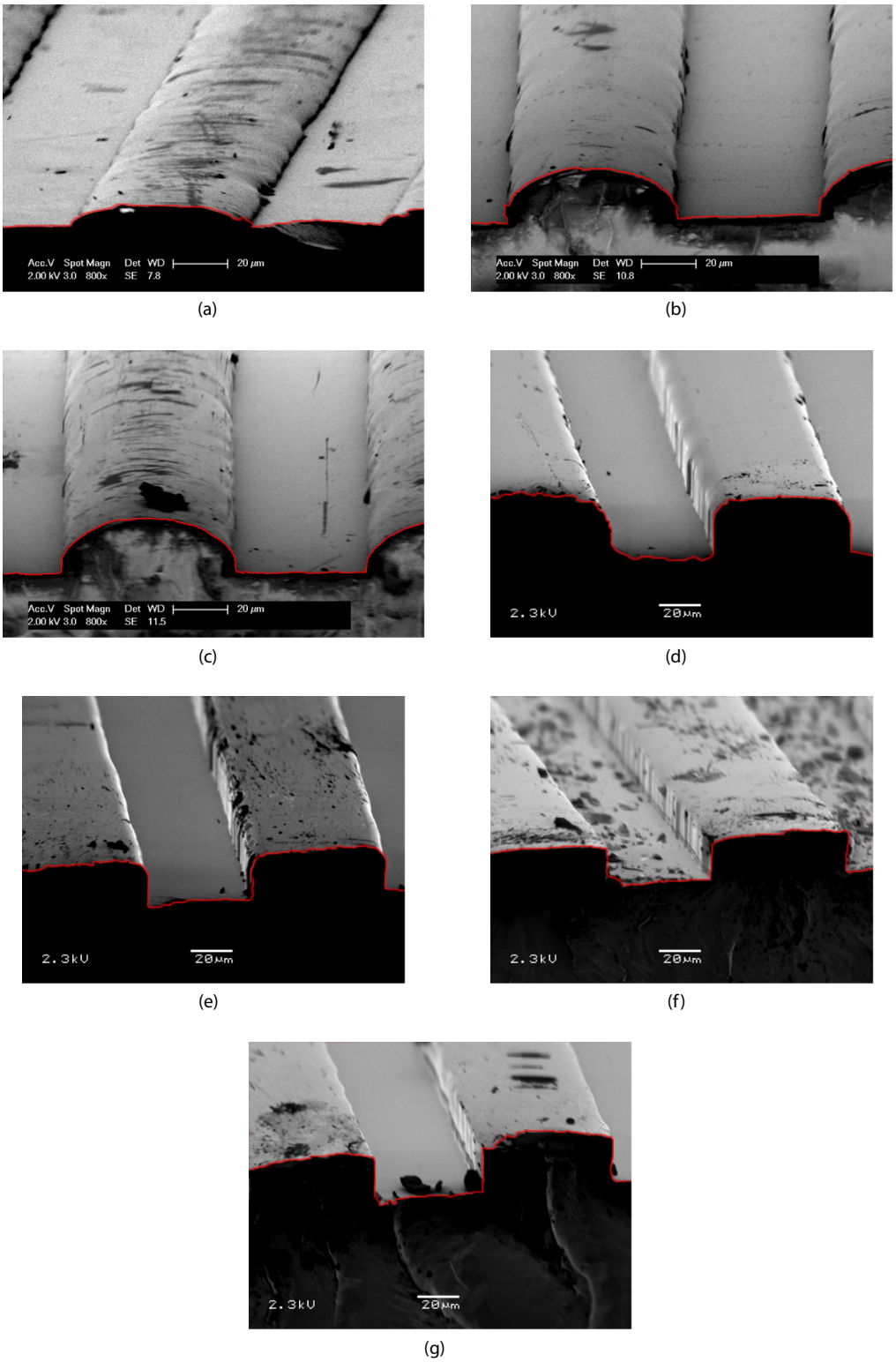

Figure 6-17: SEM images of micro-embossed PMMA parts for different embossing forces: (a) 0.3 kN, (b) 0.5 kN, (c) 0.7 kN, (d) 1.0 kN, (e) 1.5 kN, (f) 2.0 kN, (g) 2.5 kN. Images courtesy of Hayden Taylor.

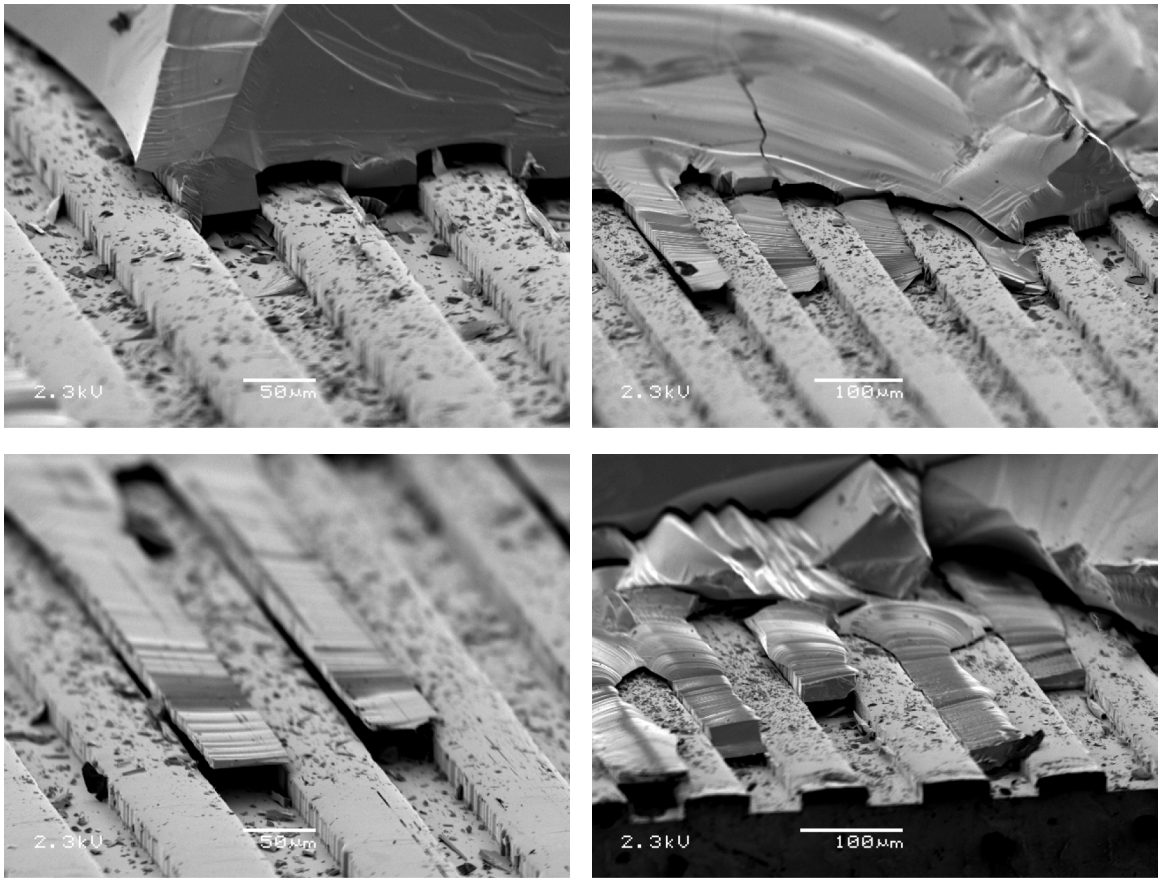

Figure 6-18: SEM images of failed silicon tool embedded in PMMA part for a micro-embossing load of 2.0 kN. Images and tool courtesy of Hayden Taylor.

6.3.2 Isothermal Plane-Strain Simulations

The schematic of the isothermal finite element setup is shown in Figure 6-19. We choose to model only a half-symmetric slice of the actual problem and assume that plane-strain conditions are satisfied. Further, because the tool features are on a pitch of 120 μm, we assume that approximately 200 features make contact with the PMMA substrate in the experiment, thus the embossing load used in the experiments will be 400 times greater than the embossing load used in the simulated half-symmetric slice.

Comparisons of SEM images from the experiments with the isothermal plane-strain micro-embossing simulations at various embossing loads are shown in Figure 6-20. The simulation images have been mirrored and repeated during post-processing to ease comparison with the experimental results. For the five embossing loads pictured, the filling pattern observed in the experiments and simulations are in excellent agreement.

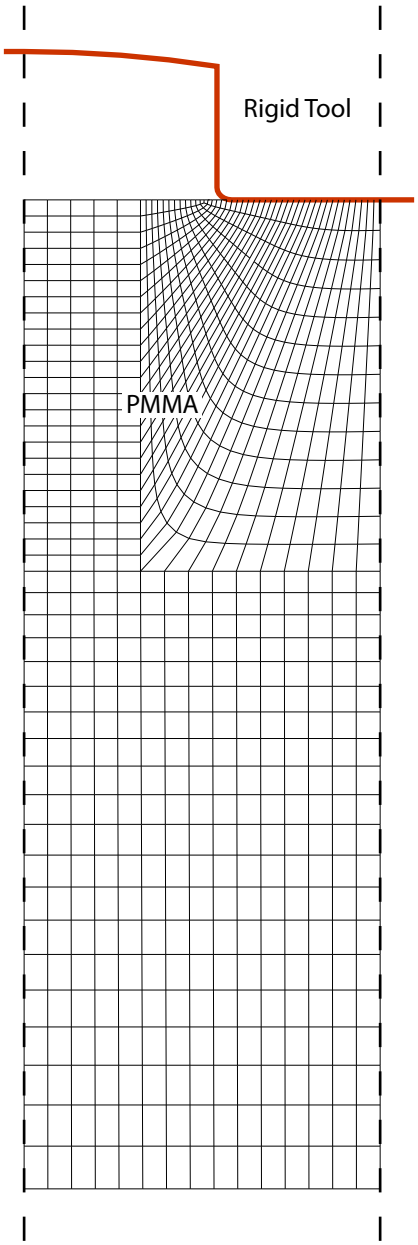

Figure 6-19: Finite element geometry for isothermal plane-strain micro-embossing simulation.

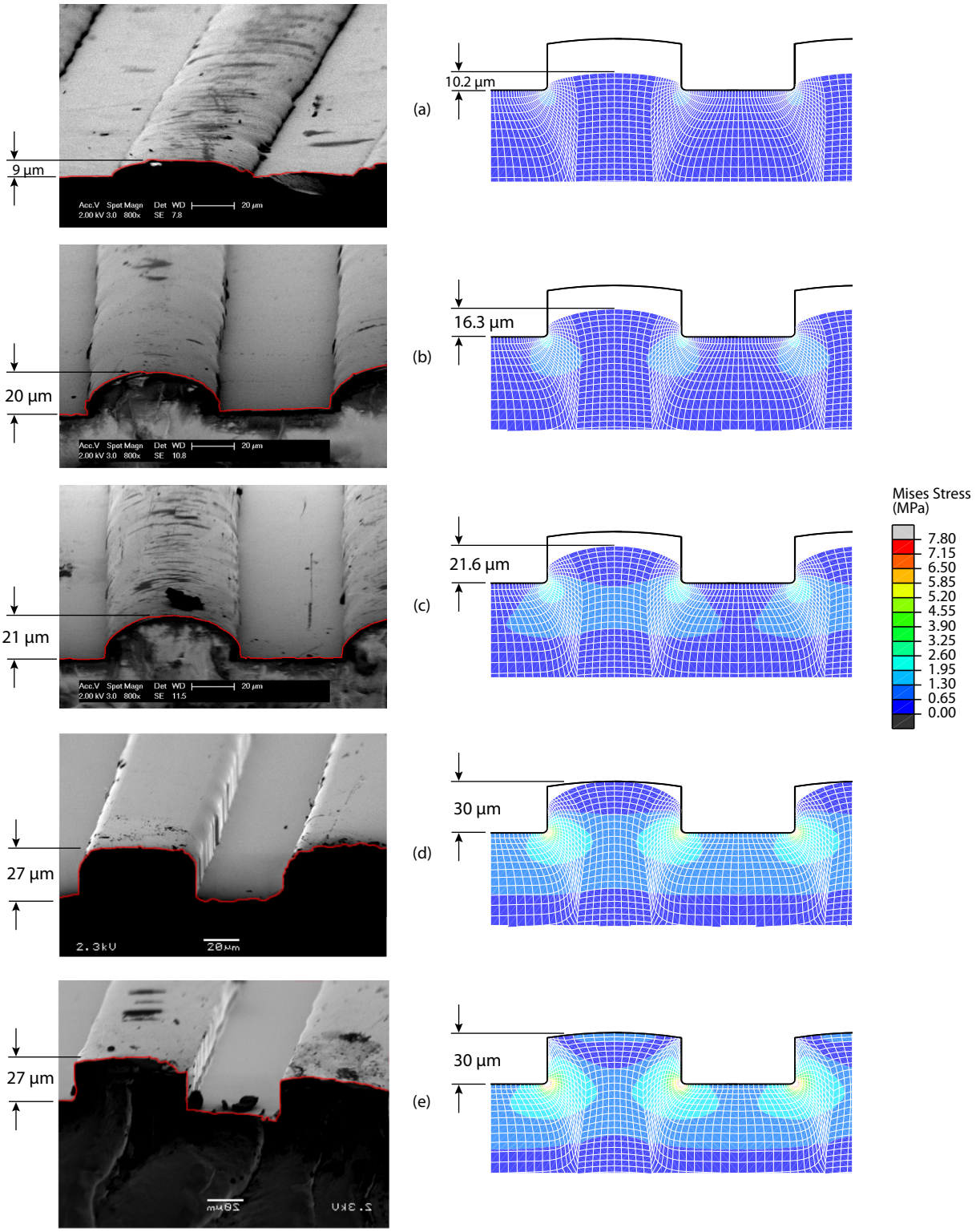

Figure 6-20: Comparisons of SEM images from experiments with isothermal plane-strain micro-embossing simulations for various embossing loads: (a) 0.3 kN, (b) 0.5 kN, (c) 0.7 kN, (d) 1.0 kN, and (e) 2.5 kN.

Bibliography

[1] Y. Guo, G. Liu, Y. Xiong, and Y. Tian. Study of the demolding processimplications for thermal stress, adhesion and friction control. *Journal of Micromechanics and Microengineering*, 17:9–19, 2007. doi: 10.1088/0960-1317/17/1/002.

[2] Y. Guo, G. Liu, X. Zhu, and Y. Tian. Analysis of the demolding forces during hot embossing. *Microsystem Technologies*, 13:411–415, 2007. doi: 10.1007/s00542-006-0225-9.

[3] M. Worgull and M. Heckele. New aspects of simulation in hot embossing. *Microsystem Technologies*, 10:432–437, 2004. doi: 10.1007/s00542-004-0418-z.

[4] M. Worgull, M. Heckele, and W. K. Schomburg. Large-scale hot embossing. *Microsystem Technologies*, 12:110–115, 2005. doi: 10.1007/s00542-005-0012-z.

[5] Y. Hirai, T. Konishi, T. Yoshikawa, and S. Yoshida. Simulation and experimental study of polymer deformation in nanoimprint lithography. *Journal of Vacuum Science and Technology B: Microelectronics and Nanometer Structures*, 22:3288–3293, 2004. doi: 10.1116/1.1826058.

[6] H. Hocheng and C. C. Nien. Numerical analysis of effects of mold features and contact friction on cavity filling in the nanoimprinting process. *Journal of Microlithography, Microfabrication, and Microsystems*, 5:011004–1–7, 2006. doi: 10.1117/1.2177286.

[7] C.-R. Lin, R.-H. Chen, and C. Hung. The characterisation and finite-element analysis of a polymer under hot pressing. *International Journal of Advanced Manufacturing Technology*, 20:230–235, 2002. doi: 10.1007/s001700200146.

[8] C.-R. Lin, R.-H. Chen, and C. Hung. Preventing non-uniform shrinking in open-die hot embossing of pmma microstructures. *Journal of Materials Processing Technology*, 140:173–178, 2003. doi: 10.1016/S0924-0136(03)00709-X.

[9] Y.-J. Juang, L. J. Lee, and K. W. Koelling. Hot embossing in microfabrication. part ii: Rheological characterization and process analysis. *Polymer Engineering and Science*, 42:551–566, 2002. doi: 10.1002/pen.10971.

[10] M. Worgull, M. Heckele, J.-F. Htu, and K. K. Kabanemi. Modeling and optimization of the hot embossing process for micro- and nanocomponent fabrication. *Journal of Microlithography, Microfabrication, and Microsystems*, 5:011005–1–13, 2006. doi: 10.1117/1.2176729.

[11] D. Yao, P. Nagarajan, L. Li, and A. Y. Yi. A two-station embossing process for rapid fabrication of surface microstructures on thermoplastic polymers. *Polymer Engineering and Science*, 47: 530–539, 2007. doi: 10.1002/pen.20721.

[12] J.-H. Jeong, Y.-S. Choi, Y.-J. Shin, J.-J. Lee, K.-T. Park, E.-S. Lee, and S.-R. Lee. Flow behavior at the embossing stage of nanoimprint lithography. *Fibers and Polymers*, 3:113–119, 2002.

[13] W.-B. Young. Analysis of the nanoimprint lithography with a viscous model. *Microelectronic Engineering*, 77:405–411, 2005. doi: 10.1016/j.mee.2005.01.024.

[14] H. D. Rowland, W. P. King, A. C. Sun, and P. R. Schunk. Simulations of nonuniform embossing: The effect of asymmetric neighbor cavities on polymer flow during nanoimprint lithography. *Journal of Vacuum Science and Technology B: Microelectronics and Nanometer Structures*, 23:2958–2962, 2005. doi: 10.1116/1.2127939.

[15] H. D. Rowland, W. P. King, A. C. Sun, and P. R. Schunk. Impact of polymer film thickness and cavity size on polymer flow during embossing: Toward process design rules for nanoimprint lithography. *Journal of Micromechanics and Microengineering*, 15:2414–2425, 2005. doi: 10.1088/0960-1317/15/12/025.

[16] D. Yao and P. Nagarajan. Cold forging method for polymer microfabrication. *Polymer Engineering and Science*, 44:1998–2004, 2004. doi: 10.1002/pen.20203.

[17] D. Yao, V. L. Virupaksha, and B. Kim. Study on squeezing flow during nonisothermal embossing of polymer microstructures. *Polymer Engineering and Science*, 45:652–660, 2005. doi: 10.1002/pen.20322.

[18] ABAQUS, 2007.

[19] M. Dirckx, H. Taylor, and D. Hardt. High-temperature de-molding for cycle time reduction in hot embossing. In *Society of Plastics Engineers Annual Technical Conference*, Cincinatti, 2007.

[20] G. T. Shoji. Modeling and control of a hot micro-embossing machine. Master's thesis, Massachusetts Institute of Technology, June 2006.

Chapter 7

Conclusions

Significant contributions to the fields of polymer-mechanics and numerical simulation of the micro-hot-embossing process for amorphous polymers have been made during the course of this study. Specifically:

1. A relatively complete experimental data set has been generated for PMMA covering a temperature range spanning room temperature to ≈ 60 C above the glass transition temperature $\vartheta_g \approx 110$ C of the material, in a strain-rate range of $\approx 10^{-4}$/s to 10^{-1}/s, and under compressive stress states in which this material does not exhibit crazing.

2. A new thermo-mechanically-coupled, large-deformation constitutive theory for amorphous polymers has been formulated. The theory has been specialized for modeling the response of amorphous polymers in a temperature range below the glass transition, and also continuously through the glass transition temperature of these materials.

3. The material parameters/functions appearing in the theory have been determined from experimental data for PMMA, and a rigorous calibration procedure for determining the material parameters has been documented.

4. The theory has been implemented in a finite element package Abaqus/Explicit [1] for the simulation and design of hot processing of amorphous polymers in the solid state.

5. A preliminary set of embossing experiments to validate the numerical simulation capability have been conducted at both the millimeter and micrometer length-scales. The flow patterns predicted by the simulations are in very good agreement with the experimental results.

While much has been accomplished, much more still remains to be done. Some outstanding issues include:

1. The material parameters/functions in the theory need to be calibrated for other amorphous thermoplastic-polymers, especially those of interest to the microfluidic community, such as the cyclic olefin copolymers (COC) and cyclic olefin polymers (COP). If the need arises, the theory needs to be modified to account for the peculiarities of these materials.

2. Fully thermo-mechanically coupled simulations that model the entire hot-embossing process from heatup to demold need to be conducted and verified with experimental data for all polymers of interest.

3. Silicon, because of its brittle nature, is not a good die material for micro-embossing of polymers. Better tooling materials need to be investigated.

Work is currently underway in our research group to address all of these issues.

Bibliography

[1] ABAQUS, 2007.

Appendix A

Experimental Procedure Details

A.1 Introduction

This appendix covers the stress/strain experiment procedures which were conducted on poly(methyl methacrylate) (PMMA) in more detail than what was described in Chapter 2.

A.2 Procedures

Because PMMA crazes in tension and is known to undergo deformation by shear-yielding in compression, compression is the optimum mode of deformation to extract properties for our large-deformation model which does not account for crazing.

The material used in these experiments was purchased from McMaster-Carr (a commercial vendor) in the form of 0.5" diameter cast rods which were cut into 0.5" tall specimens. Specimens were annealed before and after machining by heating in a furnace to slightly above the glass transition temperature of 110 C and holding at that temperature for two hours. The specimens were then allowed to slowly cool in the furnace to room temperature over a period of several hours. Before a given experiment, the specimen was allowed to anneal at the testing temperature for one hour prior to testing.

To reduce friction at the platen/specimen interface, the platens were polished and thin Teflon (PTFE) films were placed between the specimen and the platens. Oils and greases are not used as lubricants because they may attack or dissolve the PMMA specimens, or cause them to craze.

All experiments were conducted using a biaxial servo-hydraulic Instron testing machine having a normal load capacity of 220 kN over an axial travel of 100 mm and a torque capacity of 2.2 kN-m over a rotational travel of 95°. All strains were measured using an extensometer with a 12.7 mm gauge section and $\pm$ 5.08 mm travel.

Data acquisition was performed on a desktop PC. LabVIEW 6, a customizable data acquisition software package, interfaces with the Instron through a National Instruments PCI card[1] installed in the PC. Raw data was sampled at 1 kHz, however, LabVIEW performed real time averaging

[1]National Instruments PCI Multifunction Data Acquisition Card, Model AT-MIO-16E-10. Analog In: 12bit, 100 kS/s, ranges: ±10V, ±5V, ±2.5V, ±1V, ±500mV, ±250mV, ±100mV, ±50mV; Analog Out: 12bit, 100kS/s, ±10V

before recording data, resulting in a smoothed output with an artificial sampling rate ranging from 5 Hz to 100 Hz depending on the speed of the test.

A.2.1 Strain Control

All compression tests were carried out using constant true strain-rates. Our Instron is not capable of achieving true strain-rates to large final strains without the aid of software. So, to achieve the true strain-rate control LabVIEW was setup to send a displacement command signal to the Instron's actuator that approximates a true strain-rate. LabVIEW updates the command signal incrementally at a rate of about 1 kHz. The command signal increment for the n-th increment is given by

$$\Delta V_{\text{com}} = \left[l_0 \exp\left(\epsilon^{n-1}\right) \dot{\epsilon}\, \Delta t_{\text{com}}^{n-1}\right] \frac{1}{K_{mm/V}} \tag{A.1}$$

$$= \left[l_0 \exp\left(\frac{l_0 + \delta_{\text{ext}}^{n-1}}{l_0}\right) \dot{\epsilon}\, \Delta t_{\text{com}}^{n-1}\right] \frac{1}{K_{mm/V}} \tag{A.2}$$

where l_0 is the original specimen height, ϵ is the current specimen true strain measured at the start of the increment, $\dot{\epsilon}$ is the desired true strain-rate, $\Delta t_{\text{com}}^{n-1}$ is the time increment of the previous increment, $K_{mm/V}$ is the Instron conversion factor for the command signal, and $\delta_{\text{ext}}^{n-1}$ is the current total displacement measured by the extensometer at the beginning of the increment. The total command signal at increment $n-1$ is

$$V_{\text{com}}^{n-1} = \left[l_0 + \delta_{\text{ext}}^{n-1}\right] \frac{1}{K_{mm/V}} \tag{A.3}$$

so that the total command signal at increment n is then

$$V_{\text{com}}^{n} = \Delta V_{\text{com}} + V_{\text{com}}^{n-1} \tag{A.4}$$

$$= \left\{\delta_{\text{ext}}^{n-1} + l_0 \left[1 + \exp\left(\frac{l_0 + \delta_{\text{ext}}^{n-1}}{l_0}\right) \dot{\epsilon}\, \Delta t_{\text{com}}^{n-1}\right]\right\} \frac{1}{K_{mm/V}} \tag{A.5}$$

The Instron follows this LabVIEW command signal fairly well so that a closed loop strain control setup is not necessary.

This discretization of the voltage command signal imposes an upper and lower bound on the strain-rate that can be achieved with a given set of electronics. The factors that establish the lower bound on the strain-rate are:

- the resolution of the DAQ analog output channel ΔV_{min},
- the command signal conversion factor $K_{mm/V}$,
- the original specimen height l_0, and
- the maximum strain of the test ϵ_{max}.

and they are related through equation (A.1)

$$\dot{\epsilon} = \frac{\Delta V_{\text{min}}\, K_{mm/V}}{l_0\, \exp\left(\epsilon_{\text{max}}\right)\, \Delta t} \tag{A.6}$$

To minimize $\dot{\epsilon}$, $K_{mm/V}$ should be minimized according to

$$K_{mm/V} = \frac{l_f - l_0}{V_{\max}} = l_0 \left[\frac{\exp(\epsilon_{\max}) - 1}{V_{\max}} \right] \tag{A.7}$$

where $V_{\max}$ is the maximum voltage sent by the analog out channel to the Instron. This is constrained by the Instron and the analog out channel to fall in the range ± 10 V, so we assume $V_{\max}$ = 10 V. Then, by (A.6) and (A.7) $\dot{\epsilon}$ is

$$\dot{\epsilon} = [1 - \exp(-\epsilon_{\max})] \, \frac{\Delta V_{\min}}{10 \, \Delta t} \tag{A.8}$$

And because the resolution of the 12-bit analog out channel of the data acquisition card is fixed at $\Delta V_{\min}$ = 10 V / 2^{12} = 2.44 mV, and all of our tests were conducted to a maximum strain of $\epsilon_{\max}$ = -1, the strain-rate can now be directly related to the discretization time-increment

$$\dot{\epsilon} = \frac{-4.2 \times 10^{-4}}{\Delta t} \tag{A.9}$$

Therefore, in order to minimize $\dot{\epsilon}$, we must maximize the value of $\Delta t_{\max}$, however, the time increment must be minimized so that the material will not noticeably relax during the time increment. For a given strain-rate, one can then calculate the time increment and determine if it is acceptable for the material being tested. In our case, for PMMA, we have capped $\Delta t_{\max}$ = 1.4 s which gives us a lowerbound on the strain rate

$$\dot{\epsilon} \geq -3 \times 10^{-4} \text{ s} \tag{A.10}$$

If a lower strain rate is desired, it is recommended to use a data acquisition card with 16-bit analog output, instead of 12-bit.

Following a similar procedure, we can determine the upper bound on the strain-rate. The factors that establish the strain-rate upper bound are:

- the sampling rate of the DAQ analog output channel $\Delta t_{\min}$,
- the command signal conversion factor $K_{mm/V}$,
- the original specimen height l_0, and
- the maximum strain of the test $\epsilon_{\max}$.

and returning to (A.1), these factors are related by

$$\dot{\epsilon} = \frac{\Delta V \, K_{mm/V}}{l_0 \, \exp(\epsilon_{\max}) \, \Delta t_{\min}} \tag{A.11}$$

and using (A.7) gives

$$\dot{\epsilon} = [1 - \exp(-\epsilon_{\max})] \, \frac{\Delta V}{V_{\max} \, \Delta t_{\min}} \tag{A.12}$$

The sampling rate of the LabVIEW loop is set at $\Delta t_{\min}$ = 1 / 1kHz = 1 ms, and assuming $\epsilon_{\max}$ = -1, the strain-rate becomes

$$\dot{\epsilon} = -1.7 \times 10^4 \left(\frac{\Delta V}{V_{\max}} \right) \tag{A.13}$$

In order to maximize $\dot{\epsilon}$, we must maximize the ratio $\Delta V/V_{\max}$, yet this ratio describes the discretization of the voltage signal and if it becomes too large, then the actuator velocity profile will not be well discretized. In order to maintain a smooth profile we choose ΔV such that that are at least 5000 increments

$$\Delta V = V_{\max}/5000 = 0.002\, V_{\max} \tag{A.14}$$

which then gives us an upperbound on the strain rate

$$\dot{\epsilon} \leq -3.4 \times 10^{-1} \text{ s} \tag{A.15}$$

In order to obtain a higher strain-rate, the time increment can be reduced by increasing the scan rate, but the data acquisition system may not be able to handle the increased scanning rate. Additionally, the Instron may not necessarily be able to follow the command signal at higher rates.

In conclusion, for a 0.5" tall PMMA specimen being compressed to a final strain of -1, the strain-rate must fall in the range

$$-3 \times 10^{-4} \leq \dot{\epsilon} \leq -3.4 \times 10^{-1} \text{ s} \tag{A.16}$$

and the Instron conversion factor should be

$$K_{mm/V} = -8.02 \text{ mm/10 V} \tag{A.17}$$

These numbers will change for different specimen heights and different final strains.

A.2.2 Load Cells

Two different load cells were used to measure forces during testing. For temperatures below the glass transition, the 250 kN Instron load cell and accompanying electronics supplied suitable resolution. For lower load tests, a 8.9 kN load cell was used. The smaller load cell was purchased from the Sensotec Sensors division of Honeywell[2,3]. The load cell is temperature compensated in the range 21 C to 121 C. It provides an output of 2.993 mV/V, which for an excitation of 10 V[4] provides an output of 29.93 mV at full scale. Using the 12-bit National Instruments data acquisition card mentioned earlier along with software data averaging at a 100 mV input range, we are able to achieve a load resolution of 1.8 N over the 8.9 kN range.

A.2.3 Specimen Heating

A robust and easy to control heating system was designed for the experimental setup. A custom sized oven was manufactured by ATS[5]. It is shown pictured in Figure A-1 along with the heated load train. There are two configurations of the load train available as shown in Figure A-2: one with the Sensotec load cell in place and one without. The platens are manufactured from H13

[2]Sensotec Load Cell, Model AL111DL,1F. 8.9kN; Compression calibrated; Temperature compensated 21C - 121C; Output 2.993mV/V; Excitation 10V

[3]Sensotec Load Cell Cable, Model AA113. PTO6A-10-6S mating connector with 15 ft of 4 conductor cable

[4]HP/Agilent DC Power Supply, Model E3610A. 30W; 8V/3A or 15V/2A

[5]ATS Box Oven, Model 3710 Custom. Max 425C; K-type Thermocouple; Internal: 18.5"W x 18.5"D x 10.5"H; External: 23.75"W x 30.5"D x 15"H; 4" x 6" viewport; 2208W; 10.6A; 208VAC, single-phase, 60Hz; Cooling option installed

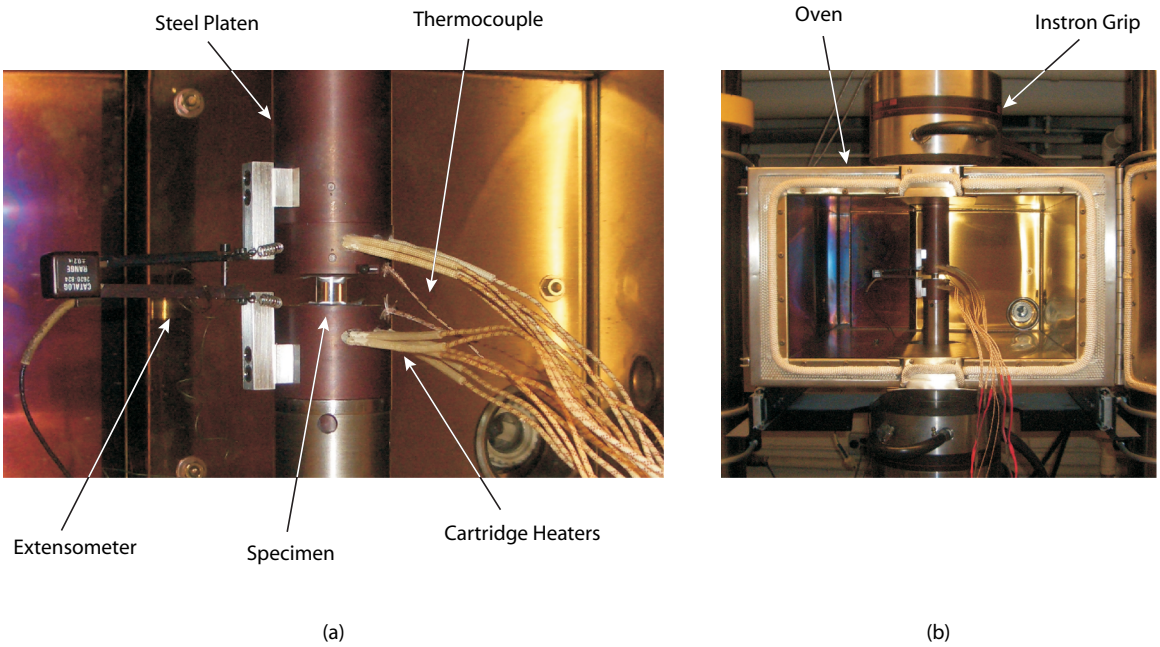

Figure A-1: Images of the experimental setup used for the heated compression experiments on PMMA. (a) Close up of setup showing the cylindrical PMMA specimen between the two heated platens. The extensometer is mounted on the left side. Cartridge heaters and thermocouples for temperature control are shown on the right. (b) Larger view of setup showing enclosing temperature-controlled oven and Instron grips.

tool steel[6], which provides decent heat conduction, but it is also very durable. There is a spherical seat integrated into the top platen to help minimize misalignment. The spherical seat is suspended from the steel connecting rod with metal springs. Additionally, the platens have an extensometer mount. Engineering drawings for the parts are shown in Figures A-3, A-4, A-5, A-6, A-7, A-8, A-9, A-10, and A-11.

[6]Carpenter Powder Products H13 Tool Stell, Model 2101308-0000. 2" dia x 24" long stock

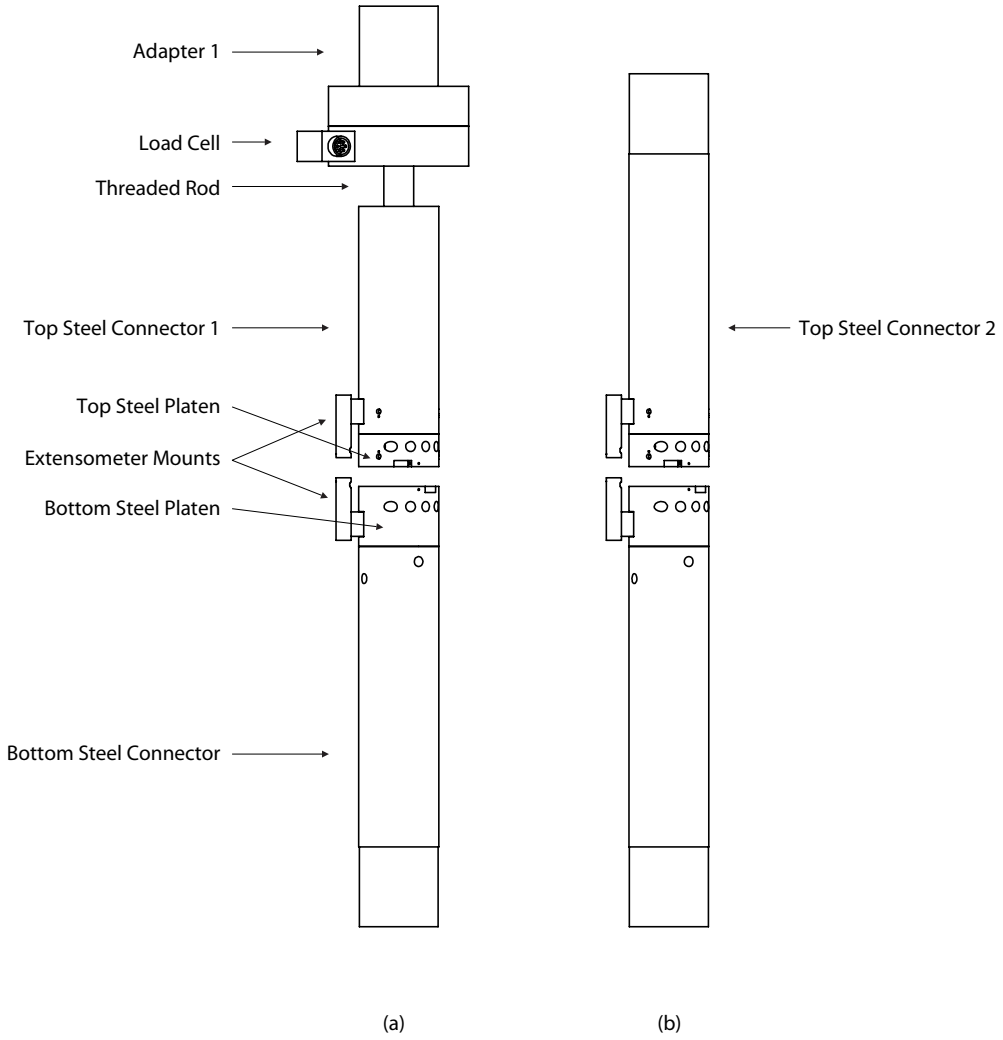

Figure A-2: Drawing of the complete second generation load train using the heated steel platens. Two versions are shown: (a) includes the Sensotec load cell in the load train; (b) without the Sensotec load cell.

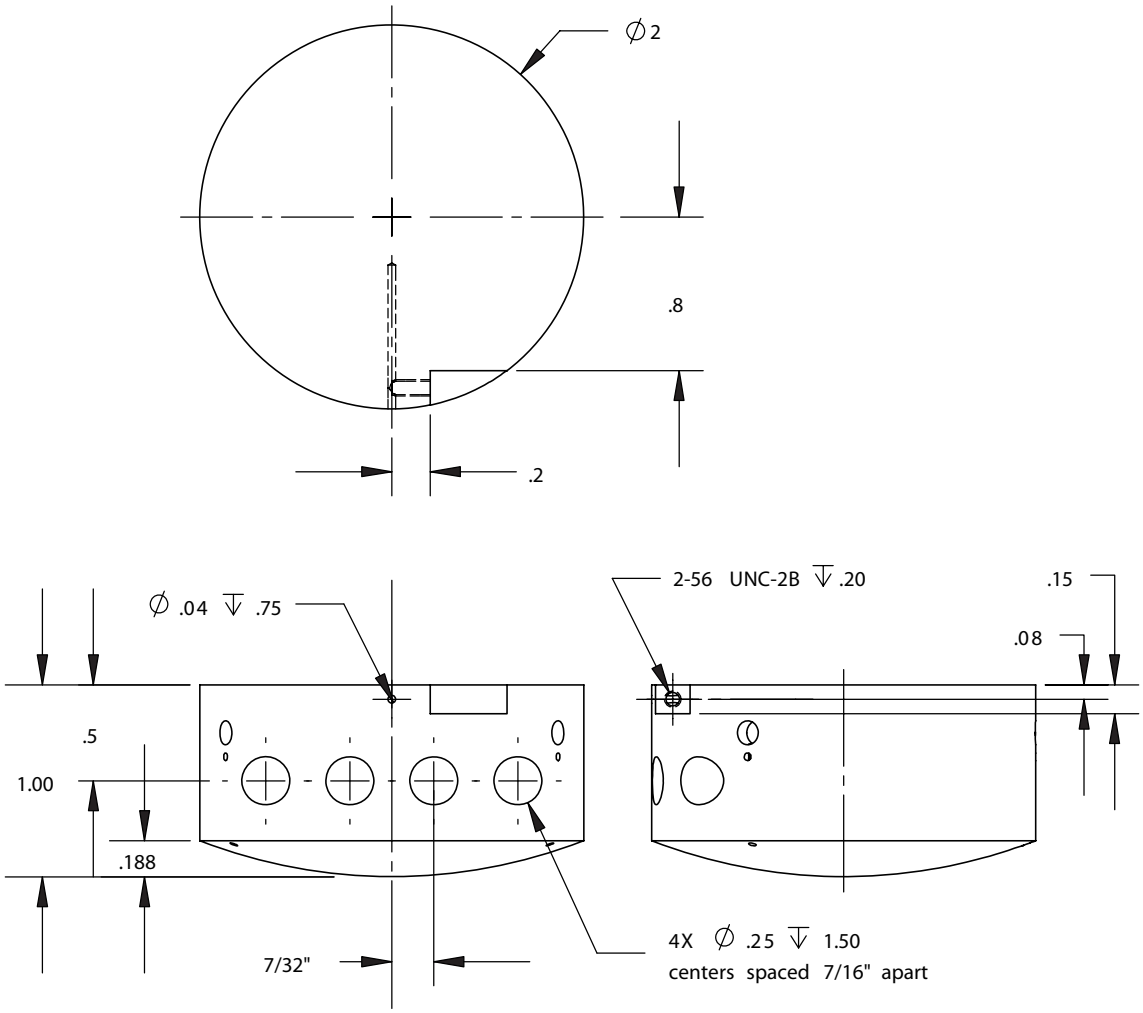

Figure A-3: Drawing of the second generation top steel heated platen. Dimensions in inches unless otherwise noted.

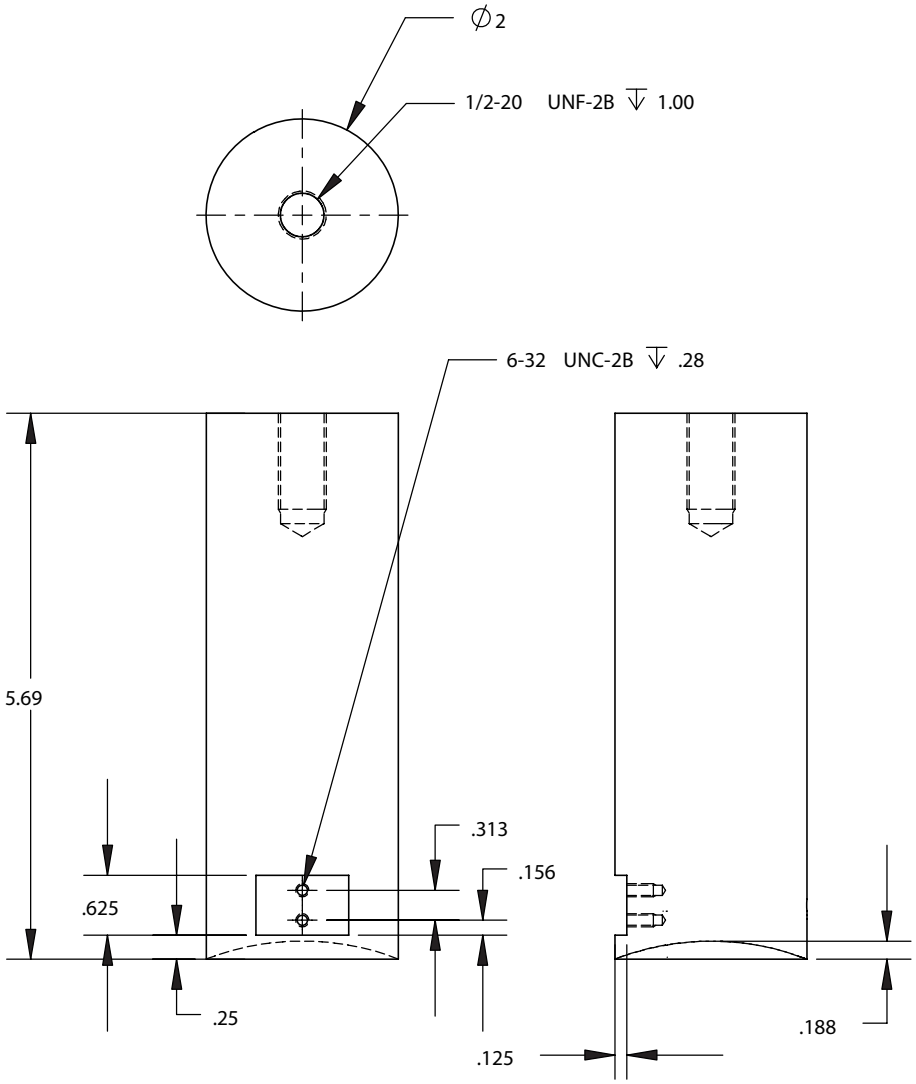

Figure A-4: Drawing of the second generation top platen connector used with the Sensotec load cell and threaded rod. Dimensions in inches unless otherwise noted.

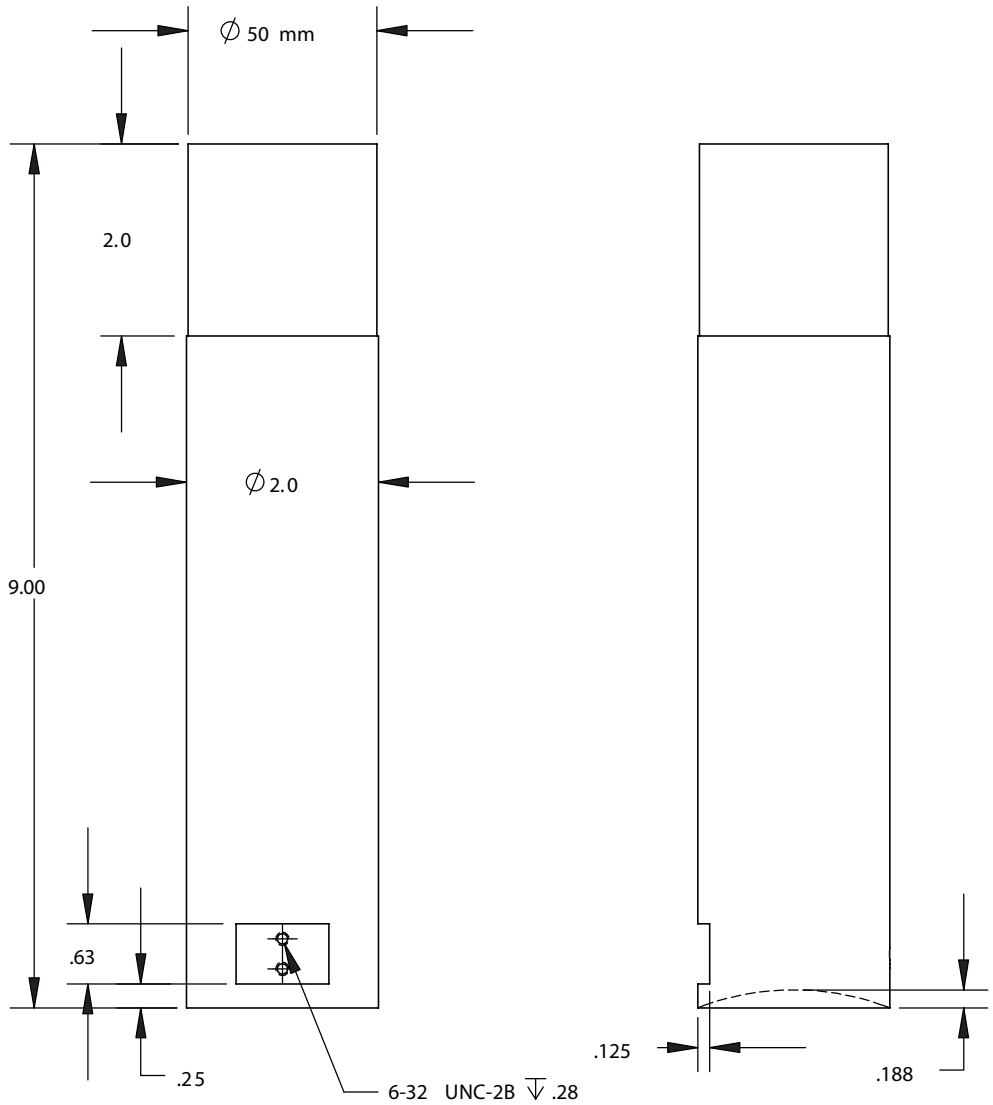

Figure A-5: Drawing of the second generation top platen connector used to connect the load train to the Instron grip when the Sensotec load cell is not used. Dimensions in inches unless otherwise noted.

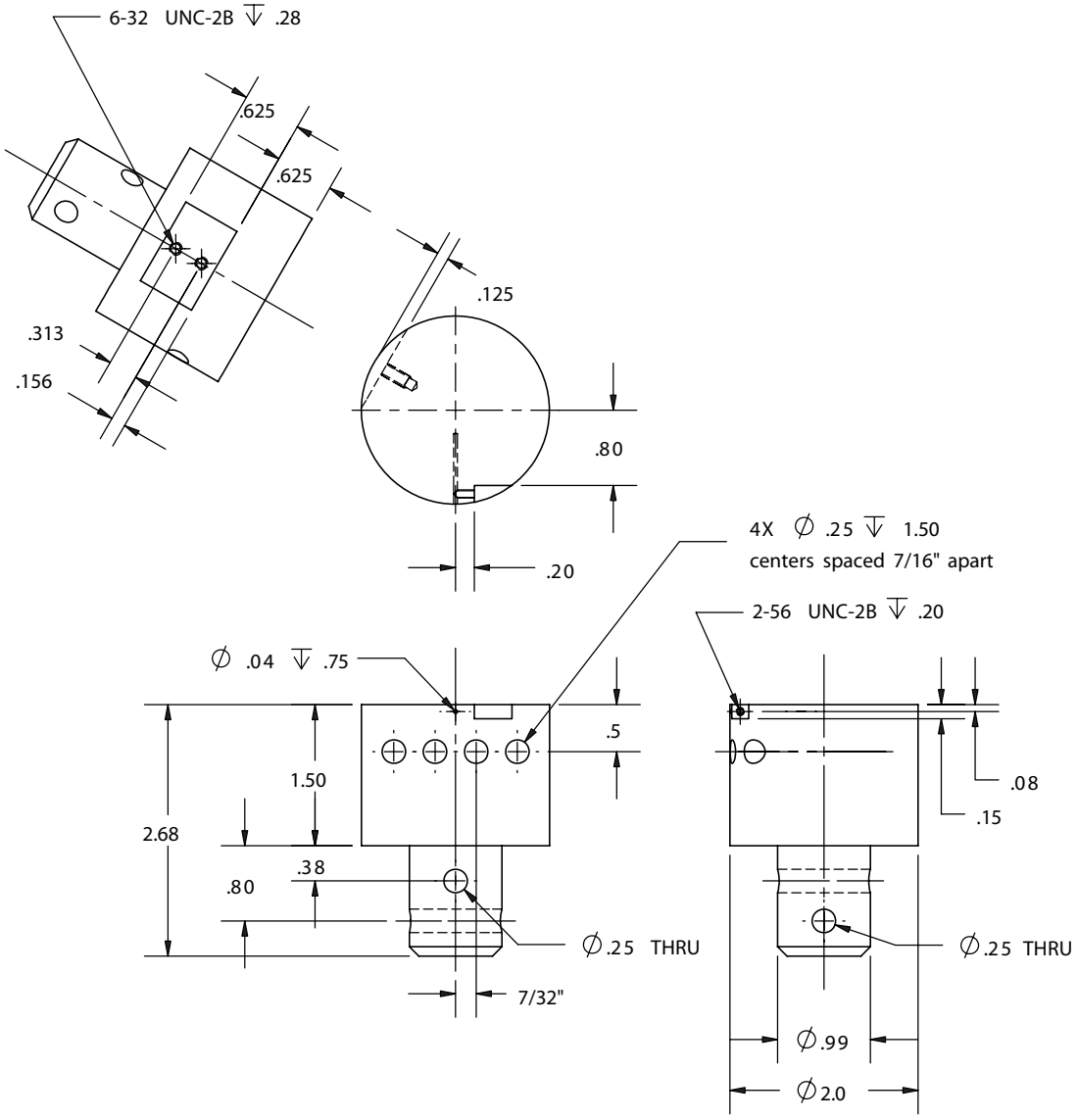

Figure A-6: Drawing of the second generation bottom steel heated platen. Uses pins to connect to bottom connector. Dimensions in inches unless otherwise noted.

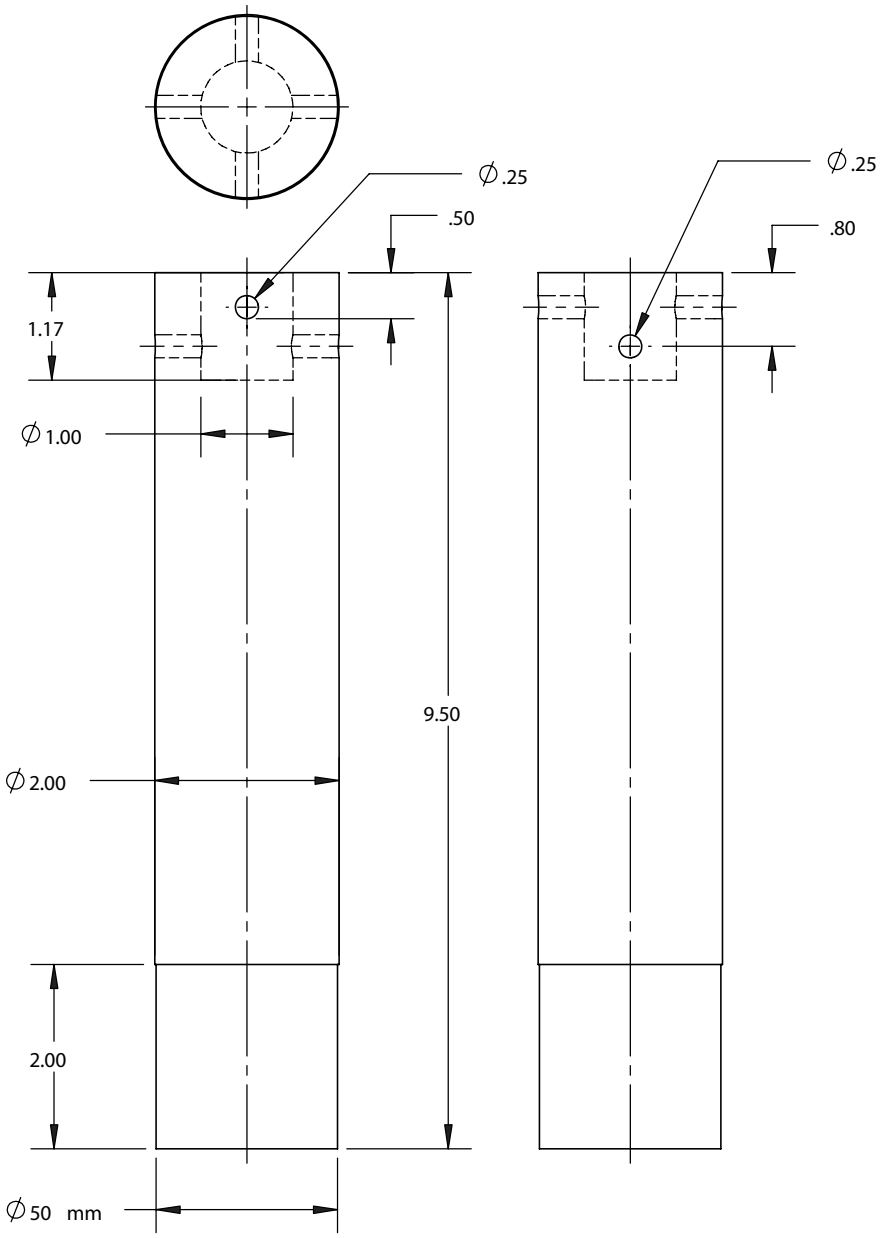

Figure A-7: Drawing of the second generation bottom platen connector used to connect the load train to the Instron grip. Dimensions in inches unless otherwise noted.

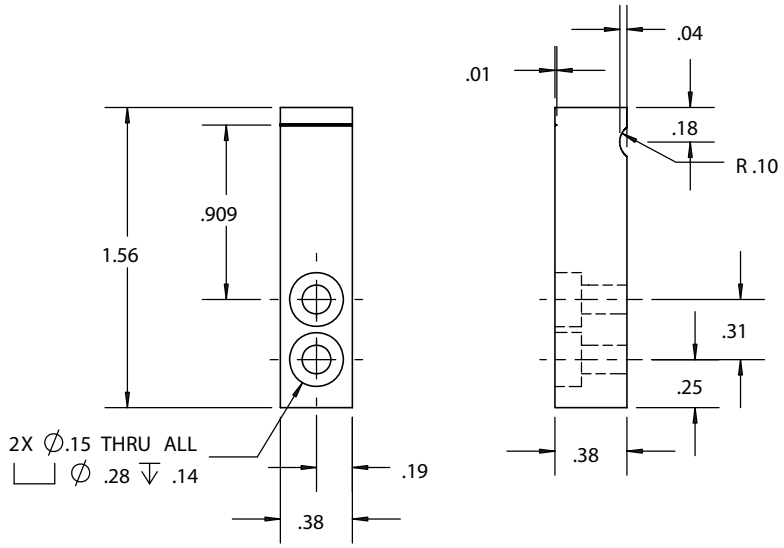

Figure A-8: Drawing of the extensometer mount. Dimensions in inches unless otherwise noted.

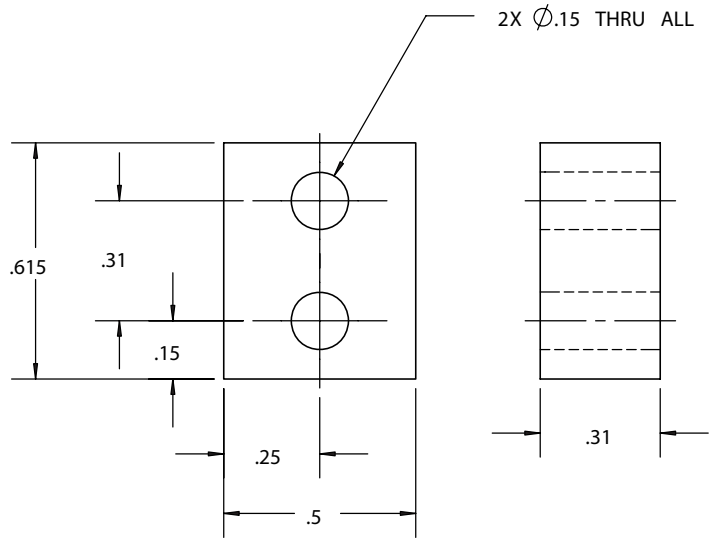

Figure A-9: Drawing of the extensometer standoff. Dimensions in inches unless otherwise noted.

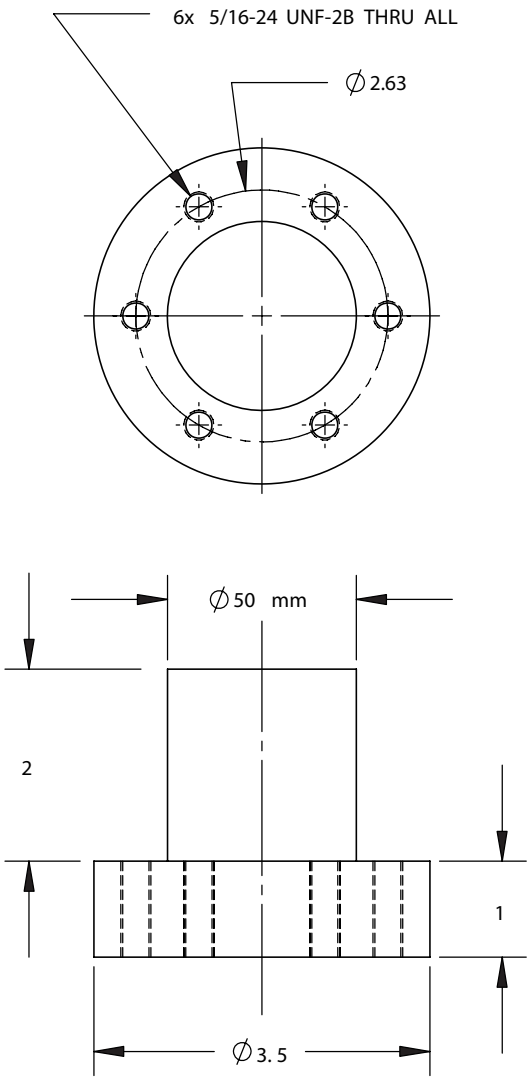

Figure A-10: Drawing of the aluminum adapter used to connect the Sensotec load cell to the Instron grip. Dimension in inches unless otherwise noted.

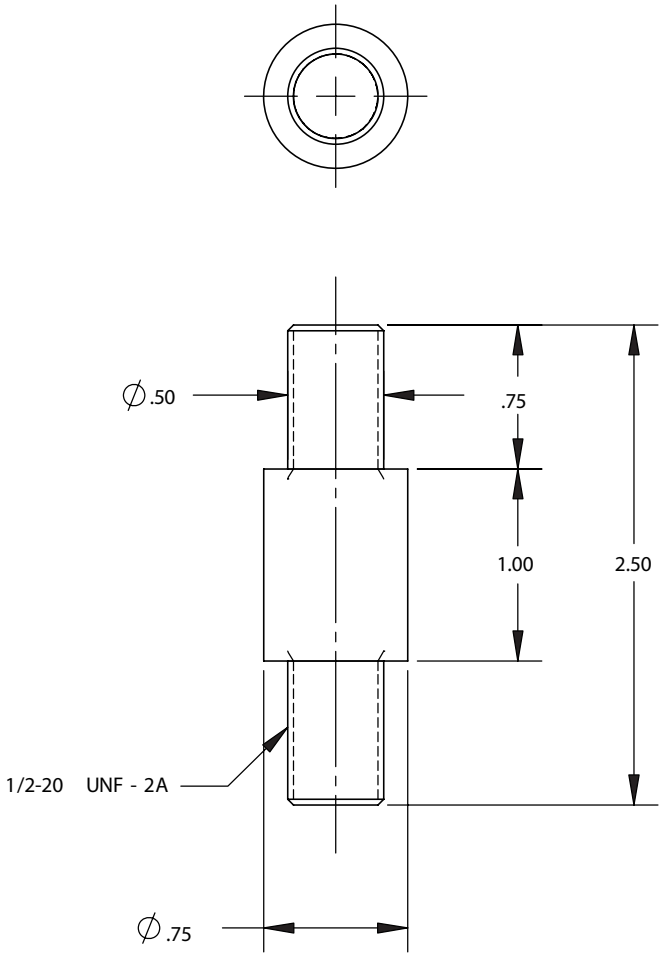

Figure A-11: Drawing of the threaded steel connecting rod used in the heated platen load train. Dimension in inches unless otherwise noted.

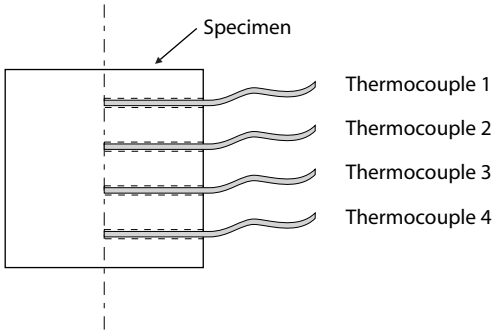

Figure A-12: Schematic drawing of the dummy cylindrical specimen with four thermocouples inserted into it to measure temperature along the specimen axis.

A.2.4 Temperature Measurement and Compensation

To verify that the PMMA compression specimens were being heated uniformly by the chamber and platens, a dummy specimen was made and four thermocouples were inserted into it as shown in Figure A-12 to measure temperature along the specimen axis.

The thermocouples were monitored using a second National Instruments data acquisition card[7] along with a LabVIEW program. The thermocouples are attached to thermocouple extension cables[8,9] connected to a National Instruments SCB-68 terminal block[10]. The terminal block was setup to use a differential measurement for each thermocouple. A resistor was used to create a bias current return path between each of the thermocouple's negative input and the terminal block ground. The SCB-68 has a cold junction channel which the software drivers use to convert the thermocouple measurement into a temperature reading.

It was found that the thermocouples used in the oven controller, platen controllers, and the SCB-68 did not all report the same value for a given ambient temperature. To correct for this, the dummy specimen was placed in contact between the platens, and the temperature of the oven and both platens was then adjusted until the four thermocouples in the dummy specimen varied by less than 0.5 C. The platen and oven controllers often reported temperatures up to 3 C different from the dummy specimen thermocouples. The test temperature reported in the experimental results is the temperature of the dummy specimen, not the setting of the oven or the platens. This procedure was performed at each temperature setting.

The extensometer used for strain measurement was positioned inside the chamber near the platens for each test. To correct strain measurements at elevated temperatures, the extensometer was placed at its zero position and allowed to heat up for approximately 20 minutes inside the heated chamber. The auto calibration procedure was then executed from the Instron controller. This procedure was performed at each new temperature setting.

[7]National Instruments PCI Multifunction Data Acquisition Card, Model PCI-6035E. Analog In: 16bit, 200 kS/s, ranges: ±10V, ±5V, ±500mV, ±50mV; Analog Out: 12bit, 1kHz, ±10V

[8]Omega J-Type Extension Wire, Model EXTT-J-24-25. Max 200C; 24 Awg; Neoflon PFA insulation

[9]Omega J-Type Female Connector, Model OST-J-F. Thermocouple connector

[10]National Instruments Shielded I/O Connector Block, Model SCB-68. 68-pin; IC sensor for CJ compensation; ±1.0C accuracy; Input: 7 thermocouples + CJ channel